

THE ANODIC DECOMPOSITION OF COPPER-RICH MATTES  
USING PARTICULATE ELECTRODES

by

DOUGLAS JOHN McKAY

B.A.Sc. The University of British Columbia, 1981

A THESIS SUBMITTED IN PARTIAL FULFILLMENT OF  
THE REQUIREMENTS FOR THE DEGREE OF  
DOCTOR OF PHILOSOPHY

in

THE FACULTY OF GRADUATE STUDIES  
(Metals and Materials Engineering)

We accept this thesis as conforming  
to the required standard

THE UNIVERSITY OF BRITISH COLUMBIA

March, 1990

© Douglas John McKay

In presenting this thesis in partial fulfilment of the requirements for an advanced degree at the University of British Columbia, I agree that the Library shall make it freely available for reference and study. I further agree that permission for extensive copying of this thesis for scholarly purposes may be granted by the head of my department or by his or her representatives. It is understood that copying or publication of this thesis for financial gain shall not be allowed without my written permission.

(Graduate Studies)  
Department of Mech & Material Engineering  
The University of British Columbia  
Vancouver, Canada

Date March 16/90

## ***ABSTRACT***

The direct anodic decomposition of copper-rich mattes using packed bed electrodes was investigated, because a practical solution to direct electrorefining of copper matte would lead to the potential elimination of copper converting and its associated sulphur dioxide emissions. Much greater copper extraction has been achieved experimentally at 50°C from a packed bed electrode consisting of 0.5-4mm diameter particles than from a massive or solid flat electrode composed of copper-rich matte, as found in earlier studies. This was shown to be attributable to natural convection mass transport processes within the inter-particle region that is not available in massive electrodes. However, while natural convection mass transfer is an important process in the packed bed electrodes, other factors were shown to be ultimately more important in terms of the maximum copper extraction which may be achieved prior to shut-down caused by total-bed polarization of these electrodes.

Total-bed polarization of copper-rich mattes during direct anodic decomposition may be attributed to (a) deteriorating electrical contact (related to the formation of elemental sulphur and lead sulphate) between the current distributor and the adjacent particles, and in thick electrodes, between the particles across the anode, (b) relative nonreactivity of iron-containing phases and (c) physical association of these phases with the reactive phases, and under certain conditions (d) crystallization of copper sulphate within the inter-particle region, blocking ionic conduction paths.

The maximum copper extraction from synthetic pure chalcocite, the predominant component of industrial copper-rich mattes, using the packed bed electrodes was found to be about 80%. The presence of 3-4wt% iron in the copper-rich mattes was shown to degrade the copper extraction considerably due to the presence of relatively nonreactive iron-rich phases which form as the matte is cooled from its liquid state. The presence of lead in copper matte was found to be a relatively unimportant impurity in terms of copper extraction, while oxygen was found to partially offset the negative effects of iron.

A simple one-dimensional mathematical model was developed to estimate the variation of copper extraction across a 2cm-thick packed bed electrode. The copper extraction was found experimentally to vary by less than a factor of two across the anode. This was attributed to (a) the relatively high electrical conductivity of the electrolyte which minimizes reaction-process overpotential gradients across the anode, and (b) the increasing impedances of the decomposition processes in the most reacted particles.

# Table of Contents

ABSTRACT .....	ii
Table of Tables .....	vii
Table of Figures .....	ix
Acknowledgments .....	xii
CHAPTER 1 INTRODUCTION .....	1
CHAPTER 2 SCOPE OF THE PRESENT STUDY .....	3
CHAPTER 3 LITERATURE REVIEW .....	6
3.1 METAL SULPHIDE ELECTROLYSIS .....	6
3.1.1 Historical .....	6
3.1.2 INCO's Nickel-Matte Electrorefining Process .....	8
3.1.3 Copper Sulphide Electrorefining Studies .....	10
3.1.3.1 Chalcopyrite Electrolysis .....	10
3.1.3.2 Chalcocite and Digenite Electrolysis .....	12
3.1.3.3 Covellite Electrolysis .....	17
3.1.3.4 Other Related Studies .....	18
3.1.3.5 Bornite Electrolysis .....	18
3.1.3.6 Electrolytes .....	19
3.2 COPPER SULPHIDE LEACHING .....	20
3.2.1 Chalcocite and Covellite .....	20
3.2.2 Bornite .....	22
3.3 EFFECTS OF IMPURITIES IN COPPER MATTES .....	23
3.3.1 Electrochemical Studies .....	23
3.3.2 Leaching Studies .....	25
3.4 SUMMARY .....	26
3.5 PHASE SYSTEMS .....	27
3.5.1 Cu-S System .....	28
3.5.2 Cu-Fe-S System .....	29
3.5.3 Cu-Pb-S System .....	29
3.5.4 Fe-Pb-S .....	30
3.5.5 Cu-Fe-Pb-S .....	31
3.6 CRYSTAL STRUCTURES .....	32
3.7 COPPER MATTES VERSUS NICKEL MATTES .....	33
3.8 MASS TRANSFER AND CONVECTION .....	36
3.9 MATHEMATICAL MODELS .....	42
3.10 ELECTRICAL CONDUCTIVITY .....	45
3.11 NOMENCLATURE .....	48
CHAPTER 4 EXPERIMENTAL TECHNIQUES .....	50
4.1 CHEMICAL SOLUTIONS AND ANALYSES .....	50

4.2 MATTE SYNTHESIS, CHARACTERIZATION AND PREPARATION FOR ANODIC DECOMPOSITION .....	50
4.2.1 Synthesis .....	50
4.2.2 Chemical Analysis and Phase Characterization .....	50
4.2.3 Preparation for Anodic Decomposition .....	55
4.3 ELECTROLYTIC CELLS: EQUIPMENT AND TECHNIQUES .....	55
4.3.1 Electrode Construction .....	55
4.3.2 Tall (Natural Convection) Electrodes .....	61
4.3.3 Horizontal (Natural Convection) Electrodes .....	62
4.3.4 Small-Scale Thick Electrodes .....	63
4.3.5 Small-Scale Thin Electrode Studies .....	66
4.4 EFFECTIVE CONDUCTIVITY MEASUREMENTS .....	66
CHAPTER 5 NATURAL CONVECTION .....	67
5.1 HORIZONTAL ELECTRODE STUDIES .....	67
5.2 VERTICAL STUDIES .....	69
5.2.1 Convection Studies .....	69
5.2.1.1 Tall Electrode Results .....	69
5.2.1.2 Small-Scale Electrode Results .....	74
5.2.2 Total-Bed Polarization .....	75
5.2.3 Copper Extraction .....	75
5.3 NOMENCLATURE .....	77
CHAPTER 6 PARTICULATE ELECTRODES (Some Fundamentals) .....	79
6.1 A GENERAL MODEL .....	79
6.2 APPLICATION TO COPPER SULPHIDE ELECTROLYSIS .....	82
6.2.1 Tafel Approximation .....	85
6.2.2 Linear Approximation .....	87
6.3 PARAMETER ESTIMATION and MODEL PREDICTIONS .....	87
6.4 NOMENCLATURE .....	93
CHAPTER 7 PERFORMANCE OF THICK PARTICULATE ELECTRODES .....	96
7.1 REACTION DISTRIBUTION .....	96
7.2 ELECTRODE "POLARIZATION" .....	99
7.3 COPPER EXTRACTION .....	101
7.4 OTHER DATA .....	104
CHAPTER 8 IMPURITIES AND DECOMPOSITION MECHANISMS .....	105
8.1 COPPER EXTRACTION AND "POLARIZATION" CHARACTERISTICS .....	105
8.1.1 Impurity Effects .....	105
8.2 IRON EXTRACTION .....	109
8.3 PHASE ANALYSES .....	112
8.3.1 X-ray Powder Diffraction .....	112
8.3.2 Scanning Electron Microscopy .....	112
8.4 GRAIN SIZE & STRUCTURE .....	118
8.5 DECOMPOSITION MORPHOLOGY .....	119

8.6 DISCUSSION .....	123
8.6.1 Phase Changes During Decomposition .....	123
8.6.2 Decomposition Morphology .....	128
8.6.3 Impurity Effects .....	132
CHAPTER 9 CONCLUSIONS .....	143
CHAPTER 10 OPPORTUNITIES FOR FUTURE WORK .....	147
REFERENCES .....	149
APPENDIX A CHEMICAL ANALYSIS OF COPPER MATTES .....	155
APPENDIX B <i>ESTIMATION</i> OF TRANSPORT NUMBERS .....	159
APPENDIX C DERIVATION OF EQUATIONS (6.11) AND (6.12) .....	166
APPENDIX D DISCUSSION OF THE LINEAR APPROXIMATION AND ESTIMATION OF THE EXCHANGE CURRENT DENSITY, $i_0$ .....	168
APPENDIX E REVERSIBLE POTENTIAL FOR THE $\text{Cu}^{2+} \text{Cu}^{\circ}$ ELECTRODE & DECOMPOSITION POTENTIALS FOR VARIOUS SULPHIDE SPECIES .....	170
APPENDIX F POWDER X-RAY DIFFRACTION DATA .....	175
APPENDIX G SOME PRACTICAL ASPECTS OF THE PROCESS .....	182

## Table of Tables

Table 3.1 Analysis of lead-copper matte electrorefined at Stolberg .....	7
Table 3.2 Data on the INCO nickel sulphide electrorefining process .....	9
Table 3.2 Comparison of the various mass transfer components through the product layers in nickel- and copper-matte electrorefining .....	35
Table 4.1 Assay summary for industrial and several synthetic mattes .....	53
Table 4.2 Distribution of particle sizes used in several small-scale 2cm-thick packed bed experiments .....	55
Table 4.3 Summary of the various electrodes employed .....	56
Table 4.4 Some properties of synthetic filter cloth-type diaphragms .....	57
Table 5.1 Summary of electrorefining tests of 2cm-thick horizontal electrodes filled with industrial matte particles .....	68
Table 5.2 Copper concentration at the current distributor and in the gap between the electrodes during electrolysis of industrial matte in a small-scale electrode .....	74
Table 5.3 Comparison between the industrial matte used in this study and the industrial matte used by previous researchers .....	76
Table 7.1 Copper composition and extraction from various positions between the current distributor and diaphragm for selected copper sulphide anodes .....	98
Table 7.2 Voltage balances just behind <i>diaphragm</i> of 2cm-thick particulate electrodes composed of group A and B mattes .....	101
Table 7.3 Increase in particle-current distributor voltage drop and voltage gradient across the anode during total-bed polarization of group A mattes .....	104
Table 8.1 Acid decrease and iron liberation during electrolysis of industrial matte in a 2cm-thick particulate electrode .....	111
Table 8.2 The predominant phases of selected copper mattes before anodic decomposition by powder X-ray diffraction analyses .....	112
Table A.1 Comparison of Atomic Absorption and EDTA titration analyses .....	158
Table B.1 Summary of equivalent conductance of CuSO <sub>4</sub> at several temperatures using Walden's rule .....	159
Table B.2 Summary of transport numbers for various species at 50°C .....	165
Table B.3 Summary of transport numbers for various species at 50°C disregarding the activity coefficients for Cu <sup>2+</sup> and SO <sub>4</sub> <sup>2-</sup> .....	165

Table E.1 Value of the fitting parameters $a(T)$ and $b(T)$ , and the absolute entropy of the hydrogen ion at several temperatures .....	171
Table E.2 Summary of the various parameters used in Eq. (E.2) .....	171
Table E.3 Summary of the free energy and reversible potential for the hydrogen and copper electrodes at 60°C and 100°C .....	172
Table E.4 Thermodynamic data for various copper sulphides .....	173
Table E.5 Reversible potential for various half-cell reactions .....	174
Table F.1 Powder X-ray diffraction data for synthetic $\text{Cu}_{2-x}\text{S}$ containing 4.7wt% Fe .....	175
Table F.2 Powder X-ray diffraction data for synthetic $\text{Cu}_{2-x}\text{S}$ containing 4.5wt% Fe .....	176
Table F.3 Powder X-ray diffraction data for synthetic $\text{Cu}_{2-x}\text{S}$ containing 4.5wt% Pb .....	177
Table F.4 Powder X-ray diffraction data for synthetic $\text{Cu}_{2-x}\text{S}$ containing 4.1wt% Pb .....	178
Table F.5 Powder X-ray diffraction data for synthetic $\text{Cu}_{2-x}\text{S}$ .....	179
Table F.6 Powder X-ray diffraction data for industrial matte .....	180
Table F.7 Powder X-ray diffraction data for re-melted industrial matte .....	181

# Table of Figures

Figure 3.1 E-pH diagram for the system Cu-S-H <sub>2</sub> O at 25°C .....	14
Figure 3.2 Potential-time curves for the anodic electrolysis of particulate and solid Cu <sub>2</sub> S electrodes .....	15
Figure 3.3 Phase diagram for the system Cu-S .....	28
Figure 3.4 Phase relations for the system Cu-Fe-S at several temperatures .....	30
Figure 3.5 Schematic representation of the changes in phase relations in the system Cu-Pb-S .....	31
Figure 3.6 Crystal structures of various copper sulphide minerals .....	32
Figure 3.7 Electrical conductivity of copper sulphide as a function of stoichiometry .....	46
Figure 3.8 Temperature dependance of electrical conductivity for several nonstoichiometric copper sulphides .....	47
Figure 4.1 Summary of the segregation study for impurity-doped synthetic mattes .....	54
Figure 4.2 Construction details of the particulate anode .....	57
Figure 4.3 Techniques for the measurement of solution and particle potentials in the particulate anodes .....	59
Figure 4.4 Summary of the various potentials measured and the terminology used throughout the thesis .....	60
Figure 4.5 Schematic of the horizontal packed bed electrode .....	63
Figure 4.6 Schematic illustration of the cell used in the small-scale electrode studies ....	64
Figure 5.1 Variation of copper concentration with vertical position in the tall particulate anode .....	71
Figure 5.2 Variation of copper, acid and total sulphate concentration with vertical position in the tall particulate anode operated as a bipolar electrode .....	73
Figure 5.3 Galvanostatic potential curves for anodic decomposition of industrial matte in a tall electrode .....	76
Figure 6.1 Schematic of a particulate electrode .....	80
Figure 6.2 Effective electrical conductivity and contact resistance at graphite for industrial matte as a function of copper extraction .....	88
Figure 6.3 Predicted reaction rate distribution in a particulate electrode composed of copper sulphide particles .....	90

Figure 7.1 Galvanostatic potential curves for anodic decomposition of synthetic chalcocite in a 2cm-thick particulate electrode .....	97
Figure 7.2 Galvanostatic potential curves for anodic decomposition of synthetic chalcocite doped with 4.7wt% Fe in a 2cm-thick particulate electrode .....	100
Figure 7.3 Effect of impurities on the copper extraction from crushed synthetic and industrial copper mattes placed in two 2cm-thick electrodes .....	102
Figure 8.1 Copper extraction from various synthetic mattes and from industrial mattes using a thin (2.9mm) particulate electrode .....	106
Figure 8.2 Galvanostatic potential curves for anodic decomposition of synthetic chalcocite and lead-doped synthetic copper matte in a thin particulate electrode .....	107
Figure 8.3 Galvanostatic potential curves for anodic decomposition of synthetic chalcocite and iron-laden mattes in a thin particulate electrode .....	108
Figure 8.4 Iron extraction and iron-copper extraction ratios for anodic decomposition of various iron-laden mattes in a thin particulate electrode .....	110
Figure 8.5 Electron back-scatter micrographs of several lead-doped synthetic copper matte ( $\text{Cu}_2\text{S}$ ) particles .....	113
Figure 8.6 Electron back-scatter micrographs of several iron-doped synthetic copper matte ( $\text{Cu}_{1.96-2}\text{S}$ ) particles .....	116
Figure 8.7 Electron back-scatter micrographs of several industrial matte particles .....	117
Figure 8.8 Electron back-scatter micrographs of several re-melted industrial matte particles .....	118
Figure 8.9 Comparison of the grain size and structure between synthetic copper matte doped with 4.5wt% lead and 4.7wt% iron .....	119
Figure 8.10 Scanning electron micrograph cross section of a synthetic chalcocite particle after total-bed polarization .....	120
Figure 8.11 Scanning electron micrograph cross section of a synthetic chalcocite particle broken apart after total-bed polarization .....	121
Figure 8.12 Scanning electron micrographs of the surface of synthetic chalcocite particles after total-bed polarization .....	122
Figure 8.13 Scanning electron micrographs of industrial matte particles broken apart after total-bed polarization .....	123
Figure 8.14 Electron back-scatter micrographs of iron-doped synthetic chalcocite and pure synthetic copper matte particles after total-bed polarization .....	124

Figure 8.15 Stoichiometry variation between the center of the particles and the particle surface .....	127
Figure 8.16 Anodic decomposition morphology model for chalcocite particles .....	129
Figure 8.17 Anodic decomposition morphology model for iron-doped synthetic copper matte particles .....	135
Figure D.1 Interfacial potential and overpotential of massive digenite ( $\approx\text{Cu}_2\text{S}$ ) anodes with respect to current density .....	168
Figure D.2 Effect of exchange current density on the reaction distribution in a particulate anode composed of copper sulphide particles .....	169

## ***ACKNOWLEDGMENTS***

There are many people who assisted in the completion of this project. In particular, I would like to thank Dr. E. Peters for his wise, steady and encouraging counsel during the course of this study and D. Dreisinger for moral encouragement at times when its successful completion appeared impossible. I am grateful for the timely editorial assistance during preparation of the final version of this manuscript given by Dr. C. Cooper.

I wish to thank my family for their unfailing love, support and encouragement and for believing that I could complete this thesis even when my own confidence was lacking. And finally, to Andrea, whose courage to marry a graduate student and belief in his abilities, and whose patience and understanding have been the inspiration necessary for the completion of this study.

I also wish to acknowledge the timely and generous financial support provided by Noranda.

---

# **CHAPTER 1**

---

## **INTRODUCTION**

More than 90 percent of the world's primary copper is derived from sulphide minerals [1]. Most commonly these minerals are subjected to pyrometallurgical treatment for copper recovery, with the result that the sulphur by-product is liberated as gaseous sulphur dioxide. While the concern for recovery of this sulphur from copper-making processes may not have been of paramount importance a century ago, producers must now wrestle with, in addition to minimizing processing costs and energy demands, the problem of reducing sulphur emissions below stringent environmental standards.

Treatment of sulphur-dioxide-laden gas for the fixation of sulphur has been focussed on two methods: reduction to elemental sulphur and manufacture of sulphuric acid. Although the latter route is favoured by the copper industry, it is by no means a perfected technology. The highly variable flow rate and sulphur dioxide content of the gases leaving the converter make sulphur recovery very difficult. Despite a considerable amount of effort over the years to develop acid plants capable of overcoming these difficulties, the capture of sulphur dioxide from this unit operation remains a problem [2]. The advantage of the reduction of sulphur dioxide to elemental sulphur is that the latter may be easily stored, and so does not require a captive market. However, reduction of sulphur dioxide is a relatively energy-intensive option, which probably accounts for the fact that this technique is not commonly practiced.

For many years hydrometallurgists have proposed processes which would not require a unit operation in which sulphur-dioxide-laden gases, particularly from the troublesome converting step, are treated for sulphur fixation. While a significant number of patents have been issued over the years, very few processes have been developed to the industrial scale. This is apparently because the hydrometallurgical processes, although controlling sulphur emissions, generally suffer from at least one of several disadvantages relative to pyrometallurgical routes [3]:

1. the copper recovery is generally lower,
2. precious metal recovery and separation of metallic impurities are generally more difficult,
3. the processes tend to be more energy-intensive and/or are of greater process complexity and
4. new installations would require capital investments leading to higher write-off costs.

A further option for copper recovery, which apparently controls sulphur emissions satisfactorily, is the direct electrochemical treatment of the sulphides and, in particular, direct electrorefining of the copper-rich matte leaving the smelter in order to bypass the converter. In an electrorefining operation, the matte is formed into an electrode and decomposed anodically in an electrolytic cell to produce copper and elemental sulphur directly. Despite this theoretical advantage, the development of such a process has not advanced to an industrial scale even though a similar development for nickel sulphide has been commercially successful.

The general objective of this thesis is to study the science of this electrometallurgical concept in an effort to understand its limitations relative to commercial application. The development of more specific objectives is provided in the next chapter.

The various potential and polarization terms used throughout the thesis are defined in Chap. 4, Fig. 4.4. Nomenclature lists for Chaps. 3, 5 and 6 are provided at the end of these chapters.

---

## CHAPTER 2

---

### SCOPE OF THE PRESENT STUDY

With the potential benefit of producing both copper and elemental sulphur directly from copper matte in a single electrorefining unit operation, the expectation might be that after over 100 years of study, a commercially viable process ought to have been developed. By comparison, an electrolytic process to recover nickel from nickel matte progressed from bench-scale studies to a commercial reality in under 20 years. Clearly, there are some difficulties unique to copper matte electrolysis that have not yet been either satisfactorily understood or overcome, the most important of which has been total polarization<sup>1</sup> of copper matte electrodes at low copper extraction.

Mao and Peters [4], following the work of Etienne [5], recognized the importance of mass transfer limitations in the many earlier copper matte electrorefining studies using solid or "massive" electrodes and were the first to demonstrate that copper extraction from these mattes may be substantially increased if the matte is formed into a particulate, or packed bed, electrode. Although particulate electrodes provide greatly extended surface areas relative to solid electrodes, and thus reduce the reaction rate requirements (including both mass transport and Faradaic processes) at the actual reaction surfaces, these studies [4], in conjunction with an analysis of nickel and copper matte electrolysis, demonstrated that natural convection mass transfer in particulate electrodes composed

---

<sup>1</sup> Total polarization and total-bed polarization are defined in the Chap. 4, Fig. 4.4. For now, it is sufficient to say that when an electrode "polarizes" during galvanostatic electrolysis, the applied voltage required to maintain a desired rate of reaction exceeds a specified value.

of these materials was also very important. This was a major factor leading to the suggestion that a packed bed of small copper matte particles may be the most promising electrode configuration in terms of potential commercial development. Consequently, the initial goal of this work was to examine the natural convection behavior in a packed bed electrode consisting of copper-rich matte particles.

This study was initiated by evaluating the difference in total-bed polarization and convection behavior between a small packed bed electrode placed in the horizontal position and a tall packed bed electrode, when both were filled with small particles (0.5-4mm) of an industrial matte. However, these electrorefining trials revealed two points: firstly, the copper extracted from the particles prior to total-bed polarization of the tall electrode was less than anticipated based on previous studies [4], and secondly, total-bed polarization of this electrode was apparently not related to natural convection processes. Since the concentration of impurities, such as lead and iron, in the industrial matte employed in the present study was greater than in the previous studies, the impurities were held accountable for the lower than expected copper recovery. It also became clear that total-bed polarization of the electrode was ultimately a combination of several independent components. The objectives of this research were then adjusted to include

- the determination of the components of total-bed polarization and
- an investigation of the effect of impurities in the matte on copper recovery and on the total-bed polarization mechanism.

Since achievement of these goals in a tall electrode was not considered feasible, a small bench-scale cell was utilized. After numerous trials with various synthetically prepared mattes it became evident that the electrical contact between the matte particles and the current distributor<sup>2</sup> was a serious problem for many of the mattes, hindering a proper evaluation of impurity effects.

---

<sup>2</sup> This component of a packed bed electrode provides the electrical link between the particles and the power supply.

Eventually, the conclusion was reached that uniform current distribution throughout a 2cm-thick packed bed electrode of matte particles could be achieved, although the design of a suitable current distributor was considered to be beyond the scope of this thesis.

Uniform current distribution was physically modelled in a series of experiments using an electrode with a thickness approximately equal to the average particle diameter (2.9mm) and filled with a very narrow size range (2-2.8mm) of particles. Also, the current densities were reduced in proportion to the reduction in particle weight. With this apparatus the effects of impurities were more tightly evaluated.

A further, relatively minor, objective of this study was to investigate the distribution of the reaction process within the particulate electrode with the aid of a relatively simple mathematical model. This was considered to be of some importance with respect to certain practical aspects of the process, most notably, the relevance of electrode thickness.

---

## CHAPTER 3

---

### LITERATURE REVIEW

#### 3.1 METAL SULPHIDE ELECTROLYSIS

##### 3.1.1 Historical

The electronic properties of metal sulphides are rather similar to those of semiconductors [6], yet the electrical conductivity of some sulphides may be as high as that for some metals. It is this property which, as pointed out by Habashi [7] and Brennet et al. [8], prompted Marchese to suggest over a century ago (1882) that metal sulphides could be decomposed into their components by direct electrorefining.

There are two possibilities for electrolytic refining. If a metal sulphide is made anodic the following reaction will occur:

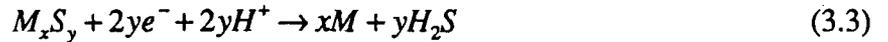


The metal goes into solution while the elemental sulphur remains behind as a "slime". The cathodic reaction is very familiar:



The advantage of these reactions is that elemental sulphur and the metal are obtained in a single step. The major disadvantage is that, for a number of reasons which will be subsequently explained, the cell voltage rises during electrolysis.

Alternatively, the metal sulphides can be electrolyzed cathodically:



The conventional anodic reaction would be the decomposition of water to produce oxygen and acid. Cathodic decomposition of chalcocite is apparently a difficult process as compared to anodic decomposition, requiring relatively high cell voltages and the processing of a hydrogen-sulphide-laden gas for sulphur recovery.

The excellent review paper by Habashi [7] illustrates the extent of development and pilot-scale work on metal sulphide decomposition by electrolysis, particularly regarding copper sulphides, performed in the late 1800's and the first decade of this century. For example, in 1885, following encouraging bench-scale tests by Marchese, a 500kg/d pilot plant was erected at Stolberg, Germany to recover copper electrolytically from a lead-copper matte (composition given in Table 3.1). The matte was cast into 124kg anodes (measuring 80x80x4cm) which were slowly cooled to prevent cracking. Electrolysis was performed in an electrolyte analyzing 27g/l copper and 15g/l iron. The idea was to dissolve copper from the anode and deposit it at the cathode, leaving sulphur behind as a "slime" which could be processed to recover silver.

**Table 3.1** Analysis of the Lead-Copper Matte Electrorefined at Stolberg, in weight percent (according to Habashi's review [7]).

Metal	Analysis
Cu	15-16
Pb	14
Fe	41-42
S	25
Ag	0.05

The plant apparently operated for only two months. It was successful for the first few days and produced good copper (99.9+%) at the cathode. However, serious difficulties developed. The cell voltage increased to five volts, thought at the time to be due to a buildup of lead dioxide at the anode, and the anodes started to break down, with the result that the project was abandoned.

Considering the high iron content in the electrolyte and the complexity of the matte, it is difficult to rationalize how the process could ever have been successful. Nevertheless, this attempt inspired numerous other investigators to study the process between 1900 and 1910.

Habashi also reported that a second copper sulphide electrolysis pilot plant campaign was attempted at Eislenben, Germany around 1906. About 10 tons of copper were produced per week. However, the process was, for reasons which were not well documented, discontinued. Subsequently, little interest in copper sulphide electrolysis was demonstrated, although a few studies were reported by Russian researchers in the 1940's. It was not until International Nickel Company's (INCO) successful pilot- and commercial-scale testing of a nickel matte electrorefining process at Port Colborne, Ontario by 1958 [10], followed by the commissioning of a full-scale facility at Thompson, Manitoba in 1961 [11], that there was renewed enthusiasm for copper sulphide electrorefining.

### 3.1.2 INCO's Nickel-Matte Electrorefining Process

Literature reports on the development and operation of the Thompson refinery are relatively limited [10-13]. Nevertheless, from these reviews a considerable understanding may be developed.

Essentially pure nickel matte,  $Ni_3S_2$ , is cast into anodes (measuring 110x72x5cm) at about 980°C. The anodes are allowed to cool rapidly to about 510°C and promptly placed in a cooling box where they are cooled under controlled conditions to 200°C. This procedure is of paramount importance because rapid cooling through the  $\beta Ni_3S_2 \rightarrow \beta' Ni_3S_2$  phase transformation at 505°C would result in severe cracking of the anodes. The duration of this step is about 25 hours. From the cooling box the anodes are transported to the tank rooms. The anode and electrolyte compositions are summarized in Table 3.2.

Nickel sulphide mattes have been reported to decompose according to the following reactions [11,16,17]:





**Table 3.2** Data on the INCO Nickel Sulphide Electrorefining Process [10].

Anode Composition		Electrolyte Composition	
Metal	Analysis (wt%)	Species	Analysis (g/l)
Ni	76.0	Ni <sup>2+</sup>	60
Cu	2.6	SO <sub>4</sub> <sup>2-</sup>	100
Co	0.5	NaCl	100
Fe	0.5	H <sub>3</sub> BO <sub>3</sub>	20
S	20.0		

A mass balance of the starting composition given in Table 3.2 shows that of the 76wt% nickel present, only about 50-52wt% exists as a sulphide. This accounts for reaction (3.4). If the anode potential is maintained above 0.6V versus a saturated calomel electrode (0.84V versus the SHE), Ni<sub>3</sub>S<sub>2</sub> apparently prefers to react according to reaction (3.5) [17]. In fact, this is the only reaction reported for Ni<sub>3</sub>S<sub>2</sub> by Spence and Cook [11]. The actual operating potential of the matte anode must be quite high because oxygen discharge (E°=0.99V at a pH of 4) is reported to consume 5-7% of the current [11].

Due to the simultaneous liberation of copper and iron that would either contaminate the nickel product or reduce current efficiency, the electrorefining is carried out in a diaphragm cell to permit anolyte purification. During the purification step, the pH is adjusted to about 4.5 to ensure that discharge of hydrogen is kept to a minimum. Furthermore, nickel is added to the catholyte to account for an imbalance between the anodic and cathodic current efficiencies.

As the anodes corrode, sulphur, forms on the anode as a sludge layer, which contains the precious metals. At the end of a 22-day refining cycle this sludge occupies roughly twice the volume of the original anode [11]. As a consequence of this growing sludge, or "slime", layer, the cell

voltage rises from approximately 3 volts with new anodes to about 5 volts at the end of the cycle. The sludge is processed for sulphur recovery and treated to obtain the precious metals, according to the methods outlined by Spence and Cook [11].

The success of this process has apparently impressed other nickel producers and there are reports describing nickel matte electrorefining at several other locations:

1. Englehard, New Jersey, USA: separation of copper and nickel in a copper-nickel-sulphur matte [7].
2. Norilsk Mining and Metallurgical Combine, USSR [7].
3. Shimura Nickel Company, Tokyo, Japan: direct nickel recovery from nickel matte [7].
4. Sumitomo Metal Mining Co. Ltd., Niihama, Japan: direct nickel recovery from nickel matte [15,16].
5. B.P. Research, UK: piloting of nickel recovery from a nickel-iron-sulphur concentrate using a slurry anode [14].

### **3.1.3 Copper Sulphide Electrorefining Studies**

There would appear to be two broad options for electrolytic processing of copper sulphides. Firstly, the concentrates, which are predominantly chalcopyrite ( $\text{CuFeS}_2$ ), may be directly electrolyzed. Secondly, the concentrates may be treated by a modern copper smelter to produce high-grade matte, composed essentially of chalcocite ( $\text{Cu}_2\text{S}$ ), which may then be electrorefined.

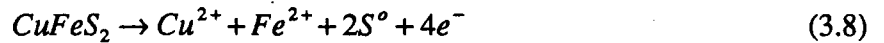
It is also of interest to review bornite ( $\text{Cu}_5\text{FeS}_4$ ) electrochemistry, since this species may, depending on the thermal history, be present in industrial copper-rich mattes.

#### **3.1.3.1 Chalcopyrite Electrolysis**

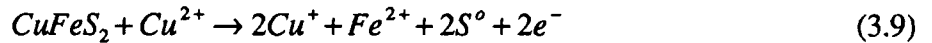
The scope of the proposed research does not pertain to chalcopyrite electrolysis. Nevertheless, several comments will be made so as to demonstrate the relative merits of copper-matte refining.

The decomposition of chalcopyrite has been studied extensively with respect to understanding both its electrochemical behaviour [18-20,26] and potential for direct treatment for copper recovery [21-30]. The picture which emerges from these studies is that there are several practical difficulties with chalcopyrite electrolysis.

Chalcopyrite oxidation at practical current densities releases both copper and iron to the electrolyte, requiring a considerable amount of continuous iron removal and fixation for disposal to the environment. In addition, some studies have shown that sulphur oxidation to sulphate may also occur, thereby reducing the current efficiency of the anodic reaction and requiring treatment of the electrolyte for recovery of this sulphur. The anodic reaction may be generally represented by Eq. (3.8).



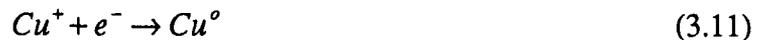
The most noteworthy development of an electrochemical process for chalcopyrite oxidation at practical current densities is the DEXTEC process [22], which has been demonstrated in a 0.5 tonne per day pilot plant. The anode in this process is essentially a slurry of chalcopyrite particles maintained at an anodic potential through contact with a graphite current distributor. Either the anodic slurry or the electrolyte re-circulating outside the cell is aerated to precipitate the iron as goethite (FeOOH), which is subsequently recovered by filtration. The proposed reactions are summarized below [3]. At the anode:



with air oxidizing the cuprous ion and precipitating iron



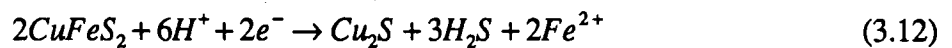
At the cathode cuprous ions are reduced:



The copper is present in solution as cuprous ions due to complexing with chloride as  $\text{CuCl}_2^-$ . Because the solution is a strong brine at  $\text{pH} \approx 3$ , the iron hydrolyzes as shown above. There are claims the process achieves very high current efficiencies because the air also oxidizes copper I to copper II, and the latter acts as a secondary lixiviant, as shown above in Eq. (3.9).

The sulphur forms as a fine suspension which is reportedly easily filtered. An advantage of the process is that only one electron per copper atom is required. However, a disadvantage of this process is that in chloride electrolytes, the dissolution potentials for silver and copper are much closer together than in sulphate electrolytes. The result of this is that silver may easily be released from the chalcopyrite and then deposit on the cathodes. Consequently, the copper deposits must be treated for silver recovery.

Chalcopyrite reduction, as demonstrated in the following equation, achieves a separation of copper and iron by releasing iron to the electrolyte and forming the second sulphide phase, chalcocite, as a reaction product layer which is subsequently treated for copper recovery. However, the disadvantages with this option are that hydrogen sulphide gas is evolved from the electrolytic cells and must be treated, iron must be recovered from the electrolyte as above and downstream processing of the chalcocite may release iron from any non-reduced chalcopyrite. Furthermore, the cathodic current efficiency is markedly less than 100% due to the discharge of hydrogen in addition to hydrogen sulphide.



No known study of chalcopyrite reduction has advanced to the piloting stage.

### 3.1.3.2 Chalcocite and Digenite Electrolysis

A continuous smelter tuned to produce high-grade matte liberates a gas stream easily processed for sulphur recovery and separates most of the iron as an inert slag. The matte may then be electrorefined directly to yield copper and elemental sulphur at high current efficiency. INCO's successful nickel-matte electrorefining process has motivated numerous researchers to investigate the electrochemistry of chalcocite [4,5,8,33-35,37,38,39,41-43] and the direct electrorefining of

copper matte [4,35-38] with the objective of developing a similar process.

Of the two methods to electrolyze chalcocite, anodic decomposition has been by far the most popular, probably owing to lower cell voltages than the cathodic route and production of elemental sulphur directly. However, chalcocite does not anodically decompose directly to sulphur and copper ions as suggested by Eq. (3.1). The decomposition is understood to proceed via a series of intermediate sulphide phases, for example, djurleite ( $\text{Cu}_{1.96}\text{S}$ ), digenite ( $\text{Cu}_{1.76-1.83}\text{S}$ ), blue-remaining covellite ( $\text{Cu}_{1.1}\text{S}$ ), and covellite ( $\text{CuS}$ ). Koch and MacIntyre [42] reported the formation of numerous decomposition intermediates in their thin-film studies:  $\text{Cu}_{1.91-1.95}\text{S}$ ,  $\text{Cu}_{1.80-1.86}\text{S}$ ,  $\text{Cu}_{1.65-1.68}\text{S}$ ,  $\text{Cu}_{1.36-1.40}\text{S}$  and  $\text{CuS}$ . Potter [43] reported the existence of the phases,  $\text{Cu}_{1.965}\text{S}$ ,  $\text{Cu}_{1.934}\text{S}$ ,  $\text{Cu}_{1.765}\text{S}$ ,  $\text{Cu}_{1.75}\text{S}$ ,  $\text{Cu}_{1.4}\text{S}$ ,  $\text{Cu}_{1.1}\text{S}$  and  $\text{CuS}$  and provided free energy data for each. These reaction sequences are often summarized as:



The reversible potentials for these reactions have been studied or reviewed by a number of researchers, for example [5,42,43,52,53,95]. Approximate values may be estimated from Fig. 3.1, which also shows the stability region of chalcocite to cathodic treatment. It is interesting to note that sulphur should theoretically be oxidized to sulphate at the potentials of these reactions and it is only the slow kinetics of sulphur oxidation which permits elemental sulphur formation in metal sulphide electrolysis.

Virtually all investigators have found that during galvanostatic electrolysis in an electrolyte very similar to that used in copper refineries (1.5-2M  $\text{H}_2\text{SO}_4$ , 0.6M  $\text{CuSO}_4$ ) chalcocite and digenite decompose at high current efficiencies (close to 100%) and low overpotentials (<0.3V, anode potential 0.5-0.7V versus the standard hydrogen electrode or SHE). However, electrolysis at low overpotentials eventually comes to an end with a rapid increase in the total overpotential to more than 1V, reduced current efficiencies and sulphur oxidation. Typical potential-time curves are shown in Fig. 3.2.

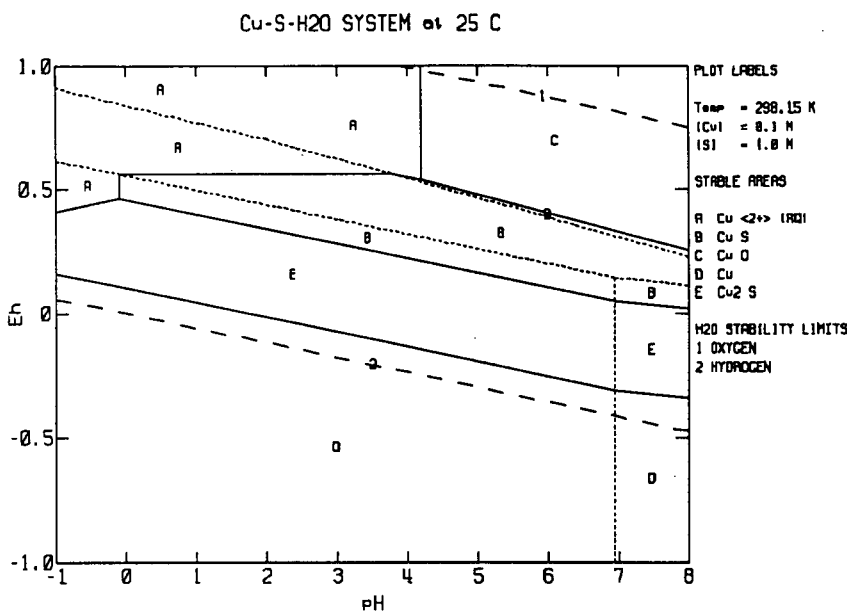


**Figure 3.1**  $E_h$ -pH diagram for the system Cu-S-H<sub>2</sub>O at 25°C. The activities of Cu<sup>2+</sup> and SO<sub>4</sub><sup>2-</sup> are 0.015M and 0.1M, respectively. An activation energy of 300kJ/mol is assigned to the formation of SO<sub>4</sub><sup>2-</sup> to reflect the fact that S° is formed during electrolytic decomposition.<sup>1</sup>

A review of the electrode configurations used by the various researchers is important because the polarization mechanism is very much dependent on the electrode type. For example, note in this Fig. 3.2 that the time of electrolysis prior to polarization in the particulate electrodes is in hours, whereas the massive anode polarizes in minutes.

When using massive electrodes, the time at which electrolysis at low overpotentials ends, which is called the transition time,  $\tau$ , is particularly sensitive to the current density,  $i$ . The polarization mechanism was debated over the years but a mechanism proposed by Etienne [5] is now generally accepted. Etienne recognized that the transition time was related to the current density and electrolysis time according to the following relation:

<sup>1</sup> This figure was generated using a program for the Personal Computer called *Thermo*, licensed by the Commonwealth Science and Industrial Research Organization, Australia.

$$i^2\tau = \text{constant}$$

(3.15)

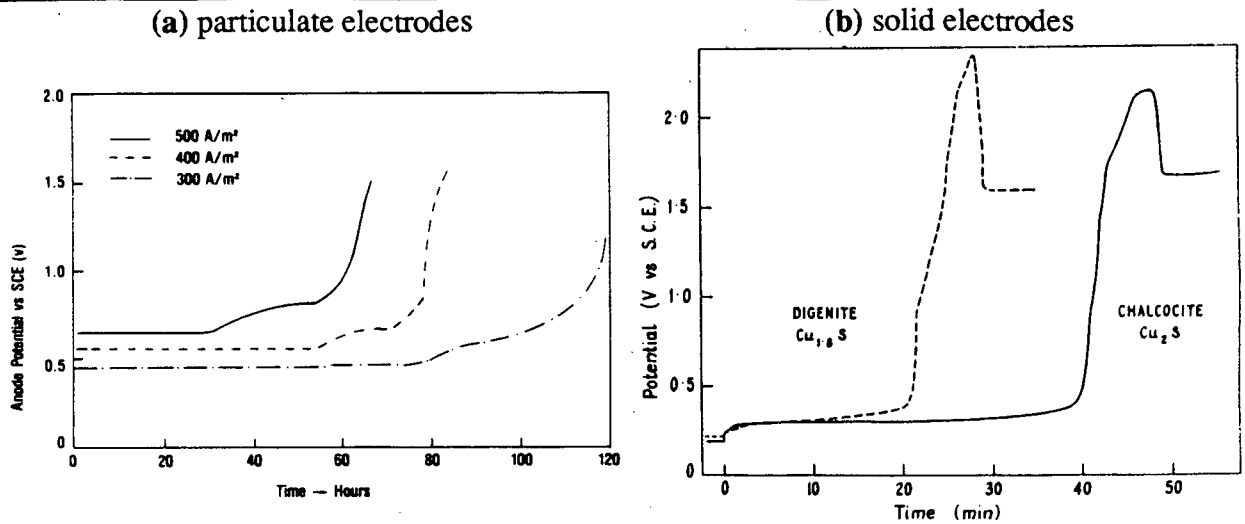


**Figure 3.2** Potential-time curves for (a), the anodic electrolysis of 2.3-3.3mm chalcocite particles using a particulate electrode (electrolyte: 0.63M CuSO<sub>4</sub>, 2M H<sub>2</sub>SO<sub>4</sub> at 40°C) [4], and for (b), the anodic decomposition of the copper sulphides, chalcocite and digenite as solid electrodes (electrolyte: 1M H<sub>2</sub>SO<sub>4</sub>, 0.1M CuSO<sub>4</sub> at 25mA/cm<sup>2</sup> and 25°C) [29].

Since this is consistent with a mass transport mechanism, it was concluded that the rate of chalcocite oxidation was controlled by the diffusion of cupric ions through the electrolyte filling the pores of the covellite-sulphur surface reaction products.<sup>2</sup> Etienne theorized that polarization was due to precipitation of copper sulphate in these pores, thereby blocking the transfer of current to the reactive surfaces of the electrode. Very little copper was extracted from the chalcocite anodes at the transition time because the reaction extracted about 50% of the copper to a depth of only about 150µm (at 200A/m<sup>2</sup>).

This is similar to the polarization mechanism on copper anodes in electrorefining operations later proposed by Abe et al. [9], who found that the slime layer inhibited the diffusion of copper ions, leading to copper sulphate precipitation on the anode surface and polarization of the anode.

<sup>2</sup> The electrode dimensions do not change during electrolysis. Since the molar density of covellite is greater than that of chalcocite, the covellite product will be porous. The theoretical porosity is 0.27 based on literature values of molar volumes for these compounds [40].

While Etienne used only sulphate electrolytes, Biegler and Swift [31] verified this theory in various other electrolytes by showing that the transition time for chalcocite electrolysis was directly related to the solubility limit of the copper salt in the electrolyte. (The concentration of copper in the bulk electrolyte was initially equal to zero). However, they pointed out that variations in the diffusivity of the cupric ion for nonzero bulk concentrations of copper, and the variability of product layer compositions and structures are also important in terms of second order effects on the transition time,  $\tau$ .

In spite of this evidence, the controversy between solid state and solution diffusion apparently still exists. In a relatively recent paper, Price [44] concluded, from a review of all previously published data (including that of Etienne [5] and Biegler and Swift [31]), that the anodic decomposition of chalcocite and digenite is controlled by a combination of solid state diffusion processes and chemical interaction between the solid and the solution. Price gave several reasons, the most notable of which were (a) there is, in practice, some variation in  $i^2\tau$  with  $i$ , and (b) the precise theoretical dependence of  $i^2\tau$  on  $(\text{Cu}_{\text{sat}}-\text{Cu}_{\text{sol}})$  is not found experimentally.

Using a fluidized bed anode and a sulphate electrolyte, MacKinnon [33] found that 50% copper extraction could be achieved at high current efficiency and constant potential before the electrode polarized (from 0.3V to 1.8V versus the SCE), leading to vigorous evolution of oxygen gas at the platinum current distributor. Since no sulphur was found in the anode residues (by x-ray diffraction), MacKinnon concluded the high overpotential which developed at 50% copper extraction was due to the difficult nucleation of sulphur on the intermediate  $\text{Cu}_{1.1}\text{S}$ , and not as a result of copper sulphate precipitation.

MacKinnon also tested chalcocite oxidation in a chloride-sulphate electrolyte and found that, while about 95% of the copper could be extracted under galvanostatic conditions, copper extraction beyond the 50% level was at increased anode potentials and accompanied by the discharge of chlorine at the platinum current distributor.

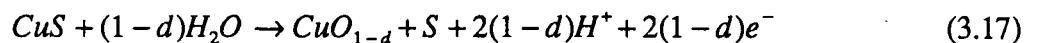
Mao and Peters [4], extending the work of Hojo and Peters [32], studied the electrolysis of particulate anodes consisting of crushed chalcocite particles (0.6-3.3mm). The idea was to maintain a high current density ( $>200\text{A/m}^2$ ) through the diaphragm while permitting a low current density at each particle. They observed that the characteristic polarization could be delayed until 65-75% extraction, even at  $400\text{A/m}^2$  across the diaphragm, provided the electrolyte temperature was greater than about  $25\text{-}30^\circ\text{C}$ . When the temperature was less than about  $25^\circ\text{C}$ , total polarization of the electrode was due to copper sulphate precipitation within the electrode. Above  $25^\circ\text{C}$  they found elemental sulphur in the packed bed at the transition time, leading to the suggestion that polarization in the particulate anode resulted from electrical insulation of the particles from the current distributor by the adhering sulphur reaction product. The delay in polarization to more than 50% copper extraction in the packed bed, as opposed to less than 50% recovery on massive electrodes, was attributed to convection of electrolyte within the bed, thereby ensuring good mass transfer of copper from within the electrode compartment through the diaphragm to the bulk solution. Thus, precipitation of copper sulphate was avoided.

The transition time in these studies was found to be almost directly proportional to the packed bed thickness,  $L$ , and inversely proportional to the current density:

$$i\tau L^{-1} = \text{constant} \quad (3.16)$$

### 3.1.3.3 Covellite Electrolysis

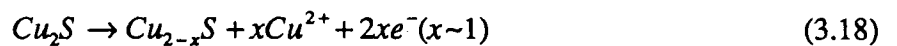
The formation of a phase with a stoichiometry close to that of covellite is inevitable during chalcocite or copper matte oxidation. Unfortunately, in sulphate electrolytes the covellite is decomposed at practical overpotentials only at low current densities ( $<10\text{A/m}^2$  [5,34,45],  $<20\text{A/m}^2$  [41]). The reason for this slow electrochemistry is not well understood. Hillrich and Bertram [34,45] suggest the decomposition may be impeded by a thin oxide layer ( $\text{CuO}_{1-d}$ ,  $d=0.33$ ). Its formation is reportedly favoured by high current densities and high pH and is only broken down at a high applied potential ( $\approx 2\text{V}$ ).



Crundwell [46] suggests the high overpotentials necessary to decompose covellite may be attributable to its crystal band structure. Peters proposes the slow electrochemistry of covellite *may* be due to the difficult nucleation of sulphur at moderate current densities [3], and *possibly* due to the blockage of reaction surface by elemental sulphur at excessive current densities [6]. Ghali et al. [47] studied covellite dissolution using a chloride electrolyte and proposed that passivation could be due principally to elemental sulphur coupled with pore diffusion and/or stoichiometry changes at the active site-electrolyte interface. They also found the peak current in potentiodynamic studies increased appreciably with increasing porosity of the covellite specimens.

#### 3.1.3.4 Other Related Studies

With the objective of achieving copper dissolution at practical current densities and temperatures, the United States Bureau of Mines [41] have recently conducted investigations using a membrane cell. Natural chalcocite and covellite specimens were used as both anode and cathode. In one of the tests, a massive chalcocite electrode was oxidized at 500A/m<sup>2</sup> until polarization occurred. The electrode polarity was then reversed for a certain period of time. Dissolution during the anodic cycle was given as:



Provided the cathodic treatment was less than 600 seconds, the time required to achieve polarization on the subsequent anodic cycle equaled the cathodic treatment time. The cathodic reaction of Cu<sub>2-x</sub>S (E°=-0.37V) was given in a general form earlier in this report (Eq. (3.3)). Similar results were obtained when a covellite electrode was used, except the electrode was treated cathodically prior to the first anodic cycle. While these experiments are intriguing, an assessment of their practicality, given the very short cycle times (9-12min) during the laboratory tests, was not provided.

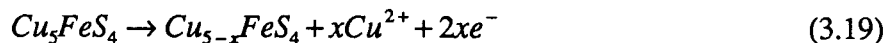
#### 3.1.3.5 Bornite Electrolysis

The electrochemistry of this species has not received as much attention as the copper sulphide species discussed in the preceding sections.

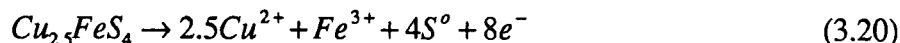
Price and Chilton [24] identified three stages during galvanostatic electrolysis of pressed, sintered discs of synthetic bornite in sulphuric acid solutions (100g/l H<sub>2</sub>SO<sub>4</sub>). They also reported that these stages appeared qualitatively different for each of two temperature regions, 20-50°C and 65-95°C. In the low temperature range and at 38.5A/m<sup>2</sup>, the first stage of electrolysis was characterized by a nearly constant anode potential of about 0.8V for a period of time (≈1hr), followed by a large increase in potential to about 4-5.5V over the next 1-2hrs. In the second dissolution stage, the potential declined slightly (≈1V) and was followed by electrolysis at nearly constant potential for a relatively short period of time. However, the anode potential eventually rose to more than 8V (3.5-4hrs after current was first switched on). This was defined as the third stage of dissolution. All potentials were measured relative to a saturated calomel electrode (0.236V).

Electrolyte analyses indicated that during the first stage of dissolution copper was dissolved preferentially from the mineral. During the second stage, iron also dissolved and some elemental sulphur formed. The overpotential for oxygen discharge on the bornite discs and the reaction products must have been very high since oxygen evolution was only reported during the third decomposition stage when the anode potential rose above 4-5.5V.

Microprobe analyses and calculations on x-ray data indicated the product of the first stage dissolution was Cu<sub>5-x</sub>FeS<sub>4</sub>, where x approached 2.5. The reaction given was:



In the second and third dissolution stages, this intermediate product decomposed according to:



### 3.1.3.6 Electrolytes

Studies of chalcocite oxidation have generally been restricted to sulphate electrolytes. Others have been investigated but each of these present problems not encountered in sulphate systems. In chloride electrolytes copper-silver separation is poor, potentially necessitating further refining of the cathodes to produce acceptable copper. At more than 50% copper extraction in some particulate electrode systems, chlorine may be discharged at the current distributor. Acidic nitrate electrolytes

are unsuitable because the preferred reaction at the cathode is reduction of the nitrate ion rather than deposition of copper. Acidic perchloric electrolytes are potentially ideal for electrochemical application since they do not form complexes with most metallic species and the electrical conductivity is good; however, they are expensive and pose a serious safety problem due to the explosive nature of dried perchlorate salts. Ammoniacal solutions are not very conductive and this leads to high cell voltages. Solutions containing acetonitrile are appealing since the cuprous ion is the stable species and therefore only one charge equivalent would be required to electrorefine a mole of copper. However, acetonitrile electrolytes pose a serious health problem due to the high toxicity of volatile organic vapours.

## **3.2 COPPER SULPHIDE LEACHING**

### **3.2.1 Chalcocite and Covellite**

Since the leaching mechanism of several lixivants, such as the ferric ion, is electrochemical [21,53], leaching studies offer some information which is helpful to the present study. However, it is important to recognize the major difference between direct electrolytic decomposition and decomposition by leaching, which is that in the former, the dissolution rate is usually fixed, while in the latter the dissolution potential remains nearly constant, with the result that the rate typically decreases with time.

Dutrizac and MacDonald [49] reviewed many studies on ferric ion leaching of various metal sulphides, including chalcocite and covellite. The results of the studies were in general agreement with the electrochemical research.

(1) Chalcocite did not decompose directly to copper ions and elemental sulphur, but dissolved in several stages. In the first stage of leaching, some reports suggested chalcocite was converted to digenite, which was subsequently converted to blue-remaining covellite; in the second leaching stage, the blue-remaining covellite dissolved to yield elemental sulphur. Some authors did not report the existence of digenite and suggested the first leaching stage ended with the formation of covellite and that this sulphide decomposed in the second leaching stage.

(2) There was, however, general agreement that (a) the first leaching stage was relatively rapid, with the leaching rate determined by the mass transfer of ferric ions to the corroding surfaces, and (b) the second stage of leaching was very much slower and had a relatively high activation energy, suggestive of chemical reaction control.

(3) Covellite leaching was characterized by a relatively high activation energy, which suggests chemical reaction control.

According to Price [44], Marcantonio's [51] leaching results showed that ferric leaching produced  $\text{Cu}_{1.2}\text{S}$  and that solid state diffusion of cuprous ion was important in the dissolution of this phase directly to sulphur.

Mao and Peters [52] studied acid pressure leaching of chalcocite and also reported that dissolution resolved into two distinguishable steps. The first step was relatively rapid conversion of chalcocite to the intermediate phase digenite, followed by conversion of the digenite to covellite. The second stage in their studies was characterized by breaking up of the particles and by partial conversion of covellite to elemental sulphur. The yield of elemental sulphur increased when ferric ion was added to the leach solutions. A mixed potential model was proposed to describe the leaching process. The first step was essentially cathodically controlled. The slow second stage was attributable to covellite passivation, leading to a high mixed potential. Depassivation occurred in the presence of ferric ions and the yield of elemental sulphur increased due to a lower mixed potential.

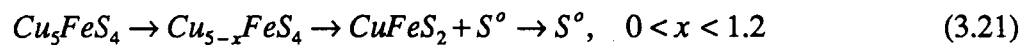
The results of King et al. [54] are consistent with the above studies in terms of the two-stage leaching process. However, microprobe and powder x-ray diffraction analyses on partially leached material led these researchers to suggest that the first leaching stage may have been characterized by the continuous removal of copper from the sulphur lattice to produce a continuous solid solution between  $\text{Cu}_2\text{S}$  and  $\text{CuS}$ . For example, they found the digenite structure in materials with an overall composition  $\text{Cu}_{1.46}\text{S}$  and the strongest line for covellite in materials of overall composition  $\text{Cu}_{1.586}\text{S}$ . Furthermore, they suggested the reaction product of the first leaching stage may have been  $\text{Cu}_{0.8}\text{S}$ , but pointed out it was impossible to be certain of this.

Muir [39] also reported a copper-deficient covellite species,  $\text{Cu}_{2-x}\text{S}$  ( $x \approx 1.3$ ) in chalcocite leaching. The evidence for the existence of this phase was obtained from leaching studies in aqueous acetonitrile solutions at temperatures below  $35^\circ\text{C}$ . At higher temperatures ( $40\text{-}70^\circ\text{C}$ ) this metastable phase apparently disproportionated at observable rates to covellite and elemental sulphur.

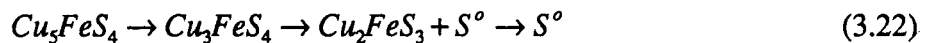
Biegler and Swift [19] also discussed the formation of non-stoichiometric phases which might exist during anodic decomposition of massive chalcocite specimens. Based in part on in-situ observation during direct electrolysis of chalcocite, but largely on previous leaching studies, they proposed that solid-state diffusion processes are too slow to allow equilibrium in massive samples. Therefore, the result is a product layer containing unstable solid solutions of copper and sulphur covering the range  $\text{CuS-Cu}_2\text{S}$ .

### 3.2.2 Bornite

In their review of metal sulphide leaching by ferric ion, Dutrizac and MacDonald [49] described several studies on bornite leaching in acidified sulphate solution. All studies showed that bornite dissolution proceeds through a series of intermediate products, although the reported stoichiometry of the intermediate products varied between investigators. The decomposition sequence proposed in one study was:



and that in another was:



In the temperature interval  $40\text{-}70^\circ\text{C}$  all studies showed the dissolution of bornite to the first reaction intermediate was relatively rapid and was thought to be controlled by solution diffusion of the ferric ion. However, dissolution of the intermediate products, particularly of the most copper-deficient, was slower and characterized by increased activation energy, suggestive of chemical or chemisorption control. The interesting point to note is that these studies showed that only copper was leached in the first two stages of the decomposition process.

In one study (in which the first of the above decomposition sequences was proposed) the rate of the first decomposition step was found to be independent of the ferric ion concentration provided it was greater than 0.1M. However, the leaching rate dropped sharply with increasing ferrous ion concentration. This suggested that bornite leaching was influenced by electrode potential, presumably because the leaching rate was in the activation polarization region for bornite and the potential of the ferric-ferrous couple was lowered with increasing concentration of ferrous ions, thus shifting the mixed potential to lower current densities.

In ferric chloride solutions, Pesic and Olson [55] also found that bornite leached in multiple stages as in Eq. (3.21), with the first stage of leaching (to  $x=1.4$ ) occurring much more rapidly than the subsequent stages. As well, they found that the first leaching stage was controlled by the solution diffusion of ferric ions, but proposed that the surface reaction of cuprous ions was also important. They suggested that the potential of the surface reaction was governed during the first stage of decomposition by the concentration of labile cuprous ions in the bornite lattice. These authors reported a transition period during the second leaching stage leading to an overall stoichiometry  $\text{Cu}_3\text{FeS}_4$ , controlled by the nucleation and growth of sulphur on this intermediate. Thereafter, the leaching rate was reported to be controlled by diffusion through the sulphur product layer.

Dutrizac et al. [50] found that up to 25% of either pyrite or digenite did not affect the leaching rate of bornite at 70°C. At 15°C, digenite had only a minor effect, while that of pyrite increased the dissolution rate slightly. In addition, minor variations in bornite's stoichiometry had no effect.

### **3.3 EFFECTS OF IMPURITIES IN COPPER MATTES**

A rigorous evaluation of the effect of impurities such as lead and iron on the anodic dissolution mechanism and copper recovery from copper-rich matte and impurity-doped synthetic chalcocite apparently has not been performed. The available electrochemical studies appear to be limited to those reviewed in the following section.

#### **3.3.1 Electrochemical Studies**

Habashi and Torres-Acuna [38] reported dissolution of a massive copper matte anode containing 0.65wt% Fe could be achieved at over 90% current efficiency under optimum conditions.

(reported as: 100A/m<sup>2</sup>, 100g/l H<sub>2</sub>SO<sub>4</sub>, 30g/l Cu, 55°C). The cathodic current efficiency was 98%. However, the duration of their tests appears to have been insufficient to extract even 50% of the copper and their data suggest that the anode actually operated under polarized conditions for an appreciable fraction of the total electrolysis time.

Venkatachalum and co-workers [35,36] tested a matte containing appreciable quantities of iron (Cu 42.47wt%; Fe 21.61wt%; Ni 3.92wt%; S 23.29wt%) in 2N H<sub>2</sub>SO<sub>4</sub> and a current density of 100A/m<sup>2</sup>. This matte can hardly be considered "high grade" and it is not surprising that the current efficiencies with respect to copper dissolution and deposition were poor. They found copper preferentially dissolved during the initial stages of electrolysis, reporting current efficiencies of only 75% and 88% for the anodic and cathodic reactions, respectively. After operating for only eight hours, the copper dissolution current efficiency actually decreased to a value lower than that for iron dissolution. Furthermore, an inspection of their results suggests the duration of their tests was sufficient to liberate only about 10-15% of the copper from the anode.

Frenay [37] electrorefined synthetic massive mattes containing various quantities of iron (10-60wt% FeS) and also found copper dissolved in preference to iron, at least during the initial stages of electrolysis, but, that this selectivity decreased with time. The ratio of ferrous iron to total iron increased with time, prompting Frenay to conclude that ferric ions were reduced at the cathode at a greater rate than ferrous ions were oxidized at the anode. No explanation was offered. Casting of the mattes containing more than 20wt% FeS required a procedure similar to that employed by INCO to prevent cracking. After a certain period of electrolysis, the cell potential suddenly increased. The duration of these tests suggests that the anode was corroded under polarized conditions for a significant fraction of the time.

Following these tests, Frenay decomposed an industrial matte (Cu 67.48wt%; Fe 4.91wt%; Zn 4.61wt% Pb 1.12wt%; S 22.73wt%) at 100A/cm<sup>2</sup> and 55°C for four days. During this period 54% of the copper and 47% of the iron dissolved from the massive test specimen. Some zinc was also liberated, resulting in dissolution current efficiencies for copper, iron and zinc of 84%, 2.4%, and 2.3%, respectively. The remaining 11.3% was likely attributable to sulphur oxidation since a

sulphur balance indicates that 10% of the original sulphide sulphur was not present in either the slime or residual anode at the end of the test. The cathodic current efficiency was 98%. Again, it would appear that a large portion of the test was carried out under polarized conditions.

In an extension of their work on pure chalcocite, Mao and Peters [6] have provided perhaps one of the most useful studies assessing the potential for commercialization of matte refining. These researchers electrolyzed a packed bed of particulate high-grade matte (73.3wt% Cu, 3.5wt%Fe, 1.4wt%Pb, 20.5wt%S) at superficial current densities of 300-400A/m<sup>2</sup>. The anodes did not polarize until 50-60% copper extraction. However, this was less than the recovery from pure chalcocite and it was proposed that polarization may have been caused by insulation of the particles from the current distributor by lead sulphate. Thus, these authors concluded that lead was a more deleterious impurity than iron. Both the anodic and cathodic current efficiencies were greater than 95%.

As part of the aforementioned study, 20 successive anodes were processed in a common electrolyte, which was adjusted only after the tenth anode by the addition of copper sulphate, to demonstrate the cathode quality which may be produced and to assess the problems which may result from impurity buildup in the electrolyte. For these tests the anodes were removed just prior to polarization. The cathode quality was acceptable despite the increasing concentration of impurities, notably iron, zinc, arsenic and antimony. Silver, gold and most of the lead and bismuth were retained in the "slimes".

### **3.3.2 Leaching Studies**

Mao and Peters [52] found that in oxygen-pressure leaching studies the leaching time required to obtain 75% copper extraction (a reference value chosen by these authors) from a high-grade commercial matte containing 3.46wt% iron was much less than the time to leach 75% of the copper from pure chalcocite and the yield of elemental sulphur was highest from the former material when the leaching solutions initially did not contain iron. Therefore, iron which dissolved from the matte during leaching increased the leaching rate and altered the leaching mechanism. However, data on the rate of iron extraction from the matte during the leaching process were not provided.

### 3.4 SUMMARY

The ideal copper-matte electrorefining process would (a) achieve 100% copper recovery at 100% current efficiency and high current densities ( $>200\text{A/m}^2$ ), (b) produce elemental sulphur, not sulphate, and (c) leave all precious metals in a "slime" which could be easily processed for precious metal recovery. The following comments may be made with respect to studies on the decomposition of copper sulphides to date.

1. Electrolysis of chalcopyrite appears to be unfavorable relative to electrolysis of chalcocite or high-grade copper mattes in terms of practical application.

2. Electrolytic reduction of chalcocite generally has not been studied with regards to development of a commercial process. This is likely attributable to a number of factors which are disadvantageous relative to chalcocite oxidation: (a) hydrogen sulphide is generated and must be recovered, (b) the current efficiency may be reduced due to discharge of hydrogen, and (c) water must be decomposed at the anode to ensure a supply of hydrogen ions to balance those consumed at the cathode (Eq. (3.3)), which leads to high cell voltages.

3. Electrorefining of massive copper matte anodes at practical current densities ( $>200\text{A/m}^2$ ) and cell voltages ( $<1\text{V}$ ) results in severe polarization at much less than 50% copper extraction due to precipitation of copper sulphate in the pores of the products layer. The impression obtained from studies using massive anodes is that when more than about 1% copper recovery is reported polarization leads to (a) the release of impurities to the electrolyte after a period of time, and (b) decreased current density and sulphate formation. In studies where polarization was not reported, it appears the duration of the experiments was too short to test for it. Therefore, this electrode configuration does not appear to be practical.

4. The extraction of copper from fluidized bed anodes of chalcocite prior to polarization is limited to 50%, while 65-75% extraction may be obtained from a packed bed electrode of particulate chalcocite material. The polarization mechanisms in massive electrodes are usually not duplicated in particulate electrodes and appear to be related to elemental sulphur formation.

5. The role of impurities with respect to copper extraction and polarization mechanisms is not understood.

6. Direct electrochemical oxidation of covellite at low overpotentials is limited to very low current densities. The reason for the relatively slow kinetics of covellite, as opposed to chalcocite, decomposition is not well understood.

7. There is evidence that bornite electrolysis requires high overpotentials at practical decomposition rates.

8. Chalcocite is leached in two stages. The first of these is relatively rapid. The second stage leach and the leaching of covellite are relatively slow. These results generally are consistent with the electrolysis studies. Bornite leaches in several stages, the first of which is relatively fast and does not liberate iron. Leaching of the intermediates is slower and yields iron.

9. During decomposition of chalcocite, metastable intermediate phases are produced having a wide stoichiometry variability.

10. The most promising electrode configuration appears to be the packed bed electrode for the following reasons:

- (a) The highest copper extraction prior to polarization is achieved with this electrode (40-80% copper extraction is possible without sulphate formation).
- (b) The anode and cathode current efficiencies are high (>95%).
- (c) Operation at high current densities and low cell voltages has been demonstrated.
- (d) The real current density at the particle surfaces is low enough for decomposition of covellite.
- (e) The cathode purity is acceptable even after many refining cycles without replacing the electrolyte.

### 3.5 PHASE SYSTEMS

Since the effects of iron and lead impurities on both copper extraction and polarization mechanisms are to be studied in this thesis, a review of their phase associations with the copper-sulphur system is worthwhile.

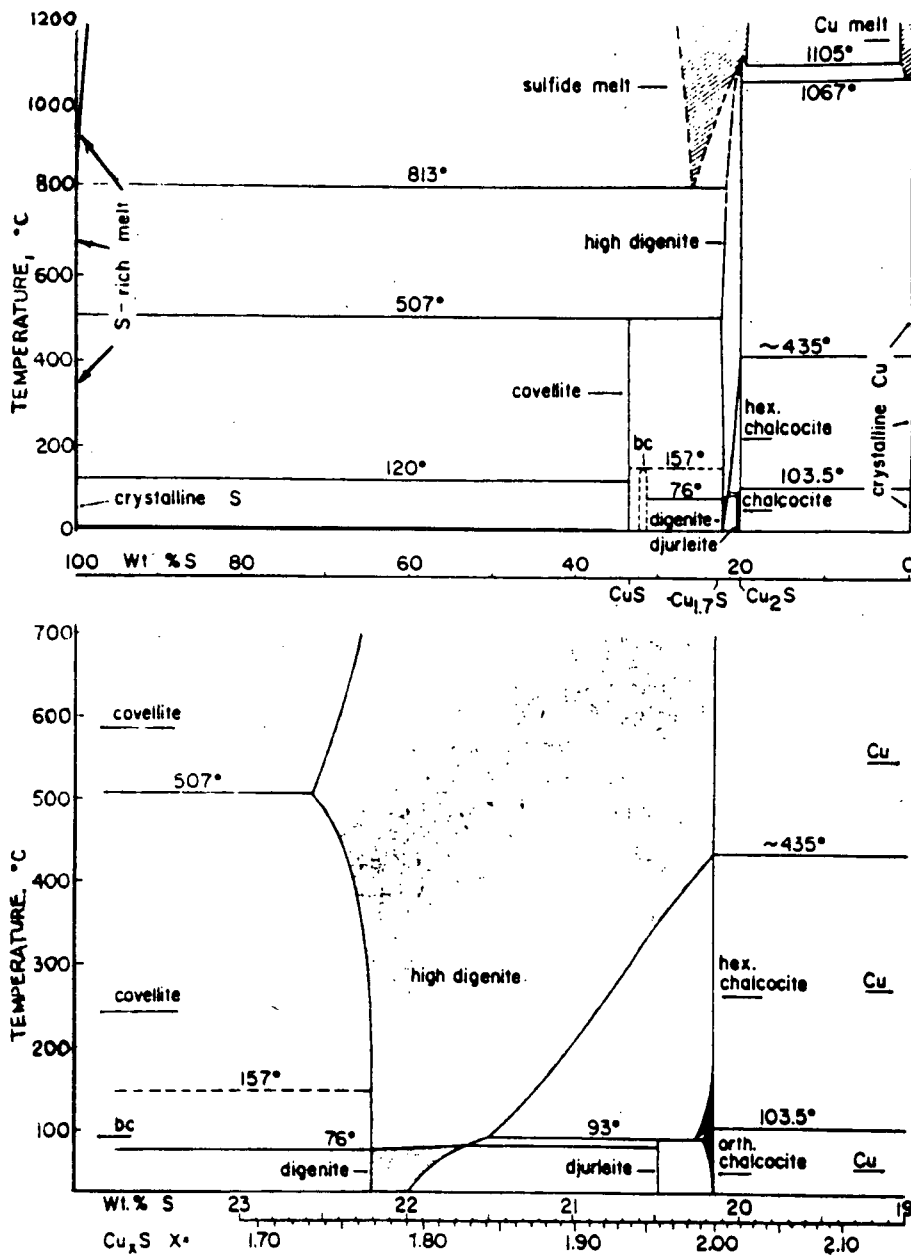


Figure 3.3 Phase diagram of the system Cu-S [56]. The abbreviation "bc" refers to "blaubleibender" covellite.

### 3.5.1 Cu-S System

Roseboom [56] combined the earlier studies on the copper-sulphur phase system with his own experiments and reported the occurrence of four thermodynamically stable phases at typical electrorefining temperatures (40-60°C): chalcocite ( $\text{Cu}_2\text{S}$ ), djurleite ( $\text{Cu}_{1.96}\text{S}$ ), digenite ( $\text{Cu}_{1.768-1.83}\text{S}$ ) and covellite ( $\text{CuS}$ ). These are shown in Fig. 3.3. Roseboom did not encounter "blaubleibender" or

"blue-remaining covellite" ( $\text{Cu}_{1.1}\text{S}$ ) as had several previous researchers; therefore, this sulphide appears as a metastable phase designated "bc" in his figures. This assessment has been generally accepted; the phase diagram for this system may be found in the reference literature [57].

Potter [43] also offered a phase diagram for this system, but showed the stoichiometry of djurleite to be variable and that of digenite to be invariant.

### 3.5.2 Cu-Fe-S System

A great amount of information on this ternary may be obtained from the work of McKinstry [58], Kullerud [59] and Yund and Kullerud [60,61]. A series of phase relations at different temperatures is shown in Fig. 3.4. Although there is appreciable solid solution between  $\text{Cu}_2\text{S}$ ,  $\text{Cu}_9\text{S}_5$  and  $\text{Cu}_5\text{FeS}_4$  at  $700^\circ\text{C}$ , separate phases should form when a mixture lying within this solid solution range is cooled to electrorefining temperatures.

However, Yund and Kullerud [60] found that all compositions along the line between  $\text{Cu}_9\text{S}_5$  and  $\text{Cu}_5\text{FeS}_4$  could be quenched to room temperature. Furthermore, they reported [61] that when a material having a composition along the line between  $\text{Cu}_2\text{S}$  and  $\text{Cu}_5\text{FeS}_4$  was rapidly cooled from  $700^\circ\text{C}$ , the room temperature x-ray pattern showed an almost continuous change from  $\text{Cu}_2\text{S}$  to  $\text{Cu}_5\text{FeS}_4$ , with intermediate phase compositions exhibiting the major reflections similar to either of these phases, but each composition giving a unique pattern.

### 3.5.3 Cu-Pb-S System

The papers by Craig and Kullerud [62,63] summarize the important aspects of this ternary with respect to this thesis. Figure 3.5 shows a series of phase transformations which take place on cooling from  $528\text{-}523^\circ\text{C}$ . On cooling below about  $485^\circ\text{C}$  the phase "A", approximately represented as  $7\text{Cu}_2\text{S}\cdot 2\text{PbS}$ , disproportionates to PbS, Pb and  $\text{Cu}_2\text{S}$ . Apparently there are several tie line changes which take place on further cooling because the stable phases below  $200^\circ\text{C}$  were reported to be PbS,  $\text{Cu}_2\text{S}$  and Cu. However, it was also reported that rapid cooling preserves phase "A" which then remains stable for several months. Furthermore, even with rapid cooling from  $500^\circ\text{C}$  they found only small amounts ( $<1\text{wt}\%$ ) of PbS in  $\text{Cu}_2\text{S}$  and no solubility of  $\text{Cu}_2\text{S}$  in PbS.

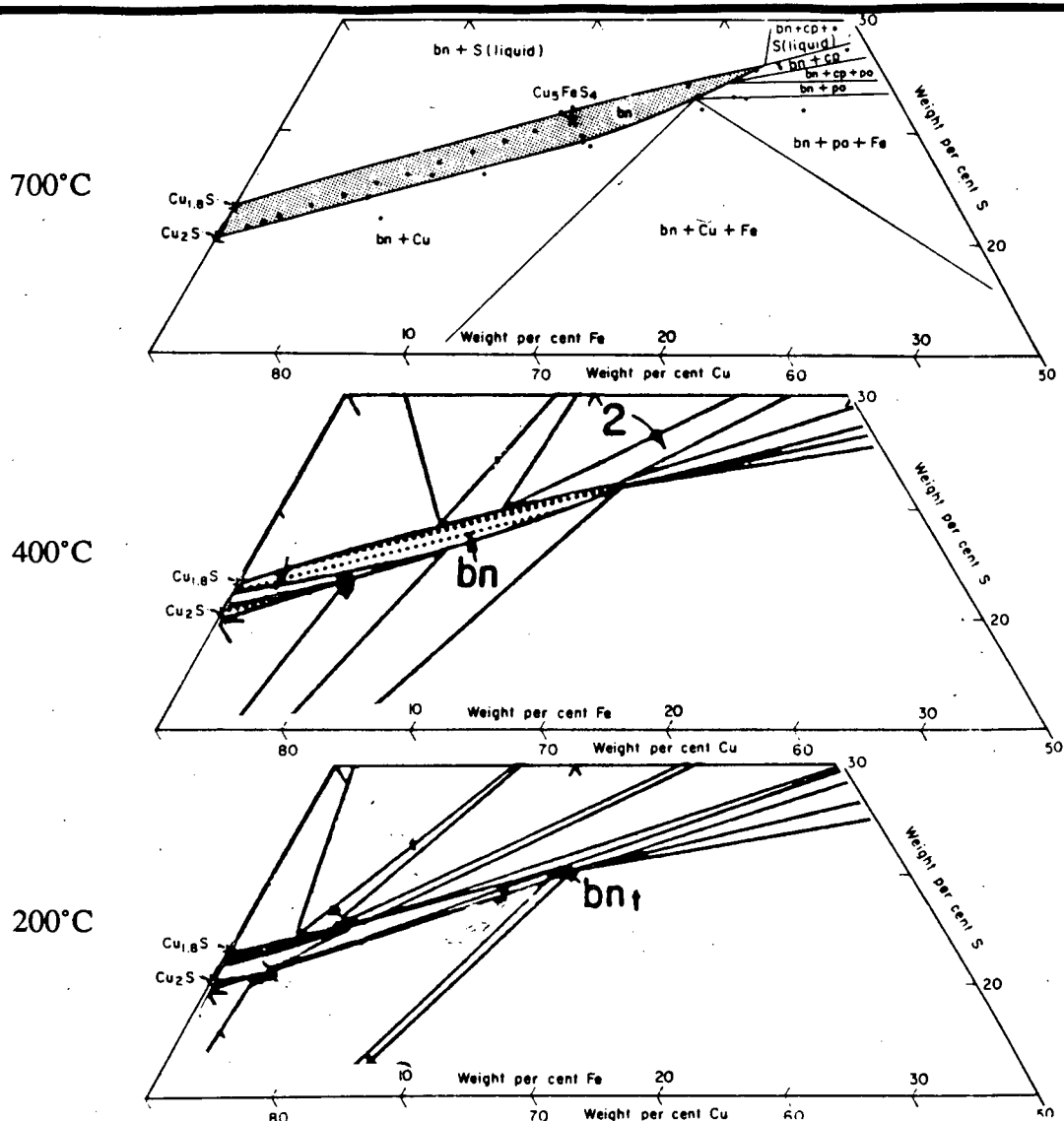


**Figure 3.4** Phase relations in the system Cu-Fe-S at several temperatures [60,61]. Note the extensive range of solid solution between chalcocite and bornite at 700°C.

A later study by Kopylov et al. [64] generally confirms the existence of the phases described by Craig and Kullerud, although there is some disagreement on the solidification temperatures along the line between  $\text{Cu}_2\text{S}$  and  $\text{PbS}$ .

### 3.5.4 Fe-Pb-S

The phase relationships in this ternary at 700°C were studied by Brett and Kullerud [65]. They found the extent of solid solution of  $\text{PbS}$  in  $\text{FeS}_2$  and  $\text{FeS}$  and the solid solution of  $\text{FeS}$  in  $\text{PbS}$

too small to be determined. In addition, x-ray powder diffraction data on liquids quenched from this temperature indicated the presence of two phases, although only slow cooling produced a separation which was visible under their microscope.

### 3.5.5 Cu-Fe-Pb-S

In their investigation of this system Craig and Kullerud [66] found no evidence for solid solution of lead into the copper-iron-sulphides or of copper or iron into PbS at 450°C. Since this study was related to natural mineral associations no discussion was provided as to the stable phases existing at other temperatures for compositions similar to copper-rich mattes.

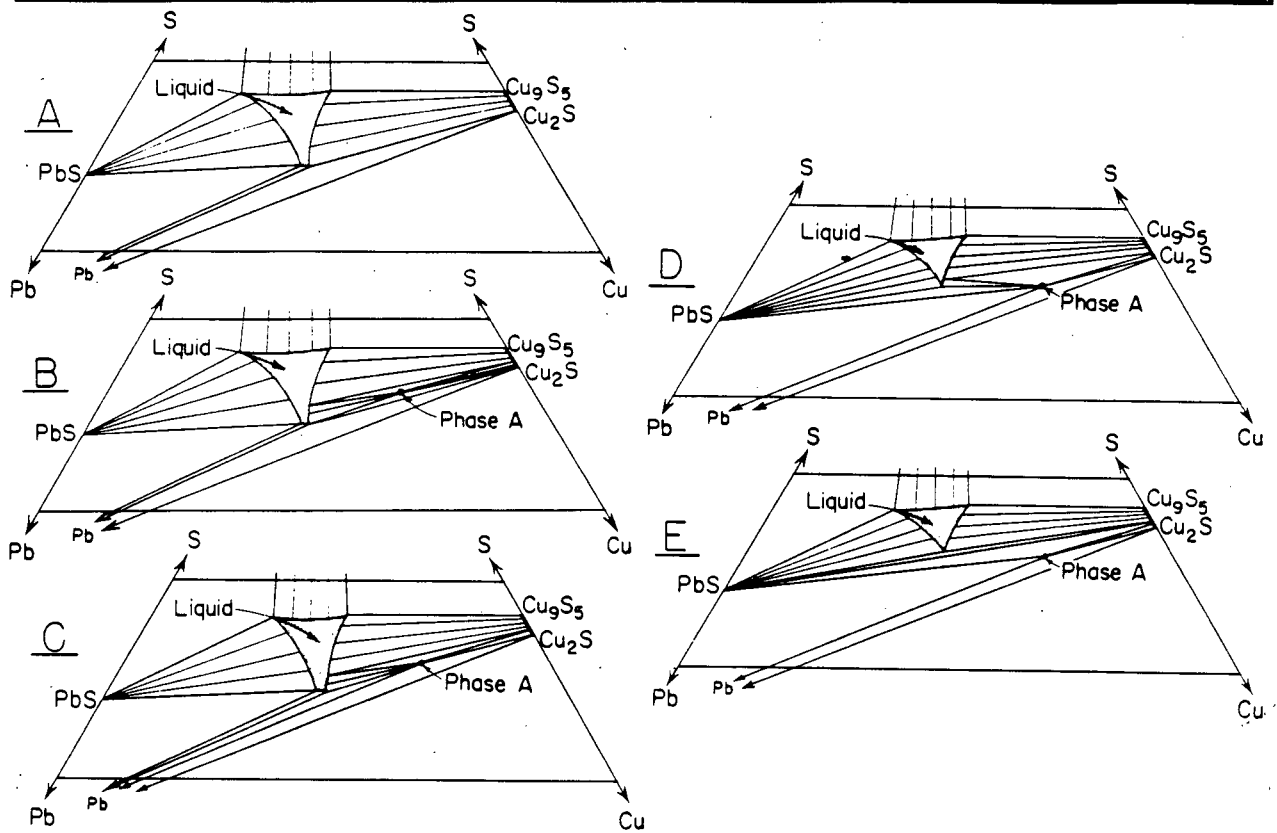
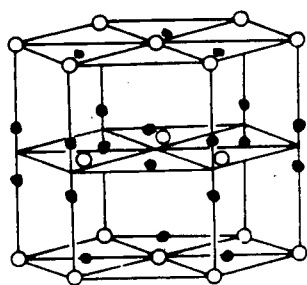


**Figure 3.5** Schematic representation of the changes in phase relations in the system Cu-Pb-S occurring in the temperature range 528-523°C (A-E) [63].

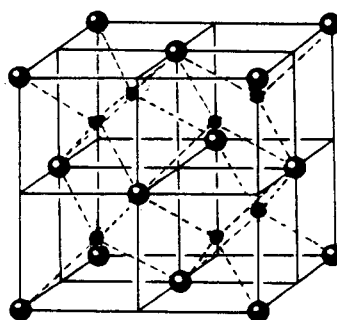
### 3.6 CRYSTAL STRUCTURES

Figure 3.6 illustrates the crystal structure of the various copper sulphides between chalcocite and covellite. The crystal structures of chalcocite and digenite are straightforward. However, covellite's structure is rather unique and has been described as dihexagonal-dipyramidal [67]. Kostov [67] describes the structure as follows:

Chalcocite (hexagonal)



Digenite (cubic)



Covellite (see text)

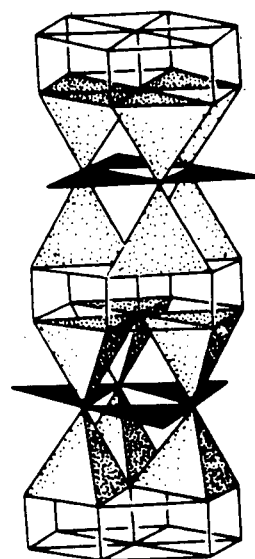


**Figure 3.6** Crystal structures of various copper sulphide minerals [67,68].

*"The structure is a typical layer type, built up of  $\text{Cu}^+$  in the centers of tetrahedra, and  $\text{Cu}^{2+}$  in the centers of equilateral triangles with apices occupied by  $\text{S}^{2-}$ . Double sulphur atoms,  $\text{S}_2^{2-}$ , of the type found in the pyrite and marcasite structures, are situated at the corners of the tetrahedra."*

In chalcocite, copper exists as  $[\text{Cu}^+]$ , but these are not located in the centers of the tetrahedral interstices, rather, they are located near the triangular faces of these interstices [99]. Although the stoichiometry range of digenite is 1.76-1.83, the crystal structure shown in the figure is only valid for the range 1.76-1.79 [68]. Again, the cuprous species are located near the triangular faces of the tetrahedral interstices [99].

Bornite's structure is cubic, with the copper and iron species occupying three quarters of the tetrahedral interstices [99]. According to Kostov [67], there are 48 possible sites for cuprous ions,

$\text{Cu}^+$ , in the structure, of which about 40 are occupied and part of the cuprous ions are oxidized to  $\text{Cu}^{2+}$  for compensation of charges. The important point is that both valence states for copper exist, with  $\text{Cu}^+$  being the most mobile species.

### 3.7 COPPER MATTES VERSUS NICKEL MATTES

If one adopted the "unit operation" approach to metal sulphide electrolysis one might be tempted to apply the principles learned during the development of the nickel matte refining technology directly to copper matte refining. Discussions in Sec. 3.4 have summarized the inherent difficulties with copper matte electrolysis. A comparison of nickel and copper matte electrolysis will demonstrate why only the former has so far been commercially successful.

Firstly, the electrolyte in nickel matte refining is considerably more neutral ( $\text{pH}\approx 3.5-4.5$ ) than in copper matte refining studies ( $\text{pH}\approx 0$ ). Consequently, the maximum solubility of nickel sulphate in a nickel refining electrolyte (3.7M at  $60^\circ\text{C}$ ) [48] is approximately three times the maximum solubility of copper sulphate in its electrolyte (1.3-1.4M at  $60^\circ\text{C}$ ). The copper concentration used in most studies is only about 0.6M, as compared to a nickel concentration of 1M. If the mass transport of the metal ions through the product layers (approximately CuS in massive copper matte refining and sulphur in nickel matte refining) is via diffusion mechanisms only, the transport rate, which is proportional to current density, at the onset of polarization due to metal salt precipitation would be three to four times greater in nickel matte refining than in copper matte refining. Here it is assumed that nickel and copper ions have similar diffusivities and that the thickness and porosity of the product layers are roughly equal.

Secondly, the relatively high pH in a nickel matte refining electrolyte has an additional effect on nickel ion mass transport. In the absence of hydrogen ions, nickel ions are forced to carry a considerable portion, perhaps as much as 40% [12], of the total current. However, in a copper refinery electrolyte (used in virtually all copper matte refining studies) the high acid concentration ensures little, perhaps less than 10% (see Appendix B), of the current is transported by copper ions. Therefore, for the same superficial current density in both systems, the mass transport of nickel

ions by electrical migration may be at least four times greater than the migration flux of copper ions in their respective electrolytes, again assuming similar product layer thickness and porosity in both sulphide systems.

Thirdly, chalcocite, the predominant copper sulphide in copper matte, does not decompose directly to produce elemental sulphur and copper ions. This was discussed previously, but the significance of the intermediate phases, for example covellite, will now be described.

Nickel matte electrode dimensions reportedly change markedly during electrolysis [10] so that, by the end of a refining cycle, the anode thickness approximately doubles. Since the molar volume of sulphur is less than that of nickel sulphide ( $16.0\text{cm}^3/\text{mole}$  versus  $41.3\text{cm}^3/\text{mole}$  [40]), the final sulphur porosity is about 0.60, as opposed to 0.22 if the anode dimensions remained constant. The thickness of the sulphur slime layer at the end of a refining cycle, through which dissolved nickel must pass to get to the bulk solution, is about 4cm. Electrical migration may account for approximately 40% of the mass transfer. If the only other transport mechanism is diffusion, the nickel concentration at the  $\text{Ni}_3\text{S}_2\text{-S}^\circ$  interface would, at  $200\text{A}/\text{m}^2$ , have to be well in excess of its solubility limit. Clearly, a mass transport mechanism, in addition to diffusion and electrical migration, must be important and that mechanism is natural convection.

Much is known about natural convection in mass transfer processes at plane vertical electrodes. Apparently, natural convection is also important in the porous slime of the nickel matte refining process. The point is that an appreciable porosity of the sulphide and sulphur phases on the anode ( $\approx 60\%$ ) may be necessary before a natural convection mechanism may adequately develop.

The situation with chalcocite refining is rather different. The electrode dimensions do not change and the covellite product layer has a porosity of only about 0.27 (based on molar volumes: chalcocite  $28.41\text{cm}^3/\text{mole}$ , covellite  $20.79\text{cm}^3/\text{mole}$  [40]) as compared to 0.44 if the chalcocite decomposed directly to sulphur. In other words the actual current density through the porous covellite layer is actually more than double the current density in the porous sulphur layer on a corroding nickel matte anode. The actual natural convection mass transfer requirements through the sulphur

and covellite product layers in nickel- and copper-matte electrorefining, respectively, are summarized in Table 3.3. The requirement for a natural convection mechanism in copper sulphide electrolysis is three to four times that required in nickel sulphide electrolysis.

**Table 3.3** Comparison of the various mass transfer components through the sulphur and covellite product layers in nickel- and copper-matte electrorefining, respectively, accounting for anode porosity.

	Nickel-matte electrorefining	Copper-matte electrorefining
Applied Current (A/m <sup>2</sup> )	200	200
- porosity (ε) of product layer	0.6 (S°)	0.27 (CuS)
(a) real current through product layer (A/m <sup>2</sup> ) <sup>1</sup>	333	740
- transport number	0.4	0.1
(b) mass transfer by migration (A/m <sup>2</sup> ) <sup>2</sup>	133	74
- product layer thickness (mm)	40	20
- max. concentration difference (mol/m <sup>3</sup> )	2.7	0.7
(c) mass transfer by diffusion (A/m <sup>2</sup> ) <sup>3</sup>	8	2
(d) mass transfer required by natural convection (A/m <sup>2</sup> ) <sup>4</sup>	192	664

Notes: 1 assume that the tortuosity is equal to 1.0

2 line (a) times the transport number

3 assume that diffusion is across the complete thickness of the product layer; the starting anode thickness is 4cm; that corrosion occurs on both sides of the anode; that diffusion occurs across the complete thickness (x) of the product layer, which remains at 2cm for Cu<sub>2</sub>S but increases to 4cm for Ni<sub>3</sub>S<sub>2</sub>; the molecular diffusivities of Ni<sup>2+</sup> and Cu<sup>2+</sup> are equal to 10<sup>-9</sup>m<sup>2</sup>/s; the maximum concentration within the product layer is 1.3M and 3.7M for the Cu<sub>2</sub>S and Ni<sub>3</sub>S<sub>2</sub> systems, respectively  
 calculation:  $I_{diffusion} = 10^5 (C_{max} - C_{bulk}) D \epsilon n F / x$

4 (a)-(b)-(c)

In fact, the porosity and permeability of the "slime" layer on corroding nickel sulphide anodes have been identified as the major parameters effecting the increase in cell voltage during electrolysis [15,16] at the Sumitomo Metal Mining Co. Ltd., Japan. The porosity is generally between 0.6 and 0.8. The voltage drop through this layer accounts for as much as 70-80% of the cell voltage increase, with the remainder due to increasing concentration gradients. As a result, after refining for ten days at about 200A/m<sup>2</sup>, the anodes at this operation are removed from the cells so the "slime" (approximately 2cm thick) can be removed, and they are replaced in the cell for a further ten days. Oddly, natural convection mass transport was not discussed, but it must have been important. The porosity and permeability probably affected the extent to which this mechanism could develop in the "slime" layer.

Unfortunately, the porosities of chalcocite decomposition products are apparently not great enough to permit natural convection of electrolyte at a massive electrode. However, in an anode composed of small chalcocite particles, the porosity may be high enough and sufficiently non-tortuous that natural convection mass transport around the particles can take place. Furthermore, in a packed bed the distances required by diffusion and migration fluxes are limited to the dimensions of the particles and the current densities at these particles are substantially less than the superficial current density.

Since electrode height is expected to be a factor in natural convection mass transfer within a packed bed electrode, it seems appropriate to study this mechanism on a tall electrode.

### 3.8 MASS TRANSFER AND CONVECTION

In Sec. 3.7 an argument was developed to suggest that if copper sulphide electrolysis stands a chance of being developed to the commercial scale, the packed bed may prevail as the appropriate electrode design because in this type of electrode there is natural convection mass transfer.

Forced convection mass transfer in packed beds has been the subject of numerous investigations. For example, Karabelas et al. [69] reviewed the findings of more than 20 previous investigators, summarizing these in a table showing the packing type, mass transfer correlation and the range of Reynold and Schmidt numbers for which the offered correlations were applicable. Some correlations have been particularly well accepted and may be found in the textbook literature [70,71].

Much effort has been given to the study of natural convection and mass transfer at plane vertical surfaces [73-78]. Natural convection mass transfer at inclined surfaces has also been studied [72]. In general, the results of all such studies are reported using Eq. (3.23), with the values of the fitting coefficients adjusted to the various physical electrode configurations.

$$Sh = a(ScGr)^b \quad (3.23)$$

where the various dimensionless groups are defined as follows:

$$Sh \quad \text{Sherwood no.} = \frac{\text{momentum mass transfer}}{\text{molecular mass transfer}} = \frac{kl}{D}$$

$$Sc \quad \text{Schmidt no.} = \frac{\text{momentum diffusivity}}{\text{molecular diffusivity}} = \frac{\eta}{\rho D}$$

$$Gr \quad \text{Grashof no.} = \frac{\text{density forces}}{\text{viscous drag forces}} = \frac{gl^3 \Delta \rho}{\rho} \left( \frac{\rho}{\eta} \right)^2, \quad \text{where} \quad \frac{\Delta \rho}{\rho} = \frac{1}{\rho} \left( \frac{d\rho}{dC} \right)$$

The other parameters are  $k$ , the mass transfer coefficient,  $l$ , the characteristic length,  $D$ , the molecular diffusivity,  $\eta$ , the electrolyte viscosity,  $\rho$ , the average of the electrolyte density at the electrode surface and in the bulk solution,  $\Delta \rho$ , the difference in density between the bulk electrolyte and that at the electrode surface,  $g$ , the gravitational constant, and  $C$ , the copper concentration.

As shown by Fouad and Ibl [75],  $Sc$  and  $Gr$  may be combined in electrochemical systems because  $Sc$  is usually about 1000. In addition, two situations have been generally recognized: laminar and turbulent natural convection.

The many reported studies have been summarized by Ettel [78] for laminar and turbulent convection, respectively:

$$Sh = 0.66(ScGr)^{1/4} \quad (3.24)$$

$$Sh = 0.31(ScGr)^{0.28} \quad (3.25)$$

with the transition estimated at  $Sc \cdot Gr \approx 10^{11}$ .

The majority of studies on natural convection at plane vertical electrodes have shown that some variation in mass transfer or electrolyte velocity along the electrode exists over at least a portion of the vertical dimension. This variation is particularly evident on short (<10-20cm) electrodes. Ibl and Muller [74], for example, found that the electrolyte velocity increased with increasing height along an 11cm electrode. Gendron and Ettel [73] found that the mass transfer coefficient at a nickel refinery cathode was the greatest at the bottom of a 40cm-tall electrode, but decreased by 25% above a height of 16cm.

Denpo et al. [76] studied natural convection at tall (1m) cathodes and from their figures one may infer that the mass transfer coefficient varied only near the bottom of the electrode; above a certain height, which depended on current density (20cm @ 200A/m<sup>2</sup>, 40cm @ 20A/cm<sup>2</sup>), the mass transfer coefficient remained constant. The authors concluded laminar natural convection prevailed near the bottom of the electrode, but, above a critical height, turbulent conditions existed. They offered the following correlations, where  $G^*$  is a modified Grashoff number defined in their paper.

$$Sh = 0.055(ScGr^*)^{2/7}, \quad ScGr > 2.5(10^{15}) \quad (3.26)$$

$$Sh = 0.628(ScGr^*)^{1/5}, \quad ScGr < 2(10^{13}) \quad (3.27)$$

These observations are in agreement with the earlier work of Fouad and Ibl [75] who also employed tall (1m) electrodes in their studies. They concluded that laminar natural convection at currents up to 300A/m<sup>2</sup> occurred only adjacent to the bottom 5cm of the electrode, while some turbulent convection was evident 10cm from the bottom of the electrode at a current density of only 40A/m<sup>2</sup>. Above a height of 15cm, turbulent convection was well developed. They found the limiting current density, in other words, the overall maximum mass transfer rate, tends to become independent of electrode height for tall electrodes. Consequently, they proposed the exponent of  $ScGr$  must necessarily be 1/3 under turbulent conditions.

Relatively little research on natural convection-induced mass transfer in packed beds has been reported in the literature. Studies which may be of some assistance have been performed using single spheres [79], vertical arrays of horizontal cylinders [80], and vertical meshes [81,82]. Interestingly, the reported correlations use fitting constants very similar to those given by Ettel [78]. For example, Sedahmed et al. [79] report the correlation shown below for natural convection mass at transport single spheres, with the characteristic length,  $l$ , equal to the sphere diameter. These authors did not indicate how the correlation for a single sphere could be extended to packed beds containing many spheres.

$$Sh = 0.15(ScGr)^{0.33}, \quad 2.85(10^{10}) < ScGr < 2.15(10^{11}) \quad (3.28)$$

These researchers also summarized previous investigations on this system and found that the following correlation had been proposed:

$$Sh = 2 + 0.59(ScGr)^{0.25}, \quad 1.22(10^7) < ScGr < 1.57(10^{10}) \quad (3.29)$$

The latter expression was apparently applicable under laminar or laminar/turbulent transition conditions while the previous equation represented turbulent conditions.

Smith and Wragg [80] offered the following expression for mass transfer at a single horizontal cylinder:

$$Sh = 0.56(ScGr)^{1/4} \quad (3.30)$$

where the characteristic length is equal to the cylinder diameter. At arrays of cylinders, the mass transfer rate, normalized with respect to a single cylinder, decreased or increased with vertical position and cylinder spacing depending on experimental conditions. In addition, there was apparently significant deviation from the single cylinder behavior. However, no correlation for multiple cylinders in a vertical array was offered.

Using an electrochemical technique, Karabelas et al. [69] studied mass transfer at a single sphere (1/2-3in diameter) in a close packed array (12x12inx21layers high, 9-layers high for the 3in spheres) of inert spheres and offered the following expressions for laminar and turbulent natural convection, respectively.

$$Sh = 0.46(ScGr)^{1/4} \quad (3.31)$$

$$Sh = 0.112(ScGr)^{1/3} \quad (3.32)$$

with the characteristic length equal to the sphere diameter. The transition between laminar and turbulent conditions was thought to occur at  $ScGr$  equal to about  $(3-5)(10^9)$ . Again, no correlation was provided for the condition in which natural convection mass transfer occurred at all the spheres in the packed bed array.

For vertical-mesh electrodes (7cm high), Wragg [82] recommended using Eq. (3.24) directly (laminar) for  $ScGr$  between  $2(10^5)$  and  $5(10^{10})$ . Wragg's earlier work on mesh electrodes [81] revealed a strong variation in mass transfer coefficient with electrode height for heights less than

or equal to 7cm. The characteristic length for the mesh electrodes was the electrode height. Wragg [81] concluded that the vertical mesh electrode exhibits very similar free convection mass transfer behavior to that of a plane vertical plate electrode of the same total surface area.

Mandebaum and Bohm [83] evaluated the contribution of natural convection to mass transfer in packed beds at low  $Re$  and compared their experimental findings with those of previous researchers. The experimental technique was similar to that of Karabelas et al. [69], except Raschig rings were substituted for spheres. The data were analyzed according to whether the applied electrolyte flow rate (forced convection component) aided or opposed natural convection and were presented in figures giving  $Sh/(ScGr)^{1/4}$  versus  $Re/Gr^{1/2}$ . Below  $Re/Gr^{1/2}$  of about 0.02 and 0.05, for aiding and opposed flow, respectively, the values for  $Sh/(ScGr)^{1/4}$  were constant at 0.645 and 0.618 (aiding and opposed flow, respectively). In other words, mass transfer at  $Re/Gr^{1/2}$  less than these values is by natural convection only and the constants are similar to those given by Ettel [78] for natural convection.

Although Mandelbaum and Bohm contend the findings of the previous investigators could be summarized satisfactorily using this approach, inspection of the appropriate figures in their paper [83] suggests that the mass transfer coefficients estimated in this way should be considered accurate to  $\pm 50\%$ .

In summary, there is evidence that the fitting coefficients  $a$  and  $b$  appropriate for natural convection at plane surfaces may, in the absence of other information, be useful as a first approximation for packed beds. However, the coefficients vary somewhat between systems and natural convection in tall packed beds has apparently not been studied. Mass transfer at a single particle in an active bed may be different than at a single particle in an inert bed. While meshes may resemble packed beds, the small heights used by Wragg [81,82] may have prevented the development of turbulent conditions.

Mao and Peters [6], following the work of Hojo and Peters [32], recognized the importance of natural convection, but chose to model mass transfer by natural convection somewhat differently than the previous authors. They assumed the complex mass transfer problem could be summarized effectively as a one-dimensional problem and utilized the corresponding flux equation:

$$\vec{N} = -D_i \frac{dC_i}{dx} - \mu_i C_i \frac{d\Phi_e}{dx} + \vec{u} C_i \quad (3.33)$$

where the three terms are for diffusion, migration and bulk convection, respectively. The variables are,  $\vec{N}$ , the total mass transport rate,  $D$ , the diffusivity,  $\mu$ , the electrical mobility,  $\Phi_e$ , the electrolyte potential, and  $\vec{u}$ , the convection velocity of the electrolyte.

Section 3.7 of this chapter provided evidence that only the third term is important in copper matte electrorefining. Mao and Peters recognized this and determined an effective mass transfer rate by estimating the effective value of  $\vec{u}$  by cyclically raising and lowering a packed bed anode during electrolysis. They found their cycling conditions to be unimportant and calculated that if the anolyte was exchanged at least every four minutes, polarization due to copper sulphate precipitation would be avoided. For their 3x5x3cm cell, this time constant corresponded to a horizontal velocity of only 5-8mm/min or a vertical velocity (assuming no horizontal component) of 10mm/min. However, the electrode was not of practical dimensions and convective velocities may be greater on a tall electrode, where turbulent conditions may fully develop.

Alkire and Plichta [84] also modelled natural convection in a particulate electrode using the flux equation. They modelled the effect of the convection velocity on the effectiveness (i.e., the utilization of available reaction surface area) of horizontal conductive porous electrodes. Their porous electrodes were completely flooded with electrolyte and the reacting species could diffuse into or out of the porous region from both the top and bottom of the electrode. The bulk electrolyte on either side of the electrode was well stirred.

In the absence of natural convection, current distribution was very sensitive to the ratio of exchange current density to diffusivity of reacting species. This ratio is essentially a measure of the

relative importance of Faradaic and diffusion impedances. When this ratio was high, the reaction tended to be primarily near the boundary between electrode and bulk solution. Reducing this ratio caused the current distribution to become more uniform.

Under natural convection conditions, the concentration gradients of reacting species through the electrode decreased and the current distribution became more uniform, increasing the effectiveness of the electrode. Unfortunately, no values on the convective velocities were reported; rather, the results were presented in the form of dimensionless variables.

### **3.9 MATHEMATICAL MODELS**

The development of a mathematical model is not considered to be a major component of this thesis. However, the utility of a model in this study is that it does provide a reasonable overview of some of the practical aspects of this concept, particularly with respect to the distribution of the decomposition reaction across the particulate anode.

The framework for the development of mathematical models of particulate electrodes has been reviewed extensively in the literature. Several papers by Newman and his colleagues [85-87] are particularly noteworthy examples. However, most of the numerous modelling studies using this framework have focused on cathodic processes, particularly the recovery of metal from dilute solutions. Modelling the anodic behaviour of a packed bed anode which becomes increasingly depleted in reactant, particularly under conditions of natural convection mass transfer, has received very little attention.

The following is a list of assumptions generally employed in the development of mathematical models for particulate electrodes.

1. Infinitely dilute solution theory is applied. According to Rousar et al. [88], in concentrated electrolytes the theory of transport in dilute solutions should be abandoned because independent diffusion of each species cannot be assumed. They propose the concept of phenomenological transport coefficients to circumvent this difficulty. Nevertheless, transport based on dilute solution theory, employing empirical diffusion data at high solute concentrations if necessary, avoids excessive mathematical complexity.

2. The pore and particle geometry is disregarded. This allows the analysis of matrix and solution current densities on a macroscopic scale.
3. No provision is made for non-isothermal operation.
4. Capacitive effects of double-layer charging are ignored. Since the anode life will be several days this assumption is certainly valid.
5. The pore dimensions are unimportant relative to the electrode dimensions. This may be reasonable because the pore size will be at least one order of magnitude smaller than the minimum electrode dimension.
6. No provision is made for edge or entrance effects.

Alkire and Place [89] modelled the anodization of a copper-coated porous stainless steel electrode for various ratios of mass transfer to charge transfer resistance. In order to decouple time from the mass balance equation, a pseudo steady-state condition was assumed: for a small time increment the concentrations of species at any position were assumed to be constant. These concentrations were then adjusted by performing an unsteady state mass balance on an elemental slice of the electrode over a length of time equal to the time increment.

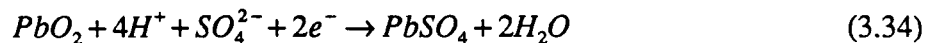
The authors predicted that, as the ratio of mass transfer to charge transfer resistance increased, the reaction was forced to the outer portion of the bed. As depletion of copper in the bed occurs, the reaction becomes more uniformly distributed.

Several assumptions these authors employed would likely not be applicable in copper matte dissolution:

1. The matrix was infinitely conductive.
2. There was no convection in the electrode.

In addition, the anode reaction did not produce a porous product layer as is the case with copper sulphide electrolysis, so ionic diffusion and migration through a product layer were not considered.

Simonsson [90,91] modelled the discharge of the porous lead dioxide electrode (Eq. (3.34)). His first model [90] did not account for structural changes within the electrode.



However, it was useful because the predicted initial reaction or current distribution based on a macroscopic treatment of matrix and solution currents (general assumption 2) was verified by experimental investigation. This study also provided evidence for a battery discharge mechanism, that is, the depletion of acid in pores in the electrode.

This discharge mechanism was the subject of a second model [91] in which structural changes, that is, decreasing porosity caused by lead sulphate precipitation in the pores in the electrodes<sup>3</sup>, were considered. The decreasing porosity resulted in an outward flow of electrolyte (in other words, convection) so mass transport occurred by diffusion, migration and convection. The reaction rate was controlled by a charge transfer mechanism.

Simonsson found that the reaction preferentially occurred in the region of the electrode closest to the bulk solution. This region eventually became coated with lead sulphate, thus inactive, forcing the reaction further into the electrode. The current density exhibited a maximum just beyond the thickening nonreactive zone. Under galvanostatic conditions this maximum increased in magnitude during discharge. At complete discharge, the acid concentration on the electrode side of the passivated or nonreactive zone was zero and the current density could not be sustained.

Newman and Tobias [86] derived relatively simple, but more general, one-dimensional models of a particulate electrode reacting anodically in order to assess how variation in current distribution in the electrode was affected by (a) the electrical conductivity ratio of solid phase (particulate matrix) to electrolyte, and (b) the rate of mass transfer of species from within the electrode to the bulk solution. When the concentration of species within the electrode was the same as in the bulk solution, they explained that the overall anodic process could be thought of as being entirely set by the rate of the Faradaic process, or "activation controlled". They investigated two limiting conditions by using the linear and Tafel polarization equations, corresponding to low and high current densities, respectively. Their results may be summarized as follows:

---

<sup>3</sup> Lead sulphate has a greater molar volume than lead dioxide.

1. When the electrical conductivity of the solid phase is low compared to the solution phase, most of the reaction occurs near the current distributor.
2. When the solid phase electrical conductivity is very high, most of the reaction occurs near the particulate electrode-solution interface.
3. When the electrical conductivity of the two phases is roughly equal, the reaction tends to occur at both of the above interfaces. However, as the electrical conductivities of both phases increase, while remaining equal, the reaction becomes uniformly distributed throughout the electrode.

When these authors accounted for concentration variations of reacting species throughout the electrode (while retaining the polarization equations to model the Faradaic processes) they found the reactions shifted towards the interface between the particulate electrode and the bulk solution.

Alkire and Plicka's model [84] evaluated the role of natural convection mass transfer on current density distribution in a particulate electrode as reviewed in Sec. 3.8. The important conclusion was that natural convection resulted in an increase in the uniformity of the reaction throughout the electrode.

A great number of other papers have been concerned with variation in Faradaic processes within three-dimensional electrodes. Often, the authors report this variation in terms of an effectiveness factor, which is a ratio of the amount of reaction actually occurring in the electrode to the amount of reaction that could occur if the reaction was 100% uniformly distributed. This factor is reported as a function of the various impedances to the overall reaction process. For example, effectiveness factor correlations may be found in the papers by Scott [92-94].

### 3.10 ELECTRICAL CONDUCTIVITY

Figure 3.7 summarizes the data on the variation of electrical conductivity of  $\text{Cu}_{2-x}\text{S}$ ,  $\sigma^\circ$ , with  $x$  from selected references [96-99]. In these studies different stoichiometries were obtained by reacting appropriate ratios of copper and sulphur in evacuated glass tubes. It would appear that significant variation may be found in natural sulphide minerals. For example, the range of conductivity reported by Shuey [99] for covellite is 100-33,000  $\Omega^{-1}\text{cm}^{-1}$ .

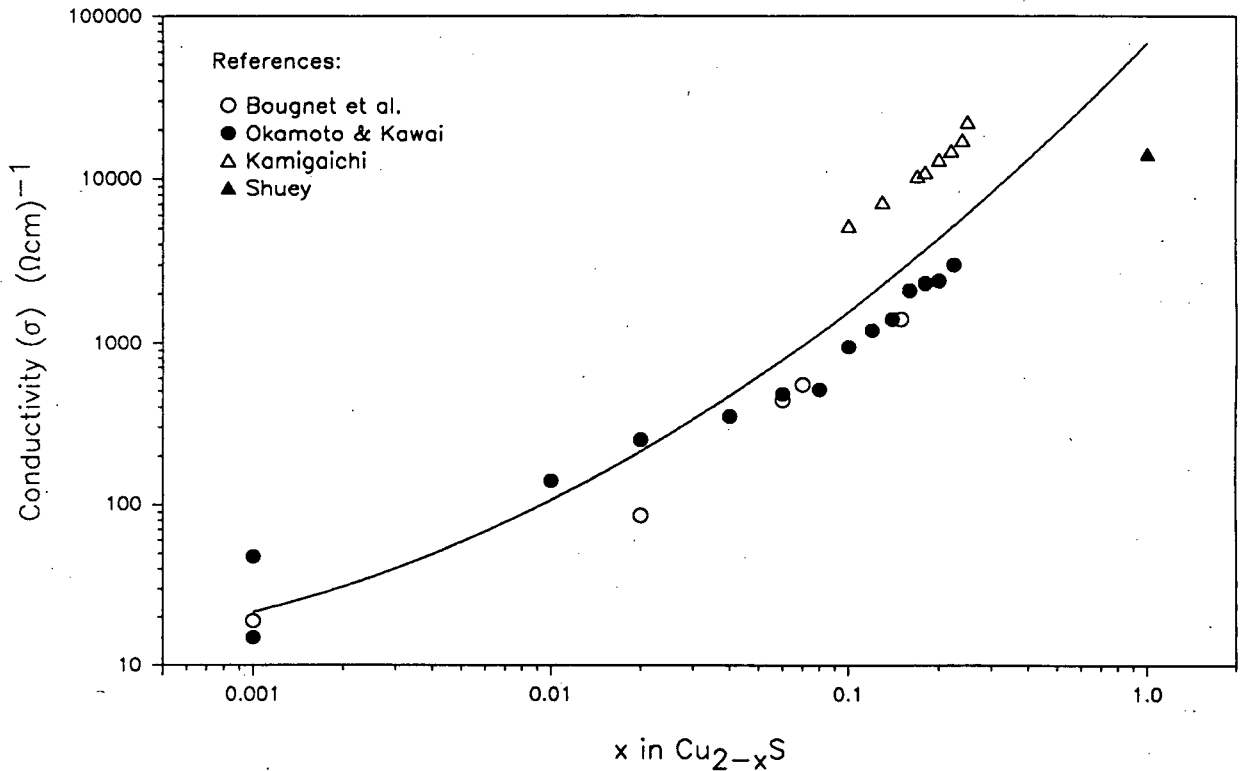


**Figure 3.7** Electrical conductivity of synthetic copper sulphide at 20°C as a function of the stoichiometric coefficient 2-x, from Bougnet et al. [96], Okamoto and Kawai [97], Kamigaichi [98] and Shuey [99]. Stoichiometric  $\text{Cu}_2\text{S}$  is shown at 2-x=0.001; slightly Cu-excess chalcocite has a conductivity about 1/10th that of stoichiometric  $\text{Cu}_2\text{S}$  [97].

The electrical conductivity of nonstoichiometric copper sulphides increases slightly with temperature between 20°C and 80°C (an expected temperature range for copper-rich matte refining at atmospheric pressure) as shown in Fig. 3.8. Changes in this conductivity-temperature tendency above about 90-95°C is attributable to phase changes [97], as may be appreciated with reference to Fig. 3.3. In the temperature interval between 20°C and 80°C, there is negligible change in the electrical conductivity of copper-excess chalcocite [97]. According to Shuey [99], the electrical conductivity of  $\text{CuS}$  increases with decreasing temperature, although no quantitative information was given.

Sample No	Composition
D1	$\text{Cu}_{1.80}\text{S}$
D4	$\text{Cu}_{1.86}\text{S}$
D6	$\text{Cu}_{1.90}\text{S}$
D7	$\text{Cu}_{1.92}\text{S}$
D9	$\text{Cu}_{1.96}\text{S}$
D11	$\text{Cu}_{1.99}\text{S}$
C1	$\text{Cu}_{2.00}\text{S}$

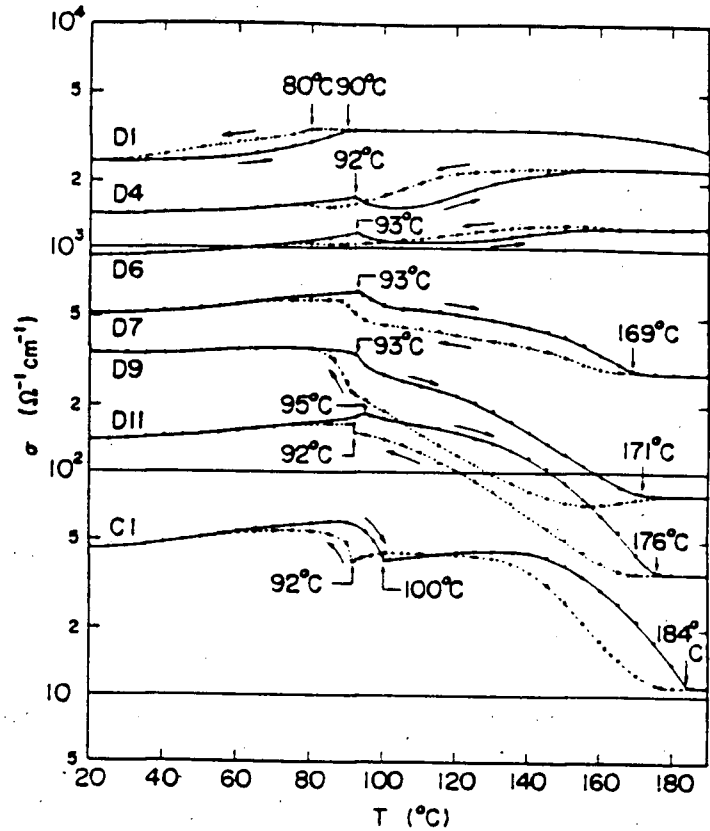


**Figure 3.8** Temperature dependence of electrical conductivity for several nonstoichiometric copper sulphides [97].

The specific conductances of copper-refining electrolytes,  $\kappa^\circ$ , which are very similar to those used in this thesis, are generally in the range  $0.6\text{-}0.7 \Omega^{-1}\text{cm}^{-1}$ . Biswas and Davenport [1] correlated data available in the literature and presented the following expression relating the electrical conductivity to temperature and to metal ion and acid concentration:

$$\frac{1000}{1.1\kappa^\circ} = 1000 + \left\{ \begin{array}{l} -7(T - 55) \\ -3(C_{\text{H}_2\text{SO}_4} - 200) \\ +6.6C_{\text{Cu}} \\ +7.6C_{\text{Ni}} \\ +8.2C_{\text{Fe}} \\ +0.7C_{\text{As}} \end{array} \right\} \quad (3.35)$$

where  $\kappa^\circ$  is in  $\Omega^{-1}\text{cm}^{-1}$ , the concentrations,  $C$ , are in  $\text{g/l}$  and the temperature,  $T$ , is in  $^\circ\text{C}$ . The accuracy of this equation was reported to be  $\pm 5\%$  for normal electrolyte conditions, given as  $175\text{-}225\text{g/l}$  acid,  $40\text{-}50\text{g/l}$  copper and  $55\text{-}60^\circ\text{C}$ .

Price and Davenport [100] offered the following correlation, which was reported to be accurate to  $\pm 10\%$  for the conditions given as 165-225g/l acid, 30-60g/l copper and 50-70°C.

$$\frac{1000}{\kappa^\circ} = 3200 + \left\{ \begin{array}{l} -15T \\ -6C_{H_2SO_4} \\ +C_{Co} \\ +2(C_{As} + C_{Mg}) \\ +3C_{Al} \\ +9C_{Cu} \\ +11C_{Ni} \\ +12C_{Fe} \end{array} \right\} \quad (3.36)$$

### 3.11 NOMENCLATURE

- a,b fitting constants for Eq. (3.23)
- C concentration of species, mol/m<sup>3</sup>
- D molecular diffusivity of species, m<sup>2</sup>/s
- g gravitational constant, 980m/s<sup>2</sup>
- Gr Grashof number,  $\frac{g l^3 \Delta \rho}{\rho \left(\frac{\rho}{\eta}\right)^2}$ , dimensionless
- i current density, A/m<sup>2</sup>
- k mass transfer coefficient, m/s
- l characteristic length, m
- L thickness of particulate electrode, m
- $\bar{N}$  flux of species, mol/m<sup>2</sup>•s
- Sc Schmidt number,  $\frac{\eta}{\rho D}$ , dimensionless
- Sh Sherwood number,  $\frac{kl}{D}$ , dimensionless
- T temperature, °C for Eqs. (3.35), (3.36)
- $\bar{u}$  electrolyte velocity, m/s
- x coordinate positions (thickness), m
- $\eta$  electrolyte viscosity, kg/m•s
- $\kappa^\circ$  absolute electrolyte conductivity, ( $\Omega \cdot \text{cm}$ )<sup>-1</sup>
- $\mu$  electrical mobility, m<sup>2</sup>/V•s

- $\rho$  electrolyte density,  $\text{kg/m}^3$   
 $\sigma^\circ$  electrical conductivity of particles,  $(\Omega\cdot\text{cm})^{-1}$   
 $\tau$  transition time (time at which electrode polarizes), hrs  
 $\Phi_e$  electrolyte potential, V

---

## **CHAPTER 4**

---

### **EXPERIMENTAL TECHNIQUES**

#### **4.1 CHEMICAL SOLUTIONS AND ANALYSES**

Electrolyte was prepared by dissolving reagent-grade hydrated copper sulphate (Allied Chemical), and by mixing reagent-grade concentrated sulphuric acid (95-98wt% BDH Chemicals) in deionized water.

Analysis of metallic species in the electrolyte were done by atomic absorption (AA). Free acid was determined by titration. The problem of metal ion hydrolysis during the titration was avoided by adding potassium oxalate as a 1.6-1.7M solution. Generally, the volume of this solution added prior to titration was 2-5 times the sample volume.

The starting electrolyte composition was 43-46g/l copper and 162-167g/l free sulphuric acid in all tests, except as otherwise noted.

#### **4.2 MATTE SYNTHESIS, CHARACTERIZATION AND PREPARATION FOR ANODIC DECOMPOSITION**

##### **4.2.1 Synthesis**

The industrial matte used in the study was supplied in a single 90kg shipment from Noranda's Horne smelter operations at Noranda, Quebec. The method by which the matte was tapped from

the furnace was not documented. Presumably, a hand-held ladle was inserted into the matte bath to obtain 2-3kg samples which were poured into molds and allowed to cool under ambient conditions [101].

Syntheses of pure and impurity-doped mattes were achieved in a two-step procedure. Firstly, chopped copper wire (99.9wt%, 10-40 mesh), supplied by Alcan Metal Powders, and sulphur "flowers", provided by Allied Chemicals, were sintered and the coherent mass was melted in a covered clay crucible placed in a gas-fired furnace. Approximately 10-15% by weight excess sulphur was used to compensate for some volatilization during synthesis. The molten material was poured into an iron mold and allowed to cool under ambient conditions. Generally, mattes were synthesized in 1-4kg batches.

Secondly, these matte castings were crushed to particles <4mm nominal diameter, separated into 700-800g aliquots and mixed with appropriate amounts of iron or lead sulphides to produce an impurity-doped aggregate. These metal sulphide mixtures were then re-melted using an induction furnace. Graphite rods were also mixed with the particles to ensure that a reducing environment existed during the re-melting process. Once molten, the matte was stirred several times before being poured into an iron mould. Again, cooling proceeded under ambient conditions. Since the mattes prepared in the first step were generally slightly copper-deficient, several of the 700-800g pure copper matte aliquots were also re-melted to release the excess sulphur and cast in order to be certain that the synthetic pure copper matte was as close to stoichiometric  $\text{Cu}_2\text{S}$  as possible. For an electrorefining control experiment, approximately 750-800g of industrial matte were re-melted using the induction furnace.

Native powdered lead sulphide, supplied by Fisher Scientific, was used as the lead impurity source. Mass balance calculations on the industrial matte indicated that the iron could be considered essentially as a 50/50 mixture of pyrite,  $\text{FeS}_2$ , and pyrrhotite,  $\text{FeS}$ . Therefore, roughly equal amounts of these species were used as the iron impurity source. The pyrite source was very high-grade natural mineral crystals from a Japanese deposit and the pyrrhotite used was supplied in the form of broken synthetic ferrous sulphide sticks by Allied Chemicals (code 1774).

#### 4.2.2 Chemical Analysis and Phase Characterization

Only the four major metallic components in the mattes (copper, iron, lead and zinc) were analyzed by the author. The sulphur content in the synthetically prepared mattes was determined by subtracting from 100% the concentrations (in wt%) of the metal species present.

All mattes were crushed to particles smaller than 4mm nominal diameter. However, only particles falling in the range between 0.5-4.0mm were used in the electrorefining experiments and for assaying. Representative samples for assaying were obtained from the bulk material using a rolling technique [103], whereby the entire assemblage was mixed on a large piece of packaging paper, followed by division of the "rolled" assemblage by taking several small, random parcels of the rolled material with a small laboratory spatula. The sample size varied between 5-15g, depending on the weight of particles loaded into the particulate anode. These samples were then ground to powder in preparation for assaying.

Copper was analyzed using an electrogravimetric technique, which consisted essentially of measuring the amount of copper from a sample that deposited on a platinum gauze electrode, and yielded results probably accurate to  $\pm 0.1\%$ . The other metals were analyzed by atomic absorption. These analyses should probably be considered accurate to only  $\pm 2-3\%$ . Further details on these techniques are provided in Appendix A.

Table 4.1 summarizes the assays performed by a commercial laboratory and by the author of as-received industrial matte, re-melted industrial matte and a few selected synthetic mattes. Matte compositions reported elsewhere in this thesis were determined by the author.

To check that bulk or "macro" segregation of the impurities in the synthetically prepared mattes had not occurred on cooling, several synthetic matte ingots were cut into several sections and a small amount of material from some of these sections was assayed. Figure 4.1 shows the location in the ingots where material was obtained for these analyses and also an assay summary. The amount of "macro" segregation shown in this figure was thought to be unimportant. A second

**Table 4.1** Assay summary for industrial and several synthetic mattes. All figures are in weight percent except those for silver which are in grams per metric ton.

Element	Industrial matte		Re-melted indus. Matte		Synthetic Matte 1		Synthetic Matte A		Synthetic Matte F		Synthetic Matte G	
Cu	69.3	69.06	70.7	71.68	73.6	73.45	77.2	77.20	73.6	73.42	76.3	76.18
S	--	20.80	--	20.97	21.9	21.72	19.8	18.96	21.9	--	19.6	19.20
Fe	4.4	4.45	4.1	3.77	4.5	4.49			4.5	4.36		
Pb	2.4	2.54	2.3	2.45		0.02	2.9	3.24			4.1	4.54
Zn	0.9	--	--	0.65								
Ni	--	--	--	0.13								
Bi	--	0.015	--	0.01								
As	--	0.22	--	0.25								
Sb	--	--	--	0.07								
Se	--	0.049	--	0.001								
Ag	--	1076	--	121.2								

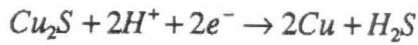
- Notes:
- the first numbers of each pair of numbers are assays by the author, the second numbers are assays by a commercial laboratory [102]
  - numbers in *italics* are obtained by subtracting from 100% the metallic species concentrations
  - assays (in wt%)
  - blanks are elements not in the matte
  - -- are not analyzed

round of segregation tests on mattes separately doped with iron and lead produced similar results, that is the concentration of these impurities did not vary significantly between several positions in the ingots.

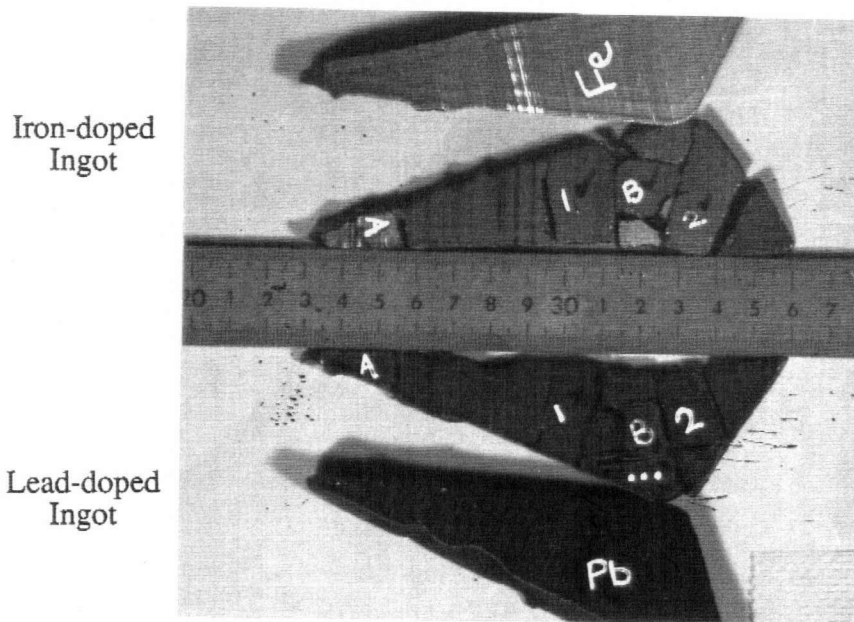
Phase segregation was investigated using scanning electron microscopy back scattered electron imaging (BSE) and X-ray energy dispersion (EDS) techniques. Unfortunately, the sulphur  $K_{\alpha}$  and lead  $M_{\alpha}$  lines very nearly coincide; therefore, quantification of lead on the EDS was based on the lead  $L_{\alpha}$  line, which is less intense. Consequently, the analyses of phases containing lead must be considered only semi-quantitative, although these analyses may be satisfactorily used to compare the relative compositions of the various phases present. X-ray powder diffraction was used to assist with identification of the predominant crystalline phases in the particles.

The grain sizes of an iron-doped and lead-doped matte were measured on longitudinal ingot cross sections. In preparation for these measurements, the sections were polished to a 6 $\mu$ m diamond finish and etched as follows:

- 1 The polished surface was reduced by placing it against a smooth flat slab of zinc wetted with a weak sulphuric acid solution ( $\approx 10\text{wt}\% \text{H}_2\text{SO}_4$ ):



- 2 The reduced surface was oxidized by submerging the ingot in a weak ferric chloride solution ( $\approx 0.5\text{MFeCl}_3$  plus enough HCl to prevent hydrolysis of the iron):



Analyses in Weight Percent				
Sample Piece	Lead-doped Ingot		Iron-doped Ingot	
	Cu	Pb	Cu	Fe
A	74.62	4.6	72.70	4.6
B	75.72	4.1	72.75	4.7
...	74.82	4.3		
comp	75.4	4.5	73.0	4.6

**Figure 4.1** Summary of the segregation study showing the location of the pieces of the ingots selected for assaying and the assays. "comp" refers to a composite of the entire ingot.

### 4.2.3 Preparation for Anodic Decomposition

For many runs, a detailed particle size distribution analysis was performed and the size distribution was adjusted so that there was reasonable consistency between runs. To ensure good mixing of the different size fractions, all particles were thoroughly mixed using the rolling method referenced in the previous section before being introduced to the packed bed electrode.

**Table 4.2** Distribution of particle sizes used in several small-scale 2cm-thick packed bed experiments. The numbers are in weight percent and the particle size ranges are in millimeters.

Experiment no.	0.5-1.0	1.0-1.4	1.4-2.0	2.0-2.8	2.8-4.0
20,24	16.2	12.2	16.7	26.0	28.4
30	13.6	10.7	16.0	28.8	30.9
32	12.5	10.9	15.3	27.7	33.7
38	14.1	11.2	15.6	27.2	32.1
40	14.1	11.1	16.1	27.5	31.2

## 4.3 ELECTROLYTIC CELLS: EQUIPMENT AND TECHNIQUES

### 4.3.1 Electrode Construction

Chapter 2, introduced the first objective of this thesis as the investigation of natural convection behaviour in a packed bed electrode. It was shown in Chap. 3, Sec. 3.7 that this would be best studied using an electrode with dimensions as close as possible to those that would likely exist in a commercial operation. Thus, these studies were conducted in a large-scale electrode or tall electrode (70x12x2cm height, width and thickness, respectively). When it became clear that total-bed polarization was not related to natural convection processes, but possibly to the amount of certain impurities in the matte, two small-scale electrodes were brought on stream. One of these electrodes was designed with the same thickness as the tall electrode and results obtained with it showed that the electrical contact resistance between the particles and the current distributor appeared to be the largest component of the total-bed potential (the potential difference measured between the current distributor and a copper reference electrode inserted in a Luggin capillary located just outside the diaphragm). Therefore, the second small-scale electrode was designed with

a thickness close to the average particle diameter (2.9mm) and operated at a proportionally reduced current density in the hopes that this problem could be overcome. Table 4.3 provides a summary of the various electrodes employed.

**Table 4.3** Summary of the various electrode employed. The 70cm-tall electrode is 12cm in width and the small-scale electrodes (11cm-tall) are 7cm in width.

Electrode Description	N <sub>2</sub> Sparge	Mode of Operation	Exper. No.	Objective of Experiment	Related Chapter
(a) 70cm-tall 20mm-thick	no	monopolar	13	natural convection studies	5
(b) 70cm-tall 20mm-thick	no	bipolar	15	natural convection studies	5
(c) 70cm-tall 20mm-thick	yes	bipolar	47	natural convection studies	5
(d) 11cm-tall 20mm-thick	yes	monopolar	16-20 23-27 30-33 38,40	impurity effects reaction distribution total-bed polarization components	7
(e) 11cm-tall 2.9mm-thick	yes	monopolar	40-46 48-51	impurity effects and mechanisms	8

Figure 4.2 is representative of the anode construction. To form the anode compartment, two plexiglas side walls were placed between the current distributor and a synthetic filter cloth-type diaphragm. The diaphragm was folded towards the current distributor at the bottom of the side walls to form the bottom of the anode compartment. This allowed the electrolyte to flow out of the bottom of the electrode. To provide support to the diaphragm, a coarse titanium screen ( $\approx 7.5$ mm openings) was placed against the outer surface of the diaphragm. In the large-scale cell only this screen was folded towards the current distributor at the bottom of the side walls. A thin retaining strip was placed on the support screen in alignment with the side walls, and the complete assembly was then secured with nylon bolts. The purpose of the retaining strip was to ensure that the pressure of the assembly bolts was distributed evenly along the full height of the electrode (which ensured a good seal between the diaphragm and the plexiglas side walls). For the tall electrode only, a bottom support was included in the construction in conjunction with the support screen.

Various materials were employed as current distributors: noble-metal-coated titanium (10g/m<sup>2</sup> platinum-iridium), graphite and gold. Titanium- and ruthenium-oxide-coated titanium were unsuccessfully tested in a few initial experiments with the large vertical electrode. Three different synthetic filter cloths were used as the diaphragms, with each having a different "tightness" or porosity. Several of the diaphragm properties are reviewed in Table 4.4. A few small-scale tests with the 2cm-thick electrode were conducted without the titanium support mesh.

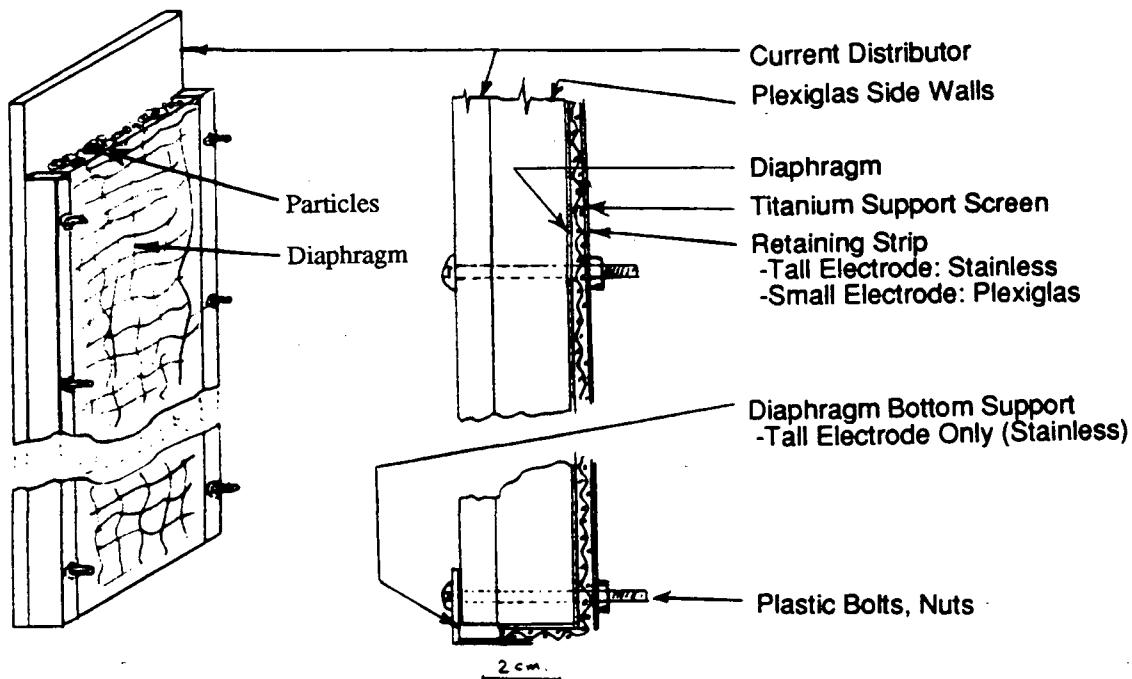


Figure 4.2 Construction details of the particulate anode.

Table 4.4 Some properties of the synthetic filter cloth-type diaphragms.

Retailer Reference <sup>1</sup>	Description	Permeability <sup>2</sup> (ft <sup>3</sup> /min)	Mesh Size	Thickness (mm)	Porosity
MF 4092C	"tight"	110-140	85	0.60	0.34
MF 4009N	"medium"	600-650	60	0.58	0.56
MF 4159N	"loose"	800+	40	0.80	0.67

Notes: 1 Barton Western, Vancouver, B.C.

2 presumably the flow rate at a fixed reference pressure drop

The measurement of the electrolyte potential at various positions within the packed bed and that of the electrolyte potential just outside the diaphragm was made possible by using copper wire

reference electrodes placed in capillary tubing and in a glass Luggin capillary, respectively. A copper reference electrode was used in place of a saturated calomel electrode (SCE) because (a) while a SCE is a more recognized reference electrode, generally it has an unknown liquid junction potential when in contact with an acid electrolyte<sup>1</sup>, and (b) a copper reference electrode has no liquid junction potential because it contacts the same electrolyte as the particles do. Therefore, it yields a direct Nernst value in copper activity. The capillaries were flooded with the cell electrolyte. Practical electrolysis was considered to have ended when the potential difference measured between the current distributor and the copper reference electrode just outside the diaphragm rose to more than 0.9-1.0V. This was referred to as "total-bed polarization" of the particulate electrode. (In one experiment, a moveable Luggin capillary was used to check for variation in this potential at different positions adjacent to the outside surface of the diaphragm during the total-bed polarization process. The variation was found to be under 10mV). At this point, the anode assembly was withdrawn from the cell and thoroughly rinsed with deionized water. Particle samples were withdrawn from various positions in the bed and analyzed for copper and, in selected runs, iron, lead and zinc.

The measurement of the particle potential at several locations in the bed (at the diaphragm, adjacent to the current distributor and midway between these positions) was made possible by placing platinum wires in the bed. To insulate the platinum wire from the current distributor a narrow strip of insulating tape (Canadian Technical Tape Ltd.) was secured to the current distributor and the platinum wire was centered on this tape and secured in position with several additional narrow pieces of the tape. The platinum wire positioned at the diaphragm was simply fastened to the diaphragm with short lengths of additional platinum wires. These construction details are shown in Fig. 4.3. The various potentials measured and the terminology used throughout the thesis to describe these potential measurements are summarized in Fig. 4.4.

---

<sup>1</sup> For example, the measured potential difference between the SCE and a copper reference electrode in the electrolyte employed in this thesis was about 65-70mV at 28°C, as compared to a value of about 45mV which would be anticipated in the absence of a liquid junction potential (using a  $\text{Cu}^{2+}$  concentration of 0.6M and an activity coefficient, from Appendix B, of 0.026).

Solution Potential Measurement:  
-Capillary Tubing Taped  
to Current Distributor

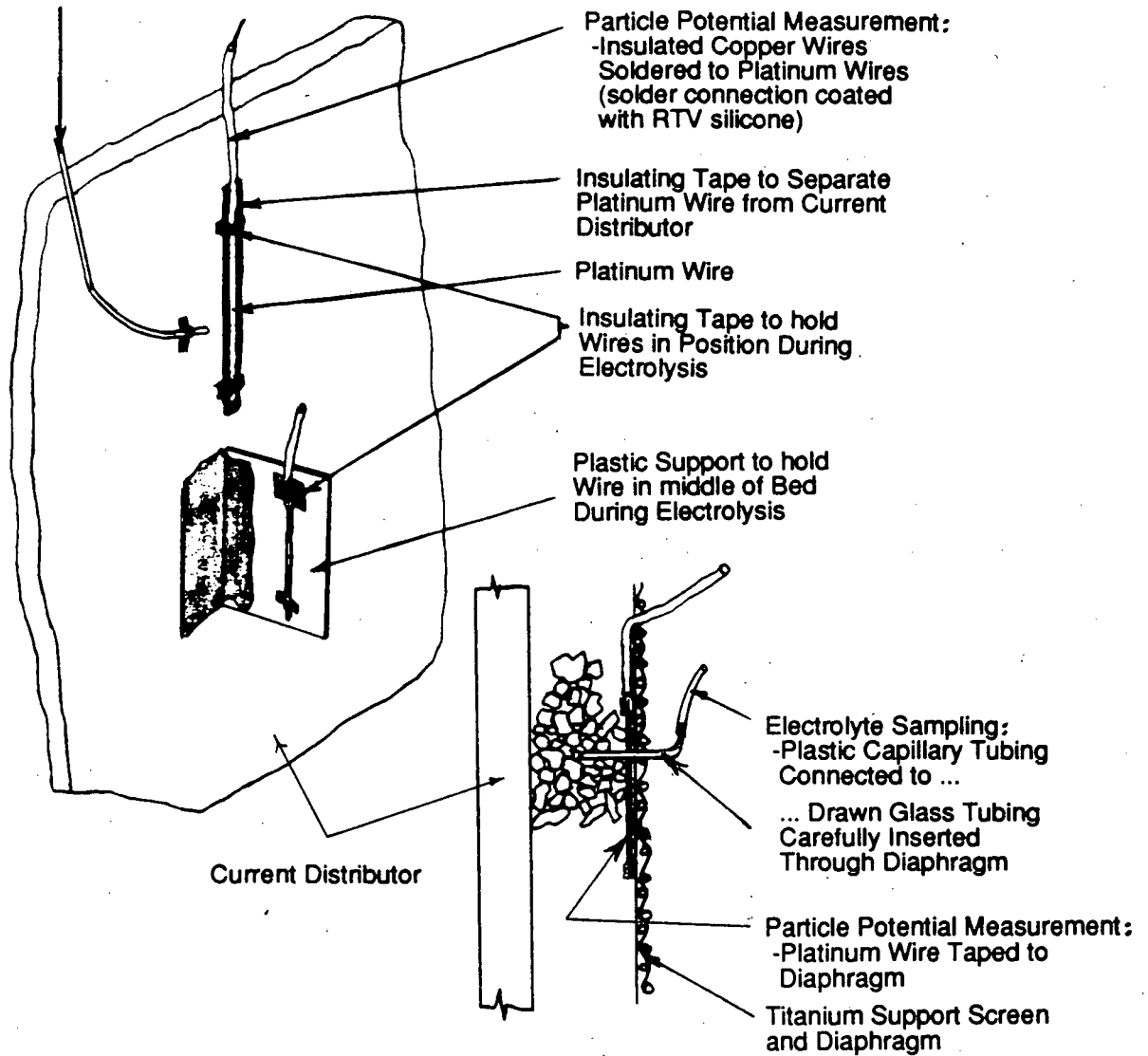
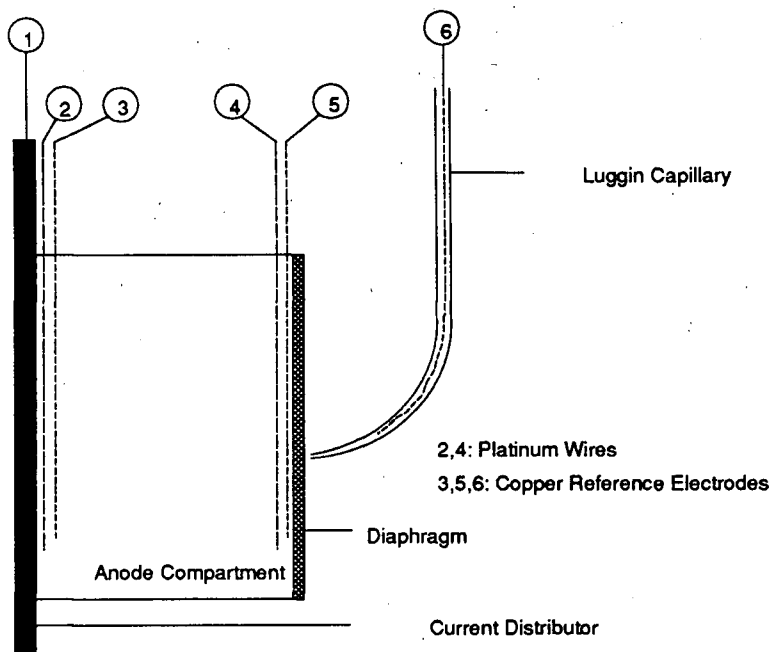


**Figure 4.3** Techniques for the measurement of solution and particle potentials in the particulate anodes, and techniques for electrolyte sampling.

Titanium was used as the cathode in all the small-scale studies. It was positioned 2.5cm and 4cm from the diaphragm for the thick and thin electrode tests, respectively. Graphite, copper plate (99.9wt% purity) and titanium were used in the tall electrode studies. These cathodes were placed 3-4cm from the diaphragm. Insulating tape or epoxy paint were used to restrict the Faradaically active surface area on the cathode to the same as the superficial area of the anode.



### TERMINOLOGY

- $\Delta E_{1,2}$  voltage drop due to contact resistances between the current distributor and the adjacent particles
- $\Delta E_{2,4}$  voltage drop across the packed bed electrode due to electronic conduction through the particles, also  $\Delta E_{1,4} = \Delta E_{1,2} + \Delta E_{2,4}$
- $\Delta E_{1,3}$  potential of the current distributor relative to the adjacent solution (electrode potential of the current distributor with respect to the  $\text{Cu}^{2+}|\text{Cu}^{\circ}$  electrode)
- $\Delta E_{2,3}$  potential of the particles in the packed bed adjacent to the current distributor relative to the solution adjacent to the current distributor (electrode potential of the particles adjacent to the current distributor with respect to the  $\text{Cu}^{2+}|\text{Cu}^{\circ}$  electrode)
- $\Delta E_{4,5}$  potential of the particles in the packed bed adjacent to the diaphragm relative to the solution just inside the diaphragm (electrode potential of the particles adjacent to the diaphragm with respect to the  $\text{Cu}^{2+}|\text{Cu}^{\circ}$  electrode)
- $\Delta E_{1,6}$  total-bed potential, **total-bed polarization is defined to be when the value for the total-bed potential,  $\Delta E_{1,6}$ , exceeds a value of 0.9-1.0V.**
- $\Delta E_r$  reversible potential of the decomposing sulphide phase
- $\Delta E_{\eta}$  reaction-process overpotential at the current distributor,  $\Delta E_{2,3} - \Delta E_r$ , or at the diaphragm,  $\Delta E_{4,5} - \Delta E_r$  (includes all processes related to the decomposition of the particles which take place within the particles)

**Figure 4.4** Summary of the various potentials measured and the terminology used throughout the thesis to describe these potential measurements.

### 4.3.2 Tall (Natural Convection) Electrodes

Natural convection studies using the tall electrode were conducted in two phases. The first phase yielded results that were generally qualitative, but provided evidence as to how quantitative information could be obtained during the second phase. The electrodes were immersed in 40l and 25l plexiglas cells for the first and second phases, respectively. The electrodes contained roughly 4500-4700g of particles and only industrial matte was used. Cell heating required to maintain temperatures of 50°C and 40°C for the first and second phases, respectively, was achieved by placing immersion heaters directly in the cells. The "tight" diaphragm was used in the first series of tests and was replaced by the "medium" diaphragm in the second test phase.

During electrolysis, electrolyte samples were drawn from a depth of approximately 1cm behind the diaphragm at eight positions between the top and bottom of the electrode through short glass capillary tubes protruding through the diaphragm. The opposite end of the glass tubes had tapered ends which were inserted into plastic capillary tubes that extended above the electrolyte surface. These details are shown in Fig. 4.3. During the first phase, electrolyte samples were withdrawn by gravity syphoning 5-10ml of electrolyte from each sample location over a 15-30min time frame. Electrolyte in the second phase was achieved by quickly withdrawing about 400-600 $\mu$ l into a 1ml syringe. Metal analyses were performed on 1ml and 100 $\mu$ l aliquots for the first and second phases, respectively, using atomic absorption. The free acid concentration was determined using these sample volumes by the titration method outlined in Sec. 4.2.

Tests during phase-one were conducted using the particulate electrode as both an anode and as a bipolar electrode. In the bipolar mode, the current density at the anode and cathode was 400A/m<sup>2</sup>, otherwise it was 225A/m<sup>2</sup>. The second testing phase employed the particulate electrode as a bipolar electrode only. A thick (1cm) copper cathode was used in this test to minimize the voltage drop

---

2 The anode and cathode in a cell containing bipolar electrodes are the only electrodes connected to the power supply. Since current may "leak" around the bipolar electrodes, the current density through these electrodes may be less than at the anode and cathode.

along its length so as to ensure even current distribution through the particulate electrode. The current density at the anode and cathode was  $400\text{A/m}^2$ . In all bipolar experiments a thick copper anode was used.

In the first series of experiments, mixing of the electrolyte in the gap between the diaphragm and the cathode, and between the anode and the cathodic surface of the current distributor in bipolar experiments, was attempted by pumping electrolyte (15-20ml/min) from the bottom of the cell between the electrodes to the top of the cell. Unfortunately, this method was not entirely reliable and was the factor leading to implementation of nitrogen sparging during the second phase to ensure uniform composition in the electrolyte outside the particulate electrode. Nevertheless, the first phase tests were valuable in that visual observation of electrolyte convection adjacent to the electrode surfaces could be easily made.

### Equipment

Power was supplied by a Hewlett Packard, Harrison 6269A (0-40V, 0-50A) DC power supply. Solution and particle potentials were recorded using Kipp & Zonen BD41 and Watanabe MC643 chart recorders. Temperature control was achieved by a YST thermistor temperature controller (model 71). Sparging flow rates were monitored using Gilmont rotameters.

### **4.3.3 Horizontal (Natural Convection) Electrodes**

Several experiments were performed with a small-scale electrode (7x11x2cm height, width and thickness, respectively) placed horizontally in a 1/ cell to confirm the importance of natural convection mass transfer in vertical packed bed electrodes. The anode was positioned below the cathode with the diaphragm facing the cathode. The anode construction is shown in Fig. 4.5.

The total-bed potential measurement was made possible by placing a Luggin capillary containing a reference electrode close to the outside surface of the diaphragm. Electrolyte samples (5-10ml) were withdrawn from a position midway between the current distributor and diaphragm and from just beneath the diaphragm, using the syphoning method outlined in the previous section.

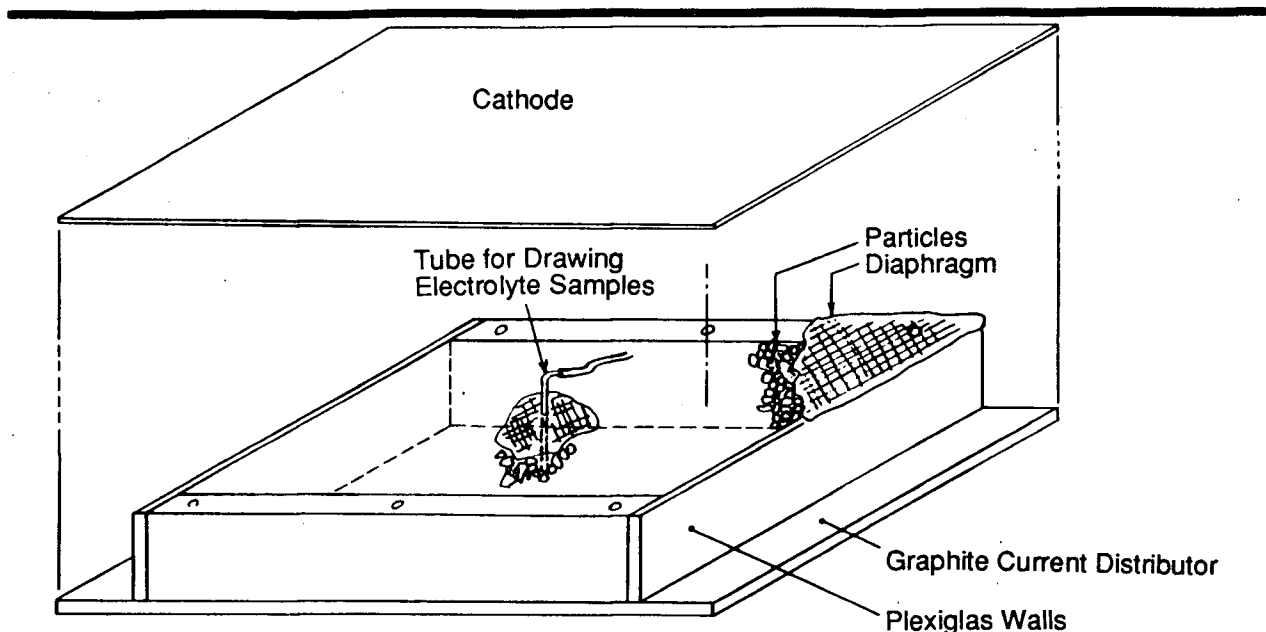


**Figure 4.5** Schematic of the horizontal packed bed anode.

Particles were loaded into the anode compartment and sufficient electrolyte was added to be certain that the solution displaced all the air from within the particulate bed before the diaphragm was placed over the particles. Following these steps, the anode was placed in the cell, the cathode positioned and the balance of the electrolyte was added. The cell was then placed in a thermostated water bath. The electrolyte in the gap between the electrodes was not agitated.

#### Equipment

Power was supplied by a Hewlett Packard 6203B (0-7V, 0-3A) DC power supply. Current was measured with a Hoyt model 653 ammeter. Temperature control was achieved by a YST thermistor temperature controller (model 71). Particle and solution potentials were recorded using the devices listed in Sec. 4.3.2.

#### **4.3.4 Small-Scale Thick Electrodes**

Small-scale studies were conducted in a 1l cell using about 800ml of electrolyte. A schematic illustration is provided in Fig. 4.6. The electrode compartment measured 7x11x2cm (width, height and thickness, respectively) and was loaded with about 470-475g of particles, although in early experiments without the titanium support mesh 500g could be loaded into the anode. A temperature

of 50°C was maintained by placing the cell in a thermostated water bath. Agitation of the electrolyte in the gap between the electrodes was achieved by sparging with nitrogen (150-200ml/min). To maintain the water balance, the cell was covered with parafilm "m" laboratory film (American Can Company) or a plexiglas cover, and deionized water was continuously added with a syringe pump. Particle and solution potentials inside the diaphragm and at the current distributor and the total-bed potential were measured using the techniques described in Sec. 4.3.2.

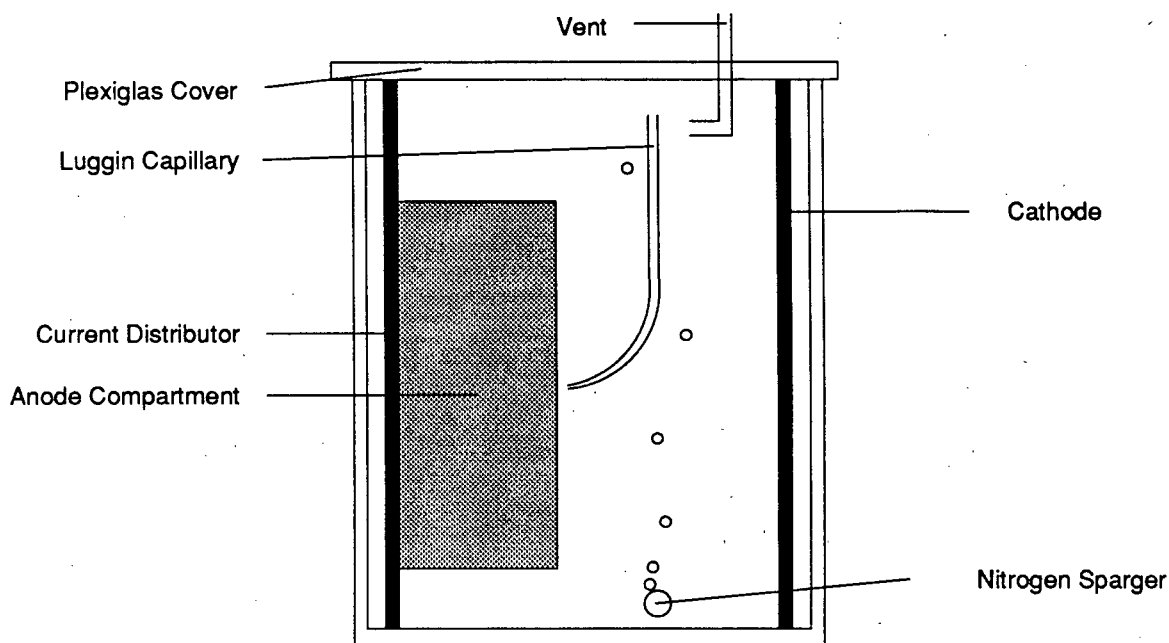


**Figure 4.6** Schematic illustration of the cell used in the small-scale electrode studies. A copper wire reference electrode was located in the Luggin capillary. The vent in the plexiglas cover ensured that nitrogen gas pressure did not develop in the cell and was designed to permit entrained electrolyte to drain back into the cell.

Prior to switching on the current, several hours were provided to ensure that the temperatures of the electrolyte and the particulate anode had stabilized at 50°C. During several runs, 300-400µl of electrolyte were withdrawn at selected times from the anode compartment, at a position adjacent to the center of the current distributor, and from the bulk electrolyte through capillary tubing into a 1ml syringe, from which 100µl aliquots were obtained and analyzed for metal ions and acid by the methods outlined previously. The bulk electrolyte sample was obtained by placing the capillary tubing as close to the center of the electrode gap as possible.

The current density used in all tests was  $400\text{A/m}^2$ . During early experiments, the total charge passing through the cell was calculated from time and current data. A coulometer was used in subsequent runs. In many experiments, a controller was used to reset the applied current to a low value ( $\approx 40\text{A/m}^2$ ) once total-bed polarization had taken place. This was useful because the expected duration of the various experiments could not be necessarily accurately predicted beforehand. Thus, for experiments which ended during the night, the current was adjusted to a value thought to be sufficiently low that the copper recovery would not be effected, but great enough to ensure that the condition of the particles was not significantly altered until they could be withdrawn and examined.

At the end of each run, the anode was thoroughly rinsed with deionized water and dried under ambient conditions. In experiments where the phase and physical structure of the particles were being investigated, several particles were carefully withdrawn for analysis before the bed dried. In experiments where reaction distribution was being investigated, about 3-5g of particles from three different positions between the diaphragm and the current distributor were carefully extracted. A representative sample of the remaining particles was obtained by the rolling technique outlined in Sec. 4.2.2. Assays on these samples were performed according to the methods described earlier.

### Equipment

Power was supplied by a Hewlett Packard 6203B (0-7V, 0-3A) DC power supply. Current was measured with a Hoyt model 653 ammeter, calibrated several times with a Sensitive Research Instrument Corporation Reference Standard Polyrange multiple meter (model C, guaranteed accuracy to 1/4%). The coulometer was a Ferranti Ltd. (Yellott Solar Energy Lab) 2-wire type FKT, which had been calibrated using a 25A Sanya shunt in a one-week test. Temperature control was achieved by a YSI thermistor temperature controller (model 71). Particle and solution potentials were recorded using the devices listed in Sec. 4.3.2. A Horizon Ecology Co. pH controller model 5997-20 was used to reset the current from the power supply to a low value ( $\approx 40\text{A/m}^2$ ) once total-bed polarization had taken place. The syringe pump was a Sage Instruments model 341 pump.

#### 4.3.5 Small-Scale Thin Electrode Studies

The procedures and equipment outlined in the previous section also apply to the small-scale thin electrode experiments; however, several exceptions should be noted:

1. Only particles between 2.0-2.8mm were used and the electrode compartment was 2.9mm thick.
2. The starting particle weight was reduced to 70-72g.
3. The superficial current density was reduced (to approximately  $60\text{A/m}^2$ ) so as to maintain the same ratio of total current to particle weight as in the small thick-electrode experiments.
4. The solution potential at the current distributor was not measured, electrolyte within the particulate bed was not sampled and only bulk particle analyses were performed.
5. The coulometer and pH controller were used in all experiments. The current was adjusted to under about  $10\text{A/m}^2$  after total-bed polarization.

Graphite was used as the current distributor in two experiments. In the first test, a mixture of four different mattes was used: synthetic pure chalcocite, synthetic chalcocite doped with iron, synthetic chalcocite doped with lead and industrial matte. Only 3-5g of the latter three materials were placed in the electrode and their locations were carefully recorded so they could be identified at the end of the run. In the second experiment, industrial matte was placed in the anode. Gold was used as the current distributor in all other thin-bed experiments.

#### 4.4 EFFECTIVE CONDUCTIVITY MEASUREMENTS

A brief investigation of the effective or apparent conductivity of the industrial matte at various copper extractions was performed by filling an 11x7x2cm container, constructed using graphite electrical contacts (11x7cm) separated by plexiglas panels. A four-electrode measurement system was employed. The potential of the matte adjacent to the graphite was measured by platinum wires positioned on insulating tape in the same manner as shown in Fig. 4.3.

---

## CHAPTER 5

---

### NATURAL CONVECTION

The objectives of the present studies are to (a) qualitatively assess, by visual inspection, the level of turbulent mixing through the diaphragm of a tall (70cm), 2cm-thick particulate electrode as compared to through a flat metal anode with a small amount of slimes accumulation, (b) estimate the extent of the downward convection motion within the anode, which should be reflected in the vertical copper concentration gradients, and (c) evaluate whether natural convection activity is related in any way to total-bed polarization ( $\Delta E_{1,6} > 0.9-1V$ ) of thick (>2cm) packed bed electrodes. Initially, however, a few experiments with a small-scale 2cm-thick horizontal packed bed electrode were performed to demonstrate that the extended surface area of particulate electrodes is unimportant if the natural convection mechanism does not develop.

#### 5.1 HORIZONTAL ELECTRODE STUDIES

The results of the horizontal particulate electrode studies are summarized in Table 5.1. Included in the table are data from two vertical electrode experiments to illustrate the important effect of electrode orientation. The  $i^2\tau$  values at total-bed polarization for the three horizontal runs were roughly equal, which suggests that the predominant mass transfer mechanism for copper from within the bed to the bulk solution through the diaphragm was molecular diffusion and that total-bed polarization was due to copper sulphate precipitation [5,31]. Copper sulphate crystals observed at the bottom of the horizontal particulate electrode in several tests conducted at  $225A/m^2$  verified

this total-bed polarization mechanism. This was expected since the horizontal orientation prevented the development of natural convection electrolyte circulation through the electrode. In other words, even though the high surface area of an electrode packed with matte particles leads to a reduction in current density at reaction interfaces, and so reduces the mass transport requirements within each particle, natural convection mass transport is still required to move the copper liberated by each particle out of the anode compartment. Note that the values of  $i^2\tau$  for the vertical experiments are nearly three orders of magnitude greater than those of the horizontal tests and that they are not equal.

**Table 5.1** Summary of electrorefining tests of 2cm-thick horizontal electrodes filled with industrial matte particles using the "tight" diaphragm (porosity: 0.34, thickness: 0.6mm). The vertical electrode data at 400A/m<sup>2</sup> and 225A/m<sup>2</sup> are from tests using the small-scale (height: 11cm) and the 70cm-tall electrodes respectively.

Current Density (A/m <sup>2</sup> ) (Experiment no.)	Horizontal			Vertical	
	10 (10)	20 (9)	225 (8)	400 (16,14A)	225 (13)
Transition Time (hr)	173-178	38-40	0.1-0.5	42-44	65-67
$i^2\tau$ (A <sup>2</sup> m <sup>4</sup> hr)	17(10 <sup>3</sup> )	16(10 <sup>3</sup> )	18(10 <sup>3</sup> )	6.9(10 <sup>6</sup> )	3(10 <sup>6</sup> )
$i\tau$ (Am <sup>2</sup> hr)	1.8(10 <sup>3</sup> )	0.8(10 <sup>3</sup> )	0.08(10 <sup>3</sup> )	17(10 <sup>3</sup> )	15(10 <sup>3</sup> )
Initial Bulk Electrolyte Conditions					
Cu (g/l)	39	42	43	45	45
H <sub>2</sub> SO <sub>4</sub> (g/l)	145	161	112	160	158
Temperature (°C)	45	46	45	50	45-50
Electrolyte in Particulate Anode at Transition Time (middle of bed, bottom of bed)					
Cu (g/l)	70, --	72, 77	61, 95	na	na
H <sub>2</sub> SO <sub>4</sub> (g/l)	129, --	79, 60	--, --	na	na
Notes: na: not applicable --: not analyzed					

The importance of natural convection in greatly extending the electrolysis time for vertical particulate copper sulphide anodes may be appreciated by comparing the values of  $i\tau$ , which is a measure of copper extraction, for the horizontal and vertical orientations. Copper extraction from the vertical electrodes is approximately 10-times greater than from a horizontal electrode operating at only 1/40th of the current density. However, the reader must not conclude that total-bed polarization of 2cm-thick vertical electrodes is also due to copper sulphate precipitation, since the

value for it is now nearly constant. The final two sections of this chapter will demonstrate that, under the electrolysis conditions employed in this thesis, total-bed polarization of a vertical particulate electrode is not related to mass transport from the anode compartment across the diaphragm to the bulk solution at all.

## **5.2 VERTICAL STUDIES**

### **5.2.1 Convection Studies**

#### **5.2.1.1 Tall Electrode Results**

The electrolyte adjacent to the surface of a corroding metal anode is enriched in metal ions, thus increasing its density relative to the bulk solution. This density difference will cause the electrolyte near the anode to descend or flow downwards along the anode's surface. At the cathode, the copper-depleted electrolyte is less dense than the bulk electrolyte and thus tends to ascend along the electrode. These natural convection flows are turbulent over most of the height of a tall electrode (height >10-15cm) and produce a mild circulation of electrolyte between the electrodes. This tends to equalize the concentration differences between the electrodes by causing a net transport of copper from the anode to the cathode. One would anticipate a similar convection mechanism to develop when a particulate anode composed of copper sulphide particles is substituted for a copper anode.

Equipment debugging tests using copper anodes and cathode demonstrated that turbulent convection activity is easily observed visually, even at anodic surfaces with modest accumulations (2-3mm-thick) of "slimes".

#### **Phase One**

Natural convection was evaluated qualitatively by making visual observations through the plexiglas cell walls. No convection through the diaphragm along the top two-thirds of the electrode was detected. However, electrolyte exiting the bottom of the packed bed and downward through the lower 5-10cm of the anode basket was easily observed. A reduced but detectable amount of downward convection could also be observed along the diaphragm surface between 10-25cm from

the bottom of the electrode. Generally the convection action, where it could be seen, did not extend beyond the thickness of the titanium support screen ( $\approx 2\text{mm}$ ) except at the bottom of the electrode or if the cell was jarred.

As a comparison, the convection action at the cathode could be readily seen as far as 10mm from the cathode surface and the convection motion along a copper anode covered with a small amount of slimes was readily observed along most of its height (with the exception of the top 15-20cm), although not as far into the bulk solution as at the cathode. Possibly, the relatively tight diaphragm (porosity: 0.34, thickness: 0.60mm) used in these tests prevented turbulent mixing between the anode compartment and the bulk electrolyte except near the bottom of the electrode.

The appreciable turbulent convection through the diaphragm at and near the bottom of the packed bed, as compared to that at higher positions, suggests the net flow of electrolyte may be to enter the top portion of the bed, pass downward between the particles, and exit through the lower portion of the bed. However, it is possible that convection along the top part of the diaphragm is not sufficiently turbulent to be easily detected visually and the titanium support mesh along the surface of the diaphragm makes observations more difficult than at smooth flat surfaces.

Nevertheless, quantitative evidence was obtained that supports the mechanism just described. Several analyses of the electrolyte extracted from different positions in the particulate electrode are shown in Fig. 5.1. These data reveal that the copper concentration increases towards the bottom of the electrode. However, unless the bulk electrolyte is vigorously mixed<sup>1</sup>, this downward convection in the anode also leads to an accumulation of copper in the gap between the anode and the cathode towards the bottom of the cell, as shown by the filled circle data points in the figure. This is an important result because it demonstrates that natural convection processes, while effectively flushing copper ions from the anode compartment, are limited to the region close to the diaphragm and are ineffective in terms of mass transfer across the gap between the electrodes.

---

<sup>1</sup> Electrolyte was not reliably circulated from the bottom to the top of the cell, with the result that occasionally there was no circulation flow. During these periods, natural convection was the only mechanism for mixing the bulk electrolyte. Although segregation of copper in the gap between the electrodes was accelerated at these times, segregation proceeded even when electrolyte was being circulated.

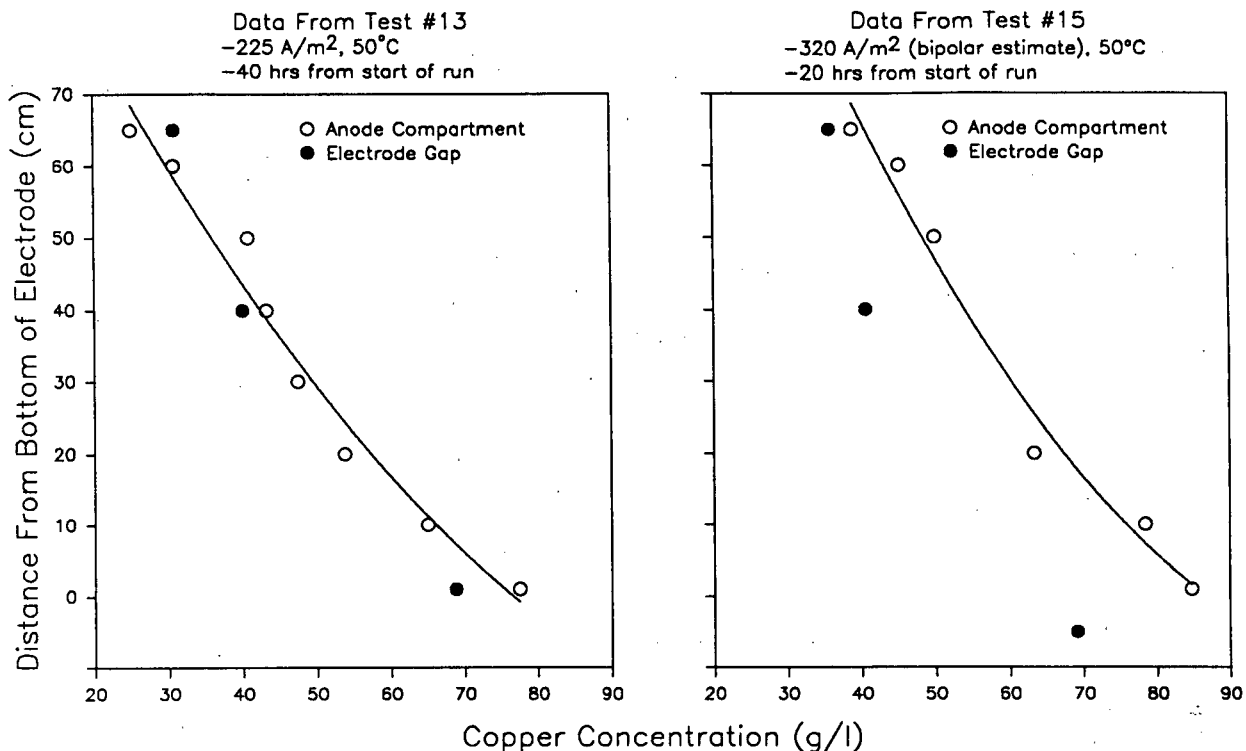


**Figure 5.1** Variation of copper concentration with vertical position in the 70cm-tall particulate anode placed in cell without nitrogen sparging. Test #15 was conducted with the particulate electrode employed as a bipolar electrode. The estimate of 320 A/m<sup>2</sup> is based on the difference between the amount of copper plated on the end cathode and on the cathodic surface of the bipolar electrode.

### Phase Two

A more open diaphragm (porosity: 0.56, thickness: 0.58mm) was employed for this testing phase. However, due to the vigorous mixing conditions created by the nitrogen sparging, convective flow adjacent to the vertical dimension of the anode was not readily seen. Nevertheless, electrolyte was observed descending through the bottom of the anode. While the greatest portion of this flow appeared to occur furthest from the current distributor, it was largely distributed across the full thickness of the electrode. This electrolyte was then rapidly entrained in the rising bulk electrolyte flow caused by the nitrogen sparging.

There are several ways to approach the problem of modelling the mass transfer of copper from within the anode compartment to the bulk solution. One method is to assume the flux of copper from the anode compartment to the bulk solution can be calculated using an *effective* mass transfer

coefficient,  $k$ , and an estimate of the copper concentration within the packed bed electrode, via Eq. (5.1), where the mass transfer coefficient is determined from an appropriate dimensionless equation for natural convection conditions from packed bed electrodes, such as Eq. (3.23).

$$N = -k(C_{Cu^{2+}}^{bed} - C_{Cu^{2+}}^{bulk}) \quad (5.1)$$

$$Sh = a(ScGr)^b \quad (3.23)$$

A second method is to treat the mass transfer problem as a flux of copper from within the packed bed through the diaphragm to the bulk solution with the flowing electrolyte. Although the convective flow of electrolyte under natural convection conditions undoubtedly has both horizontal and vertical components, it is interesting to first consider one of the two limiting cases, that is when the convective flow is entirely vertical.

The analyses presented in Fig. 5.2 suggest that the bulk motion of electrolyte indeed has a significant vertical component, as the copper concentration increases towards the bottom of the electrode. Furthermore, the electric field in the anode will cause hydrogen ions, which may carry as much as 60-80% of the total current, to migrate away from the anode and sulphate ions, which may transport approximately 15-20% of the current, to move into the compartment. The estimation of these values is provided in Appendix B. If the net flow of electrolyte in the compartment is downwards, the hydrogen ions and total sulphate ion concentrations should decrease and increase, respectively, towards the bottom of the anode. The right plot of the figure shows this to be the case.

Data from Fig. 5.2 may be used to estimate the downward convective velocity and the residence time of a parcel of electrolyte flowing through the anode compartment. The important assumptions may be reviewed as follows:

1. Copper is transported only by convection. The other mechanisms are too small to matter.
2. Although there is mixing of electrolyte from within the anode compartment to the bulk solution along the full height of the electrode, the net effect is a downward motion through the electrode, with electrolyte entering near the top and leaving at the bottom.
3. The electrolyte moves downward in plug flow.

Data From Test #47  
 -385 A/m<sup>2</sup> (bipolar estimate), 40°C  
 -9 hrs from start of run

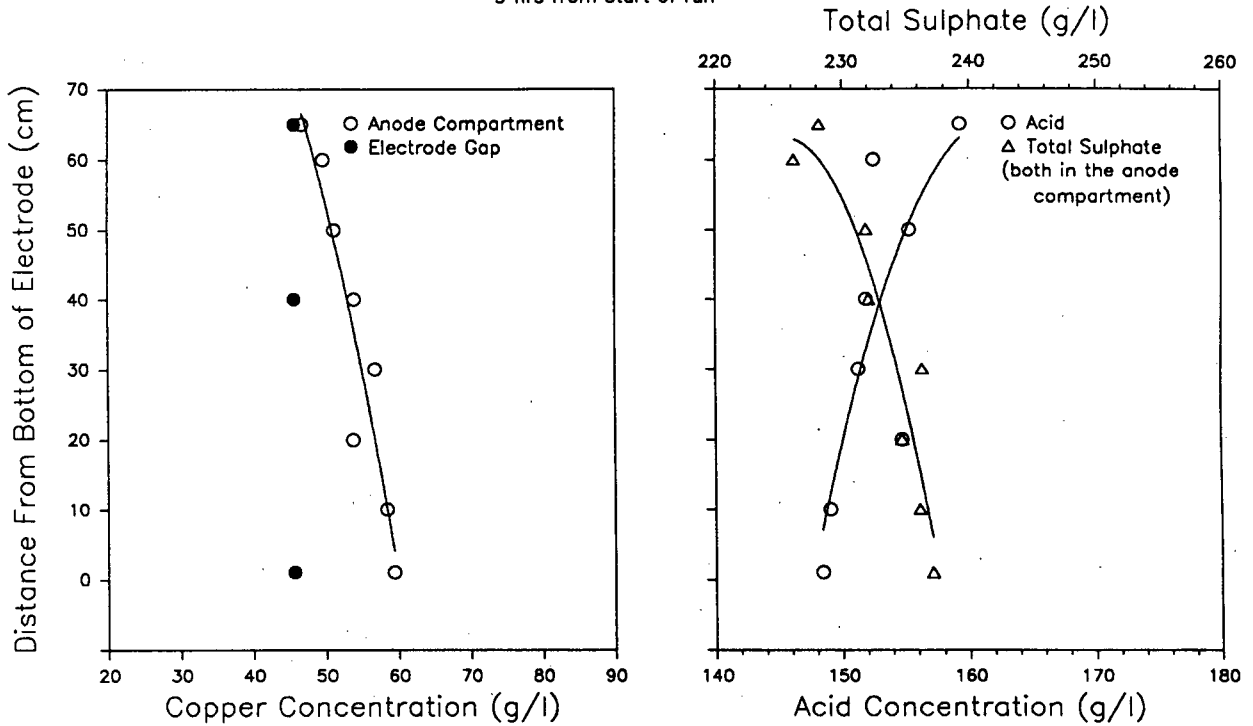


**Figure 5.2** Variation of copper, acid and total sulphate concentrations with vertical position in the 70cm-tall particulate anode operated as a bipolar electrode. The estimate of 385 A/m<sup>2</sup> is based on the difference between the amount of copper plated on the end cathode and on the cathodic surface of the bipolar electrode. Nitrogen sparging of the bulk electrolyte was employed in this test.

The electrolyte velocity and residence time may be obtained by solving a mass balance on a differential slice of the anode of height  $dy$ . This results in the following equation:

$$V = -\frac{iMz}{10nF} \frac{dy}{dC}$$

where  $y$  is the vertical position (0-70cm),  $C$  is the copper concentration in g/l (59 @  $y=0$ , 47 @  $y=70$ ),  $V$  is the volumetric flow rate in cm<sup>3</sup>/min,  $z$  is the electrode's width (10cm),  $M=63.54$  g/mol,  $nF=192,974$  coulombs/mol and  $i=385$  A/m<sup>2</sup>, and the constant 10 in the denominator is a conversion factor.

Solution of this equation gives a flow rate of only about 44cm<sup>3</sup>/min, equivalent to a superficial velocity of approximately 2cm/min (superficial flow area: 20cm<sup>2</sup>) and a residence time of around 14min (bed porosity≈0.45). In the absence of any transport mechanism, the time required to saturate

the bed in copper sulphate is about 30-35min (72g/l CuSO<sub>4</sub> at 165g/l H<sub>2</sub>SO<sub>4</sub>, 40°C [48]), or double the residence time, which demonstrates that natural convection processes through the anode are sufficient to prevent precipitation of copper sulphate in the spaces between the particles in the packed bed electrode. Therefore, total-bed polarization of the electrodes should not be related to natural convection processes.

If convection is considered to be completely horizontal, a superficial velocity of only 0.06 cm/min (superficial area: 700cm<sup>2</sup>) would completely exchange the electrolyte in the compartment every 14min.

### 5.2.1.2 Small-Scale Electrode Results

Analyses of copper in the electrolyte adjacent to the current distributor in a small-scale study provide some information regarding the magnitude of natural convection. These are summarized in Table 5.2.

**Table 5.2** Copper concentration at the current distributor and in the gap between the electrodes during electrolysis of industrial matte in a small scale electrode. Current density: 400A/m<sup>2</sup>; anode dimensions: 2x7x11 thickness, width, height.

Time (hrs)	Copper Concentration (g/l)		
	Curr. Dist.	Electrode Gap	Diff.
0.5	50	46	4
12.5	47	45	2
22.5	45	45	0
36.5 ( $\tau$ ) <sup>1</sup>	46	43	2

Notes: 1.  $\tau$  represents the transition time or the time of total-bed polarization

It will be shown in the following chapter that decomposition preferentially occurs near the current distributor when the current is first switched on. Thus, the copper concentration gradients between the current distributor and the gap between the electrodes at 30min likely represents the maximum value which is attained during electrolysis. If there is no mass transfer at all, 30min of electrolysis at 400A/m<sup>2</sup> should result in the average copper concentration in the particulate anode increasing to about 71g/l, much higher than the concentration at even the current distributor. Furthermore, if the only mass transfer mechanism is diffusion, the concentration gradient of 4g/l

across a 2cm-thick electrode at 30min is capable of supporting a current density of less than  $1\text{A/m}^2$  (assuming a diffusivity of about  $10^{-5}\text{cm}^2/\text{s}$  for the cupric ion). In other words, natural convection mass transport accounts for virtually all of the mass transfer. In fact, total-bed polarization of the anode in this test occurred at 36.5hrs without any significant increase in copper concentration in the electrode. This suggests that total-bed polarization is due to other factors. These are introduced in the following sections.

These data may be used to estimate the convection velocity, with the flux equal to  $400\text{A/m}^2$ , or  $13.2(10^{-6})\text{g/cm}^2\cdot\text{s}$ , and the average copper concentration in the electrode equal to about  $46\text{g/l}$ . If the convection is considered to be completely horizontal, the convection velocity is slightly less than  $0.02\text{cm/min}$ . This is roughly equal to the horizontal velocity for the tall electrode calculated earlier and verifies that, if convection is considered in the horizontal direction only, the effective flow rates necessary to achieve high mass transfer rates are very small.

### 5.2.2 Total-Bed Polarization

This research has shown that the total-bed potential,  $\Delta E_{1,6}$ , initially decreases from a relatively high "start-up" value as shown in Fig. 5.3. This was not reported in previous studies on packed bed copper matte refining [4,32]<sup>2</sup>. Also shown on the figure are the potentials of the particles adjacent to the current distributor,  $\Delta E_{1,2}$ , and diaphragm,  $\Delta E_{1,5}$ . The declining and rapidly rising values of these potentials during the first few hours and at the end of the run, respectively, are in very close synchronization with the behaviour of the total-bed potential, which suggests that total-bed polarization of the electrode is related to particle-current distributor and/or inter-particle electrical conductivity and may be unrelated to Faradaic or mass transport processes.

### 5.2.3 Copper Extraction

Copper recovery at total-bed polarization of the packed bed for the experiment shown in Fig. 5.3 was about 37-39%. This was considerably less than the extraction values of slightly over 50% reported by Mao and Peters [4] for industrial mattes. The mattes used by these authors contained

---

<sup>2</sup> One curve from reference 32 shows a similar feature, but this not discussed.

more copper and less impurities than the industrial matte tested in the present studies, as summarized in Table 5.3, leaving the impression that copper recovery is very sensitive to the presence and amount of certain impurities.

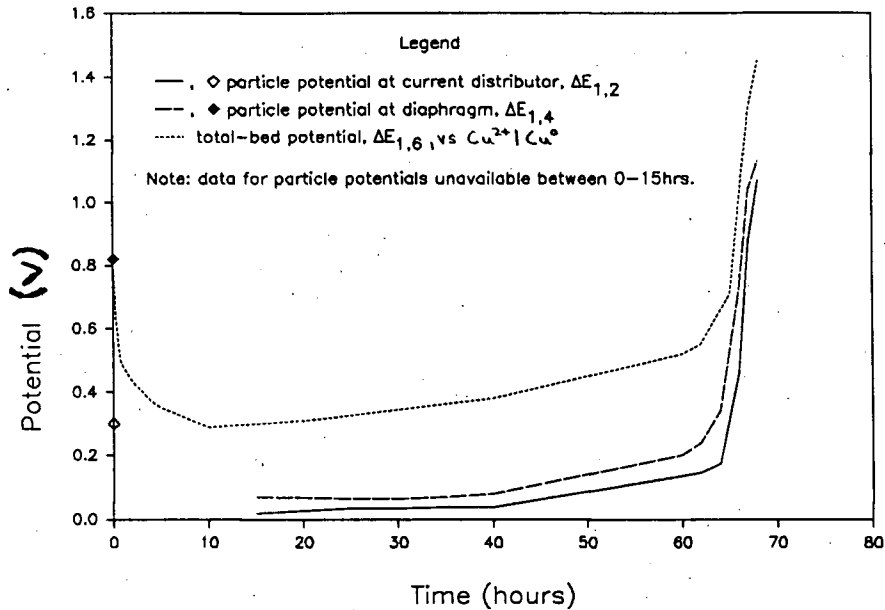


**Figure 5.3** Galvanostatic potential curves for anodic decomposition of industrial matte in a 70cm-tall, 2cm-thick packed bed electrode. Particle diameter: 0.5-4.0mm; current density: 225A/m<sup>2</sup>; electrolyte: 45g/l Cu, 159g/l H<sub>2</sub>SO<sub>4</sub>, 2g/l Fe, 50°C. (Test 13)

**Table 5.3** Comparison between the industrial matte used in this study and the industrial mattes used by Mao and Peters [4]. Analyses are in weight percent.

Species	This Thesis	Mao & Peters
Cu	69.3	73.3
S	20.8	20.5
Fe	4.4	3.46
Pb	2.4	1.42
Zn	0.9	0.32

This result, in conjunction with those of the previous sections, reveals that while natural convection mass transport within the particulate matte anode is the key to extended copper extraction as compared to the electrolysis of massive (solid) matte electrodes, total-bed polarization mechanisms, possibly related to electrical contact between the current distributor and particles, and

other factors, such as impurity content, appear to be ultimately more important in terms of the final copper recovery possible and indeed, the potential development of a process. These other "polarization" mechanisms and factors constitute the main focus of this thesis and are discussed in the subsequent chapters.

However, inasmuch as natural convection mass transfer permits greatly extended copper recovery from particulate electrodes, the fact that the convection motion is predominantly downwards and leads to vertical copper concentration gradients within the electrode, is an important result. Furthermore, this pattern is independent of the extent to which the electrolyte in the gap between the electrodes is mixed and is independent of the diaphragm properties selected in this thesis. Therefore, the expectation is that, without appropriate design considerations, there may be a limit to the height of these particulate electrodes. In addition, the convection activity within the electrode is ineffective in terms of mass transfer across the gap between the diaphragm and the current distributor. Thus, agitation of the electrolyte in this gap is necessary. Such design considerations are not part of the scope of this thesis.

### 5.3 NOMENCLATURE

a,b fitting constants for Eq. (3.23)

C concentration of species, g/l or mol/m<sup>3</sup>

F Faraday's constant, 96487 coul/equiv

Gr Grashof number,  $\frac{g^2 \Delta \rho}{\rho} \left( \frac{\rho}{\eta} \right)^2$ , dimensionless

i current density A/m<sup>2</sup>

k mass transfer coefficient, m/s

M molecular weight of copper, g/mol or kg/kmol

n number of equivalents per mole of copper (2)

N flux of species, mol/m<sup>2</sup>·s

Sc Schmidt number,  $\frac{\eta}{\rho D}$ , dimensionless

Sh Sherwood number,  $\frac{k}{D}$ , dimensionless

V volumetric flow rate through packed bed electrode, cm<sup>3</sup>/min or m<sup>3</sup>/s

x coordinate positions (thickness), cm or m

y vertical position in packed bed electrode, cm or m

z width of the particulate electrode

$\tau$  the transition time (the time at which the total-bed potential exceeds a value of 0.9-1.0V), s or hr

---

## **CHAPTER 6**

---

### **PARTICULATE ELECTRODES (Some Fundamentals)**

In a particulate electrode, Faradaic activity is, in general, distributed throughout the entire volume of the electrode. This arises because the current has two parallel paths available to flow from the current distributor to the bulk solution: through the solid material (electronic conduction) and through the solution (ionic conduction). Eventually, all the current must leave the electrode via the solution. Therefore, between the current distributor and the surface of the electrode adjacent to the bulk solution, current is transferred from the solid phase to the electrolyte. Distribution of this current transfer is a function of the relative impedances of these phases (i.e., the effective conductivities) and of the relative impedance of the Faradaic process (i.e., charge transfer) to processes in which species are transferred into and/or out of the electrode (i.e., mass transfer). It is entirely possible that the current transfer is not evenly distributed within the electrode. A relatively simple mathematical model is developed to assess the variation in anodic decomposition rates of copper mattes at different positions across the particulate anode. This was considered to be of importance with regards to the effect of electrode thickness on overall copper extraction.

#### **6.1 A GENERAL MODEL**

It is useful to start with general equations in order to place into perspective the assumptions necessary to simplify the mathematics. Some assumptions have already been listed in Sec. 3.9 of

Chap. 3. Formulation of the model follows the approach of Newman and Tobias [86] and begins with a mass balance in a differential volume element of the electrode, shown in Fig. 6.1. The mass balance equation is

$$-\nabla \cdot \vec{N} + r_{ig} = \frac{d(\epsilon C_i)}{dt} \quad (6.1)$$

where  $\vec{N}$  is the flux of species through the volume element,  $r_{ig}$  is the net generation of species  $i$  within the volume element and  $d(\epsilon C_i)/dt$  accounts for the change in electrode structure and species concentration with time.

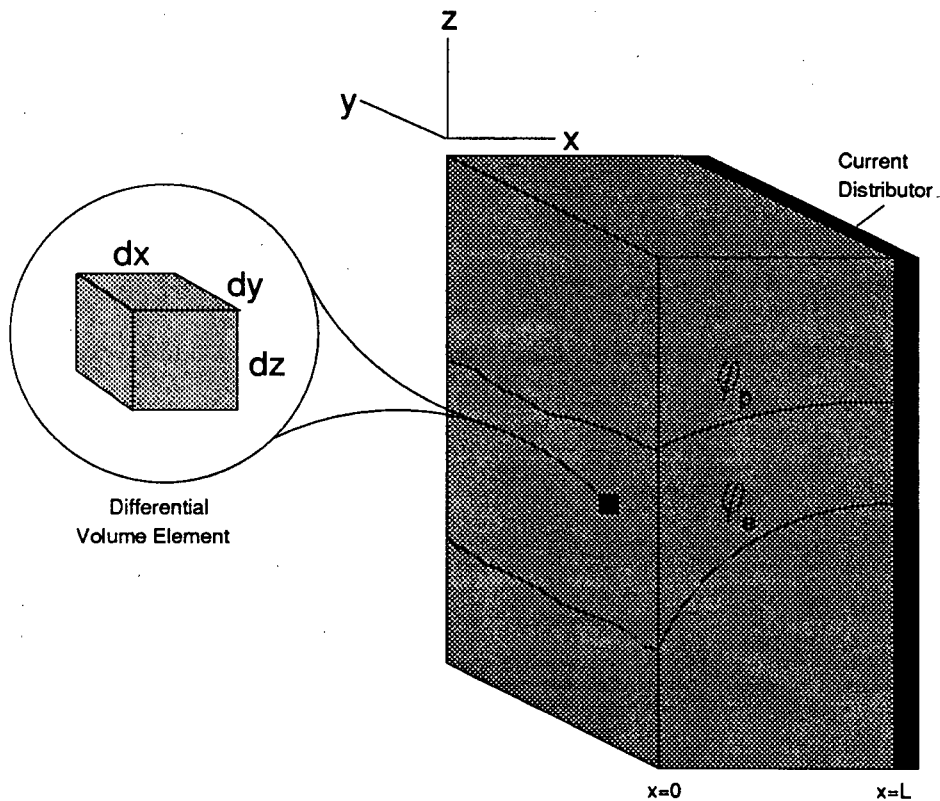


**Figure 6.1.** Schematic of a particulate electrode.  $\Phi_p$  and  $\Phi_e$  represent the potential of the solid and electrolyte phases respectively.

The flux of each species is given by Eq. (3.33), with  $\nabla \cdot$  replacing  $d/dx$  to include the three space dimensions and  $\epsilon$  is included to account for the bed porosity. In some systems,  $\epsilon$  is probably more accurately represented as a function,  $f(\epsilon)$ , to account for bed tortuosity as well as porosity.

$$\frac{\vec{N}}{\varepsilon} = -\mathcal{D}_i \nabla \cdot C_i - \mu_i C_i \nabla \cdot \Phi_e + \frac{\vec{u} C_i}{\varepsilon} \quad (3.33)$$

By treating the bed and electrolyte on a macroscopic scale, it is possible to define a potential in the solid material (particles),  $\Phi_p$ , and another in the electrolyte filling the pores of the particulate electrode,  $\Phi_e$ . The difference term,  $\Phi_p - \Phi_e - E_r$ , represents the local overpotential of the electrode. Similarly, two current densities may be defined:  $i_p$  referring to current density in the solid phase and  $i_e$  describing the current density in the electrolyte.

It is convenient to refer to the projected or superficial area of the electrode, rather than to the areas of the individual phases. Ohm's law may then be applied to the solid phase, giving

$$\vec{i}_p = -\sigma \nabla \cdot \Phi_p \quad (6.2)$$

where  $\sigma$  is the effective conductivity of this phase. The flux of charged species, when appropriately summed, yields an expression for the current density in the electrolyte.

$$\vec{i}_e = F \sum_i z_i \vec{N}_i \quad (6.3)$$

where  $z_i$  is the charge on species  $i$ . It is reasonable to assume that the solution is electrically neutral, that is,

$$\sum_i z_i C_i = 0 \quad (6.4)$$

Therefore, the convection term of Eq. (3.33) does not contribute in Eq. (6.3).

If there are no reactions occurring in the electrolyte phase, the local reaction rate,  $r_{ig}$ , is equal to the transfer of current from the solid to the electrolyte and is, in general, a function of the local overpotential, species concentrations and, possibly, particle parameters such as particle diameter and porosity for reactions occurring within particles of a particulate electrode. The general expression is

$$r_{ig} = \frac{s_i}{nF} \nabla \cdot \vec{i}_p = \frac{a}{nF} f \left( \Phi_p - \Phi_e - E_r, \frac{C^o}{C_i}, d_p, \varepsilon, \dots \right) \quad (6.5)$$

where  $s_i$  is the fraction of the total current consumed by species  $i$ ,  $a$  is the interfacial area of the electrode and  $C_i^\circ$  is a reference concentration for each species participating in the reaction.

Finally, there is no accumulation of charge in the electrode, so Eq. (6.6) may be written.

$$\vec{i}_p + \vec{i}_e = I \quad (6.6)$$

These equations form the basis of the model. Difficulties arise in estimating the convective velocity,  $\vec{u}$ , and selecting an appropriate expression for the local reaction rate,  $r_{ig}$ .

## 6.2 APPLICATION TO COPPER SULPHIDE ELECTROLYSIS

Although the concentration of species within the anodic compartment may not remain exactly constant during anodic decomposition of the copper sulphide particles, it is reasonable to assume that, over a short period of time, electrolysis proceeds under steady-state conditions. In addition, the bed porosity is not expected to change significantly during electrolysis. Therefore,  $d(\epsilon C_i)/dt=0$ .

The expansion of Eq. (6.3) under the electroneutrality condition, Eq. (6.4), is

$$\vec{i}_e = -\kappa \nabla \cdot \Phi_e - F \sum_i z_i \mathcal{D}_i \nabla \cdot C_i \quad (6.7)$$

where  $\kappa$  is the effective the conductivity of the electrolyte, which accounts for the porosity and tortuosity of the electrode. The true electrolyte conductivity,  $\kappa^o$  is given by

$$\kappa^o = \sum_i z_i \lambda_i C_i \quad (6.8)$$

with  $\lambda_i$  defined as the equivalent ionic conductance of species  $i$  ( $\mu_i = \lambda_i/F$  and  $\lambda_i$  has the same sign as  $z_i$ ).

It would be convenient to ignore the second term, the diffusion potential, on the right side of Eq. (6.7) and this would be readily justified if the diffusion coefficients of all the species were equal. Nevertheless, in this system, there is a great abundance of supporting electrolyte (acid) and appreciable electrolyte convection, with the result that the concentration variation of the major diffusion potential components through the thickness of the electrode are likely to be rather small. Therefore, the diffusion potential will be neglected and an effective conductivity,  $\kappa$ , may be taken

as essentially constant throughout the electrode, simplifying Eq. (6.7) to

$$\vec{i}_e = -\kappa \nabla \cdot \Phi_e \quad (6.9)$$

There are several possibilities for an expression of the local reaction rate in this system, depending upon the mechanism assumed to be controlling the reaction process. The problem is simplified by assuming that no leaching occurs and that impurity dissolution of zinc and iron, for example, consumes too little of the total current to matter. The local reaction rate is proportional to the rate at which current is exchanged between the particles and the solution,  $\nabla \cdot \vec{i}_p$ .

The first step in the reaction mechanism sequence is the Faradaic or charge transfer process, for which the general rate expression is given by an extended form of the Butler-Volmer equation.

$$\nabla \cdot \vec{i}_p = ai_o \left\{ \frac{C}{C^o} \exp \left[ -\alpha \frac{n^* F}{RT} (\Phi_p - \Phi_e - E_r) \right] - \frac{C_{ss}}{C_{ss}^o} \exp \left[ (1 - \alpha) \frac{n^* F}{RT} (\Phi_p - \Phi_e - E_r) \right] \right\} \quad (6.10)$$

where  $i_o$  is the exchange current density at the reference concentration of copper in the electrolyte,  $C^o$ , and in the sulphide phase,  $C_{ss}^o$ ,  $\alpha$  is the transfer coefficient (usually assumed to be equal to 0.5 in the absence of other information) and  $n^*$  is the number of electrons exchanged in the actual electron transfer step (usually assumed to be equal to one in the absence of other information). Note that  $n^*$  may be different than the number of electrons exchanged in the over-all electrode reaction,  $n$ , which is 2 for  $\text{Cu}^{2+}$ .

Once copper is released from the sulphide to the electrolyte, it must pass through the developing cracks and pores within the particles to the bulk solution within the particulate anode. If the particles are assumed to react according to a shrinking-core reaction model, the local reaction rate may be expressed as (see Appendix C):

$$\nabla \cdot \vec{i}_p = 3nF(1 - \epsilon) \mathcal{D}_e M^{-1} (C_c - C) \frac{1}{r_p^2} \left( \frac{r_c}{r_p - r_c} \right) \quad (6.11)$$

where  $r_p$  is the particle radius,  $r_c$  is the shrinking core radius,  $C_c$  and  $C$  are the copper concentrations (in  $\text{g/cm}^3$ ) at the base of the pores and in the spaces between the particles in the anode, respectively,  $M$  is the molecular weight of copper, and  $\epsilon$  is the porosity of the *electrode*. There is an overall decrease in the radius of the shrinking core with increasing copper extraction. Provided the radius of the shrinking core and copper extraction are directly related, Eq. (6.12) may be used to estimate the shrinking core radius as a function of time.

$$t = \frac{\rho_M r_p^2}{6D_e M^{-1}(C_c - C)} \left[ 1 - 3 \left( \frac{r_c}{r_p} \right)^2 + 2 \left( \frac{r_c}{r_p} \right)^3 \right] \quad (6.12)$$

with  $\rho_M$  defined as the molar density of copper sulphide.

One could argue that consideration should also be given to a mechanism involving the mass transfer of copper from the particle surfaces to the bulk electrolyte within the anode compartment. However, the convection action within the anode is likely to maintain the surface concentrations of copper close to the bulk value within the anode, and it is difficult to imagine that this mass transfer step could be slower than the transfer of copper from within the particle to the particle surface. Therefore, this mechanism is assumed to be unimportant. It should also be noted that the mass transfer of copper from within the electrode to the bulk solution outside the electrode has already been accounted for in Eq. (6.1) via  $\bar{N}$ .

Finally, there is the possibility that the local reaction rate may be controlled by re-crystallization processes. Such processes become thermodynamically favoured when sufficient copper is extracted from the sulphur sub-structure to form the intermediate phases, such as digenite and covellite. The expectation is that these processes may be relatively slow when the sulphur lattice must be rearranged into the crystal structure of the newly forming phases, for example during the phase change from chalcocite or djurleite (hexagonal close-packed) to digenite (cubic close-packed), from digenite to covellite (dihexagonal-dipyramidal) and from covellite to elemental sulphur (which can have several crystal structures). These structures were shown in Fig. 3.6.

To acquire some appreciation of the extent to which the reaction is distributed throughout a copper sulphide particulate anode, consider the situation when the current is first switched on, that is, before concentration gradients and convection activity have developed and before the reaction has penetrated the particle. In this case, the problem is essentially one-dimensional, with variation in reaction rate occurring with electrode thickness,  $x$ , and Eq. (6.10) may be solved independently of Eq. (6.1).

Two generally accepted approximations of Eq. (6.10) permit it to be solved analytically. Firstly, if the overpotential,  $\Phi_p - \Phi_e - E_r$ , is small, the exponentials can be expressed using just the first terms of their Taylor series expansions. The reaction rate is then a linear function of the overpotential. Secondly, if the overpotential is large, one of the exponential terms can be neglected. These are referred to as the linear and Tafel approximations, respectively.

In general, the error introduced in making the linear and Tafel approximations is limited to 5% if the overpotential is less than about 30mV and greater than about 75mV, respectively ( $n^* \approx 1$ ). The error is still within 15% when either the linear approximation is extended to an overpotential of 50mV or the Tafel approximation is used at overpotentials of only 50-60mV.

### 6.2.1 Tafel Approximation

For an anodic process Eq. (6.10) reduces to

$$\frac{di_p}{dx} = -ai_o \frac{C_{ss}}{C_{ss}^o} \exp\left[(1-\alpha)\frac{n^*F}{RT}(\Phi_p - \Phi_e - E_r)\right] \quad (6.13)$$

Differentiation of this equation and elimination of  $i_e$ ,  $\Phi_p$  and  $\Phi_e$  by means of Eqs. (6.2), (6.6) and (6.9) gives

$$\frac{d^2i_p}{dx^2} = \frac{di_p}{dx} \left\{ \beta \left[ \frac{I}{\kappa} - i_p \left( \frac{1}{\sigma} + \frac{1}{\kappa} \right) \right] + \frac{C_{ss}}{C_{ss}^o} \frac{d \ln C_{ss}}{dx} - \frac{dE_r}{dx} \right\} \quad (6.14)$$

$$\beta = (1-\alpha)\frac{n^*F}{RT}$$

Since at the start of electrolysis, the particle composition across the thickness of the anode is constant,  $dE_r/dx=0$  and  $dC_{ss}/dx=0$ .

Newman and Tobias [86] and Newman [87] reported the solution to this equation, under the following boundary conditions

$$\begin{aligned} @ x = 0, & \quad i_p = 0, \quad i_s = I \\ @ x = L, & \quad i_p = I, \quad i_s = 0 \end{aligned} \quad (6.15)$$

is given by

$$j = \frac{2\theta}{\delta} \tan(\theta y - \psi) + \frac{\gamma}{\delta} \quad (6.17)$$

where  $y$ ,  $j$ ,  $\delta$  and  $\gamma$  are dimensionless variables

$$y = \frac{x}{L}, \quad j = \frac{i_p}{I}, \quad \delta = L|I|\beta \left( \frac{1}{\kappa} + \frac{1}{\sigma} \right), \quad \gamma = \frac{L|I|\beta}{\kappa} \quad (6.18)$$

and  $\theta$  and  $\psi$  are integration constants

$$\tan \theta = \frac{2\delta\theta}{4\theta^2 - \gamma(\delta - \gamma)}, \quad \tan \psi = \frac{\gamma}{2\theta} \quad (6.19)$$

Since anodic currents are, by Newman's [86] convention for the development of these equations, negative, the absolute value for  $I$  must be used when calculating the dimensionless parameters  $\delta$  and  $\gamma$  (because  $|I|$  was used in Eq. (6.13)).

Differentiation of Eq. (6.17) produces an expression for the current distribution through the electrode.

$$\frac{dj}{dy} = \frac{2\theta^2}{\delta} \sec^2(\theta y - \psi) \quad (6.20)$$

Mica [104] approached the mathematics differently from Newman and Tobias [86] and derived an expression that was reported to correspond exactly to Eq. (6.20). There is evidence in the literature that Newman's result has been generally accepted. It was recently included in a treatise of electrochemistry by Goodridge and Wright [105] and provided the framework for a model on the effectiveness of porous electrodes under Faradaic reaction control by Scott [92].

## 6.2.2 Linear Approximation

There are reports that electrolysis of chalcocite and digenite takes place at relatively low overpotentials [4,5], which encourages the use of the linear approximation. Certainly, the extended surface area of the particulate anode contributes to this condition. Therefore, an investigation using this approximation is a worthwhile exercise.

At the start of electrolysis the problem is described by Eq. (6.10), which, when linearized in one-dimension gives

$$\frac{di_p}{dx} = ai_o \left[ \frac{C}{C^o} - \frac{C_{ss}}{C_{ss}^o} - \frac{n^*F}{RT} (\Phi_p - \Phi_e - E_r) \left( \alpha \frac{C}{C^o} + (1 - \alpha) \frac{C_{ss}}{C_{ss}^o} \right) \right] \quad (6.21)$$

where the concentration ratios are equal to one when the current is first switched on.

Solution for the reaction rate,  $di_p/dx$ , follows the same procedure as for the Tafel analysis, that is, differentiation of this equation, elimination of  $i_e$  and the potential terms using Eqs. (6.2), (6.6) and (6.9), integration to obtain  $i_p$  as a function of  $x$  using the boundary conditions of Eq. (6.15) and differentiation of that result. The solution is [86]

$$\frac{dj}{dy} = \frac{\upsilon \kappa}{(\kappa + \sigma) \sinh \upsilon} [\cosh \upsilon y + \sigma/\kappa \cosh \upsilon(1 - y)] \quad (6.22)$$

where several dimensionless variables have been defined

$$j = \frac{i_p}{I}, \quad y = \frac{x}{L}, \quad \upsilon = L \sqrt{ai_o \frac{n^*F}{RT} \left( \frac{\sigma + \kappa}{\sigma \kappa} \right)} \quad (6.23)$$

This solution is also included in the treatise by Goodridge and Wright [105].

## 6.3 PARAMETER ESTIMATION and MODEL PREDICTIONS

The true electrolyte conductivity,  $\kappa^o$ , may be estimated with the aid of either Eq. (3.35) or Eq. (3.36). For the electrolyte conditions used in this thesis, the calculated value of  $\kappa^o$  is approximately  $0.6 \Omega^{-1} \text{cm}^{-1}$ . However, the value required by Eqs. (6.20) and (6.22) is the effective conductivity. Estimation of effective conductivity values from values of true conductivity and void fraction of the non-conducting phase has been the subject of several papers [106-108]. The following

equation will be employed

$$\kappa = \kappa^o \frac{2\varepsilon}{3 - \varepsilon} \quad (6.24)$$

where  $\varepsilon$  is the volume fraction of electrolyte in the particulate anode (porosity) and will be taken as 0.45.

Figure 3.7 shows that the true conductivity of copper sulphide increases rapidly with decreasing copper content. Direct measurements of effective conductivity of industrial matte at various copper extractions are qualitatively consistent with these data as shown in Fig. 6.2. Therefore, it will be instructive to vary the bed's conductivity in the model, assigning values approximately one-half, equal to and much larger than the effective conductivity of the electrolyte. The effective conductivity of the bed will be assumed to be approximately constant across its thickness.

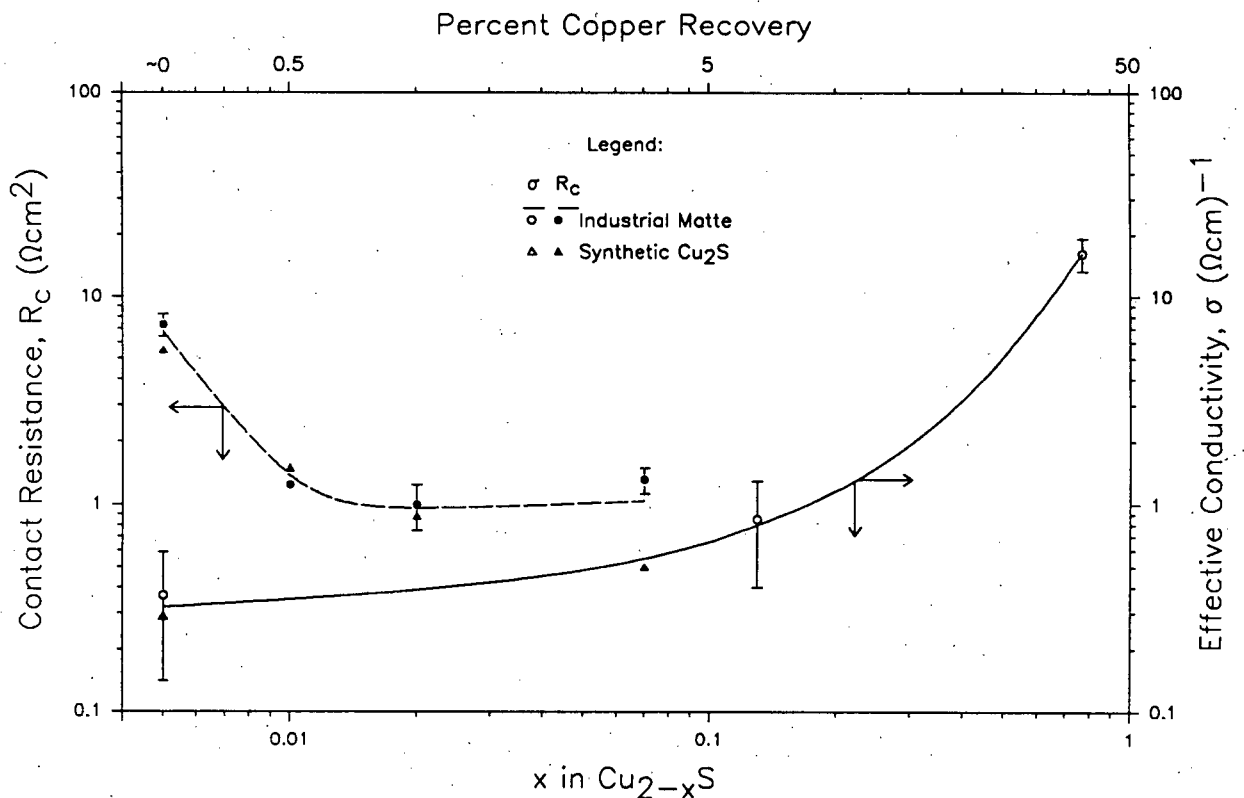


**Figure 6.2.** Effective electrical conductivity at 25°C and contact resistance at 50°C at graphite for industrial matte as a function of copper extraction. Contact resistance was interpreted from particle potential data obtained during electrolysis at 50°C.

Estimation of the reaction surface area per unit volume of the particulate anode,  $a$ , and assignment of an appropriate value for the exchange current density,  $i_0$ , will be necessary in order to make predictions using the linear approximation.

Electrochemical methods have been proposed for determination of the specific reaction surface area,  $a$ . In the absence of such data, the minimum value may be estimated by assuming the copper sulphide particles are spherical, in which case Eq. (6.25) may be applied.

$$a = \frac{6(1 - \epsilon)}{d_p} \quad (6.25)$$

For  $0.5 < d_p < 4\text{mm}$ ,  $a$  lies in the range  $8\text{-}66\text{cm}^{-1}$ . However, based on the particle size distribution employed in the present study, the appropriate average particle diameter to use is probably  $3.0\text{-}3.25\text{mm}$ , leading to a value for  $a$  of about  $10\text{cm}^{-1}$ .

Since the particles are not perfect spheres the actual value for  $a$  is in excess of  $10\text{cm}^{-1}$ . Furthermore, when the reaction penetrates the particle surface, the active surface area may be extended. In addition, there are really two reaction interfaces to consider: solid-solid and solid-electrolyte. These will be discussed in Chap. 8, Sec. 8.6.2. However, in order to simplify the problem, the reaction will be referred to only the external surface area of the particle. A surface area enhancement of about 50% may be inferred from specific surface area measurements on beds of sand presented by MacMullin and Muccini [109]. Therefore, a factor of 1.5 will be applied to the copper sulphide particles, leading to the final estimate for  $a$  of  $15\text{cm}^{-1}$ .

The exchange current density,  $i_0$ , for the anodic oxidation of chalcocite does not appear to have been explicitly investigated. From the polarization data which is available for various metal sulphides [6,110], assignment of a value between  $0.01\text{-}1\text{A/m}^2$  seems appropriate. The linear approximation and the exchange current density are reviewed further in Appendix D.

Model predictions are presented in Fig. 6.3. Although the Tafel model predicts greater variation in reactivity across the anode than the linear model, since these are limiting approximations, the true solution probably lies between the model predictions. With this in mind, the interesting result is that when the bed's effective conductivity is roughly one-half the electrolyte's effective

conductivity, the portion of the bed closest to the current distributor is the most active. When the effective conductivities are equal, the reaction is rather evenly distributed throughout the bed, although the activity near the current distributor and near the diaphragm are slightly greater than in the center of the bed. When the bed conductivity is very much larger than the electrolyte's, the portion of the bed closest to the diaphragm is the most active. However, there still is a large amount of reaction occurring within the remainder of the bed. The linear model predicts less variation in reaction distribution through the anode than the Tafel model because the former under estimates the current density if the overpotential is increased beyond the values for which the model is applicable. This will occur at the current distributor near the start of electrolysis and eventually at the diaphragm when the bed conductivity increases.

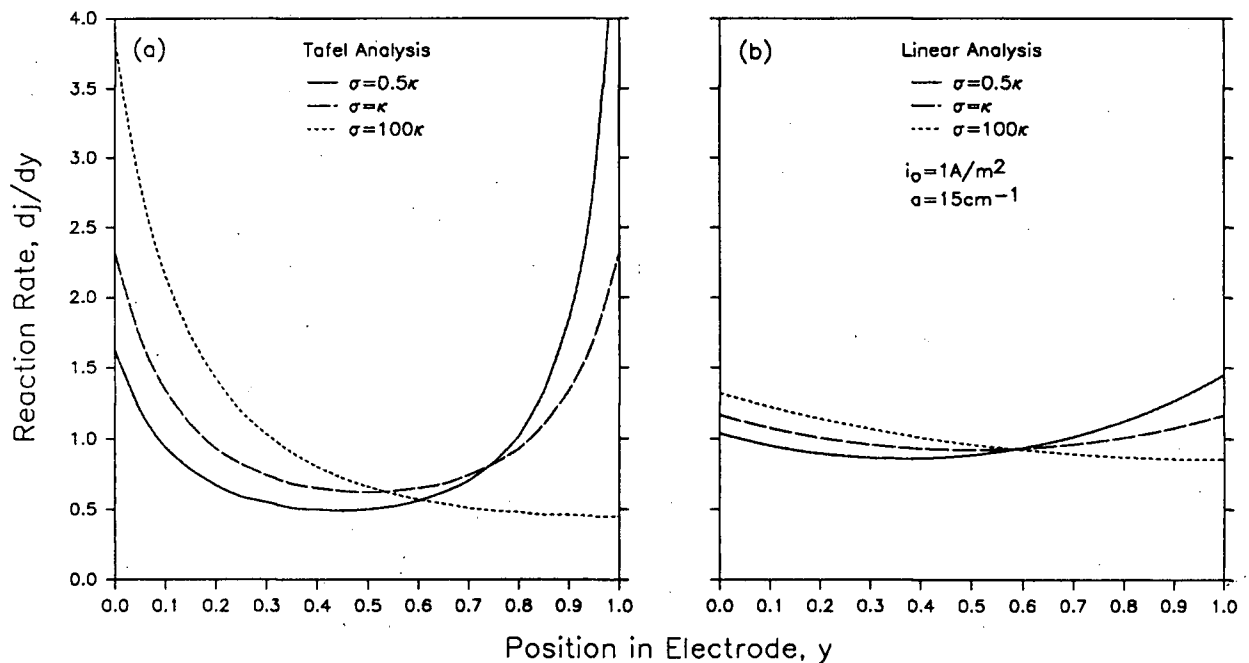


**Figure 6.3.** Predicted reaction rate distribution in a 2cm-thick particulate anode composed of copper sulphide particles.  $T=50^\circ C$ ,  $I=400A/m^2$ ,  $\kappa=0.21\Omega^{-1}cm^{-1}$ .

One might have expected that when the solid phase is infinitely conductive, the portion of the bed shown in Fig. 6.1 closest to the interface between the electrode and the bulk solution is by far the most active. Consequently, one would have anticipated the reaction distribution to have become more non-uniform with an increase in the conductivity of the particles than shown in Fig.

6.3. In this system, however, the electrolyte conductivity is relatively high, which means it can support a relatively high percentage of the total current density without an appreciable voltage drop. This minimizes the overpotential near the diaphragm, thus reducing the reaction rate there.

If the copper concentration gradients between the current distributor and diaphragm remain small, with adequate natural convection mass transfer to the bulk electrolyte, Eqs. (6.20) or (6.22) may also be used to estimate the performance of the anode with increasing copper extraction.

At the beginning of a run, the bed conductivity is relatively low and Fig. 6.3 shows that much of the reaction occurs close to the current distributor. As copper is extracted from the particles, the bed conductivity at this location increases and the reaction spreads towards the diaphragm. Figures 3.7 and 6.2 suggest that very little copper extraction may be necessary to substantially increase the particle conductivity, thus the reaction quickly becomes relatively evenly distributed across the anode. Once the conductivity of the entire bed has improved, the extraction of copper occurs relatively evenly throughout the electrode.

Figure 6.2 also shows that the contact resistance between the particles and the current distributor decreases significantly with a very small amount of copper extraction. Although this parameter does not affect reaction distribution in the anode, it is important in terms of the overall cell voltage and energy considerations.

In the previous chapter, data was presented which demonstrated that the electrolyte flow through a tall particulate anode of copper sulphide appears to be predominantly downwards, thus producing vertical copper concentration gradients. Since the current direction is predominantly horizontal, the anode is essentially a "flow-by" electrode and Eqs. (6.1) and (6.10) should be solved simultaneously for both the vertical,  $z$ , and horizontal,  $x$ , dimensions. Furthermore, as the reaction proceeds, Eqs. (6.11) and (6.12) are likely to be important. Simultaneous solution of these four equations would be a rather involved process and will not be undertaken. Nevertheless, the concentration effects will be discussed qualitatively.

The first effect to consider is that of concentration changes occurring in the electrolyte filling the pores between the particles. If the reaction is in the Tafel region, inspection of Eq. (6.13) shows that the reaction rate is independent of the concentration of copper in solution. Therefore, concentration changes in the spaces between the particles would have no effect. However, for the linear analysis, the local reaction rate would decrease where the copper concentration,  $C$ , is increased. For example, suppose the copper concentration at the current distributor or near the bottom of the anode compartment increased to a value 25% larger than the concentration just inside the diaphragm, which, for the moment, will be assumed to be equal to the reference concentration,  $C^\circ$ , and that the activity of copper in the sulphide phase remains approximately constant across the anode. The relative change in the reaction rate,  $di_p/dx$ , may be estimated using Eq. (6.21). At an overpotential of 10mV,  $n^*F(\Phi_p - \Phi_e - E_r)/RT = 0.36$  and  $\alpha C/C^\circ + (1-\alpha)C_{[Cu]}/C_{[Cu]}^\circ = 1.13$  ( $\alpha = 0.5$ ), therefore, the new reaction rate is  $1.25 - 1.0 - 0.36(1.13) = -0.16a_{i_0}$ , as compared to  $-0.36a_{i_0}$  in the absence of concentration gradients.<sup>1</sup> This is a 55% decrease in the reaction rate. At an overpotential of 20mV, the reaction rate decrease is about 22%.

The second effect is that of concentration gradients within the particles. The expectation is that diffusion of copper within the corroding particles will tend to counter-balance the effect just described. This is because (a) the copper must diffuse furthest in the most reacted particles, thus increasing the mass transfer resistance in the most reacted particles, and (b) in the linear analysis, the copper concentration increase at the reaction interface necessary to drive this diffusion process will reduce the charge transfer rate as discussed above.

A further consideration is the variation in the particle composition across the electrode. The expectation is that this factor will contribute to reaction uniformity within the anode. As copper is extracted from the copper sulphide, phase changes occur and the reversible potential,  $E_r$ , increases, leading to a decline in the reaction rate for a constant value of  $\Phi_p - \Phi_e$ . Phase changes will occur

---

<sup>1</sup> Recall that anodic current densities are, by the convention of Newman and Tobias [86], negative.

soonest in the most reacted particles, thus forcing the reaction to other locations in the bed. In addition, re-crystallization processes occurring during phase changes are likely to reduce the reaction rate, thus also tending to make the reaction distribution relatively uniform.

In summary, the reaction distribution shown in Fig. 6.3 may be an acceptable representation of the actual behaviour of copper sulphide particulate anodes. Actual reaction distribution measurements are presented in the following chapter.

## 6.4 NOMENCLATURE

- a electrode interfacial area,  $\text{cm}^{-1}$  or  $\text{m}^{-1}$
- C concentration of copper in the electrolyte at the sulphide-electrolyte interface,  $\text{mol}/\text{cm}^3$  or  $\text{kmol}/\text{m}^3$
- $C^\circ$  concentration of copper in the bulk electrolyte,  $\text{mol}/\text{cm}^3$  or  $\text{kmol}/\text{m}^3$
- $C_{ss}^\circ$  concentration of copper in the bulk of the sulphide phase,  $\text{mol}/\text{cm}^3$  or  $\text{kmol}/\text{m}^3$
- $C_c$  concentration of copper at the base of the pores in a corroding sulphide particle,  $\text{mol}/\text{cm}^3$  or  $\text{kmol}/\text{m}^3$
- $C_{ss}$  concentration of copper in the solid state at the sulphide-electrolyte interface,  $\text{mol}/\text{cm}^3$  or  $\text{kmol}/\text{m}^3$
- $d_p$  particle diameter, cm or m
- $D_l$  molecular diffusivity of species,  $\text{cm}^2/\text{s}$  or  $\text{m}^2/\text{s}$
- $D_e$  effective diffusivity of copper in the pores of a decomposing sulphide particle,  $\text{cm}^2/\text{s}$  or  $\text{m}^2/\text{s}$
- $E_r$  reversible potential of a Faradaic reaction, V
- F Faraday's constant, 96,487 coulombs/equiv
- i current density,  $\text{A}/\text{m}^2$
- $i_0$  exchange current density at a concentration of  $C^\circ$  or  $C_{ss}^\circ$ ,  $\text{A}/\text{m}^2$
- $i_e$  current density in the electrolyte,  $\text{A}/\text{m}^2$
- $i_p$  current density through the particles,  $\text{A}/\text{m}^2$
- I total or superficial current density across the diaphragm,  $\text{A}/\text{m}^2$
- j dimensionless reaction rate
- L electrode thickness, cm or m
- M molecular weight of a species, g/mol or kg/mol
- n number of equivalents of charge per mole of a species

- $n^*$  number of equivalents of charge per mole of a species involved in the electron transfer step of a Faradaic process
- $\vec{N}$  flux of species, mol/cm<sup>2</sup>•s
- $r_c$  radius of the undecomposed core of a particle, cm or m
- $r_{ig}$  rate of generation of species  $i$  in a unit volume of the electrode, mol/cm<sup>3</sup>•s, or kmol/m<sup>3</sup>•s
- $r_p$  radius of particle, cm or m
- $R$  universal constant, 1.987 cal/mol•°K
- $s_i$  fraction of the total current consumed by Faradaic reactions involving species  $i$
- $t$  time, s
- $\vec{u}$  electrolyte velocity, cm/s or m/s
- $x, y, z$  coordinate positions (thickness, width, height respectively), cm or m
- $y$  dimensionless position across the thickness of the packed bed electrode (dimensionless  $x$  coordinate)
- $z_i$  charge on an ion, including its sign
- $\alpha$  charge transfer coefficient
- $\beta$  constant,  $(1 - \alpha) \frac{n^* F}{RT}$ , dimensionless
- $\gamma$  constant,  $\frac{L|I|\beta}{\kappa}$
- $\delta$  constant,  $L|I|\beta \left( \frac{1}{\kappa} + \frac{1}{\sigma} \right)$ , dimensionless
- $\epsilon$  porosity of the packed bed electrode
- $\eta$  electrolyte viscosity, g/cm•s or kg/m•s
- $\theta$  integration constant defined by Eq. (6.19)
- $\kappa^o$  absolute electrolyte conductivity, ( $\Omega \cdot \text{cm}$ )<sup>-1</sup>
- $\kappa$  effective electrolyte conductivity accounting for electrode porosity, ( $\Omega \cdot \text{cm}$ )<sup>-1</sup>
- $\lambda$  equivalent ionic conductance,  $\Omega^{-1} \text{cm}^2 \text{mol}^{-1}$
- $\mu$  electrical mobility, cm<sup>2</sup>/V•s
- $\nu$  constant,  $L \sqrt{a i_o \frac{n^* F \sigma + \kappa}{RT}}$ , dimensionless
- $\rho_M$  molar density of sulphide species, mol/cm<sup>3</sup> or kmol/m<sup>3</sup>
- $\sigma$  effective electrical conductivity of particles accounting for electrode porosity and particle-particle contact resistances, ( $\Omega \cdot \text{cm}$ )<sup>-1</sup>

$\Phi_e$  potential in the electrolyte, V

$\Phi_p$  potential of the particles, V

$\psi$  integration constant defined by Eq. (6.19)

Other Operators

$f$  a function

$\nabla \cdot df(x,y,z)/dx + df(x,y,z)/dy + df(x,y,z)/dz$

---

## CHAPTER 7

---

### PERFORMANCE OF 2cm-THICK PARTICULATE ANODES

The expectation is that the practical application of particulate electrorefining of copper-rich mattes would employ packed bed anodes several centimeters thick. In this chapter, the reaction distribution, the components of the total-bed potential during total-bed polarization of two broad classes of mattes, and the effects of iron and lead impurities on the overall copper extraction using a 2cm-thick, small-scale packed bed electrode are discussed.

#### 7.1 REACTION DISTRIBUTION

Figure 7.1 is generally representative of the variation in (a) particle potentials adjacent to the current distributor and diaphragm,  $\Delta E_{1,2}$  and  $\Delta E_{1,4}$ , respectively, (b) the potential of the solution just outside the diaphragm relative to the particles adjacent to the diaphragm,  $\Delta E_{4,6}$ , and (c) total-bed potential,  $\Delta E_{1,6}$ , during decomposition of synthetic chalcocite in a packed bed anode. The distribution of anodic decomposition throughout the anode may be inferred from an analysis of the potential of the particles adjacent to the current distributor and diaphragm.

When the current is first switched on, the potential of the particles adjacent to the current distributor,  $\Delta E_{1,2}$ , and the voltage drop across the electrode,  $\Delta E_{2,4}$ , are relatively high. Figure 3.7 demonstrates that the electrical conductivity of synthetic copper sulphide increases as the stoichiometry is changed from  $\text{Cu}_2\text{S}$  to  $\text{CuS}$ . Figure 6.3 demonstrates that a similar increase in copper matte effective electrical conductivity occurs when the stoichiometry is changed by anodic

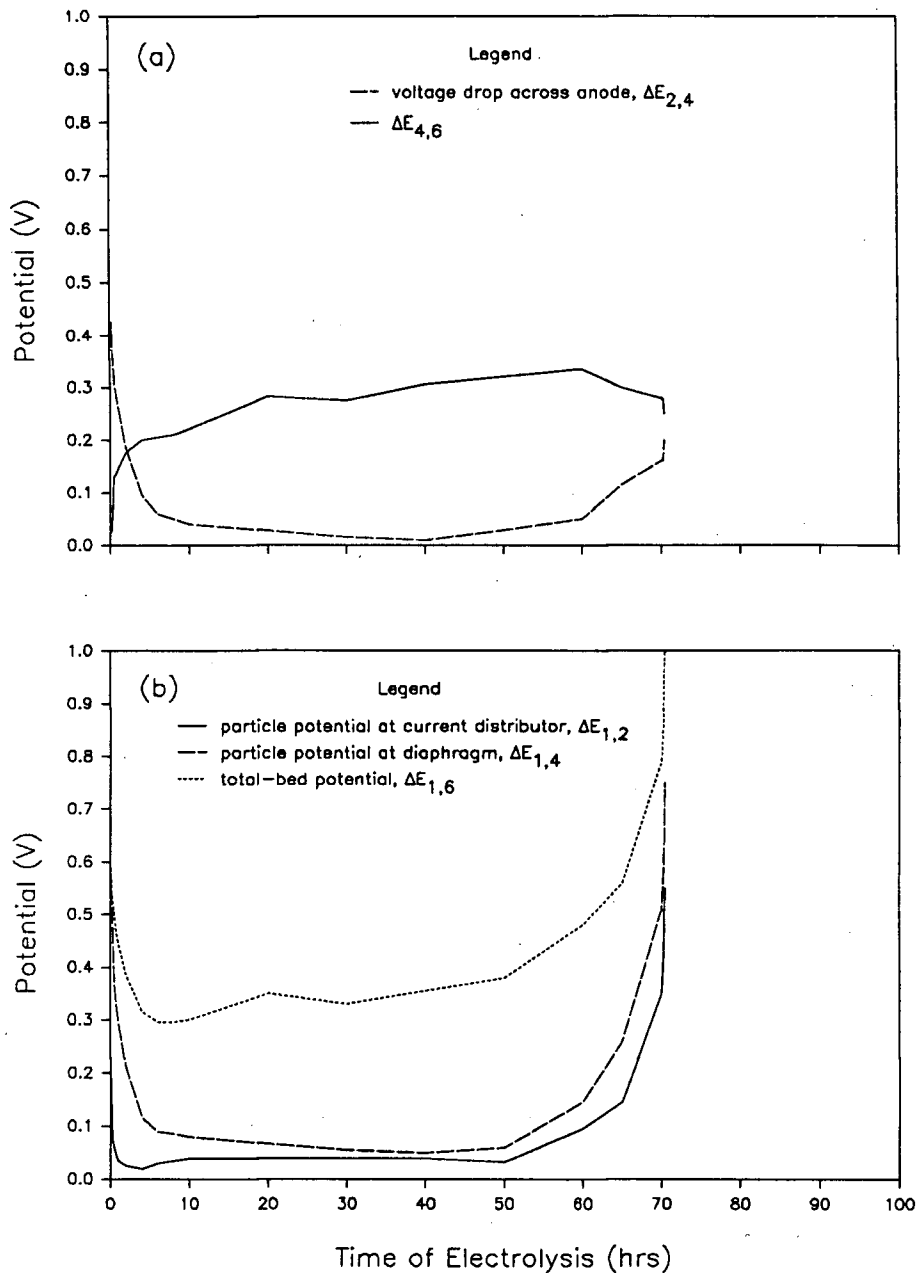


**Figure 7.1** Galvanostatic potential curves for anodic decomposition of synthetic chalcocite in a 2cm-thick particulate electrode. Current density:  $400\text{A/m}^2$  ( $200\text{A/m}^2\cdot\text{cm}$  or  $0.84\text{A/m}^2\cdot\text{g}$ ); particles: 0.5-4.0mm dia; electrolyte: 45g/l  $\text{Cu}^{2+}$ , 165g/l  $\text{H}_2\text{SO}_4$ ,  $50^\circ\text{C}$ ; current distributor: Pt-Ir coated Ti; "medium" diaphragm tightness (Test 23).

decomposition. This increasing electrical conductivity explains why the contact resistance at the current distributor (which is reflected in the voltage drop between the current distributor and the particles adjacent to it,  $\Delta E_{1,2}$ ) and the voltage drop across the bed decrease during the first few hours of electrolysis, as was also shown in Fig. 5.3.

However, the important point with respect to reaction distribution across the electrodes is that the potential of the particles adjacent to the current distributor declines more rapidly and reaches a minimum value earlier than the potential of the particles adjacent to the diaphragm. This means that immediately after the current is switched on, a very significant portion of the decomposition process occurs close to the current distributor. Then, as the effective electrical conductivity of the particles and the electrical contact between the current distributor and the adjacent particles improves due to copper extraction, the decomposition process quickly spreads towards the diaphragm. This is reflected in the decreasing voltage drop across the anode and, of course, the drop in the potential of the particles adjacent to the diaphragm.

The overall distribution of anodic decomposition across a packed bed anode composed of various copper sulphides is summarized in Table 7.1. The amount of copper extraction varies across the anode by less than a factor of two, with most of the extraction occurring near the diaphragm. These results are consistent with the qualitative assessment of particulate anode refining of copper sulphide discussed at the end of the previous chapter. In other words, there is not a high variation in overall decomposition across the electrode, although the greatest extraction does occur close to the diaphragm.

**Table 7.1** Copper composition and *estimated* extraction at total-bed polarization for various positions (at the current distributor, in the middle of bed, and at the diaphragm) and copper sulphide materials in 2cm-thick, small-scale packed bed anodes.

Matte Description (experiment no.)	Start Cu	Final Cu Composition (wt%)			Estimated Cu Extraction (%) <sup>1</sup>		
		Curr. Dist.	Middle of Bed	Diaph.	Curr. Dist.	Middle of Bed	Diaph.
syn. chalcocite (18)	80.1	61.5	59.8	40.2	60.3	63.0	83.3
syn. matte/4.4wt% Fe (20)	73.6	63.3	62.6	57.9	39.7	42.0	52.5
syn. matte/4.5wt% Fe (24)	73.8	63	62	60	40	42	47
syn. matte/2.9wt% Pb (26)	77.2	57.5	57.2	35.8	59.2	60.1	84.2
syn. matte/1.7wt% Fe (27)	77.4	63.6	62.1	43.8	48.8	52.5	77.3
industrial matte (38)	69.3	62.1	62.3	54.6	31.8	31.0	56.0

Notes: 1 For mattes containing lead and iron, the estimates for copper extraction assume that the concentrations of these impurities are approximately constant across the anode.

The *overall* copper extraction for these experiments is 73.5%, 45.3%, 43.8%, 66.3%, 58.7%, and 38.7%, respectively.

Particles that were dried and broken apart several hours after being extracted from "polarized" beds of iron-containing mattes ( $\approx 4\text{wt}\%$  iron) showed evidence that particle decomposition may be approximately described by the shrinking core model. At about 40% overall copper extraction, the particle cores retained a metallic grey appearance similar to the starting material and the reacted shell was blue-grey, possibly indicating the phase "blue-remaining" covellite. Particles extracted shortly after total-bed polarization of a thin anode containing pure synthetic copper sulphide had a thick grayish layer and a bluish core. In some particles, the bluish core was very small, while in the largest particles, the diameter of the core was approximately one-third of the overall particle diameter.

## 7.2 ELECTRODE "POLARIZATION"

The total-bed polarization behaviour of 2cm-thick particulate anodes composed of copper sulphides generally can be described by two types of potential-time curves. Figure 7.1 is applicable to synthetic copper sulphide ( $\text{Cu}_{2.00-2.04}\text{S}$ ), synthetic copper sulphide doped with 0-4.5wt% lead and doped with less than about 4.5wt% iron, and industrial mattes. For the purpose of the following discussion, these materials will be designated group A. The total-bed polarization behaviour of synthetic mattes containing more than about 4.5wt% iron is represented by Fig. 7.2. These mattes will be designated group B.

The total-bed potential is the sum of several components: (a) the voltage drop between the current distributor and the adjacent particles,  $\Delta E_{1,2}$ , (b) the voltage drop across the anode through the particles,  $\Delta E_{2,4}$ , (c) the ionic voltage drop across the diaphragm,  $\Delta E_{5,6}$ , (d) the Faradaic reversible potential for the decomposition reaction,  $E_r$ , and (e) the reaction process overpotential at the diaphragm,  $\Delta E_\eta$ . The latter is related to the mechanisms responsible for controlling the decomposition process within the particles. These may be Faradaic (or charge transfer) processes, solid-state diffusion processes within the corroding particles, solid-state re-crystallization processes, and electrolyte-based diffusion processes within the fissures of the particles. These were discussed in Chap. 6, Sec. 6.2.

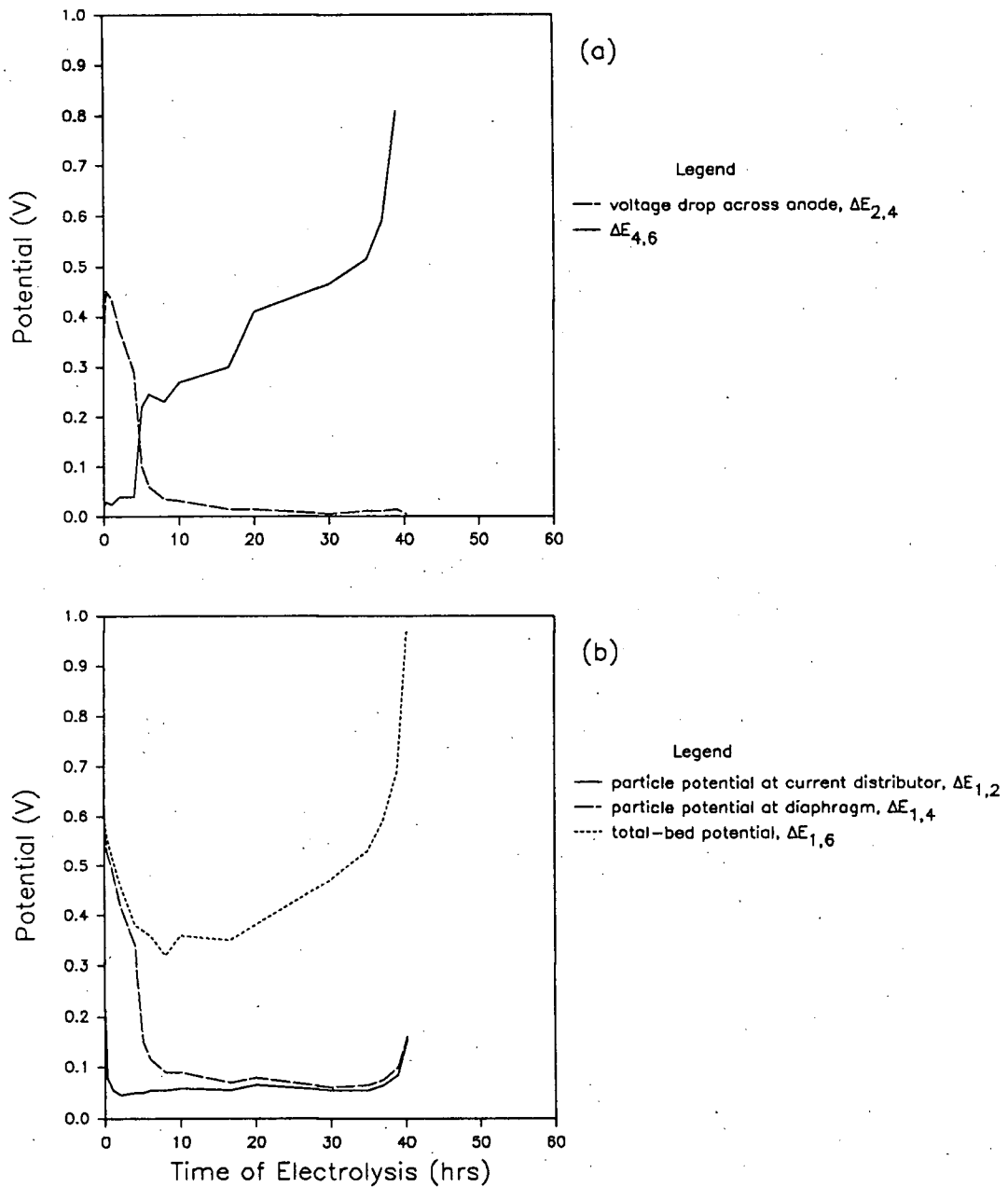


**Figure 7.2** Galvanostatic potential curves for anodic decomposition of synthetic copper sulphide doped with 4.7wt% iron in a 2cm-thick particulate electrode. Current density:  $400\text{A/m}^2$  ( $200\text{A/m}^2\cdot\text{cm}$  or  $0.84\text{A/m}^2\cdot\text{g}$ ); particle diameter: 0.5-4.0mm; electrolyte: 45g/l  $\text{Cu}^{2+}$ , 165g/l  $\text{H}_2\text{SO}_4$ ,  $50^\circ\text{C}$ ; current distributor: Pt-Ir coated Ti; "medium" diaphragm tightness (Test 32).

Approximate voltage balances for the two groups of materials is presented in Table 7.2. Total-bed polarization of group A materials is caused by deteriorating electrical contact between the current distributor and the adjacent particles and by an increasing voltage drop across the anode. The reaction process overpotential actually decreases during the last several hours of electrolysis.

The distinguishing characteristic of group B materials is that the voltage drop across the anode and the contact resistance between the current distributor the adjacent particles either remain nearly constant or increase only slightly during total-bed polarization.

These conclusions may also be appreciated by inspecting the  $\Delta E_{4,6}$ -time curve for the two groups of materials. For group A materials this parameter remains relatively constant and for group B materials it increases during total-bed polarization.

**Table 7.2** Voltage balances just inside the *diaphragm* of 2cm-thick particulate electrodes composed of group A and B mattes 10hrs before total-bed polarization ( $\tau-10$ ) and at total-bed polarization ( $\tau$ ), where  $\tau$  is the time at which the total-bed potential exceeds a value of 0.9V (i.e., the transition time).

Voltage Component	Group A		Group B	
	$\tau-10$	$\tau$	$\tau-10$	$\tau$
total-bed potential, $\Delta E_{1,6}$ , vs. $\text{Cu}^{2+} \text{Cu}^{\circ}$ <sup>1</sup>	0.48	1.00	0.47	0.97
reference electrode potential ( $\text{Cu}^{2+} \text{Cu}^{\circ}$ ) <sup>2</sup>	0.34	0.34	0.34	0.34
..... total-bed potential vs. SHE	0.82	1.34	0.81	1.31
less .....				
(a) contact voltage drop <sup>1</sup> , $\Delta E_{1,2}$	0.10	0.55	0.06	0.16
(b) voltage drop across electrode <sup>1</sup> , $\Delta E_{2,4}$	0.05	0.20	0.01	0.01
(c) voltage drop across diaphragm <sup>3</sup> , $\Delta E_{5,6}$	0.01	0.01	0.01	0.01
(d) reversible potential <sup>4</sup> , $E_r$	0.59	0.59	0.53	0.53
net .....				
(e) reaction process overpotential, $\Delta E_{\eta}$	0.07	-0.01	0.20	0.60

Notes: 1 measured from the galvanostatic potential-time curves of Figs. 7.1 and 7.2.

2 at 50°C, see Appendix E.

3 calculated at 400A/m<sup>2</sup> using an effective electrical conductivity,  $\kappa$ , of 0.28 (using a diaphragm porosity of 0.56 in Eq. (6.24)) and a diaphragm thickness of 0.58mm.

4 calculated using data from reference 40 for the reaction associated with group A mattes and using Etienne's data [5] for the reaction associated with the group B mattes and assuming the following equilibrium reactions (see Appendix E):

group A mattes (>50% copper extraction):  $\text{Cu}^{2+} + 2e^- + \text{S} = \text{CuS}$ ,  $E_r = 0.59\text{V}$

group B mattes (<50% copper extraction):  $0.765\text{Cu}^{2+} + 1.53e^- + \text{CuS} = \text{Cu}_{1.765}\text{S}$ ,  $E_r = 0.53\text{V}$

### 7.3 COPPER EXTRACTION

Figure 7.3 summarizes the effect of metallic impurities on copper extraction at the point of total-bed polarization of 2cm-thick particulate electrodes. The conclusions which may be drawn when considering the impurity content in terms weight percent are that (a) iron impurities reduce copper extraction more than lead impurities and (b) copper recovery from industrial mattes and from synthetic mattes containing the same amount of iron are very similar. This suggests the low

copper removal from the industrial materials is due to the presence of iron. These observations contradict those of an earlier paper [4] which reported the low copper extraction from industrial matte was attributable to lead impurities.

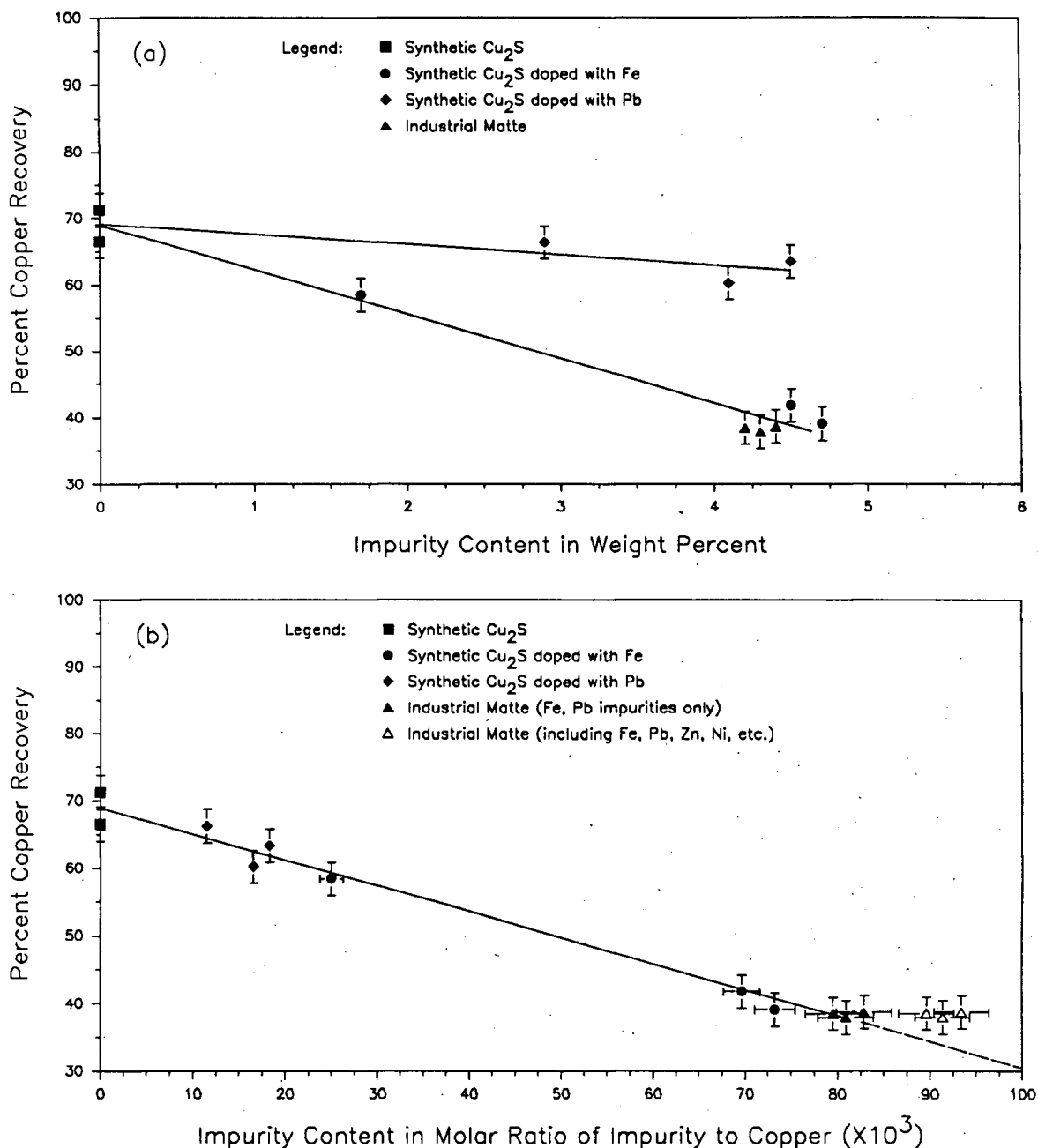


**Figure 7.3** Effect of impurities on the copper extraction from crushed synthetic and industrial mattes (0.5-4.0mm dia) placed in 2cm-thick packed bed anodes. Current density:  $400\text{A/m}^2$  ( $0.84\text{A/m}^2\cdot\text{g}$ ); electrolyte: 44-46g/l  $\text{Cu}^{2+}$ , 163-167g/l  $\text{H}_2\text{SO}_4$ ,  $50^\circ\text{C}$ ; current distributor Pt-Ir coated Ti, except two of the tests on industrial matte in which graphite and gold were used; "medium" diaphragm tightness.

When copper extraction is interpreted in terms of the total molar ratio of metallic impurities to copper, the impression is initially obtained that the effects of iron and lead are additive, and simply related to the number of moles of each present. However, this assessment may not explain the results for the industrial matte when the other metallic impurities, notably zinc and nickel, are included. These data points should lie on the dotted line portion of the curve in Fig. 7.3b.

While these data offer some information regarding the potential copper recovery limitations of the copper matte electrorefining process in thick particulate electrodes, they may be misleading because the total-bed polarization mechanisms are not equal in all cases. For example, the ultimate extraction possible from the group A materials may have been obscured in these experiments by the deteriorating electrical contact between the current distributor and the adjacent particles. The important point to appreciate is that all of the current must pass through the first "layer" of particles adjacent to the current distributor. This places an extremely high burden on the electrical conduction between these particles and the current distributor. A small increase in electrical contact resistance results in a very large voltage drop at this location. As the current moves through the bed, it transfers to the electrolyte via Faradaic processes, and thus the electrical conductivity requirements between the particles decreases with increasing distance from the current distributor. This explains why the contact voltage drop generally increases more than the voltage drop across the electrode during total-bed polarization of group A mattes. Some examples are summarized in Table 7.3.

The implication of this analysis is that electrical contact problems at the current distributor may not necessarily be responsible for total-bed polarization of copper matte particulate anodes under the limiting condition where each particle, even in a thick particulate electrode, is placed in direct contact with the current distributor. With this design, even if the contact resistance increased modestly, the voltage drop at the contact points would remain relatively low because the current would be distributed to the particles across the full thickness of the anode. As a result, decomposition processes could continue. Only if these contact resistances increased sufficiently to cause total-bed polarization of the anode, would the ultimate copper extraction be legitimately related to deteriorating electrical contact between the current distributor and the adjacent particles.

**Table 7.3** Increase in both the particle-current distributor voltage drop,  $\Delta E_{1,2}$ , and voltage drop across the anode,  $\Delta E_{2,4}$ , during total-bed polarization of selected group A mattes in a 2cm-thick, packed bed electrode.

Matte Description (experiment no.)	Contact Voltage, $\Delta E_{1,2}$	Bed Voltage Drop, $\Delta E_{2,4}$
synthetic $\text{Cu}_2\text{S}$ (23)	0.51	0.17
synthetic $\text{Cu}_2\text{S}$ doped with 4.1wt% Pb (25)	0.60	0.14
synthetic $\text{Cu}_2\text{S}$ doped with 2.9wt% Pb (26)	0.31	0.23
synthetic $\text{Cu}_2\text{S}$ doped with 4.5wt% Pb (31)	0.48	0.17
synthetic $\text{Cu}_2\text{S}$ doped with 1.7wt% Fe (27)	0.32	0.23
industrial matte (30)	0.45	0.06
industrial matte (34)	0.45	0.00

Direct contact between all the particles in a thick anode and the current distributor was physically modelled using a thin electrode. These studies are discussed in the following chapter.

#### 7.4 OTHER DATA

The current efficiency at both electrodes generally was between 95% and 97% and the difference between the anodic and cathodic current efficiency generally was less than 1%. There was some evidence that the electrical properties of the platinum-iridium coating (i.e., the ability of the coating to transfer current to the particles) deteriorated somewhat during the course of the experimental work. Unfortunately, this deterioration was not specifically tested. Nevertheless, the data in Fig. 7.3 should be considered reproducible to about  $\pm 2\%$ . The gold current distributor employed in the thin-bed studies eliminated this difficulty.

---

## CHAPTER 8

---

### IMPURITIES AND DECOMPOSITION MECHANISMS

In the previous chapter, the increasing voltage drop between the current distributor and the adjacent particles,  $\Delta E_{1,2}$ , and, to a lesser extent, the increasing voltage drop across the electrode,  $\Delta E_{2,4}$ , were shown to result in total-bed polarization of a thick (>2cm) packed bed anode for most copper-rich mattes, with the exception being synthetic mattes containing more than about 4% iron. However, these "polarization" mechanisms may not necessarily limit the ultimate performance (i.e., the copper extraction obtained at total-bed polarization) of thick packed bed anodes of various copper-rich mattes that otherwise might be possible using an electrode designed so that all the particles contact a current distributor, even for a thick packed bed. Such a design may be modelled physically using an electrode only one particle diameter in thickness, and operated at an appropriately reduced current density. In this chapter, the effects of lead, iron and oxygen impurities on copper-rich matte electrorefining are evaluated from the results of thin (2.9mm) packed bed anode experiments.

#### 8.1 COPPER EXTRACTION AND "POLARIZATION" CHARACTERISTICS

##### 8.1.1 Impurity Effects

Figure 8.1 summarizes the copper recovery obtained in the thin (2.9mm) electrode experiments. A comparison between Figs. 7.3 and 8.1 shows that the 2cm-thick-anode tests represent the ultimate copper recovery only for synthetic copper sulphides doped with more than 3wt% iron.

This indicates that copper extraction in thick anodes containing pure synthetic copper sulphide, lead-doped copper sulphide and industrial matte is indeed limited by electrical contact problems between the particles and the current distributor.

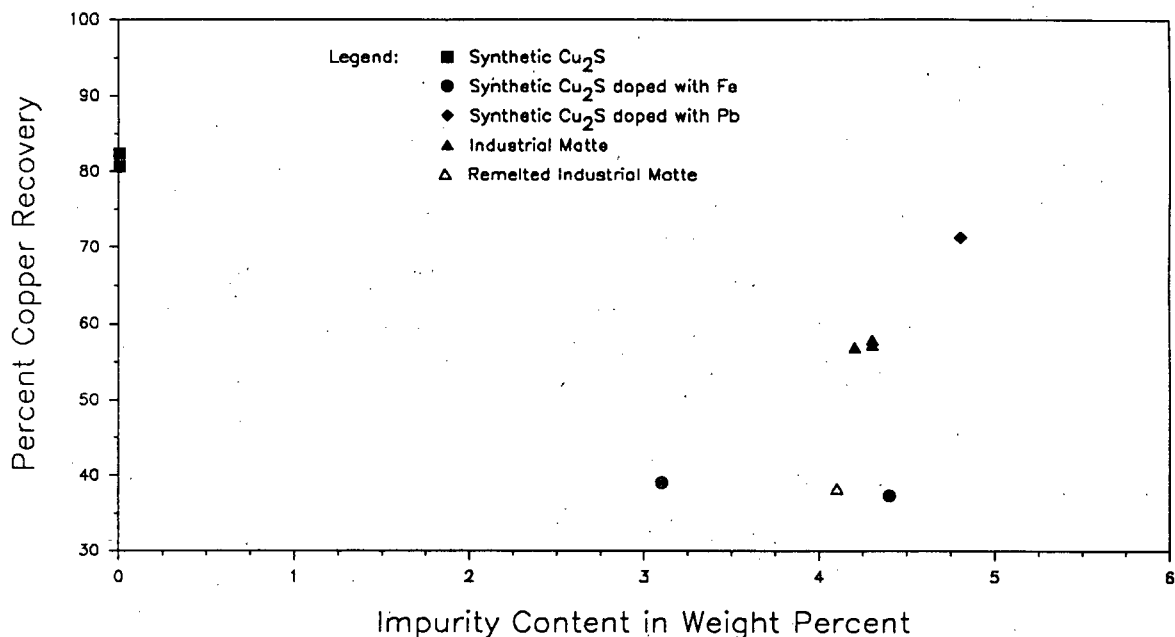


**Figure 8.1** Copper extraction from various synthetic mattes and from industrial mattes using a thin (2.9mm) particulate electrode. Particle diameter: 2.0-2.9mm; current density: 60A/m<sup>2</sup> ( $\approx 0.84\text{A/m}^2 \cdot \text{g}$ ); electrolyte: 45g/l Cu<sup>2+</sup>, 160-166g/l H<sub>2</sub>SO<sub>4</sub>, 50°C; current distributor: Au; diaphragm: "medium".

In addition, the important points to note are that (a) the copper extraction from industrial matte is now nearly 20% greater than from synthetic material containing the same amount of iron, and (b) the extraction from re-melted industrial matte is the same as that from synthetic material with a similar iron content. What now remains is to develop an explanation for these differences in copper extraction.

Potential-time curves for all of these materials, which includes the total-bed potential,  $\Delta E_{1,6}$ , the potential of the particles adjacent to the diaphragm relative to the solution just outside the diaphragm,  $\Delta E_{4,6}$ , and the potential of the particles adjacent to the diaphragm,  $\Delta E_{1,4}$ <sup>1</sup>, are presented

<sup>1</sup>  $\Delta E_{1,4}$  is essentially a measure of the voltage drop between the current distributor and the particles or the contact resistance between the current distributor and the particles.

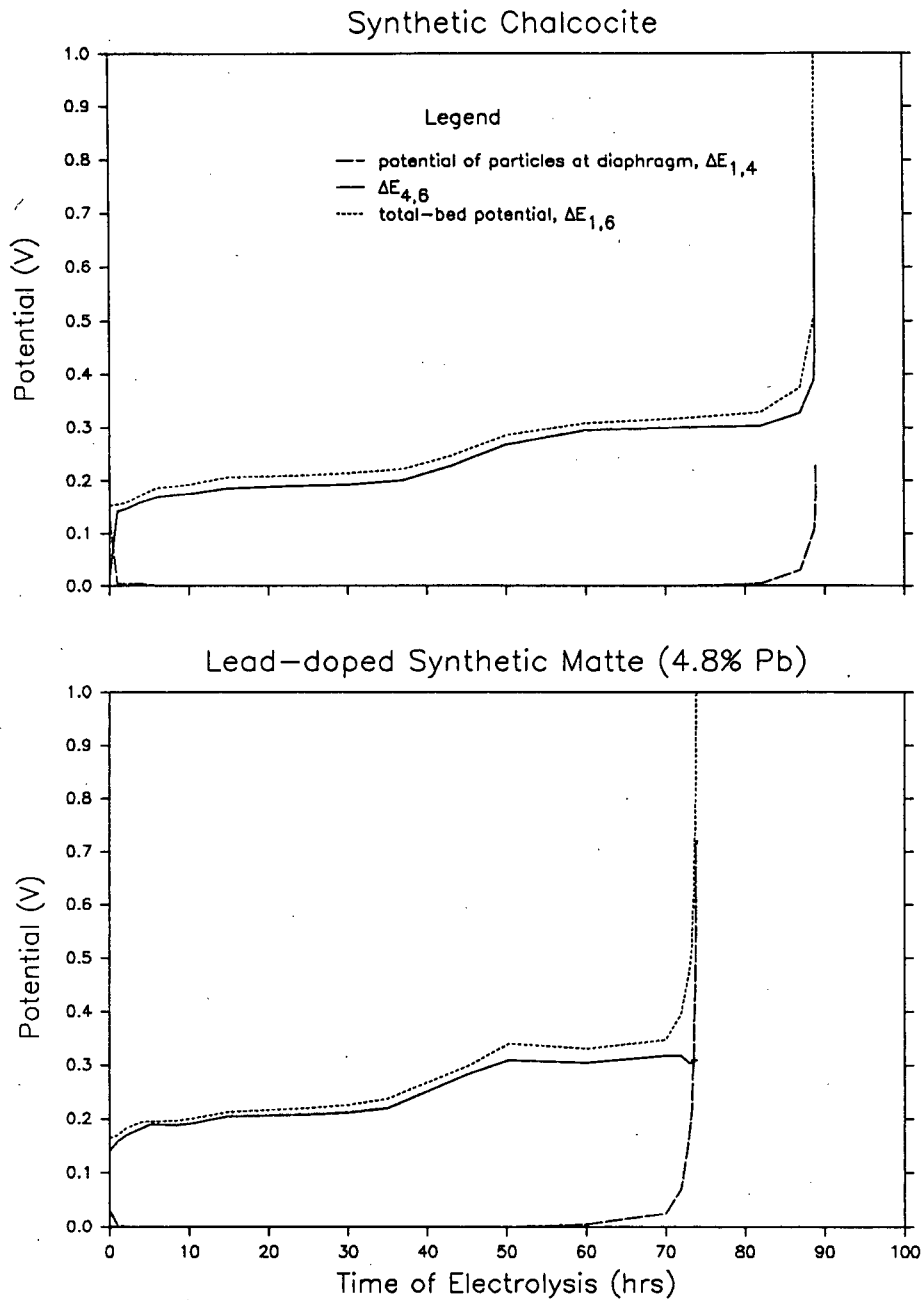


**Figure 8.2** Galvanostatic potential-time curves for anodic decomposition of synthetic chalcocite (Test 45) and lead-doped synthetic copper matte (Test 46) in a thin (2.9mm) particulate electrode. Particle diameter: 2.0-2.9mm; current density:  $60\text{A/m}^2$  ( $\approx 200\text{A/m}^2\cdot\text{cm}$  or  $0.84\text{A/m}^2\cdot\text{g}$ ); electrolyte:  $45\text{g/l Cu}^{2+}$ ,  $160\text{-}166\text{g/l H}_2\text{SO}_4$ ,  $50^\circ\text{C}$ ; current distributor: Au; diaphragm: "medium".

in Figs. 8.2-8.3. Total-bed polarization of the synthetic mattes doped with about 3-4.5wt% iron is, as in the 2cm-thick packed bed studies, attributable to increasing impedances of reaction processes

within the particle. Total-bed polarization of re-melted industrial matte is also due to these processes. The important point with respect to the untreated industrial matte is that total-bed polarization of thin electrodes containing this material is now also due to these mechanisms.

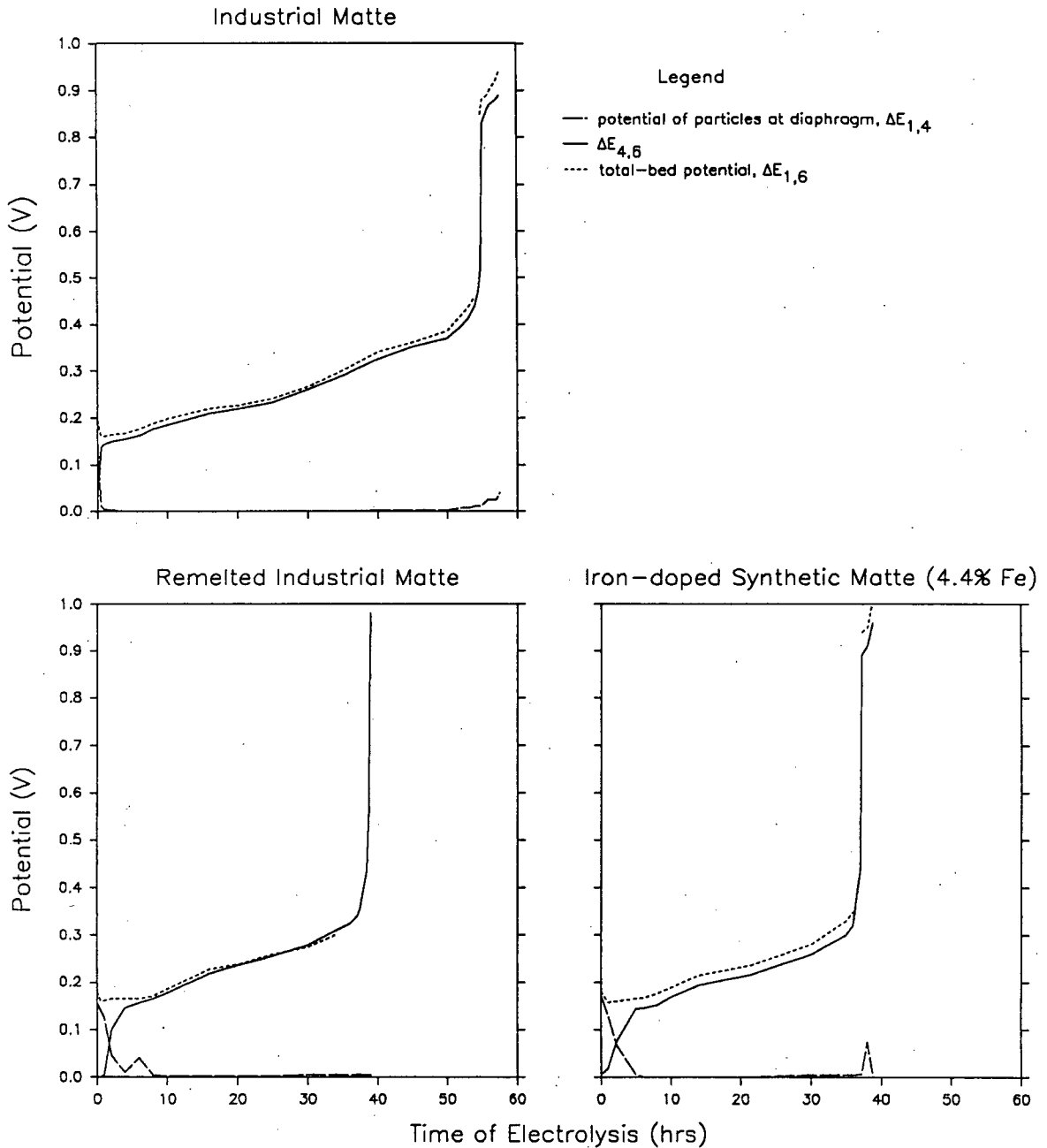


**Figure 8.3** Galvanostatic potential-time curves for anodic decomposition of various iron-laden mattes in a thin (2.9mm) particulate electrode: industrial matte (Test 41), re-melted industrial matte (Test 51) and iron-doped synthetic copper matte (Test 49). Particle diameter: 2.0-2.9mm; current density:  $60\text{A/m}^2$  ( $\approx 200\text{A/m}^2\cdot\text{cm}$  or  $0.84\text{A/m}^2\cdot\text{g}$ ); electrolyte:  $45\text{g/l Cu}^{2+}$ ,  $160\text{-}166\text{g/l H}_2\text{SO}_4$ ,  $50^\circ\text{C}$ ; current distributor: Au; diaphragm: "medium".

However, total-bed polarization of lead-doped synthetic material continues to be due to deteriorating electrical conductivity between the current distributor and the adjacent particles. On the other hand, total-bed polarization of pure synthetic copper sulphide apparently may be due to a combination of mechanisms since both  $\Delta E_{1,4}$  and  $\Delta E_{4,6}$  abruptly increase, thus causing total-bed polarization.<sup>2</sup>

## 8.2 IRON EXTRACTION

Since iron does not deposit on the cathode, its degree of extraction from the mattes is reflected in its concentration in the bulk electrolyte. Iron extraction from the three different iron-laden mattes is shown in Fig. 8.4. The concentration of iron in the electrolyte, in g/l, may be obtained by dividing the percentage iron extraction by 1.27.

The first point to note is that some iron appeared in the electrolyte before the current was switched on. This represented iron which was leached from the mattes. Secondly, nearly five times as much iron was leached before application of current from industrial matte than from either re-melted industrial matte or synthetic matte doped with iron. The amount of iron leached from the latter two matte types was equal. Thirdly, with the exception of approximately the final five hours during electrolysis of the iron-doped material, the amount of extraction from this matte and from the re-melted industrial matte was virtually equal. Finally, the overall iron removed from the industrial matte was four and eight times greater than from the iron-doped matte and re-melted industrial matte, respectively.

These data may be combined with calculated copper extraction data (based on 97% current efficiency) to yield iron-copper incremental and cumulative extraction ratios. These extraction ratios are also shown in Fig. 8.4. The cumulative extraction ratio is a maximum at the start of electrolysis and generally declines during electrolysis, reflecting the fact that iron is leached from the mattes before current was applied.

---

<sup>2</sup> The data shown in the figure suggests that the increase in particle potential,  $\Delta E_{1,4}$ , is a minor component of the total-bed potential,  $\Delta E_{1,6}$ , during total-bed polarization. However, data from an experiment not reported in this thesis shows that the increase in particle potential was the largest component of the total-bed potential during total-bed polarization.

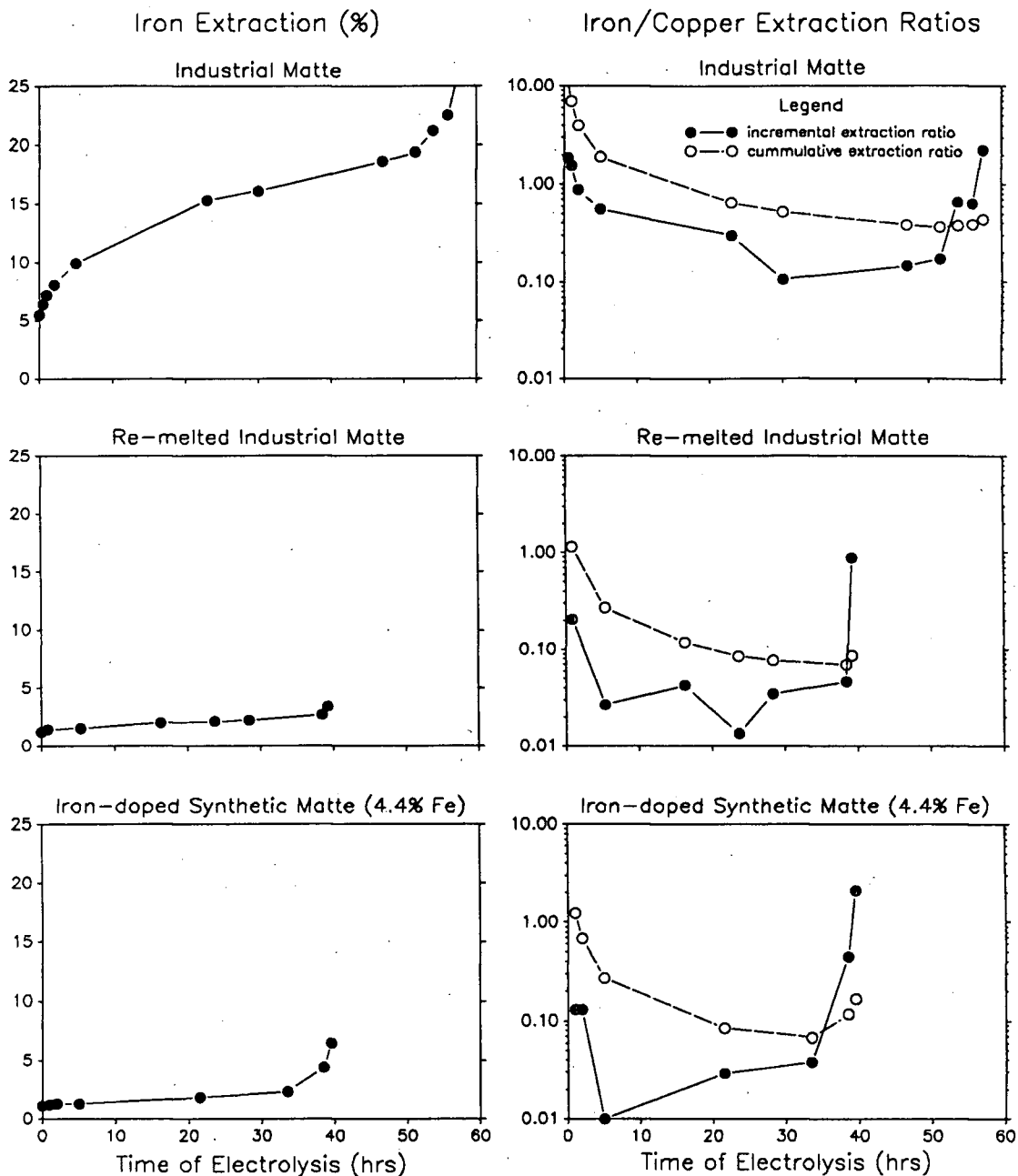


**Figure 8.4** Iron extraction and iron-copper extraction ratios (based on percent extraction) for anodic decomposition of various iron-laden mattes in a thin (2.9mm) particulate electrode: industrial matte, re-melted industrial matte and iron-doped synthetic copper matte (same tests as Fig. 8.3). Particle diameter: 2.0-2.9mm; current density: 60A/m<sup>2</sup> ( $\approx 200\text{A/m}^2\cdot\text{cm}$  or  $0.84\text{A/m}^2\cdot\text{g}$ ); electrolyte: 45g/l Cu<sup>2+</sup>, 160-166g/l H<sub>2</sub>SO<sub>4</sub>, 50°C; current distributor: Au; diaphragm: "medium".

The incremental extraction ratio, which is essentially a ratio of iron and copper extraction rates, in %/hr, had a very low value until the final few hours during electrolysis of iron-doped synthetic copper sulphide and re-melted industrial matte. Near the end of these tests, the incremental

ratio dramatically increased. Reference to the corresponding potential-time curves (Fig. 8.3) shows that the rise in the incremental ratio near the end of electrolysis corresponded very closely with the increasing value of  $\Delta E_{4,6}$ . This suggests that further extraction of iron from these mattes may begin to occur only at high electrode potentials.

The incremental extraction ratio for industrial matte rapidly declined during the first five hours of electrolysis from a relatively high initial value. During the following 30hrs, this ratio continued to slowly decrease and then remained relatively constant before increasing rapidly during the final several hours of electrolysis. Again, reference to the corresponding potential-time curve (Fig. 8.3) illustrates that the rise in incremental extraction near the end of electrolysis corresponds closely with an increasing value of  $\Delta E_{4,6}$ . More iron is released to the electrolyte from industrial matte than from the other two iron-laden mattes, although most of the iron is in a form which is difficult to extract, much like the iron in the other iron-containing mattes. In addition, iron extraction from the industrial matte is accompanied by a decrease in acidity. This is best illustrated in the 2cm-thick electrode experiments as shown in Table 8.1.

**Table 8.1** Acid decrease and iron liberation during electrolysis of industrial matte in 2cm-thick particulate anodes at 400A/m<sup>2</sup> and 50°C (after correcting for a water balance). Also shown are results from several experiments on iron-doped synthetic material (\*) containing the same amount of iron as the industrial matte for comparative purposes.

(exp no.)	Acid Balance				Iron Liberation		Ratio <sup>1</sup>
	Start (g/l)	End (g/l)	Loss (g/l)	Loss (mol/l)	(g/l)	(mol/l)	
(19)	165	155	10	0.10	6.6	0.12	0.86
(30)	165	154	11	0.11	5.3	0.09	1.18
(38)	162	153	9	0.09	5.2	0.09	0.99
(40)	166	155	11	0.11	5.9	0.10	1.06
(*24)	166	167	<0.01	<0.01	0.5	<0.01	
(*32)	168	167	<0.01	<0.01	0.4	<0.01	

Notes: 1 mole ratio of acid loss to iron liberated

## 8.3 PHASE ANALYSES

### 8.3.1 X-ray Powder Diffraction

X-ray powder diffraction analyses of various mattes performed prior to electrolysis are presented in Appendix F. A summary of these analyses is given in Table 8.2.

**Table 8.2** X-ray powder diffraction analyses of selected copper mattes before anodic decomposition. Brackets indicate that only a few lines close to the most intense lines of the reference cards for these phases were present in the diffraction pattern.

Material	Detected Phases
synthetic $\text{Cu}_2\text{S}$	$\text{Cu}_2\text{S}$
synthetic $\text{Cu}_2\text{S}$ doped with 4.1wt% Pb	$\text{Cu}_2\text{S}$ , Pb, $(\text{Cu}_{14}\text{Pb}_2\text{S}_{9-x})$ , (PbS)
synthetic $\text{Cu}_2\text{S}$ doped with 4.5wt% Pb	$\text{Cu}_2\text{S}$ , Pb, $(\text{Cu}_{14}\text{Pb}_2\text{S}_{9-x})$ , (PbS)
synthetic $\text{Cu}_2\text{S}$ doped with 4.5wt% Fe	$\text{Cu}_{1.96}\text{S}$ , $\text{Cu}_2\text{S}$ , $(\text{Cu}_5\text{FeS}_4)$
synthetic $\text{Cu}_2\text{S}$ doped with 4.7wt% Fe	$\text{Cu}_{1.96}\text{S}$ , $\text{Cu}_2\text{S}$ , $(\text{Cu}_5\text{FeS}_6)$
industrial matte	$\text{Cu}_{1.96}\text{S}$ , $\text{Cu}_2\text{S}$ , Pb, $(\text{Cu}_5\text{FeS}_4)$ , $(\text{Cu}_{14}\text{Pb}_2\text{S}_{9-x})$ , (PbS)
re-melted industrial matte	$\text{Cu}_{1.96}\text{S}$ , $\text{Cu}_2\text{S}$ , Pb, $(\text{Cu}_5\text{FeS}_4)$ , $(\text{Cu}_{14}\text{Pb}_2\text{S}_{9-x})$ , (PbS)

### 8.3.2 Scanning Electron Microscopy

Back-scatter image and energy dispersion analyses (EDS) of selected copper mattes conducted before electrolytic decomposition are shown in Figs. 8.5-8.8.

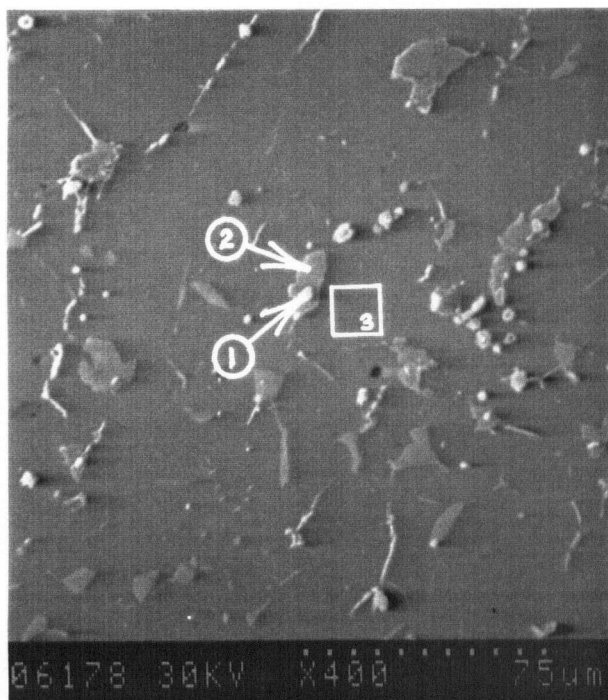
#### Synthetic Mattes Containing Lead (Fig. 8.5)

According to Craig and Kullerud [62,63], the solubility of lead in chalcocite is negligible, even under rapid cooling conditions. Also, for the overall composition used in this thesis, the stable phases that ought to exist below 200°C are copper, chalcocite and galena. However, the copper-lead-sulphur phase "A" [62,63]<sup>3</sup>,  $\text{Cu}_{14}\text{Pb}_2\text{S}_9$ , is also reported to be metastable, provided the material is cooled quickly. In summary, it may be inferred that several lead-containing phases may exist in the copper sulphide mattes.

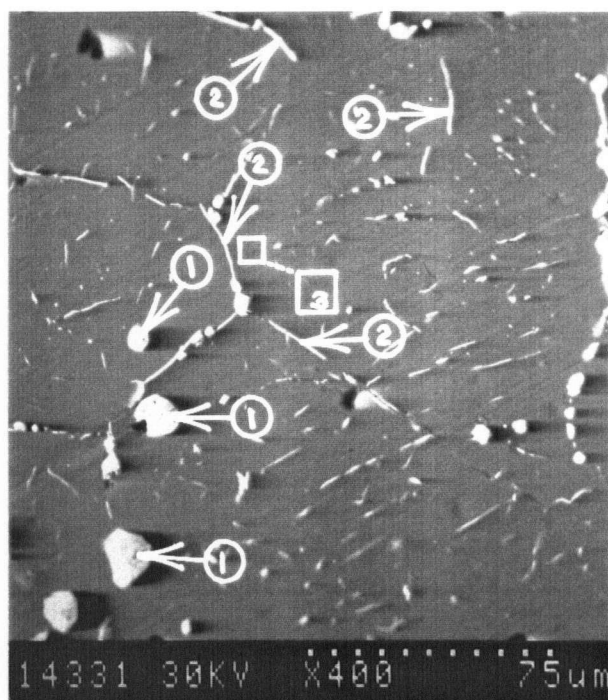
The evidence from Fig. 8.5 indicates that there is indeed a variety of phases appearing in the mattes synthetically prepared for this thesis. There are copper-lead phases, copper-lead-sulphur phases, lead-sulphur phases and, of course, copper-sulphur phases indicative of chalcocite. A lead

<sup>3</sup> Phase "A" is a designation assigned by Craig and Kullerud [62,63] and is adopted for convenience in this thesis.

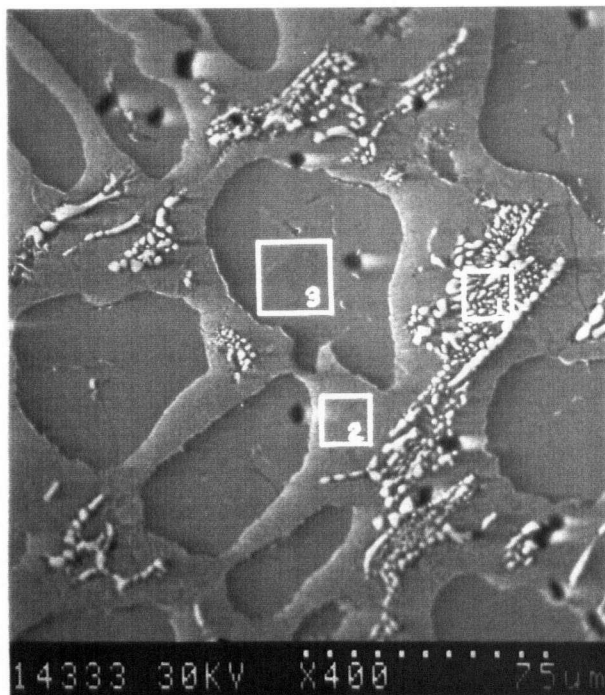
(a) 4.5wt% Lead



(b) 4.8wt% Lead



(c) 16wt% Lead



Phase Analyses in wt% by EDS

	AREA			BULK	CHEM
	1	2	3		
(a)					
S	6	18	24		
Cu	9	55	75		
Pb	86	28	2		
(b)					
S	8	13	18	15	20.4
Cu	13	50	81	78	74.8
Pb	80	37	1	7	4.8
(c)					
S	15	15	13	17	20.0
Cu	8	55	85	65	64.0
Pb	77	30	2	18	16.0

**Figure 8.5** Electron back-scatter micrographs of several lead-doped synthetic copper matte ( $\text{Cu}_2\text{S}$ ) particles. Note that "CHEM" refers to a chemical analysis of the matte and that "BULK" refers to the entire SEM field.

phase should also be considered based on the x-ray diffraction analyses. Although the EDS analyses do not correspond exactly to the stoichiometry of, for example, phase "A" or chalcocite, the x-ray diffraction results suggest these phases are present in the particles. Certainly chalcocite is present. This is a reasonable conclusion because EDS analyses should not be considered rigorously quantitative, particularly when the material contains both sulphur and lead, and probably accounts for the small amount of lead detected in the chalcocite phases.

The important conclusion to be drawn from Fig. 8.5 is that, at the concentration of lead in the mattes electrolyzed, lead segregates into separate phases (that may be associated with some copper) which are dispersed in the chalcocite phase. There is some tendency shown at 4.8wt% lead for segregation of these phases at the grain boundaries. Certainly at 16wt% lead, segregation of lead-rich phases tends to occur along what would appear to be grain boundaries. Eventually, a lead-rich phase, possibly phase "A", completely encapsulates the lead-free copper sulphide phase. Also, at the highest lead concentration analyzed, there are two clearly distinguishable lead-rich phases, with the most lead-rich of these, probable PbS, existing as "islands" in the other, probably a phase similar to "A".

The point should also be made that there was some variation in the appearance of the back-scatter images among the particles selected for these analyses and some variation in the back-scatter images for different positions in the ingot shown in Fig. 4.1. However, the reader is reminded, with reference to that figure, that lead was, in fact, quite uniformly distributed throughout that sample ingot; thus, these differences are not considered to be important.

### **Synthetic Mattes Containing Iron (Fig. 8.6)**

The appearance of these materials differs considerably from that of lead-doped synthetic copper sulphide. There appear to be two phases in these mattes, which essentially form a finely divided eutectoid mixture. Above about 3wt% iron, the eutectoid covers the entire SEM field.

Due to the grating-like physical structure of the eutectoid, individual phase analyses is somewhat difficult by EDS. Increased magnification only reveals an even more finely divided eutectoid mixture. (The very light coloured phase areas in the samples containing 0.5wt% and 1.7wt% iron are copper and the small dark areas in the sample containing 6.9wt% iron are voids.)

The diagrams of Yund and Kullerud [60,61], Fig. 3.4, show that the extensive Cu-Fe-S solid solution which exists at 500°C should yield two phases upon cooling to room temperature: bornite and a djurleite-chalcocite phase containing a small amount of iron ( $\approx 0.5\text{wt}\%$ ). Based on these data and on x-ray diffraction analyses summarized in Table 8.2, it is probably reasonable to assume that the light coloured phase component of the eutectoid mixture is either iron saturated ( $\approx 0.5\text{wt}\%$  iron) djurleite or chalcocite and that the dark phase component is approximately bornite. The eutectoid point may lie close to 3.1wt% iron, since the large areas of djurleite-chalcocite which appear with the eutectoid mixture at 1.7wt% iron are absent at the higher iron concentrations analyzed.

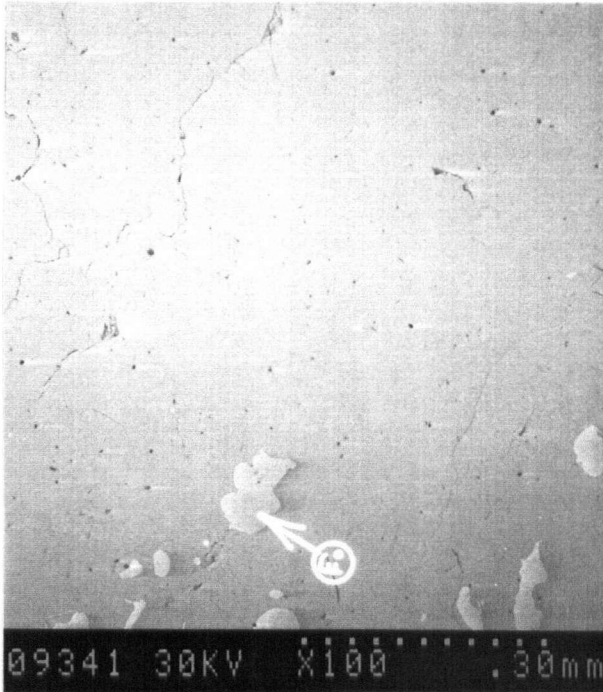
### **Industrial Matte (Fig. 8.7)**

There is some variation in the phase structure of this material among particles. In general, the following conclusions may be drawn: (a) there are "fields" or phase "regions" that are like the eutectoid phase mixture of the synthetic copper sulphide doped with about 3-4wt% iron, (b) there are phase "fields" that contain very little or no iron, (c) lead is segregated into separate lead-rich phases as in the lead-doped synthetic mattes containing the same amount of lead, (d) zinc is also segregated into separate phases (which appear to be sulphides), and (e) there is evidence that a few small metallic phases are present. As reviewed in Secs. 3.4.4 and 3.4.5, there is probably no solubility of lead in the copper-iron-sulphide phases.

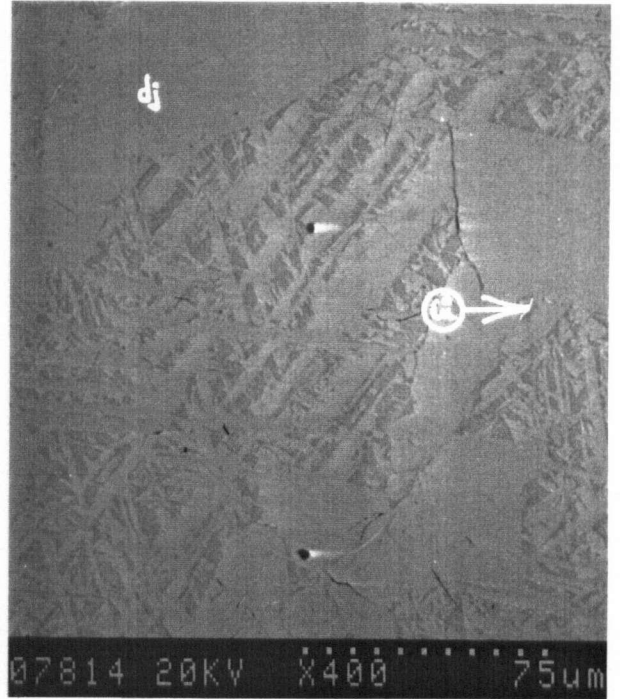
### **Re-melted Industrial Matte (Fig. 8.8)**

The most noteworthy feature of this material is the presence of the eutectoid "field" or phase "region" over the entire SEM field, which is identical to the iron-doped synthetic matte containing the same amount of iron. Also, segregation of lead and zinc is unchanged from the as-received industrial matte, although the occurrence of lead-rich phases at the grain boundaries is slightly increased.

(a) 0.5wt% Iron



(b) 1.7wt% Iron



(c) 3.1wt% Iron



(d) 6.9wt% Iron

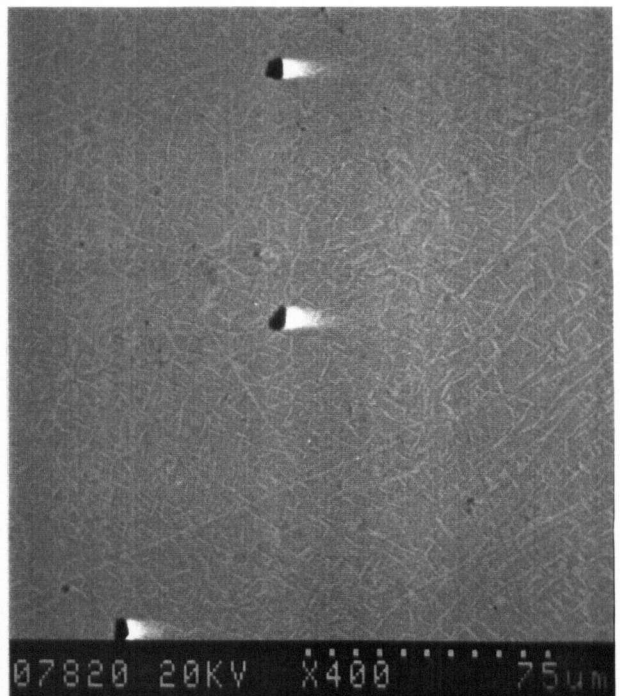


**Figure 8.6** Electron back-scatter micrographs of several iron-doped synthetic copper matte ( $\text{Cu}_{1.96-2.0}\text{S}$ ) particles. The light phase areas in the particles containing 0.5wt% and 1.7wt% iron are copper. The black areas in the particles containing 1.7wt% and 6.9wt% iron are voids.

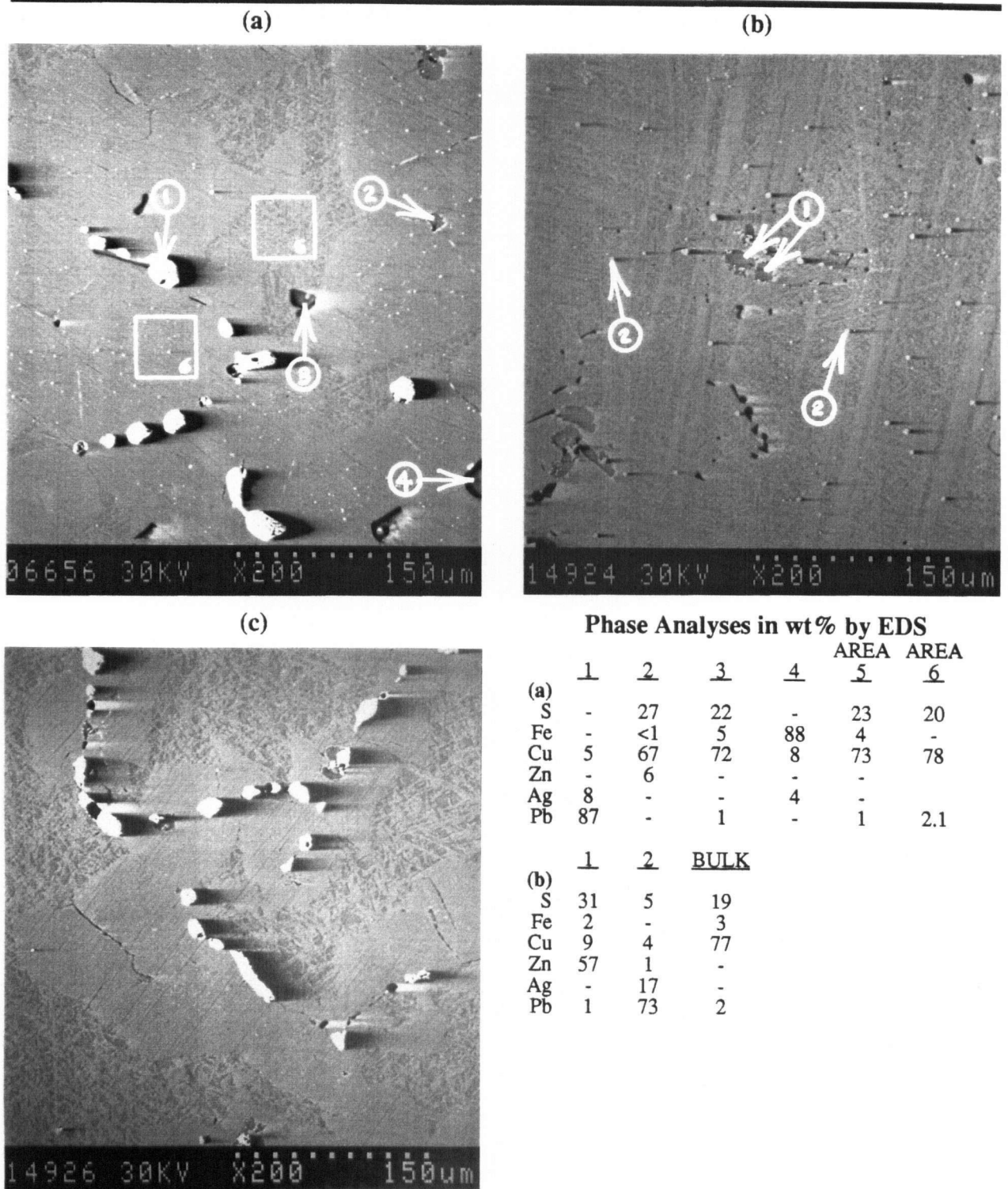
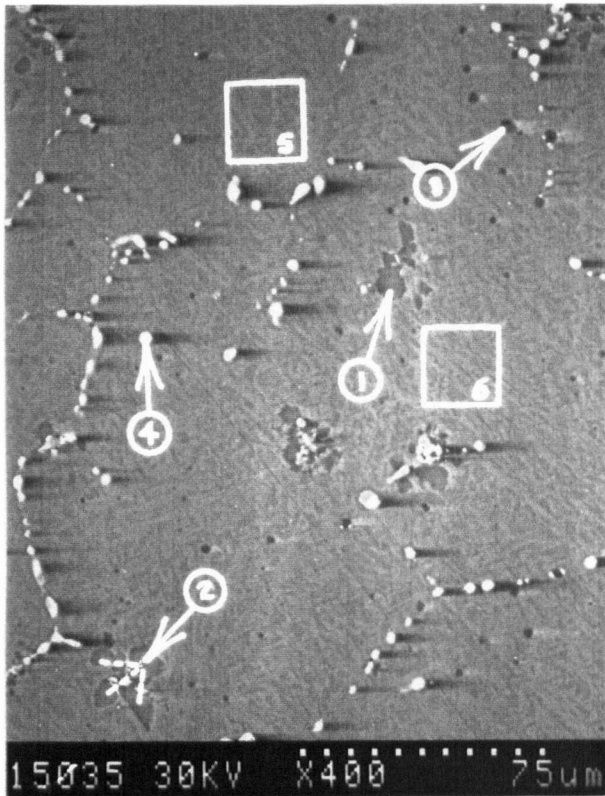


**Figure 8.7** Electron back-scatter micrographs of several industrial matte particles. Note the variation amongst the particles in terms of the amount of the eutectoid phase "field", AREA 5 in (a), and the djurleite-like phase, AREA 6 in (a). Also, "BULK" for sample (b) refers to the entire SEM field.

### Re-melted Industrial Matte



### Phase Analyses in wt% by EDS

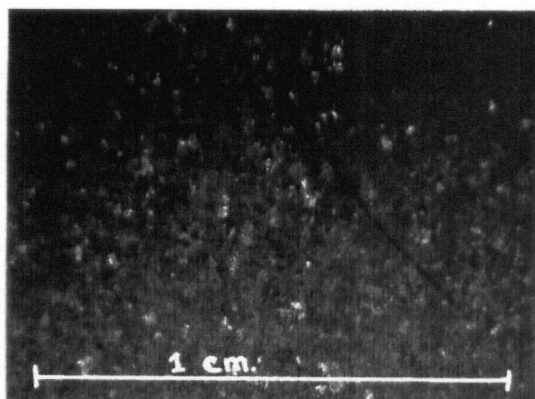
	<u>1</u>	<u>2</u>	<u>3</u>	<u>4</u>	AREA <u>5</u>	AREA <u>6</u>
S	23	28	20	5	20	20
Fe	4	3	5	1	4	4
Cu	48	11	73	16	74	75
Zn	24	54	-	-	-	-
Ag	-	-	-	<1	-	-
Pb	2	3	2	77	1	1

**Figure 8.8** Electron back-scatter micrograph of a re-melted industrial matte particle. The chemical analyses for this material are provided elsewhere in this thesis.

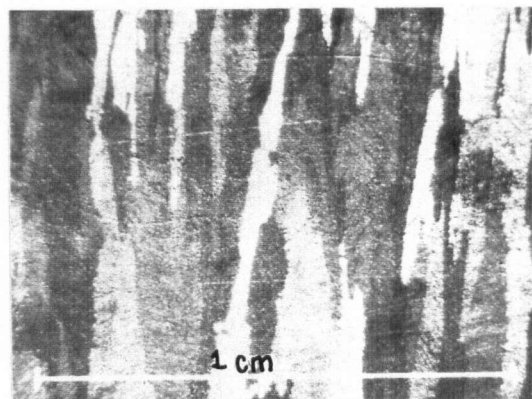
## 8.4 GRAIN SIZE & STRUCTURE

Figure 8.9 illustrates the difference in grain size and structure between the mattes containing iron and lead impurities (4.7wt% iron and 4.5wt% lead). The iron-doped matte is composed of relatively long columnar crystals, whereas the lead-doped copper sulphide is composed of equiaxed grains. When the iron content is more than about 7wt%, the ingots are very brittle and crack on cooling. The texture of the industrial matte is similar to the iron-doped mattes containing the same amount of iron.

**Lead-doped Synthetic Matte**



**Iron-doped Synthetic Matte**



**Figure 8.9** Comparison of the grain size and structure between synthetic copper mattes doped with 4.5wt% lead and 4.7wt% iron.

### 8.5 DECOMPOSITION MORPHOLOGY

During anodic decomposition, the reacted portions of the particles become fractured and porous. This was discussed in Chap. 3, Sec. 3.7. Although this fracturing leads to fragmentation of the particles at 50% copper extraction during acid pressure leaching [52], the present evidence suggests that up to at least 80% copper recovery can be achieved by direct electrochemical decomposition without the particles breaking apart.

Qualitatively, the observation was made that at greater than 50% copper extraction, the particles were more easily ground to powder for chemical assaying than at less than 50% extraction. At 80% extraction, the particles were very easily prepared for assaying and some of these broke apart while being carefully extracted from the electrode. Thus, the breakup of particles during leaching is probably attributable to the very turbulent conditions in the autoclaves, as well as increased friability of the particles.

Figure 8.10 demonstrates the extent of fracturing at 80% copper extraction from synthetic copper sulphide. Figure 8.11 is representative of the internal regions of these copper-depleted mattes when these particles are carefully broken apart after total-bed polarization. These figures suggest that the particles may fracture and develop porosity in two ways: firstly, at grain boundaries and secondly, by delamination of the individual grains. The latter are identified as parallel fractures within the grains.

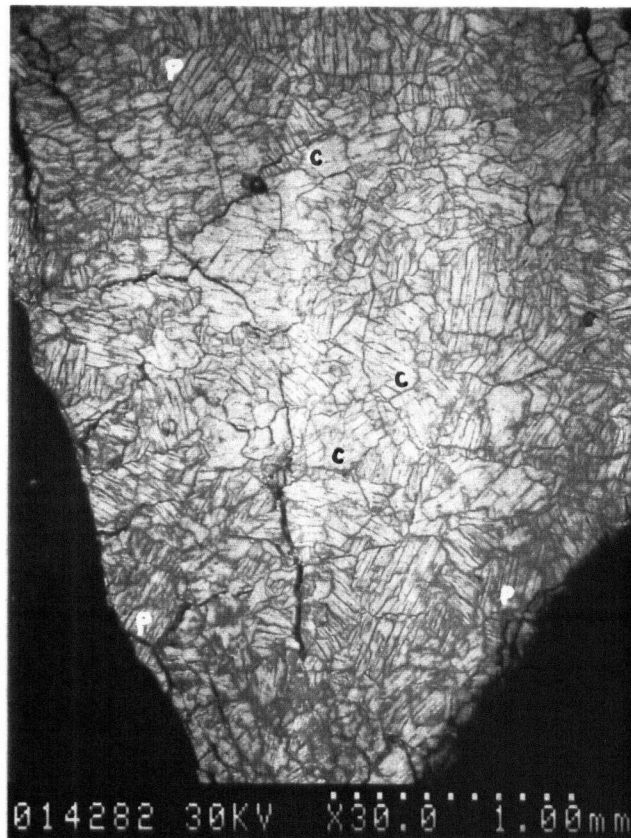
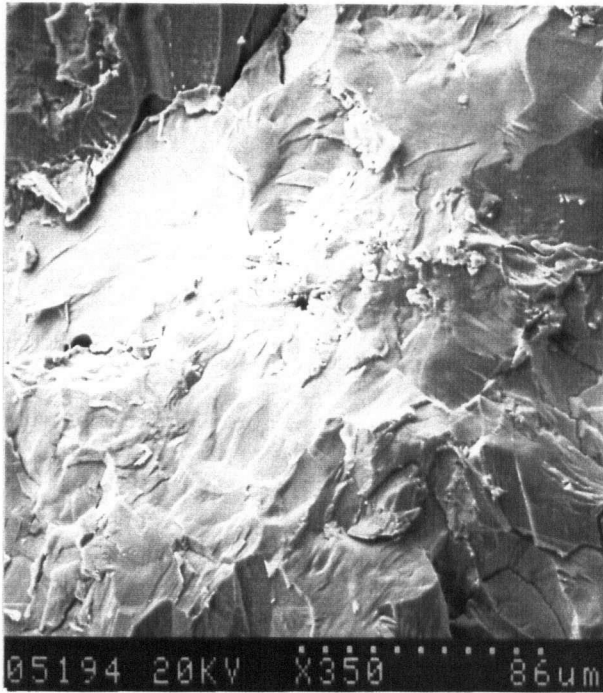


**Figure 8.10** Scanning electron micrograph cross section of a synthetic chalcocite particle after total-bed polarization. Note the increased delamination type fracturing of the grains near the outer edge of the particle, labeled "p", as compared to near the center of the particle, labelled "c".

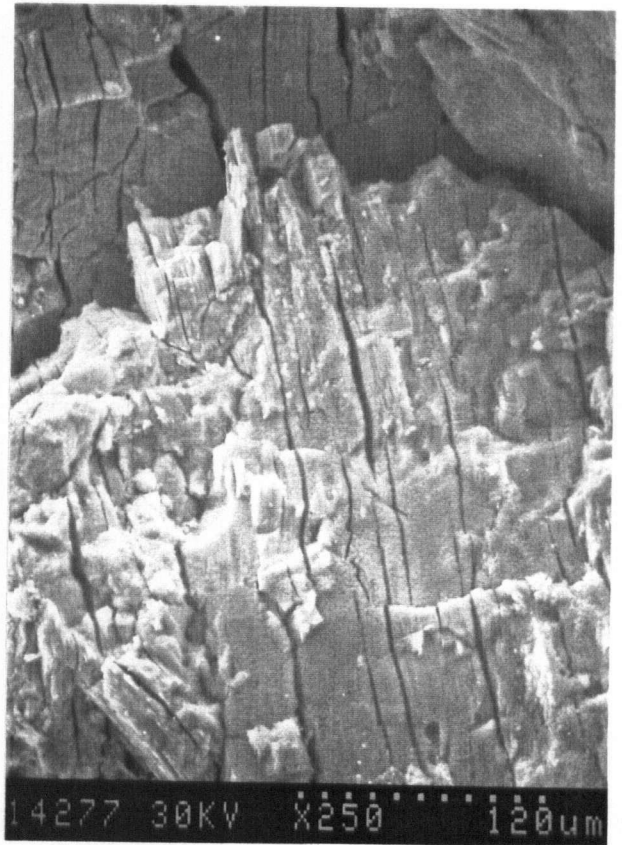
Figure 8.12 shows the characteristics of the surface of synthetic copper sulphide particles at about 80% copper extraction. It is undoubtedly sulphur over the entire surface shown at the high magnification.

Inspection of Figs. 8.11b and 8.11c suggests that the fractures in "polarized" copper sulphide particles occurring along grain boundaries may be somewhat larger than the delamination fracturing within the individual grains. This suggests that corrosion near grain boundaries may precede decomposition within the grains and that phase changes, which are likely to eventually occur with extensive (or sufficient) removal of copper from the grains, lead to delamination. Close examination of Fig. 8.10 shows that much of the increased amount of fracturing at the edge of the particles, as compared to near the particle's center, is largely due to appreciable delamination of the grains. At the center of the particle, fractures along the grain boundaries are relatively more easily distinguished

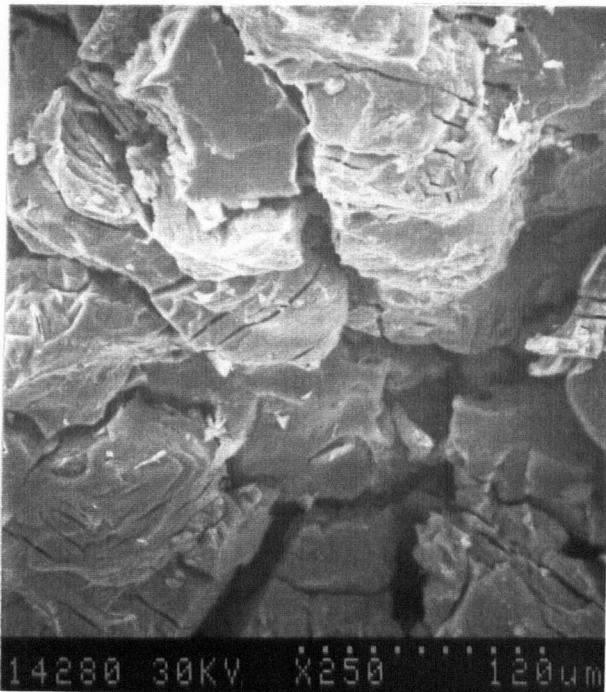
(a) Before Electrolysis



(b) After Electrolysis



(c) After Electrolysis



(d) After Electrolysis

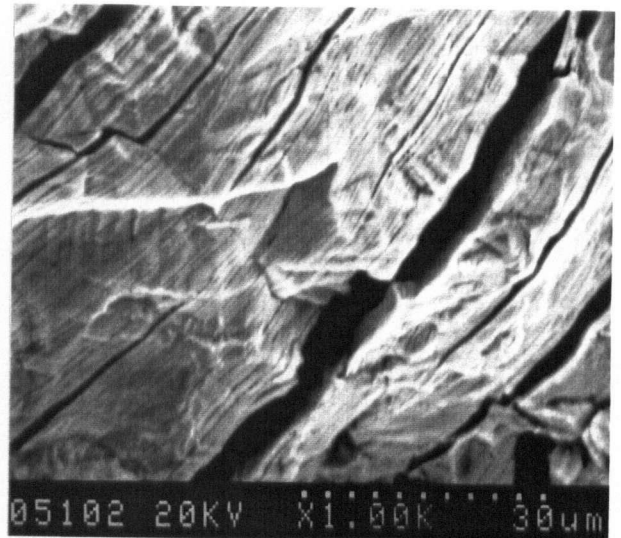


**Figure 8.11** Scanning electron micrographs of a synthetic chalcocite particle broken apart prior to electrolysis and of several particles broken apart after total-bed polarization. Note the grain boundary and delamination fracturing of the polarized particles.

than grain delamination fracturing. For example, the grains labelled "c" (particle center) may be compared to those labelled "p" (particle perimeter or shell). Obviously, fracturing along all the grains of this particles did not occur, otherwise it would have broken apart before or while being extracted from the anode.

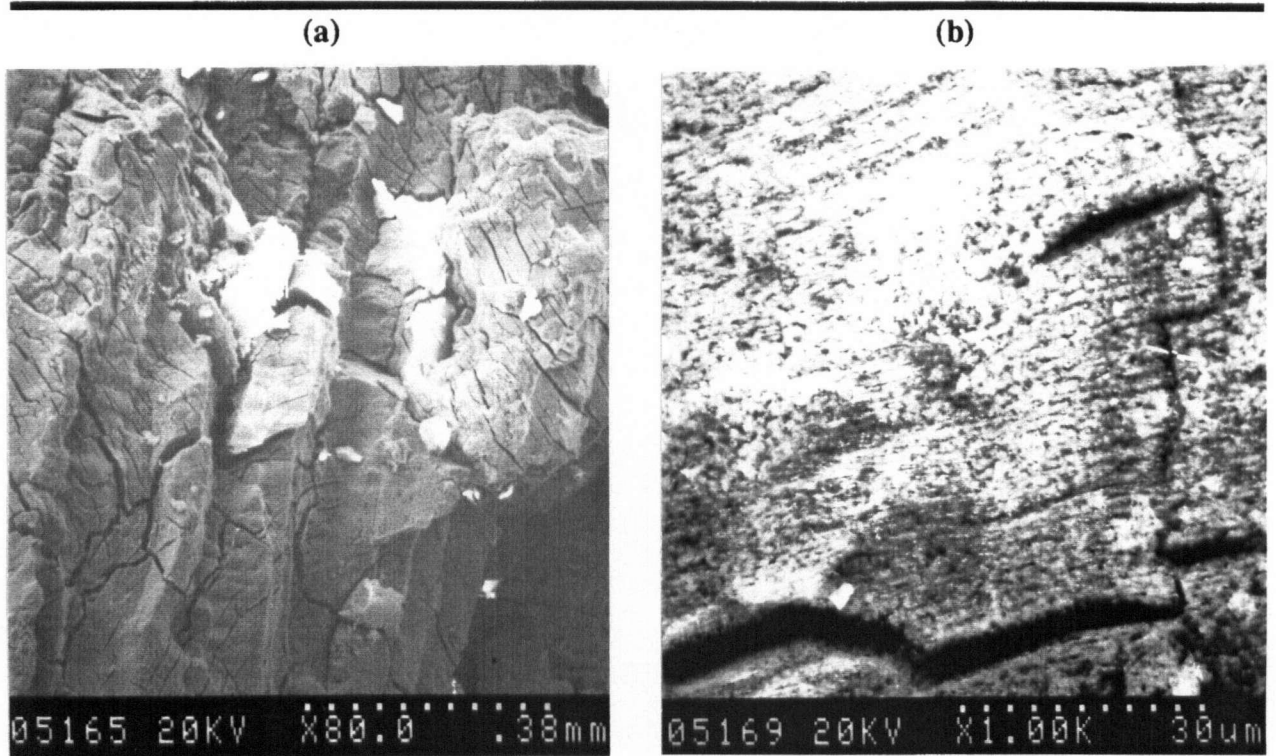


**Figure 8.12** Scanning electron micrographs of the surface of synthetic chalcocite particles after total-bed polarization.

Similar fracturing mechanisms were observed at the surface of copper depleted lead-doped (2.9wt% lead) synthetic particles extracted from positions adjacent to the diaphragm in a thick-anode experiment (corresponding to about 80% copper extraction). Figure 8.13 shows that some grain delamination occurs during decomposition of industrial matte.

No micrographs showing the internal surface morphology of iron-doped particles (3-4.5wt%) broken apart after copper depletion were obtained. However, particles containing this amount of iron have much more structural integrity after copper depletion than the copper depleted chalcocite particles and are *relatively* difficult to break apart. Further, the impression is obtained from

back-scatter analyses of copper depleted particles containing 3-4.5wt% iron, that the amount of fracturing of these particles during electrolysis is less than the fracturing of pure chalcocite. This is shown in Fig. 8.14.

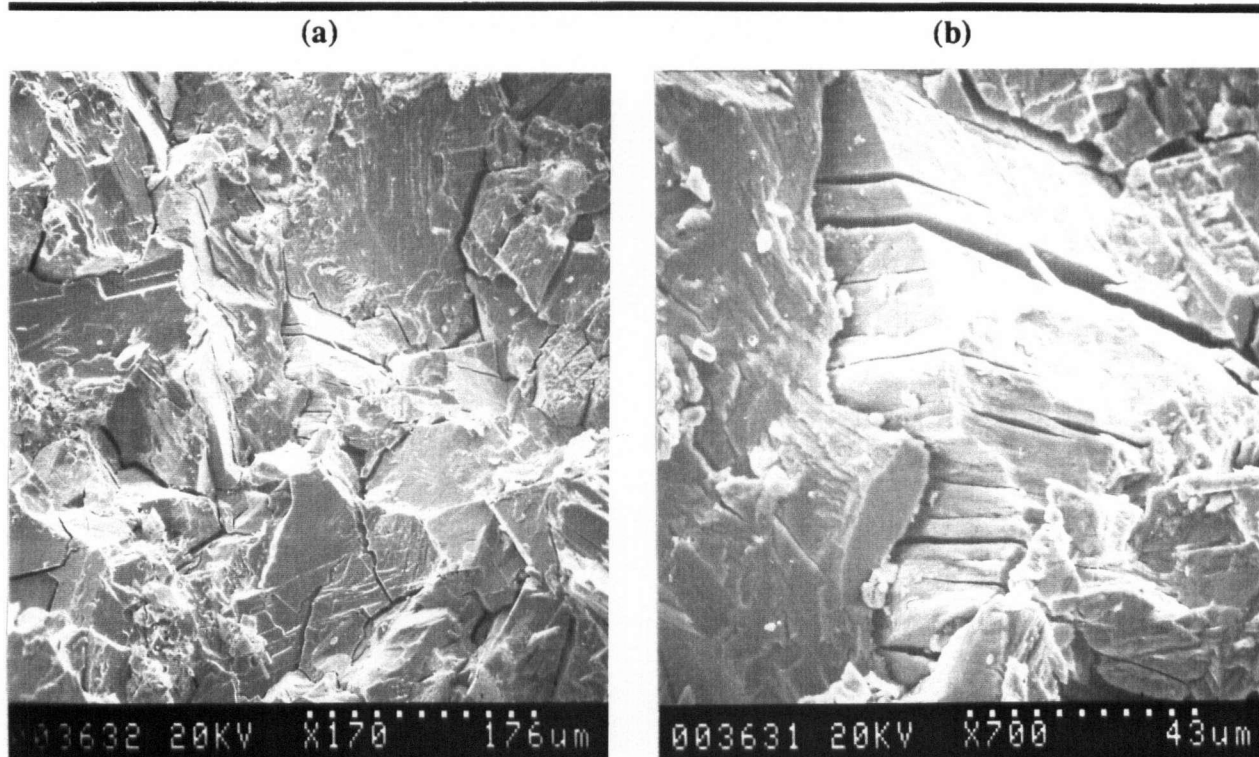


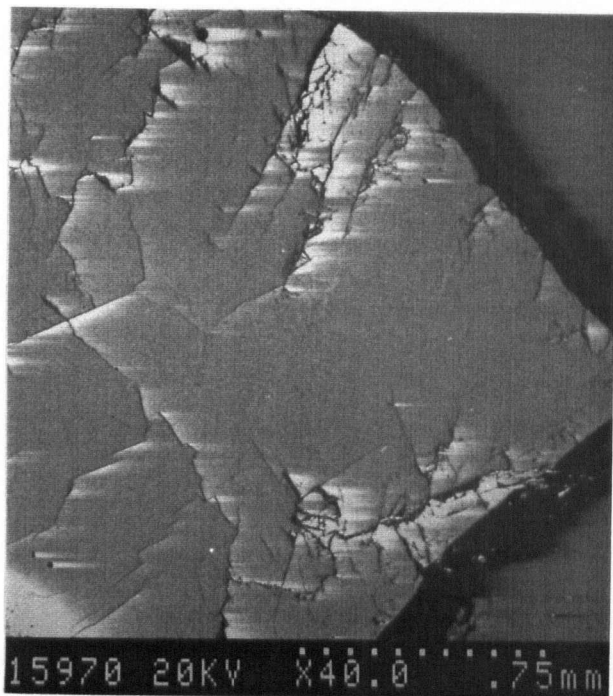
**Figure 8.13** Scanning electron micrographs of industrial matte particles broken apart after total-bed polarization.

## 8.6 DISCUSSION

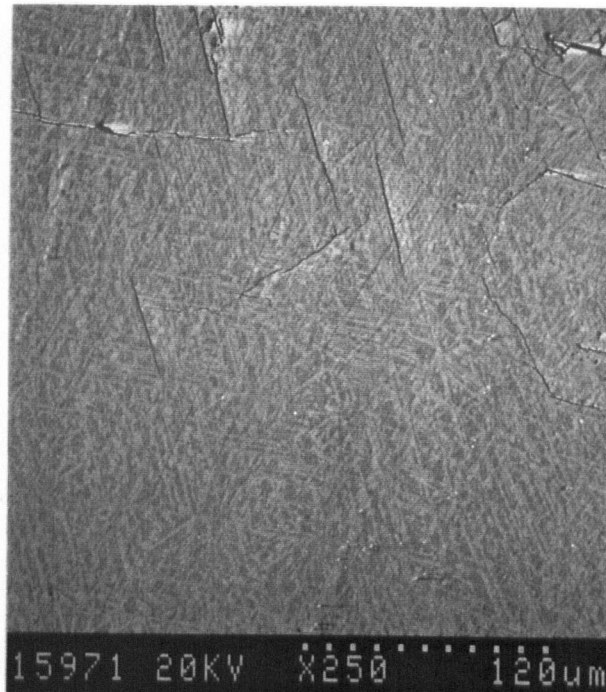
### 8.6.1 Phase Changes During Decomposition

Reference to the potential-time curves for chalcocite in Fig. 8.2 reveals that  $\Delta E_{4,6}$  rises in several increments during electrolysis. There is a rapid potential increase during the first hour; between 1hr and 35hrs the rate at which this parameter increases (0.14-0.20V) gradually declines and is approximately constant between 15hrs and 35hrs (0.185-0.20V); from 35hrs to 60hrs there is a relatively large increase in  $\Delta E_{4,6}$  (0.20-0.30V); it remains relatively constant after that time until the anode begins to "polarize" at 85hrs. The value of  $\Delta E_{4,6}$  for the lead-doped synthetic copper sulphide also shows these incremental increases.

(a) Iron-doped Synthetic Copper Matte



(b) Iron-doped Synthetic Copper Matte



(c) Pure Synthetic Chalcocite

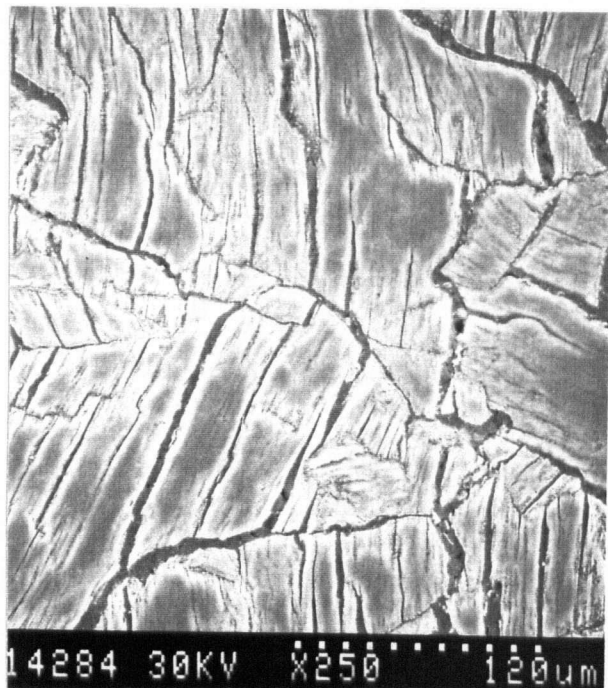


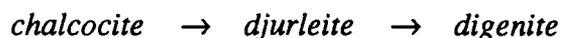
**Figure 8.14** Electron back-scatter micrographs of an iron-doped (4.4wt% iron) synthetic copper matte and of a pure synthetic copper matte obtained after total-bed polarization showing particle fracturing.

When the current was first switched on,  $\Delta E_{4,6}$  was very small (about 0.015V). However, during the first hour of electrolysis it increased rapidly to a value of about 0.14V. The starting stoichiometry of this chalcocite was  $\text{Cu}_{2.04}\text{S}$ , thus the amount of copper present slightly exceeded its solubility limit of  $\text{Cu}_{2.00}\text{S}$ . This excess copper was readily removed during the first hour of electrolysis, but as the stoichiometry approached  $\text{Cu}_{2.00}\text{S}$ , the value of  $\Delta E_{4,6}$  rapidly increased to the decomposition potential of stoichiometric chalcocite.

Close inspection of the  $\Delta E_{4,6}$ -time curve for the first 15hrs of the run suggests that between about 1hrs and 5hrs (0.14-0.17V) the slope of the curve is greater than the slope between 5hrs and 15hrs (0.175-0.185V). In fact,  $\Delta E_{4,6}$  for the lead-doped material appears to have a brief plateau between about 5hrs and 10hrs, and then a small rise between about 10hrs and 15hrs. This detail is not as easily detected on the curve for chalcocite.

Electrolysis between 1hr and 5hrs corresponds to an overall stoichiometry change in the anode from  $\text{Cu}_{1.98}\text{S}$  to  $\text{Cu}_{1.90}\text{S}$ , which encompasses the reported stoichiometry for djurleite,  $\text{Cu}_{1.96}\text{S}$ . Electrolysis from 5hrs to 15hrs corresponds to a stoichiometry change in the anode from  $\text{Cu}_{1.90}\text{S}$  to  $\text{Cu}_{1.75}\text{S}$ , which encompasses the reported stoichiometry range for digenite,  $\text{Cu}_{1.83-1.765}\text{S}$ .

The conclusion from these observations is that the decomposition sequence over the first 15hrs of electrolysis may be approximately given by

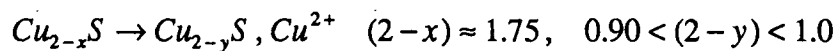


However, if phases with precise stoichiometry decompose and are produced during decomposition, the  $\Delta E_{4,6}$ -time curve should be characterized by abrupt stepwise increases at about 5hrs and 10-15hrs corresponding to the initiation of djurleite and digenite decomposition, respectively, and *no* increase between these times. This was not observed. Therefore, over this time frame, (a) there may be a more or less continuous range in stoichiometry from  $\text{Cu}_{2.00}\text{S}$  to  $\text{Cu}_{1.75-1.85}\text{S}$  between the surface and interior of the particles, and (b) the transformation of one phase to another probably occurs over a range of stoichiometry for both phases.

These arguments are reasonable for several reasons. Firstly, the solid-state diffusion of copper may be too slow, relative to the applied current density, to allow formation of equilibrium phases (which should occur at specific copper extractions) over the thickness of the particles. Thus, the particles may contain solid solutions of copper and sulphur in the range between  $\text{Cu}_2\text{S}$  and  $\text{Cu}_{1.75}\text{S}$ . This was also discussed by Beigler and Swift [31]. Secondly, the decomposition products have lower molar volumes than chalcocite, thus the particles develop cracks during electrolysis. In order to maintain the flow of current in the electrolyte within the cracked, porous product layer, potential gradients develop. Since the reversible decomposition potential does not increase appreciably between chalcocite and copper-lean digenite ( $\text{Cu}_{1.765}\text{S}$ ), perhaps by less than 0.03V (see the data from reference 42, Table E.5, Appendix E), at some point, the potential gradient along these developing cracks and pores may be large enough that variation in electrolyte potential along cracks may permit the simultaneous decomposition of chalcocite, djurleite and possibly digenite.

The expectation is that the starting material is probably largely depleted in chalcocite and djurleite after 10-15hrs, so that electrolysis over the next 45hrs likely represents decomposition of the digenite-like phase (For example, 90% conversion of chalcocite to digenite only requires the reaction to penetrate the particle to a depth slightly more than  $0.5r_p$ ). The slow increase in  $\Delta E_{4,6}$  (0.185-0.20V) over the first 20hrs of time period corresponds to an overall stoichiometry change from  $\text{Cu}_{1.75}\text{S}$  to  $\text{Cu}_{1.37}\text{S}$ . The relatively large stepwise increase in  $\Delta E_{4,6}$  between 35hrs and 60hrs (0.20-0.30V), coincides with an overall stoichiometry change from  $\text{Cu}_{1.37}\text{S}$  to  $\text{Cu}_{0.90}\text{S}$ .

Inasmuch as the solid solution of copper and sulphur (supersaturated in sulphur) may change continuously between  $\text{Cu}_{1.75}\text{S}$  and  $\text{Cu}_{0.9}\text{S}$ , and probably varies across the particle, the interesting point is that the increase in  $\Delta E_{4,6}$  between 35hrs and 60hrs is much larger than the increase during the previous 20hrs. The explanation is identical to the one given above for the corrosion of chalcocite to approximately digenite, and is further illustrated in this case in Fig. 8.15a, with the decomposition process summarized as follows



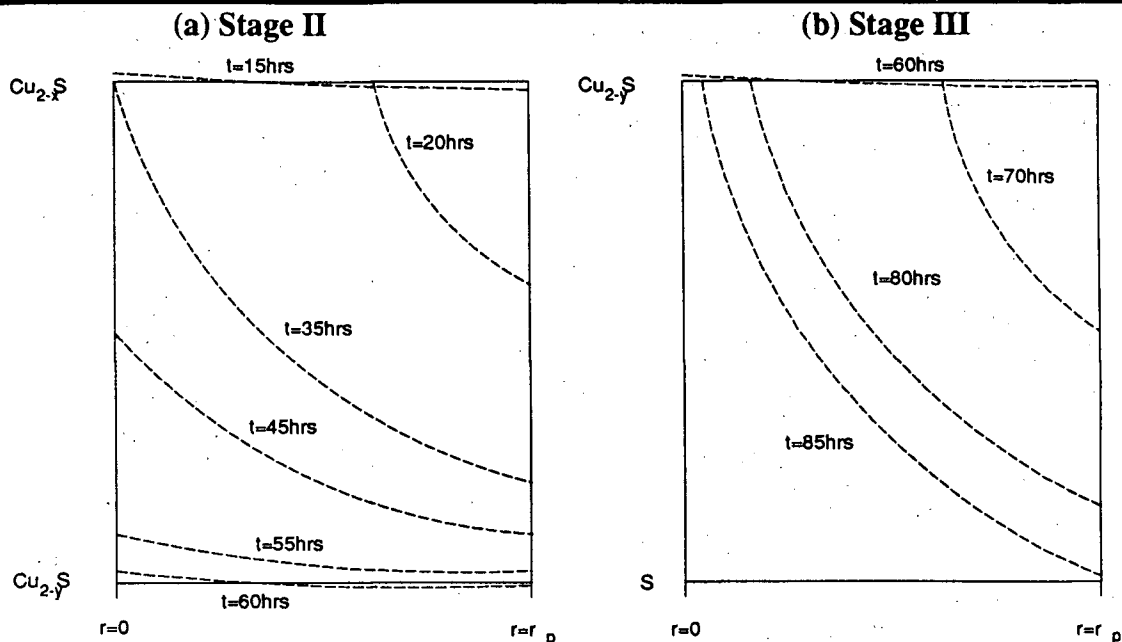
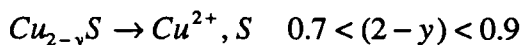


**Figure 8.15** Proposed stoichiometry variation between the center of the particles and the particle surfaces, between the center of grains and the inter granular cracks in the particles or across grain delaminations.  $r=0$  is the center of the particle, grain or grain delamination,  $r=r_p$  is the edge of the particle, grain or grain delamination and is adjacent to the electrolyte.

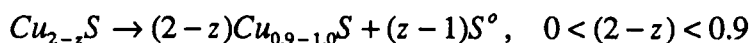
The average stoichiometry of the particles is related to the area under the stoichiometry curves at various times. As this average for the particles approaches approximately  $\text{Cu}_{1.37}\text{S}$ ,  $\Delta E_{4,6}$  begins to rapidly increase because the phase  $\text{Cu}_{2-x}\text{S}$  becomes largely depleted. Thus, further electrolysis results in a continuous decrease in copper activity, which results in a continuous increase in the decomposition potential. Eventually, the bulk of the particle approaches the approximate composition of a covellite-like phase, which is relatively stable thermodynamically, and the value of  $\Delta E_{4,6}$  remains relatively constant as this phase decomposes. Note that the stoichiometry of the solid solution at  $r=r_p$  may not be equal to  $\text{Cu}_{0.9-1.0}\text{S}$  until some time between 35hrs and 55hrs and that this phase probably begins to decompose at  $r=r_p$  before the stoichiometry at  $r=0$  reaches this value (i.e., when the potential at  $r=r_p$  is equal to the reversible potential at  $r=r_c$  plus the potential gradient in the electrolyte through the fractures in the particle). Also, the modest increase in  $\Delta E_{4,6}$  between 15hrs and 35hrs may represent the increase in the diffusion resistance of  $\text{Cu}^+_{ss}$  and  $\text{Cu}^{2+}$  in the solid state and electrolyte, respectively, as the depletion of  $\text{Cu}_{2-x}\text{S}$  extends towards the center of grain delaminations and the center of the particle.

The curious aspect about continued electrolysis at a relatively stable value of  $\Delta E_{4,6}$  beyond about 55hrs is that elemental sulphur formation is expected due to direct decomposition of the covellite-like material  $\text{Cu}_{2-y}\text{S}$ . Since sulphur is not an electrical conductor, the decomposition process should quickly deteriorate at this point as the particles become insulated from the current distributor by sulphur. Yet, the decomposition process doesn't deteriorate until about 80-83% of the copper has been extracted, which is consistent with an overall stoichiometry of  $\text{Cu}_{0.35-0.5}\text{S}$ .

These observations may be understood with reference to Fig. 8.15b. Again, any small increase in  $\Delta E_{4,6}$  beyond 55hrs and before total-bed polarization may represent the increase in the diffusion resistance of  $\text{Cu}^+_{ss}$  and  $\text{Cu}^{2+}$  in the solid state and electrolyte, respectively. The corrosion step is



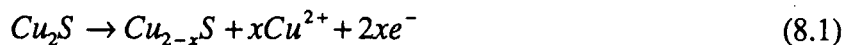
Sulphur is eventually produced when the copper-sulphur solid solution eventually becomes sufficiently depleted in copper. Certainly, any portion of the particle having a stoichiometry  $\text{Cu}_{2-y}\text{S}$  with  $2-y$  less than about 0.7-0.9 is unstable because there are no thermodynamically stable phases when  $2-y$  is less than 1.0. Thus, at some value for  $2-y$  between 0.7 and zero, there may be a disproportionation reaction, resulting in the formation of  $\text{Cu}_{0.9-1.0}\text{S}$  and  $\text{S}^\circ$ .



The implication of sulphur formation on the availability of reaction interfaces and on the effective electrical conductivity of the particles is discussed in the next section.

### 8.6.2 Decomposition Morphology

The morphology changes which take place during direct anodic decomposition of the particles are modelled physically in Fig. 8.16. Stage I of the decomposition is represented by Eq. (8.1).



where  $\text{Cu}_{2-x}\text{S}$  includes the stoichiometry range for djurleite and digenite.

In two dimensions, the intersection of the three phases participating in the reaction, that is the starting material,  $\text{Cu}_2\text{S}$ , the reaction product,  $\text{Cu}_{2-x}\text{S}$ , and the electrolyte, is at a point. In three

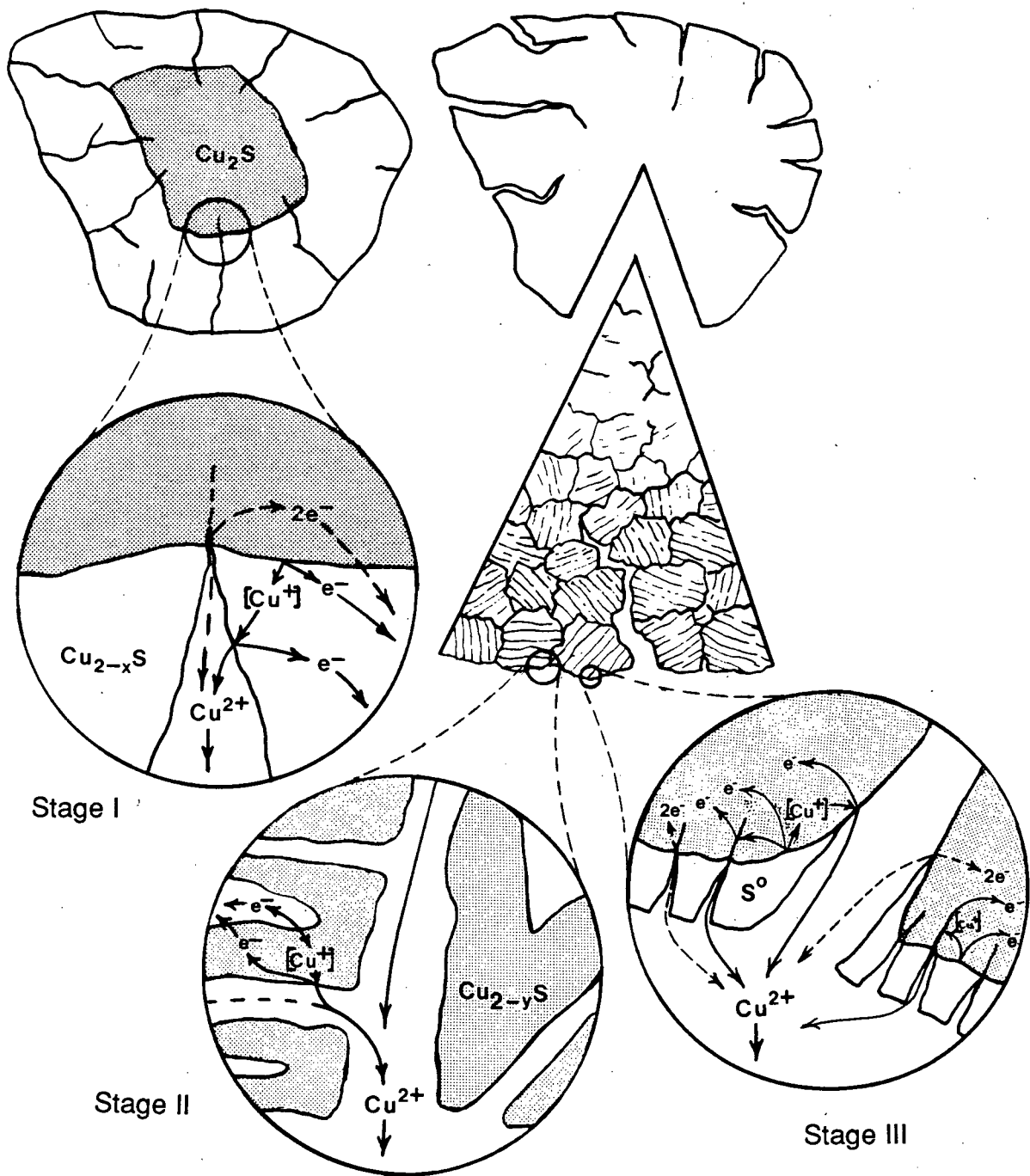
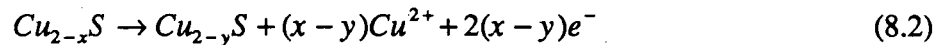


Figure 8.16 Anodic decomposition morphology model for chalcocite particles. Stage I:  $\text{Cu}_2\text{S}$  to  $\text{Cu}_{2-x}\text{S}$ ,  $(2-x) \approx 1.75$ ; stage II:  $\text{Cu}_{2-x}\text{S}$  to  $\text{Cu}_{2-y}\text{S}$ ,  $0.9 < (2-y) < 1.1$ ; stage III:  $\text{Cu}_{2-y}\text{S}$  to  $\text{S}$  at particle surfaces and to an overall composition of  $\text{Cu}_{0.35-0.50}\text{S}$ . Approximate cumulative volume reductions based on the complete phase changes  $\text{Cu}_2\text{S} \rightarrow \text{Cu}_{1.765}\text{S}$ ,  $\text{Cu}_{1.765}\text{S} \rightarrow \text{CuS}$  and  $\text{CuS} \rightarrow \text{S}$ : 7.6%, 24.4% and 43.6%, respectively.

dimensions these phases intersect along a line. But a line is one-dimensional and the reaction requires a two-dimensional surface. Therefore, the reaction probably occurs in one of two ways. At the atomic scale, the three phases may not precisely intersect. This is because  $\text{Cu}_{2-x}\text{S}$ , due to its lower molar volume than  $\text{Cu}_2\text{S}$ , is cracked and porous. Theoretically, these developing cracks should expose nonreacted  $\text{Cu}_2\text{S}$  directly to the electrolyte allowing the reaction to continue. However, the porosity of  $\text{Cu}_{2-x}\text{S}$  may not be particularly high. For example, if  $\text{Cu}_{2-x}\text{S}$  represents digenite,  $\text{Cu}_{1.76-1.83}\text{S}$ , the porosity is only 0.07 [52].

Therefore, the expectation is that an appreciable fraction of the reaction may actually occur at the  $\text{Cu}_2\text{S}$ - $\text{Cu}_{2-x}\text{S}$  interface, with the copper then moving from this interface to the  $\text{Cu}_{2-x}\text{S}$ -electrolyte interface via solid state diffusion of cuprous ions,  $\text{Cu}^+$ , through  $\text{Cu}_{2-x}\text{S}$  as shown in the figure. This solid-state diffusion mechanism was also proposed by Mao and Peters [52] in a morphology model for the acid pressure leaching of chalcocite. An interesting aspect of the solid-state diffusion model is that electrons are generated at both the  $\text{Cu}_2\text{S}$ - $\text{Cu}_{2-x}\text{S}$  and  $\text{Cu}_{2-x}\text{S}$ -electrolyte interfaces. Finally, all electrons must pass through the product layer in order to transfer to the current distributor.

Stage II of the decomposition process is represented by Eq. (8.2)



where  $(2-x) \approx 1.75$  and  $0.7 < (2-y) < 0.9$ . Decomposition of  $\text{Cu}_{2-x}\text{S}$  may lead to the grain delamination fracturing or cracking. For example, if the solid-state mobility of cuprous ions in  $\text{Cu}_{2-y}\text{S}$  is less than in  $\text{Cu}_{2-x}\text{S}$  (even though the electronic conductivity of  $\text{Cu}_{2-y}\text{S}$  is greater than that of  $\text{Cu}_{2-x}\text{S}$ ), the corrosion process must proceed in a way that minimizes the distance cuprous ions must move in the solid state. This can be physically achieved if the grain corrodes in thin layers. Reference to Fig. 8.11d shows that these layers can be very thin ( $< 1\mu\text{m}$ ).

Alternatively, due to its semi-conductor properties,  $\text{Cu}_{2-x}\text{S}$  may exhibit electrochemical anisotropy, thus corrosion may preferentially take place along one axis or plane, leading to delamination cracking of the grains. Inspection of Fig. 8.10 reveals that the orientation of delamination fracturing is random amongst the grains. This implies that orientation is probably not related to the direction of electric vectors, but rather to grain orientations.

Stage III of the decomposition model is given by Eq. (8.3)



where  $0.7 < (2-y) < 0.9$ . Sulphur formation poses two problems. Even though cuprous ions,  $\text{Cu}^{+}_{ss}$ , may be able to diffuse through the sulphur lattice to the sulphur-electrolyte interface, this diffusion process will not occur because sulphur's electrical properties prohibit it from conducting the electrons away from the sulphur-electrolyte interface that would be generated during oxidation of  $\text{Cu}^{+}_{ss}$  to  $\text{Cu}^{2+}$ . Consequently,  $\text{Cu}^{+}_{ss}$  can only be oxidized to  $\text{Cu}^{2+}$  at  $\text{Cu}_{2-y}\text{S}$ -electrolyte interfaces, and with increasing copper extraction, these interfaces become limited to the cracks and voids in the increasing coverage of the sulphur product layer. Eventually, a depletion in these interfaces leads to very high local reaction rates, which (a) quickly depletes the concentration of  $\text{Cu}^{+}_{ss}$  at the  $\text{Cu}_{2-y}\text{S}$ -electrolyte interfaces, resulting in rapid concentration "polarization" in the solid state, and/or (b) rapidly increases the Faradaic process overpotential at these interfaces. The other problem was previously discussed, that is sulphur may eventually insulate the particles from the current distributor by forming at the electrical contact points of the particles. In this case the reaction process overpotential (which includes points (a) and (b) above) remains constant, but the "contact" voltage drop at the current distributor,  $\Delta E_{1,2}$ , rapidly increases. When a mixture of these mechanisms occurs, sulphur formation at the electrical contact points between the particles and the current distributor is evidently delayed relative to its formation elsewhere within the particle and on the particle's surface, thus extending the time of electrolysis over that which would have occurred had sulphur crystallized uniformly over the entire particle surface.

In the morphology model illustrated in Fig. 8.16, the particles corrode on the macroscopic scale like the shrinking-core model, but on the microscopic scale, like a multiple-grain model [111]. Since the interior regions of the particle are always less reacted than the exterior regions, its macroscopic appearance corresponds to the shrinking-core model, as described in Sec 7.1.

### 8.6.3 Impurity Effects

#### Iron

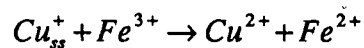
The low copper extraction from industrial matte compared to from pure synthetic copper sulphide is attributable to iron. Mattes containing iron form a finely divided bornite-djurleite eutectoid-like physical structure at all compositions above iron's solubility limit in djurleite ( $\approx 0.5\text{wt}\%$ ). This eutectoid is distributed throughout the entire volume of iron-doped mattes when the iron content approaches about  $3\text{wt}\%$ .

The presence of bornite retards the extraction of copper in several ways. Firstly, with respect to 100% copper liberation, it is a relatively nonreactive species. Secondly, due to bornite's physical association with djurleite in the eutectoid-like structure, its relative nonreactivity also essentially "ties up" a portion of the djurleite, thus preventing this phase from decomposing completely. Finally, its presence may limit the amount of fracturing, particularly the grain delamination-type fracturing, that would otherwise occur in pure synthetic chalcocite at the same copper extraction. This places a burden on reaction processes in the particle, for example, the solid state diffusion process.

Many studies on the ferric ion leaching of synthetic and natural bornite specimens [49,50,55] have shown that its decomposition takes place in several stages, as outlined in Chap. 3, Sec. 3.2.2. The first leaching stage is relatively rapid and comes to an end at a stoichiometry of about  $\text{Cu}_{5-x}\text{FeS}_4$  ( $1.2 < x < 2$ ), corresponding to about 25-40% copper extraction, although most of the reports give a value for  $x$  between 1.2 and 1.5, or 25-30% copper extraction. The general consensus is that the leaching rate is controlled in this stage by the transport rate of ferric ions to the mineral surface, but Pesic and Olson [55] reported that the rate of reduction of these ions at the mineral surface is also an important consideration. This is apparently because the availability of cuprous ions, which are considerably more mobile than the cupric species, controls the electrode potential. In fact, a charge balance on bornite,  $\text{Cu}_5\text{FeS}_4$ , shows that the five copper atoms have a total charge of +6. Therefore, 80% of these atoms are essentially the mobile cuprous species. However, a charge balance

on the reaction intermediate,  $\text{Cu}_3\text{FeS}_4$ , reveals that the three copper atoms still have a total charge of +6, with the result that all the copper atoms are the immobile cupric species. The important result is that after 40% copper extraction, mobile copper species in the structure no longer exist.

Decomposition of the intermediate,  $\text{Cu}_{5-x}\text{FeS}_4$ , is considerably slower than that of bornite. Although some reports [50] suggest a further reaction intermediate, such as chalcopyrite or a phase like idaite,  $\text{Cu}_3\text{FeS}_4$ , are formed, the relatively recent study by Pesic and Olson [55] showed that  $\text{Cu}_{5-x}\text{FeS}_4$  ( $x \approx 1.4$ ) decomposed directly to elemental sulphur. They reported a transition period between  $\text{Cu}_{5-x}\text{FeS}_4$  and  $\text{Cu}_3\text{FeS}_4$ , with the dissolution rate of the latter controlled by the diffusion rate of cuprous ions,  $\text{Cu}_{ss}^+$ , through the forming sulphur layer. This mechanism is permitted in leaching because electrons are exchanged between cuprous ions and ferric ions at the sulphur-electrolyte interfaces, as copper is transferred to the solution.



However, this mechanism is not permitted in direct electrolysis. The electrons which would be released by the cuprous ions in the solid state in producing cupric ions in the electrolyte cannot be conducted through the product sulphur layer. This was also discussed in Sec. 8.6.2. In addition, even though there may be a small concentration of iron in the electrolyte from the dissolution of iron in the djurleite phase (in the thin-bed experiments  $\leq 0.005\text{M}$  for iron-doped synthetic matte and remelted industrial matte, and  $\leq 0.02\text{M}$  for the industrial matte), the concentration of ferric ions which can be maintained in equilibrium with ferrous ions at the electrode potential which exists prior to total-bed polarization ( $\leq 0.43\text{-}0.63\text{V}$  and  $\leq 0.43\text{-}0.68\text{V}$  versus SHE for the iron-doped synthetic matte and remelted industrial matte, and for the industrial matte, respectively, using a value of  $E = 0.28\text{V}$  for  $\text{Cu}^{2+}|\text{Cu}^{+4}$ ) is probably too small to matter.

Biegler [29] reported that about 25% of the copper in bornite was extracted by direct electrolysis using a slurry anode. No further data were provided in this paper; thus, it must be inferred that 25% represented the extraction limit, probably related to anode potential.

---

4 Calculated in Appendix E for the actual concentration and temperature conditions used in this thesis.

These analyses may be applied to the electrorefining of iron-laden copper mattes as follows. Every 1wt% iron in bornite is associated with 5.69wt% copper. In an iron-laden matte containing 4.4wt% iron, approximately 90-93% of the iron appears as bornite, with the remainder appearing in solid solution in the djurleite-chalcocite phase. Thus, the copper associated with the bornite is about 23wt%. Since the total copper concentration in a 4.4wt% iron-doped matte is about 73.5wt%, the amount of copper present as djurleite is only about 50wt%. Suppose, for example, that only 25% of the copper is extracted from the bornite portion of the eutectoid, but that 80% extraction may be achieved from the djurleite phase. The overall copper extraction would then be about 5.75wt% from the bornite and 40wt% from the djurleite, for a total of 45.75wt%, or about 60% on a percentage basis. However, reference to Fig. 8.1 shows that the actual copper extraction from a 4.4wt% iron-doped matte is actually about 37%, equivalent to less than 60% extraction from the djurleite-like phase fields<sup>5</sup>. Therefore, in addition to essentially "locking-up" copper in a relatively nonreactive phase (bornite decomposition intermediate), decomposition of the iron-saturated djurleite may be impeded due to its physical association with bornite in the eutectoid structure. In other words, some djurleite may be "trapped" and unavailable for decomposition, at least beyond the amount of decomposition that may be achieved from the bornite phase. This is illustrated in Fig. 8.17, and may explain why back-scatter image analyses of reacted iron-doped particles (3-4.5wt% iron) show a phase structure which is quite similar to the structure before electrolysis. The phase structure of a reacted iron-doped particle is shown in Fig. 8.14 and may be compared with the structure of an iron-doped particle prior to electrolysis presented earlier in Fig. 8.6.

Another way to consider the detrimental role of bornite is to assume that it does not decompose at all at the electrode potentials necessary to corrode either djurleite or chalcocite. For example, Pesic and Olson [55] pointed out that the potential of the surface reaction in the first leaching stage is controlled by the labile cuprous ion concentration. This is an important consideration with respect to galvanostatic decomposition of bornite, which is the situation in this thesis. Although the ferric

---

<sup>5</sup> In fact, 37% over all copper extraction is equivalent to  $[37(73.5)-25(23)]/50$ , or only about 43% extraction from the djurleite-like phase fields.

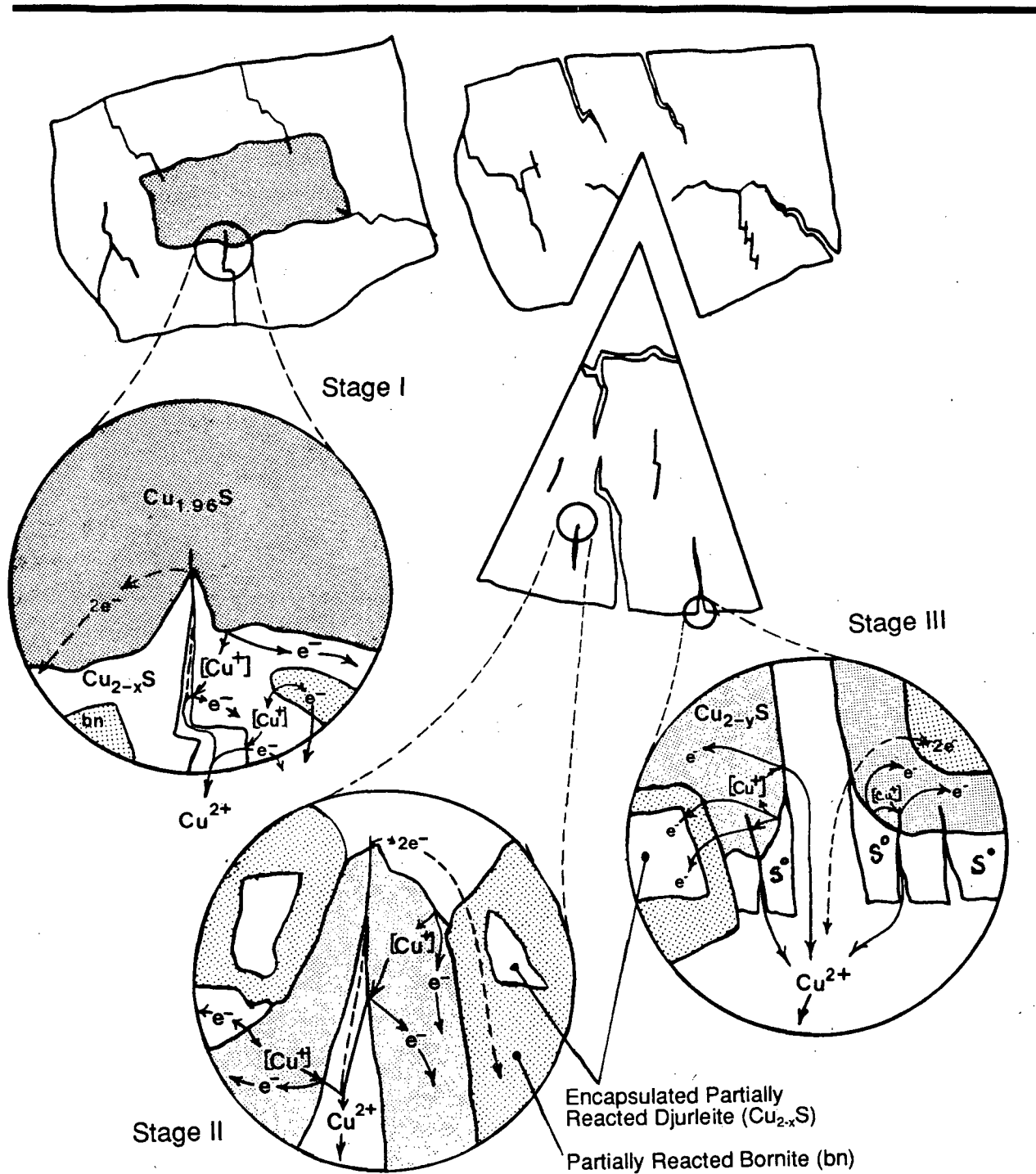


**Figure 8.17** Anodic decomposition morphology model for iron-doped synthetic copper matte particles. Note the presence of the djurleite-like phase component of the eutectoid which remains encapsulated by the nonreactive bornite-like phase during electrolysis.

ion leaching studies show that the first stage of leaching is relatively fast, the leaching potential is not reported. The reversible potential of the ferric/ferrous couple under standard conditions of unit

activities is 0.77V, which is more than 0.1V higher than the value of  $\Delta E_{4,6}$  of 0.64V (0.30V versus the  $\text{Cu}^{2+}|\text{Cu}^{\circ}$  electrode from Fig. 8.2), for the final decomposition process prior to total-bed polarization of the synthetic chalcocite anodes in this thesis.

Furthermore, Price and Chilton's data [24] suggest that direct electrolysis of bornite requires an electrode potential of 1.04V (0.8V versus a saturated calomel electrode (SCE), or 0.7V versus  $\text{Cu}^{2+}|\text{Cu}^{\circ}$ ) at  $38.5\text{A/m}^2$  and  $30^{\circ}\text{C}$  as compared to an electrode potential for chalcocite dissolution of only about 0.49V at  $250\text{A/m}^2$  and  $25^{\circ}\text{C}$  (0.25V versus SCE or 0.15V versus  $\text{Cu}^{2+}|\text{Cu}^{\circ}$ ) found by Biegler and Swift [31] (or see Fig. 3.2b). Certainly, the expectation is that the reversible potential of bornite would be higher than that of djurleite or chalcocite due to the reduced activity of copper in bornite species compared with the other species.

The  $\Delta E_{4,6}$ -time curves for the industrial matte and the synthetic matte containing the same amount of iron provide some support for this theory. The abrupt increase in total-bed potential at total-bed polarization is interrupted at a value of about 0.85-0.90V (versus  $\text{Cu}^{2+}|\text{Cu}^{\circ}$ ), a rise of about 0.55-0.60V from the pre-total-bed polarization value of about 0.3V (versus  $\text{Cu}^{2+}|\text{Cu}^{\circ}$ ), and even results in a relative plateau for the electrolysis of industrial matte. This plateau may represent the rapid acceleration of continued bornite dissolution. Unfortunately, a total-bed potential of 0.90-1.0V was defined as the "cut-off" point for practical electrolysis and chosen as the end of an experiment in this study; thus, this theory was not tightly evaluated.

Of course, by reducing the overall copper extraction, the extent of fracturing ought to be similarly reduced. But, the nonreactive bornite-like component of the eutectoid may introduce an additional effect by providing a relative resistance in the particle to fracturing, particularly the grain delamination-type fracturing. The effect of reduced fracturing is to reduce the availability of nonreacted portions of the particles to the electrolyte. This increases, for example, the burden on the cuprous ion mobility in the solid state because it must move further to arrive at an aqueous interface, and restricts the growth of new solid-electrolyte surface area. Figure 8.14 compares the extent of fracturing in an iron-doped particle with the fracturing taking place in a chalcocite particle. The reduced fracturing in the former is readily apparent.

The reaction surface area which develops during decomposition was also recognized as an important parameter by Pesic and Olson [55]. According to their report on bornite leaching, subcrystallites form near the end of the first leaching stage (as the stoichiometry approaches  $\text{Cu}_{5-x}\text{FeS}_4$ ,  $x \approx 1.4$ ), which results in a fifty-fold enhancement in surface area. Then, the transition period from this intermediate to  $\text{Cu}_3\text{FeS}_4$  was reportedly controlled by the nucleation and growth of sulphur on these new reaction surfaces, a relatively high activation energy process (18kcal/mol). Also, in this transition period, the remaining labile cuprous ions were removed, which, as reviewed by these authors, helped to release the lattice strain of  $\text{Cu}_3\text{FeS}_4$  (presumably arising from the extraction of copper).

Although elemental sulphur is produced on the relatively reactive surfaces of the particle, the electrical contact does not deteriorate significantly because there are sufficient amounts of bornite decomposition intermediates or nonreacted bornite available to act as the electrical contact points. Thus, when the relatively reactive portions of the eutectoid are depleted, the total-bed potential rapidly rises to a value necessary to begin decomposition of the bornite or its decomposition intermediate. These analyses are also applicable to the re-melted industrial matte.

However, inasmuch as iron is predominantly responsible for the poor copper recovery from industrial mattes tested in this thesis, there are several important differences between these mattes and synthetic materials containing the same amount of iron. For example, the copper extraction from industrial mattes is greater (Fig. 8.1) and the iron extraction from these mattes is greater (Fig. 8.4) than from the synthetic mattes. In addition, the acidity decreases during electrolysis of the former, as shown earlier in Table 8.1. The most probable explanation for these differences is that the industrial matte contains oxygen.

### Oxygen

The conditions in copper smelters, converters and continuous reactors are oxidizing. Biswas and Davenport [1] pointed out that the mattes produced in conventional smelting, that is, mattes containing 40-60% copper, may contain up to 3wt% oxygen. They also summarized experimental

data on the blister copper-matte-slag-magnetite system, important in the continuous production of blister copper, and stated that at 1250°C, the matte (essentially Cu<sub>2</sub>S) which is in equilibrium with the blister copper is magnetite (Fe<sub>3</sub>O<sub>4</sub>)-saturated.

The assays given in Table 4.1 for industrial matte do not add to 100%. (Analyses for the re-melted industrial material may be used when no information is given for the industrial matte). The difference is about 1-2wt% and may be attributable to oxygen. Note that the assays for the re-melted industrial matte add to 100%, thus oxygen is below the sum of analytical error limitation in the assays. Also, there are probably no other species present in significant amounts.

Since the order for oxygen affinity of the metallic species in the matte is zinc-iron-copper, the expectation is that the oxygen "dissolved" in the industrial mattes is present as oxides of zinc and iron. The zinc content is low, so most of the oxygen will be "scavenged" by the iron, provided, of course, that there is enough iron.

From the summary of Biswas and Davenport [1], it may be inferred that iron oxide is present as solid magnetite, even when the matte is in the molten state, due to its high melting point (1594°C) and insolubility in molten matte and slag. Therefore, the assumption may be made that oxygen is probably present as an iron oxide phase (except for small amounts associated with zinc or zinc ferrites [3]) in an industrial matte cooled under ambient conditions.

Table 8.1 shows that the molar ratio of acid depletion to iron liberation is approximately unity. This suggests the presence of the iron oxide phase wustite, FeO, although it is likely unresolved at the magnifications of Figs. 8.6-8.8 and 8.14. Although this oxide is probably largely associated with bornite, because this phase contains the high concentration of iron, there is undoubtedly some associated with the djurleite phase. During anodic decomposition, wustite readily dissolves chemically as it becomes exposed to the electrolyte, leading to the acidity decrease:



The argument for the presence of wustite, as opposed to magnetite, in the air-cooled mattes is that magnetite may react with sulphur in the matte during solidification and cooling. This reaction is favoured because the SO<sub>2</sub> pressure is suddenly reduced when the matte is tapped from the furnace.



Alternatively, if magnetite is the oxide phase in the mattes, the decomposition process will require electrons



which will be provided by co-decomposition of copper sulphide as in Eq. (3.14).



The electrons are exchanged *within* the particles and so are not a part of the applied current. Therefore, the decomposition of magnetite should lead to a relative increase in the anodic current efficiency and an acid depletion-iron liberation molar ratio of 1.33, provided the dissolution of iron sulphide dissolved in the djurleite phase is negligible. (This is likely the situation because very little iron is released from the iron-doped synthetic mattes as shown in Table 8.1).

Although the experimental data may not be sufficiently accurate to discriminate between these options, the important point with respect to the presence of oxygen in the mattes is unchanged: that is the amount of iron leached from the industrial matte during electrolysis is greater than from the other two iron-laden mattes because the latter mattes contain virtually no wustite or magnetite. The iron extracted from the industrial matte prior to the application of current is likely due to the dissolution of wustite or magnetite exposed directly to the solution in the matte.

If wustite stoichiometry is assumed, every 1wt% oxygen is accompanied by 3.49wt% iron, thus a significant amount of the iron in the industrial matte may be present as iron oxide. As a result, the amount of the bornite-like phase is substantially reduced and the amount of the djurleite-like phase is substantially increased relative to a synthetic matte of similar iron composition. Of course,

bornite depletion leads to a reduced amount of the eutectoid mixture. This explains why the eutectoid field does not occupy the entire area of the SEM field for the industrial matte, as may be appreciated with reference to Fig. 8.7a,c, but does for the remelted industrial matte, as shown in Fig. 8.8.

The explanation for increased copper extraction from industrial mattes relative to synthetic mattes containing the same amount of iron is now clear. In the industrial mattes, a smaller fraction of the copper is associated with the eutectoid, either as nonreactive bornite (or as a nonreactive decomposition intermediate of bornite) or physically "trapped" within the eutectoid structure, so that the amount of copper available as djurleite is greater than in the synthetic mattes.

The re-melted industrial matte behaves exactly like the synthetic matte containing the same amount of iron because oxygen is virtually eliminated during the mildly reducing re-melting treatment.

Since ferric ion leaching of bornite is reported to proceed in several stages [49,50,55] and the first of these does not release iron to the electrolyte, the question then arises as to the origin of the iron which appears in solution during electrolysis of the re-melted industrial matte and the iron-doped synthetic matte. According to an earlier analysis, about 8% of the total iron in these mattes is probably associated with the djurleite component of the eutectoid. From Fig. 8.4, the total iron extraction from the iron-doped synthetic and re-melted industrial mattes was only about 6% and 3%, respectively, and 50% of the extraction from the former occurred during the final 5-10hrs of electrolysis. Therefore, the dissolution of iron from this phase may easily account for the iron appearing in solution during electrolysis. Since the amount of iron appearing in solution is actually less than that associated with the djurleite, some iron continues to occupy interstitial sites in the sulphide lattice. This *may* result in a small decrease in the reactivity of this phase compared to pure, iron-free chalcocite.

However, the fact that some iron appears in solution before the application of any current in these tests suggests that some iron may be present in these mattes as an oxide. Possibly all the iron which is removed from these materials during electrolysis at low total-bed potentials ( $<0.3V$  versus  $Cu^{2+}|Cu^{\circ}$ ) is present as oxides. The amount of acid which would have been consumed to achieve

this was too small to measure in the cells used in this thesis. In any event, the rapid increase in the iron extraction rate during total-bed polarization indicates that iron is essentially liberated only at high total-bed potentials.

### Lead

At the concentrations studied, lead is not as serious an impurity as iron because it segregates into separate phases which do not interfere with the electrochemistry of chalcocite. The problem with the lead-rich metallics and lead sulphide is that when lead is extracted, it immediately precipitates as lead sulphate. Unfortunately, this salt is nonconductive and contributes to electrical isolation of the particles from the current source. This explains why  $\Delta E_{4,6}$  remains constant during total-bed polarization of anodes containing lead-doped mattes.

Unfortunately no information regarding the decomposition potential and relative reactivity of the metastable copper-lead-sulphur phases, such as those with stoichiometries roughly given by phase "A",  $\text{Cu}_{14}\text{Pb}_2\text{S}_{9-x}$ , are available. They might be expected to decompose at higher electrode potentials than chalcocite because the copper activity in them is certain to be reduced. This may result in a small amount of copper being inaccessible to electrolytic decomposition at practical total-bed potentials (potentials less than that at which oxygen theoretically could be discharged), thus slightly reducing the copper extraction.

The important point to remember is that the concentration of lead (on either a weight percentage or mole fraction basis) in high-grade copper mattes is expected to be very low. At  $1200^\circ\text{C}$ , near the operating temperatures of copper smelters, the vapour pressure of  $\text{PbS}$  is roughly 0.6 atmospheres [112]. Consequently, the gas phase being stripped from the matte (i.e.  $\text{SO}_2$  from the tuyere injection of oxygen) will remove  $\text{PbS}$  in proportion to its partial pressure, which will have a value equal to its vapour pressure multiplied by its activity in the matte. Therefore, the expectation is that most of the lead impurity should be eliminated by volatilization. Since the industrial matte obtained for this thesis is probably generally representative of the lead/iron ratio and iron concentration likely to be routinely achievable in commercial practice, it would appear that the

effect of 2-3wt% lead on the electrolysis of copper-rich mattes is of relatively minor importance. Furthermore, a copper matte laden with 16wt% lead can hardly be considered high-grade, thus the dissolution kinetics of lead rich phases is of academic interest.

---

## CHAPTER 9

---

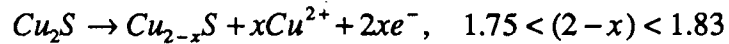
### CONCLUSIONS

The development of natural convection mass transport processes within vertical particulate anodes has been confirmed to be the key to achieving relatively high copper extraction from copper-rich mattes. This mass transport mechanism does not develop in corroding solid matte electrodes. The natural convection motion or flow is predominantly downwards through the particulate electrode, which produces vertical concentration gradients of the various ionic species within the electrode. The electrolyte flow rates necessary to achieve mass transfer from the particulate anode across the diaphragm to the bulk solution are very small, on the order of only about 2cm/min.

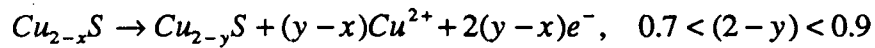
However, inasmuch as the natural convection mass transport mechanism between the particulate electrode across the diaphragm to the bulk solution is a fundamental requirement of copper matte electrorefining, other factors are ultimately more important in terms of the maximum copper extraction which may be achieved at practical total-bed potentials, and thus, the potential development of the concept into a commercial process. Other factors leading to total-bed polarization of the particulate anodes are (a) the electrical contact voltage drop which develops between the current distributor and the particles,  $\Delta E_{1,2}$ , and in thick anodes, the increasing voltage drop across the bed,  $\Delta E_{2,4}$ , (b) the relative nonreactivity of certain phases which form during the solidification

of the mattes, and (c) the physical phase association which develops during the solidification of the mattes between these nonreactive phases and the more reactive phases. The relative significance of these factors in different type of mattes is influenced by the presence and amount of lead, iron and oxygen impurities.

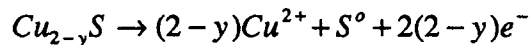
The anodic decomposition of pure synthetic chalcocite occurs may be characterized by a three stage process. Stage-one decomposition is represented by



This reaction leads to crack formation along grain boundaries and may be more or less complete before the second stage of decomposition begins to take place at significant rates:



During this stage of the electrorefining process, the individual grains begin to delaminate as copper is extracted from them. This minimizes the distance cuprous ion must diffuse in the solid state and maximizes the solid-electrolyte surface area. In the final stage of decomposition



the grain boundary and delamination fracturing increase. However, elemental sulphur formation is delayed until this reaction is about 55-60% complete, which corresponds to about 80% overall copper extraction.

Evidently, elemental sulphur formation at this point leads to total-bed polarization of the particulate electrode due to a combination of (a) the rapid deterioration of electrical contact between the particles and the current distributor, and (b) a reduction in electronically conducting solid-electrolyte reaction interfaces. These interfaces are limited to those exposed at the base of the cracks in the quickly forming the sulphur product. This condition eventually leads to a rapid rise in the reaction-process overpotential (such as concentration "polarization" caused by the depletion of cuprous ion in the solid state).

When lead is present in a synthetic copper sulphide at concentrations typical of high-grade mattes (<5wt% by weight) the copper extraction is only modestly reduced. For example, the copper extraction from mattes containing about 4.8wt% lead is slightly over 70%. This is because lead segregates into several different phases which are dispersed throughout the chalcocite main phase and do not interfere with the decomposition of the chalcocite. Copper extraction is limited by deteriorating electrical contact between the current distributor and the particles due to the formation of elemental sulphur and insoluble lead sulphate. The latter precipitates during oxidation of lead-containing inter-metallics and of lead sulphide phases. These effects are additive and contribute to the reduced copper extraction.

Some copper is associated with the lead in copper-lead-sulphur phases, which are probably thermodynamically unstable with respect to disproportionation to PbS and Cu<sub>2</sub>S. The electrochemistry of such phases has not been studied. However, the expectation is that they may be more difficult to decompose than chalcocite since the copper activity in them is certain to be reduced. This may essentially "tie-up" a small amount of the copper, making it unavailable for decomposition at low total-bed potentials.

At concentrations typical of high-grade mattes ( $\approx$ 3-5wt% by weight), iron is a much more detrimental impurity than lead because it forms a finely divided eutectoid-like structure, composed of (a) a djurleite-chalcocite solid solution saturated in iron ( $\approx$ 0.5wt%), and (b) a bornite-like phase. Unfortunately, the latter phase is relatively nonreactive. This makes a portion of the copper inaccessible to decomposition at practical total-bed potentials (below the potential at which oxygen theoretically may be discharged). In addition, mattes doped with 3-5wt% iron do not appear to develop significant grain fracturing, perhaps due to the physical structure of the eutectoid, which results in the encapsulation or "trapping" of modest amounts of the more reactive djurleite-like phase in the eutectoid-like structure, thus restricting the copper extraction from these "trapped" phase volumes to the level of extraction from the bornite phase. The copper extraction from mattes containing 3-5wt% iron is only about 35-40%.

The presence of oxygen in iron-laden mattes is beneficial in terms of copper extraction because iron preferentially sequesters oxygen, thereby reducing the amount of the eutectoid. Unfortunately, mattes containing oxygen consume acid, through leaching of the iron oxide phases, which, of course, leads to an acid balance problem and the release of iron to the electrolyte.

The effective electrical conductivity of the particulate matte anode at the start of electrolysis is slightly less than or approximately equal to the effective conductivity of the electrolyte. As a result, an appreciable portion of the decomposition process occurs adjacent to the current distributor when the current is first switched on. However, the conductivity of the corroding matte increases dramatically during the first several hours of electrolysis as copper is extracted, despite the fracturing which takes place in the particles. Consequently, the decomposition process quickly becomes distributed across the anode toward the diaphragm. Thereafter, the decomposition process remains relatively uniformly distributed, with the variation in copper extraction across a 2cm-thick anode equal to less than a factor of two. This low variation is attributable to (a) the high conductivity of the electrolyte which minimizes reaction-process overpotential gradients across the anode, and (b) the increasing impedances of the decomposition processes in the most reacted particles.

---

## CHAPTER 10

---

### OPPORTUNITIES FOR FURTHER STUDY

The natural convection mass transport of ionic species within a vertical particulate electrode was studied sufficiently rigorously to propose a predictive relationship, such as those reviewed in Chap. 3, Sec. 3.8. While such a study was originally envisioned, it was abbreviated so as to study other factors which were found ultimately to be more important in terms of the potential development of the concept into a commercial process. However, such a study may prove fruitful in terms of evaluating, for example, how much mixing actually occurs across the diaphragm as a function of the vertical position and diaphragm porosity and, since a significant portion of the convective flow is downwards through the anode compartment, over what vertical portions of the diaphragm this mixing results in a net flow of electrolyte into and then out of the anode.

Since the ultimate copper extraction from synthetic chalcocite appears to be about 80%, it is likely that this process may not be developable into a commercial process, at least not without careful consideration of methods to recover the remaining copper from the electrorefining residues, since these residues contain both unrecovered copper and the precious metals. Nevertheless, there are several areas in which an understanding of copper-rich matte electrolysis in particulate electrodes may be improved.

All experiments in this thesis were performed at a single ratio of current density to bed thickness ( $200\text{A}/\text{m}^2\cdot\text{cm}$  or about  $0.84\text{A}/\text{m}^2\cdot\text{g}$ ). Since the termination of chalcocite and lead-doped

synthetic chalcocite electrolysis is apparently related to elemental sulphur formation, the ultimate copper extraction is then dependant upon how long its formation, or at least the effect of its formation on the decomposition process, can be delayed after 50% copper removal has been achieved. At high current densities, the concentration gradients of cuprous ion in the solid state are high. Therefore, the copper sulphide phase adjacent to the electrolyte quickly becomes depleted in copper, resulting in sulphur formation. Unfortunately, at high current densities, a small amount of sulphur formation leads to high reaction-process resistances and/or to high electrical contact resistances, and the anode "polarizes". If the current density is very low, the burden of solid state diffusion of cuprous ions to the decreasing reaction surface areas is low, but the copper sulphide phase  $\text{Cu}_{2-y}\text{S}$ , with  $(2-y) < 1.0$ , is only metastable and could readily disproportionate to  $\text{CuS}$  and  $\text{S}$ . The balance between these effects should be considered if further research into copper matte electrorefining is undertaken.

This study has shown that the electrolytic decomposition of high grade copper mattes is impeded by the presence of copper-iron-sulphur phases and the physical association of these phases with the reactive copper-sulphur phase. Switching of the electrolysis mode for iron-laden mattes from galvanostatic to potentiostatic during total-bed polarization may provide some information on the reactivity of these copper-depleted materials at specific high anode potentials. If copper-rich mattes containing 3-4% iron are not quenchable, and some reports [59-61] suggest that this may be so, then further work on copper matte electrolysis must focus on mattes low in iron, perhaps less than 1%.

Oxygen is probably an inevitable component of an industrial matte and an important impurity in terms of copper extraction, thus the effect of this species should be studied if future research on copper matte electrorefining is undertaken, particularly if commercial mattes low in iron are to be employed.

The effect of particle size should also be considered in future studies. As the particle size is increased, the expectation is that both the contact resistance and mass transfer within the particles are likely to be of increasing importance. As the particle size is decreased, the expectation is that natural convection mass transfer within the bed may be impaired.

---

## REFERENCES

---

1. Biswas A.K., Davenport W.G., "Extractive Metallurgy of Copper", an International Series on Science and Technology, Vol 20, Pergaman Press, 1976.
2. Cooper W.C., "Recent Developments in the Extractive Metallurgy of Copper, Nickel and Cobalt and Their Industrial Applications", *Can. Met. Q.*, **23**, 365-375, (1984).
3. Peters E., Private discussions during development of this thesis.
4. Mao M.H., Peters E., "Direct Electrorefining of Cuprous Sulphide Based Particulate Anodes", *Can. Met. Q.*, **22**, 437-446, (1983).
5. Etienne A., "Electrochemical Aspects of the Aqueous Oxidation of Copper Sulphides", PhD Thesis, University of British Columbia, 1970.
6. Peters E., "The Electrochemistry of Sulphide Minerals", from Trends in Electrochemistry, ed. Bockris J.O.M., Rand D.A.J., Welch B.J., Plenum Publishing Corporation, 1977.
7. Habashi F., "The Electrometallurgy of Sulphides in Aqueous Solutions", *Miner. Sci. Engng.*, **3**, 3-12, (1971).
8. Brennet P., Jafferli S., Vanseveren J.M., Vereecken J., Winand R., "Study of the Mechanism of Anodic Dissolution of  $\text{Cu}_2\text{S}$ ", *Met. Trans.*, **5**, 127-134, (1974).
9. Abe S., Burrows B.W., Ettl V.A., "Anode Passivation in Copper Refining", *Can. Met. Q.*, **19**, 289-296, (1980).
10. Renzoni L.S., McQuire R.C., Barker W.V., "Direct Electrorefining of Nickel Matte", *J. Metals*, **10**, 414-418, (1958).
11. Spence W.W., Cook W.R., "The Thompson Refinery", *Can. Inst. Min. Metal.*, **67**, 257-267, (1964).
12. Boldt J.R. Jr., "The Winning of Nickel, Its Geology, Mining and Extractive Metallurgy", Longmans Canada Limited, 1967 (p. 363).
13. Ettl V.A., Tilack B.V., "Electrolytic Refining and Winning of Metals", Chapter 6 of Comprehensive Treatise of Electrochemistry, vol 2, ed Bockris J.O.M. Plenum Press, 1980.
14. Mahamond M.N., Page P.W., Turner A.K., Fogarty P.O., Spencer J.E.D., "Nickel Recovery from Sulphide Concentrates by Slurry Electrolysis", paper presented at the Reinhardt Schuhmann Int. Symp. on Innovative Technology and Reactor Design in Extractive Metallurgy, Colorado Springs, Colorado, November 9-12, 1986.
15. Inami T., Tsuchida N., Tomoda K., Shigemura H., "Studies on Anodic Dissolution of Nickel Sulphides in the Nickel Matte Electrolysis", CIM 25th Annual Conference of Metallurgists, August 17-20, Toronto, Ontario, 1986.

16. Inami T., Ishikawa Y., Tsuchida N., Hirao M., "Effect of (the) Slime Layer on the Anodic Potential in Nickel Matte Electrorefining", 1988 AIME Annual Meeting.
17. Power G.P., "The Electrochemistry of the Nickel Sulphides-2", *Electrochimica Acta.*, **27**, no3, 359-364, (1982).
18. Parker A.J., Paul R.L., Power G.C., "Electrochemical Aspects of Leaching Copper from Chalcopyrite in Ferric and Cupric Salt Solutions", *Aust. J. Chem.*, **34**, 13-34, (1981).
19. Beigler T., Swift D.A., "Anodic Electrochemistry of Chalcopyrite", *J. Appl. Electrochem.*, **9**, 545-554, (1979).
20. Jones D.L., Peters E., "Electrochemical Experiments With Chalcopyrite Electrodes in Aqueous Solutions", *NACE-4*, 443-458, (1976).
21. Wadsworth M.E., "Sulphide and Metal Leaching Reactions", *Min. Eng.*, **37**, 557-562, (1985).
22. Everett P.K., "The Dextec Copper Process", *Proc. Symp. Extr. Metal.*, 1981, *Inst. Min. Metal.*, London, 1981
23. Spencer P.A., "The Electrolysis of Metals and Metal Sulphides in Chloride Solutions", PhD Thesis, University of New South Wales, Australia, 1980
24. Price D.C., Chilton J.P., "The Electroleaching of Bornite and Chalcopyrite", *Hydrometallurgy*, **5**, 381-394, (1980).
25. Stankovic Z.D., "Anodic Oxidation of the Pulverized Chalcopyrite as the Packed Bed Electrode", *Copper*, **37**, 3-7, (1984).
26. Beigler T., Swift D.A., "The Electrolytic Reduction of Chalcopyrite in Acid Solution" *J. Appl. Electrochem.*, **6**, 229-235, (1976).
27. Beigler T., Constable D.C., "Continuous Electrolytic Reduction of a Chalcopyrite Slurry", *J. Appl. Electrochem.*, **7**, 175-179, (1977).
28. Beigler T., Swift D.A., "Upgrading and Activation of Chalcopyrite Concentrates by Slurry Electrolysis", *Trans. Inst. Min. Metal.*, **85**, C23-C29, (1977).
29. Beigler T., "Sulphide Mineral Electrolysis: A Practical Way to Extract Metals from Minerals?", *Chem. Aust.*, **44**, 193-197, (1977).
30. Felker D.L., "Electrochemical Dissolution of Copper Sulphides Using a Fluidized Bed Electrochemical Reactor", PhD Thesis, Iowa State University, 1974.
31. Beigler T., Swift D.A., "Dissolution Kinetics of Copper Sulphide Anodes", *Hydrometallurgy*, **2**, 335-349, (1976/77).
32. Hojo M., Peters E., "Direct Electrorefining of Chalcocite", *J. Electroanal. Chem.*, **118**, 245-364, (1981).

33. MacKinnon D.J., "Fluidized Bed Anodic Dissolution of Chalcocite", *Hydrometallurgy*, **1**, 241-257, (1976).
34. Hillrichs E., Bertram R., "Anodic Dissolution of Copper Sulphides in Sulphuric Acid Solution I. The Anodic Decomposition of  $Cu_{2-x}S$ ", *Hydrometallurgy*, **11**, 181-193, (1983).
35. Venkatachalam S., Mullikarjunan R., "Direct Electrorefining of Cuprous Sulphide and Copper Matte", *Trans. Inst. Min. Metal.*, **77**, C45-C52, (1986).
36. Mehendale S.G., Venkatachalam S., Mallikarjunan R., "Studies on the Anodic Dissolution of Copper Matte", *Hydrometallurgy*, **9**, 195-204, (1982).
37. Frenay J.N., "Direct Electrorefining of Copper Matte", *Ind. Chem. Eng. Symposium Series* no. 42, 1975.
38. Habashi F., Torres-Acuna N., "The Anodic Dissolution of Copper I Sulphide and the Direct Recovery of Copper and Elemental Sulphur from White Metal", *Trans. AIME*, **242**, 780-787, (1968).
39. Muir D.M., Parker A.J. Giles E., "Cuprous Hydrometallurgy Part IV: Rates and Equilibria in the Reaction of Copper Sulphides with Copper II Sulphate in Aqueous Acetonitrile", *Hydrometallurgy*, **2**, 127-140, (1976).
40. Hand Book of Chemistry and Physics, 60th edition.
41. Gebhardt J.E., McCarron J.J., Richardson P.E., Buckley A.N., "The Effect of Cathodic Treatment on the Anodic Polarization of Copper Sulphides", *Hydrometallurgy*, **17**, 27-28, (1986).
42. Koch D.F.A., McIntyre R.J., "The Application of Reflectance Spectroscopy to a Study of the Anodic Oxidation of Cuprous Sulphide", *J. Electroanal. Chem.*, **71**, 285-296, (1976).
43. Potter R.W., "An Electrochemical Investigation of the System Copper-Sulphur", *Econ. Geol.*, **72**, 1524-1542, (1977).
44. Price D.C., "Application of Chronopotentiometric Analysis to the Anodic Treatment of Copper Sulphides", *Met. Trans. B*, **12B**, 231-239, (1981).
45. Hillrichs E., Bertram R., "Anodic Dissolution of Copper Sulphides in Sulphuric Acid Solution II. The Anodic Decomposition of  $CuS$ ", *Hydrometallurgy*, **11**, 195-206, (1983).
46. Crundwell F.K., "The Influence of the Electronic Structure of Solids on the Anodic Dissolution and Leaching of Semiconducting Sulphide Minerals", *Hydrometallurgy*, **21**, 155-190, (1988).
47. Ghali E., Dandapani B., Lewenstam A., "Electrodissolution of Synthetic Covellite in Hydrochloric Acid", *J. Applied Electrochem.*, **12**, 369-376, (1982).
48. Seidell A., Linke W.F., Solubilities of Organic and Metal Inorganic Compounds, Amer. Chem. Soc., 1965.

49. Dutrizac J.E., MacDonald R.J.C., "Ferric Ion as a Leaching Medium", *Miner. Sci. Engng.*, **6**, no.2, 59-100, (1974).
50. Dutrizac J.E., MacDonald R.J.C., Ingraham T.R., "Effect of Pyrite, Chalcopyrite and Digenite on the Rate of Bornite Dissolution in Acidic Ferric Sulphate Solutions", *Can. Met. Q.* **10**, no1, 3-7, (1971).
51. Marcantonio J.P., PhD Thesis, University of Utah, 1976.
52. Mao M.H., Peters E., "Acid Pressure Leaching of Chalcocite", *Hydrometallurgy Research, Development and Plant Practice, proceedings of the 3rd International Symposium on Hydrometallurgy, Atlanta Georgia, March 6-10, 1983.*
53. Wadsworth M.E., "Electrochemical Processes in Leaching", *proceedings of the Darken Conference on Physical Chemistry in Metallurgy, Monroville, Pennsylvania, August 23-25, 1976.*
54. King J.A., Burkin A.R., Ferreira R.C.H., "Leaching of Chalcocite by Acidic Ferric Chloride Solutions", from *Leaching and Reduction in Hydrometallurgy 36-38*, A.R. Burkin ed., *Inst. Mining Metal.*, 1975.
55. Pesic B., Olson F.A., "Leaching of Bornite in Acidified Ferric Chloride Solutions", *Met. Trans. B*, **14B**, 577-588, (1983).
56. Roseboom E.H. Jr., "An Investigation of the System Cu-S and Some Natural Copper Sulphides Between 25°C and 700°C", *Econ. Geol.*, **61**, 641-672, (1966).
57. Massalaski T.B., p956 of Binary Alloy Phase Diagrams, VolII, Am. Soc. Metals, Ohio, 1986.
58. McKinstry H., "Mineral Assemblages in Sulphide Ores: The System Cu-Fe-S-O", *Econ. Geol.*, **54**, no.6, 975-1001, (1959).
59. Kullerud G., "The  $Cu_9S_5$ - $Cu_5FeS_4$  Join", *Carnegie Inst. Wash. Year Book*, **59**, 114-116, (1960).
60. Yund R.A., Kullerud G., "The Cu-Fe-S System: Phase Relations at 700°C", *Carnegie Inst. Wash. Year Book*, **59**, 111-114, (1960).
61. Yund R.A., Kullerud G., "Thermal Stability of Assemblages in the Cu-Fe-S System", *J. Petrol.*, **7**, no.3, 454-488, (1966).
62. Craig J.R., Kullerud G., "The Cu-Pb-S System", *Carnegie Inst. Wash. Year Book*, **65**, 342-344, (1965-66).
63. Craig J.R., Kullerud G., "Phase Relations and Mineral Assemblages in the Copper-Lead-Sulphur System", *Amer. Mineral.*, **53**, 145-161, (19).
64. Kopylov N.I., Toguzov S.M., Yarygin V.I., Kalganov I.M., "The Phase Diagram of the  $Cu_{2-x}S$ -PbS System", *Russian Metallurgy*, **3**, 226-228, (1976).
65. Brett R., Kullerud G., "The Fe-Pb-S System", *Econ. Geol.*, **62**, 354-369, (1967).

66. Craig J.R., Kullerud G., "The Cu-Pb-Fe-S System", Carnegie Inst. Wash. Year Book, **65**, 334-352, (1965-66).
67. Kostav I., Mineralogy, (part II of Systematic Mineralogy), p. 151-153, Oliver and Boyd, London, 1968
68. Nickless, Inorganic Sulphur Chemistry, p. 725-726, Elsevier, 1968
69. Karabelas A.J., Wegner T.H., Hanratty T.J., "Use of Asymptotic Relations to Correlate Mass Transfer Data in Packed Beds", Chem. Eng. Sci., **26**, 1581-1589, (1971).
70. Treybal R.E., Mass Transfer Operations, (p 74, 204), 3rd ed., McGraw Hill, 1980.
71. Fahidy T.Z., "The Estimation of Mass Transfer Coefficients", Chapter 4 of Principles of Electrochemical Reactor Analysis, Chem. Eng. Mono. 18, Elsevier 1985.
72. Patrick M.A., Wragg A.A., Pargeter D.M., "Mass Transfer by Free Convection During Electrolysis at Inclined Electrodes", Can. J. Chem. Eng., **55**, 432-438, (1977).
73. Gendron A.S., Ettl J.A., "Hydrodynamic Studies in Natural and Forced Convection Electrowinning Cells", Can. J. Chem. Eng., **53**, 36049, (1975).
74. Ibl N., Muller R.H., "Studies of Natural Convection at Vertical Electrodes", J. Electrochem. Soc., **105**, 346-353, (1958).
75. Fouad M.G., Ibl N., "Natural Convection Mass Transfer at Vertical Electrodes Under Turbulent Flow Conditions", Electrochimica Acta., **3**, 233-243, (1960).
76. Denpo K., Teruta S., Fukunaka Y., Kondo Y., "Turbulent Natural Convection Along a Vertical Electrode", Met. Trans. B, **14**, 633-643, (1983).
77. Wilke C.R., Eisenburg M., Tobias C.W., "Correlation of Limiting Currents Under Free Convection Conditions", J. Electrochem. Soc., **100**, 513-523, (1953).
78. Ettl V. "Fundamentals of Electrochemistry", Chapter 3 of Hydrometallurgy: Theory and Practice Course Notes, Centre for Metallurgical and Process Engineering, Department of Metals and Materials Engineering, University of British Columbia, 1986
79. Sedamed G.N., Mansour I.A.S., El-Sherify T.H., Hussein A.K., "Natural Convection Mass Transfer at Spheres", J. Appl. Electrochem., **14**, 91-95, (1984).
80. Smith A.J.F., Wragg A.A., "An Electrochemical Study of Mass Transfer in Free Convection at Vertical Arrays of Horizontal Cylinders", J. Appl. Electrochem., **4**, 219-228, (1974).
81. Wragg A.A., "Free Convection Mass Transfer at Mesh Electrodes", Int. J. Heat Mass Trans., **11**, 979-984, (1968).
82. Wragg A.A., "Natural Convection at Planer and Mesh Electrodes in the Ferro-Ferricyanide System", J. Appl. Electrochem., **7**, 363-365, (1977).

83. Mendebaum J.A., Bohm J., "Mass Transfer in Packed Beds at Low Reynolds Numbers", *Chem. Eng. Sci.*, **28**, 569-576, (1973).
84. Alkire R., Plichta R., "Natural Convection Within Porous Electrodes During Electrolysis", *J. Electrochem. Soc.*, **120**, no 8, 1060-1066, (1973).
85. Newman J., Teidman W., "Porous Electrode Theory with Battery Applications", *AIChE J.*, **17**, 25-41, (1975).
86. Newman J.S. Tobias C.W., "Theoretical Analysis of Current Distribution in Porous Electrodes", *J. Electrochem. Soc.*, **109**, 1183-1191, 1962.
87. Newman J., "Engineering Design of Electrochemical Systems", *Ind. Eng. Chem.*, **60**, 12-27, (1968).
88. Rousar I., Micka K., Kimla A., "Transport Equations for Concentrated Electrolytes", Chapter 2 of Electrochemical Engineering 1", *Chem. Eng. Mono.* 21, Elsevier, 1986.
89. Alkire R., Place B., "Transient Behavior During Reactant Depletion in Porous Electrodes", *J. Electrochem. Soc.*, **119**, 1687-1692, (1972).
90. Simonsson D., "Current Distribution in the Porous Lead Dioxide Electrode", *J. Electrochem. Soc.*, **120**, 151-157, (1973).
91. Simmonson D., "A Mathematical Model for the Porous Lead Dioxide Electrode", *J. Appl. Electrochem.*, **3**, 261-270, (1973).
92. Scott K., "Short Communication on the Effectiveness of Particulate Bed Electrodes Under Activation Control", *Electrochimica Acta.*, **27**, no.3, 447-451, (1982).
93. Scott K., "The Role of Diffusion on the Performance of Porous Electrodes", *J. Appl. Electrochem.*, **13**, 709-724, (1983).
94. Scott K., "The Influence of Mass Transport on the Effectiveness of Particulate Bed Electrodes", *Electrochimica Acta.*, **28**, no.9, 1191-1200, (1983).
95. Vershinin N.N., Malov Yu I., Nadkina S.E., "Electrochemical Study of Copper Sulphides", *Inst. New Chem. Prob., Academy of Sci. of the USSR, Moscow*, Translated from *Élektrokhimiya*, **21**, no 1, 111-113, (1985).
96. Bougnot J., Guastavino F., Luguët H., Sodini D., "On the Electrical Properties of  $Cu_xS$ ", *Phys. Stat. Sol.(a)*, **8**, K93-K96, (1971).
97. Okamoto K., Kawai S., "Electrical Conduction and Phase Transition of Copper Sulphides", *Jap. J. Appl. Phys.*, **12**, no 8, 1130-1138, (1973).
98. Kamigaichi T., "Electrical Conductivity of  $Cu_{1.8}S(Cu_9S_5)$ ", *J.Sci. Hiroshima Univ.*, **A16**, 325-330, (1952).
99. Shuey R.T., Semiconducting Ore Minerals, Elsevier, 1975.

100. Price D.C., Davenport W.G., "Physio-Chemical Properties of Copper Electrorefining and Electrowinning Electrolytes", *Met. Trans.B*, **12B**, 639-643, (1981).
101. Claessens P., Private Discussions, January 17, 1989.
102. SGS, General Testing Laboratories, Vancouver, B.C., October 28, 1987, February 17, May 18 and July 20, 1989.
103. Taggart A.E., Handbook of Mineral Dressing, John Wiley and Sons Inc., sec. 19.7, 70-71, 1945.
104. Mica K., "Theory of Polarization of Porous Electrodes", Chap. 6 in Fuel Cell Systems, Advances in Chemistry Series 47, American Chemical Society, 1965.
105. Goodridge F., Wright A.R., "Porous Flow-Through and Fluidized Bed Electrodes", Chap. 6 in Comprehensive Treatise of Electrochemistry Vol.6, eds. Yeager, Conway, Bockris, Sarangapani, Plenum Press, 1980.
106. Meredith R.E., Tobias C.W., "Evaluating the Effective Resistances of Diaphragms and Electrolytic Separators", *J. Electrochem. Soc.*, **110**, no.12, 1257-1260, (1963).
107. Koh J.C.Y., Fortini A., "Prediction of Thermal Conductivity and Electrical Resistivity of Porous Metallic Materials", *Int. J. Heat Mass Transfer*, **16**, 2013-2021, (1973).
108. Katan T., Bauman H.F., "Relating Structural Variables of Porous Electrodes", *J. Electrochem. Soc.*, **122**, 77-80, (1975).
109. MacMullin R.B., Muccini G.A., "Characteristics of Porous Beds and Structures", *AIChE J.*, **2**, no.3, 393-403, (1956).
110. Peters E., "Leaching of Sulphides", from Advances in Mineral Processing, Chap. 26, Conference Proceedings, Society of Mining Engineers, Littleton, Colorado, ed. Somasondairan, 1986.
111. Szekeley J., Evans J.W., "Studies in Gas-Solid Reactions: PartI. A Structural Model for the Reaction of Porous Oxides with a Reducing Gas", *Met. Trans.* **2**, 1691-1710, (1971).
112. Yazawa A., Azakami T., "Thermodynamics of Removing Impurities During Copper Smelting", *Can. Met. Q.*, **8**, no.3, 257-261, (1969).
113. Hotlos J., Jaskula M., "Densities and Viscosities of  $\text{CuSO}_4\text{-H}_2\text{SO}_4\text{-H}_2\text{O}$  Solutions", *Hydrometallurgy*, **21**, 1-7, (1988).
114. Baes C.F., "The Estimation of Bisulphate Ion Dissociation in Sulphuric Acid-Sodium Sulphate Solutions", *J. Am. Chem. Soc.*, **79**, 5611-5617, (1975).
115. Marshall W.L., Jones E.V., "Second Dissociation Constant of Sulphuric Acid from 25 to 350° Evaluated from Solubilities of Calcium Sulphate in Sulphuric Acid Solutions", *J. Phys. Chem.*, **70**, no 12, 4028-4040, (1966).

116. Meissner H.P., Kusik C.L., "Electrolyte Activity Coefficients in Inorganic Processing", from Fundamental Aspects of Hydrometallurgical Processes, AIChE Symp. Ser., 74, no174, 14-20, (1978).
117. Meissner H.P., "Prediction of Activity Coefficients of Strong Electrolytes in Aqueous Systems", from Thermodynamics of Strong Aqueous Systems with Industrial Applications, Am. Chem. Soc. Symp. Ser. 133, Am. Chem. Soc., 495-511, (1980).
118. Tozawa K., Sasaki K., "Effect of Coexisting Sulphates on Precipitation of Ferric Oxide from Ferric Sulphate Solutions at Elevated Temperatures", Proceedings on Iron Control in Hydrometallurgy, Metallurgical Society of the CIM, Toronto, Canada, October 19-27, 1986.
119. Bates R.G., Staples B.R., Robinson R.A., "Ionic Hydration and Single Ion Activities in Unassociated Chlorides at High Ionic Strengths", *Anal. Chem.*, 42, no8, 867-871, (1970).
120. Sillen L.G., Stability Constants of Metal-Ion Complexes, The Chemical Society, London, 1967.
121. Helgeson H.C., "Thermodynamics of Complex Dissociation in Aqueous Solutions at Elevated Temperatures", *J. Phys. Chem.*, 71, no 10, 3121-3136, (1966).
122. Majima H., Peters E., Awakura Y., Park S.K., "Electrical Conductivity of Acidic Sulphate Solution", *Met. Trans. B*, 18B, 41-47, (1987).
123. Majima H., Peters E., Awakura Y., Park S.K., Aoki M., "Electrical Conductivity of Chloride Sulphate Solution", *Met. Trans. B*, 19B, 53-57, (1988).
124. Levenspiel O., Chemical Reaction Engineering (2nd edition), Chap. 12, John Wiley and Sons, 1972.
125. King E.H., Alla D.M., Pankratz L.B., "Thermodynamic Properties of Copper and Its Organic Compounds", US Bureau of Mines Thermodynamic Laboratory
126. Criss C.M., Cobble J.W., "The Thermodynamic Properties of High Temperature Aqueous Solutions. IV. Entropies of the Ions up to 200°C and the Entropy Correspondance Principle", *J. Electrochem. Soc.*, 86, 5385-5390, (1964).
127. Criss C.M., Cobble J.W., "The Thermodynamic Properties of High Temperature Aqueous Solutions. V. The Calculation of Ionic Heat Capacities up to 200°C. Entropies and Heat Capacities above 200°C", *J. Electrochem. Soc.*, 86, 5390-5393, (1964).
128. Kelly K.K., "Contributions to the Data on Theoretical Metallurgy", Bureau of Mines Bull. 584, US Government Printing Office, Washington, 1960.

---

## APPENDIX A

---

### CHEMICAL ANALYSIS OF COPPER MATTES

For the electrogravimetric method (EG), 0.25-0.3g of powdered sample was digested in 10ml of a 2:1 HNO<sub>3</sub>-HCl solution, while for the atomic absorption analyses (AA), 0.7-0.9g of powdered sample was digested in 30-40ml of a 1:1 HNO<sub>3</sub>-HCl solution. All digestions were performed using low heat; elemental sulphur produced during the digestion was oxidized with bromine under very low heating conditions.

The EG solutions were boiled until near dryness, and allowed to cool prior to addition of 10ml of concentrated H<sub>2</sub>SO<sub>4</sub> were added. This mixture was heated to liberate sulphuric acid fumes, cooled and carefully diluted to about 60ml with deionized water. When lead was present in the matte, the solutions were filtered into a 150ml electrolytic beaker through Schlecher & Schuell analytic filter paper (12.5cm 100 circle, lot no. R01-5469) to remove the insoluble lead salts and diluted to 100-125ml. The other solutions were transferred directly to 100ml electrolytic beakers and diluted to 80-90ml. A platinum gauze cathode and platinum wire anode were inserted into the beakers. The electrolysis current was initially set at about 0.5-1amp, but was increased to 2-3amp after a period of about 1-2min.

Since the EG method consisted essentially of weighing the amount of copper from the digested sample which had plated onto platinum gauze electrodes, it was important that the deposit adhered properly. This was achieved by adding about 3mls of a 10wt% HNO<sub>3</sub> solution to the plating solutions. For samples containing iron, the ferric/ferrous couple, which would otherwise have prevented complete copper extraction from the plating solutions, was controlled by complexing the ferric ion with additions of tartaric acid (added as crystals).

The platinum gauze electrodes were prepared by double rinsing in both deionized water and in alcohol, "flamed" in a gas flame and weighed. Copper extraction from the plating solutions was complete when hydrogen began discharging on the platinum electrode. The electrodes were then quickly removed from the solution, double rinsed in both deionized water and alcohol, dried and weighed. The solutions were then analyzed for copper by AA to verify that all the copper had been recovered. Generally, the amount of copper remaining in the plating solutions was negligible.

The AA procedure is well known. Analyses were performed in the 0-20mg/l range. It is worth pointing out that 10-20mls of 250g/l NaCl solution were added during the first dilution of lead containing solutions to ensure that lead did not precipitate during subsequent dilutions. Also, to improve the AA results, copper was run on the AA, and the ratio of EG to AA analyses was applied to correct the iron, lead and zinc assays.

All EG and AA assays were performed in duplicate. The accuracy of the AA technique was evaluated by comparing copper AA analyses with copper ETDA titration analyses on two solutions. The comparison is reviewed in Table A.1 and shows the AA results to be accurate to about 2%.

**Table A.1** Comparison of Atomic Absorption and EDTA titration analyses for copper. Analyses are in g/l.

Sample	by AA	by EDTA	Error %
45E	44.9	45.6	+1.6
46E	44.4	45.4	+2.2
1000mg/l AA standard		1000.9	

---

## APPENDIX B

---

### ESTIMATION OF TRANSPORT NUMBERS

The estimation of transport numbers for  $\text{Cu}^{2+}$ ,  $\text{SO}_4^{2-}$ ,  $\text{HSO}_4^-$  and  $\text{H}^+$  which follows is based on several assumptions.

1. The equivalent ionic conductance,  $\lambda_i^\circ$ , of all ionic species except  $\text{H}^+$  may be calculated using Walden's rule, that is  $\lambda_i^\circ \mu^\circ$  ( $\mu^\circ$  is the electrolyte viscosity) is equal to a constant, and that the equivalent ionic conductances of  $\text{HSO}_4^-$  and  $\text{SO}_4^{2-}$  are equal. Furthermore, the assumption will be made that Walden's rule may be applied in concentrated solutions, that is  $\lambda_i \mu$  is equal to a constant.
2. The equivalent ionic conductance of  $\text{H}^+$  is related to the activity of water in the electrolyte.
3. The transport number is defined as

$$t_i = \frac{z_i \lambda_i C_i}{\sum z_i \lambda_i C_i}$$

where  $C_i$  is the actual concentration of each ion in solution, accounting for formation of the ion pair  $\text{Cu}^{2+}\text{SO}_4^{2-}$  and for partial dissociation of bisulphate, and  $z_i$  is the ion's charge.

#### Equivalent Ionic Conductance of $\text{Cu}^{2+}$ , $\text{HSO}_4^-$ and $\text{SO}_4^{2-}$

The viscosity of pure water,  $\mu^\circ$ , and the equivalent molar conductance of  $\text{CuSO}_4$  at infinite dilution,  $\Lambda^\circ$ , are available in the reference literature [40]. At 25°C the values are 0.8904 centipoise and  $133.6 \Omega^{-1} \text{cm}^2 \text{equiv}^{-1}$  respectively. From these values, Walden's constant may be calculated, and then used to determine the equivalent molar conductance at other viscosities. A summary is given in Table B.1 for water at various temperatures.

---

**Table B.1** Summary of the equivalent molar conductance of  $\text{CuSO}_4$  at several temperatures using Walden's rule.

---

Temperature	0°C	20°C	25°C	50°C
Viscosity of pure water, $\mu^\circ$ (centipoise)	1.786	1.002	0.8904	0.5468
Equivalent molar conductance, $\Lambda^\circ$ ( $\Omega^{-1} \text{cm}^2 \text{equiv}^{-1}$ )	66.6	118.7	133.6	217.6
Walden's product, $\mu^\circ \Lambda^\circ$	119	119	119	119

---

The equivalent molar conductance of  $\text{CuSO}_4$  in the electrolyte used in this thesis,  $\Lambda^*$  may then be estimated using the following simple relationship

$$\Lambda^* = \Lambda^\circ \frac{\mu^\circ}{\mu^*} \quad (\text{B.1})$$

where  $\mu^*$  is the viscosity of the electrolyte used in this thesis. The equivalent molar conductance of  $\text{CuSO}_4$ ,  $\Lambda^*$ , is equal to the sum of the individual equivalent ionic conductances,  $\lambda_i$ . At infinite dilution the value of  $\lambda_i$  for  $\text{SO}_4^{2-}$  at  $25^\circ\text{C}$  is  $79\Omega^{-1}\text{cm}^2\text{equiv}^{-1}$  [40]. Therefore, the value of  $\lambda_i$  for  $\text{Cu}^{2+}$  is equal to  $133.6-79$  or  $54.6\Omega^{-1}\text{cm}^2\text{equiv}^{-1}$ . The fraction of the total equivalent ionic conductance of  $\text{CuSO}_4$  due to the cupric ion is then  $54.6/133.6$  or  $0.41$ . In the absence of a suitable correlation for electrolytes of practical concentration, this value will be assumed to be independent of the solution viscosity, total ionic strength and ionization of  $\text{CuSO}_4$ .

### Viscosity of $\text{CuSO}_4\text{-H}_2\text{SO}_4$ Electrolytes at $50^\circ\text{C}$

A number of predictive relationships have been published [100,113]. For example, Price and Davenport [100] offer the following correlation.

$$\frac{1}{\mu} = 0.7 - 10^{-3} \left\{ \begin{array}{l} 4.6C_{As} \\ +8.3C_{Cu} \\ +8.8C_{Fe} \\ +1.6C_{H_2SO_4} \\ +10C_{Ni} \\ -18t \end{array} \right\} \quad (B.2)$$

where the concentrations of the species are in g/l,  $t$  is in  $^\circ\text{C}$  and  $\mu$  is in centipoise (cp). For the electrolyte composition and temperature used in this thesis (45g/l Cu, 165g/l  $\text{H}_2\text{SO}_4$  and  $50^\circ\text{C}$ ) this equation gives a value of 1.039cp.

Hotlos and Jaskula [113] presented a fitting correlation which may essentially be summarized as follows:

$$\mu = 10^{-5} \rho \left\{ \begin{array}{l} 164 \\ +48C_{CuSO_4} \\ +13C_{H_2SO_4} \\ +32C_{CuSO_4}^2 \\ +2C_{CuSO_4}C_{H_2SO_4} \\ +3C_{H_2SO_4}^2 \end{array} \right\} \exp\left(\frac{E}{RT}\right) \quad (B.3)$$

where the concentrations are in mol/kg( $\text{H}_2\text{O}$ ),  $T$  is in K,  $E=15.74\text{kJ/mol}\cdot\text{K}^1$  and  $\rho$  is in  $\text{g/cm}^3$ . The conversion from g/l to mol/kg( $\text{H}_2\text{O}$ ) may be achieved using Eq. (B.4)

$$\text{mol/kg}(\text{H}_2\text{O}) = M_i \left[ \frac{1}{\rho - \frac{1}{1000} \sum C_i} \right] \quad (B.4)$$

---

<sup>1</sup> The authors confuse several values for  $E$  in their paper. However, the value given in this appendix is the one which makes the equation predict the data given in the paper [113] and the one from which the equation ((B.3)) must have been derived.

with the density in  $\text{g/cm}^3$  and the concentration terms  $C_i$  and  $M_i$  in  $\text{g/l}$  and  $\text{mol/l}$  respectively. The term  $\frac{1}{1000} \sum C_i$  for the electrolyte used in this thesis is equal to  $\frac{1}{1000}(165\text{g/l H}_2\text{SO}_4 + 113\text{g/l CuSO}_4)$  or about 0.277.

Hotlos and Jaskula [113] offered the following density correlation

$$\rho = 10^{-3}(842 + 1.95C_{Cu} + 0.48C_{H_2SO_4}) \exp\left(\frac{E_p}{T}\right) \quad (B.5)$$

where the concentrations are in  $\text{g/l}$  and the value for  $E_p$  is 53K. For the electrolyte used in this thesis, the density according to this equation is  $1.188\text{g/cm}^3$ .

Price and Davenport [100] also provided a correlation for estimating the density of copper refinery electrolytes.

$$\rho = 1.022 + 10^{-3} \left\{ \begin{array}{l} 1.04C_{As} \\ +2.24C_{Cu} \\ +2.37C_{Fe} \\ +0.55C_{H_2SO_4} \\ +2.24C_{Ni} \\ -0.58t \end{array} \right\} \quad (B.6)$$

where the concentrations and temperature are in the same units as the viscosity correlation (Eq. (B.2)). The calculated value for the electrolyte used in the present study is  $1.185\text{g/cm}^3$ .

Using a value of  $1.187\text{g/cm}^3$ , the molal concentrations of  $\text{CuSO}_4$  and  $\text{H}_2\text{SO}_4$  ( $\text{mol/kg(H}_2\text{O)}$ ) are calculated to be 0.778 and 1.846 respectively. Using these concentrations, the viscosity of the electrolyte according to Eq. (B.3) is 1.056cp. A value of 1.045cp will be assumed. The equivalent ionic conductances for  $\text{Cu}^{2+}$ ,  $\text{SO}_4^{2-}$  and  $\text{HSO}_4^-$  are approximately

$$\begin{aligned} \lambda_{\text{Cu}^{2+}} &= (0.41) \frac{119}{1.045} \\ &= 46.7 \Omega^{-1} \text{cm}^2 \text{equiv}^{-1} \end{aligned}$$

$$\begin{aligned} \lambda_{\text{SO}_4^{2-}} = \lambda_{\text{HSO}_4^-} &= \frac{(1 - 0.41)}{0.41} 46.7 \\ &= 67.2 \Omega^{-1} \text{cm}^2 \text{equiv}^{-1} \end{aligned}$$

### Species Concentrations

The concentration of species in the  $\text{CuSO}_4\text{-H}_2\text{SO}_4$  system may be determined by solving the following system of equations. There are three mass balance equations

$$2C_1 = [H^+] + [HSO_4^-] \quad (B.7)$$

$$C_1 + C_2 = [HSO_4^-] + [SO_4^{2-}] + [CuSO_4] \quad (B.8)$$

$$C_2 = [Cu^{2+}] + [CuSO_4] \quad (B.9)$$

where  $C_1$  and  $C_2$  are the acid and  $\text{CuSO}_4$  concentrations, respectively. There are also two equilibrium conditions.

$$K^\circ = \frac{a_{\text{H}^+} a_{\text{SO}_4^{2-}}}{a_{\text{HSO}_4^-}} = \frac{[\text{H}^+][\text{SO}_4^{2-}] \gamma_{\text{H}^+} \gamma_{\text{SO}_4^{2-}}}{[\text{HSO}_4^-] \gamma_{\text{HSO}_4^-}} \quad (\text{B.10})$$

$$K_M^\circ = \frac{a_{\text{Cu}^{2+}} a_{\text{SO}_4^{2-}}}{a_{\text{CuSO}_4}} = \frac{[\text{Cu}^{2+}][\text{SO}_4^{2-}] \gamma_{\text{Cu}^{2+}} \gamma_{\text{SO}_4^{2-}}}{[\text{CuSO}_4] \gamma_{\text{CuSO}_4}} \quad (\text{B.11})$$

For the bisulphate equilibrium, Baes [114] and Marshall and Jones [115] provided values of an equilibrium constant in terms of concentration units,  $K$ , which incorporates a value for both  $K^\circ$  and the activity coefficients,  $\gamma_i$ . For systems at 50°C, Marshall and Jones [115] offered the following correlation

$$\log K = -2.275 + \frac{2.135\sqrt{I_R}}{1 + 1.07\sqrt{I_R}} \quad (\text{B.12})$$

where  $I_R$  is the real, as opposed to stoichiometric or formal, ionic strength.

A similar correlation for the ionization of  $\text{CuSO}_4$  is not available. Fortunately, however, Meissner and Kusic [116] and Meissner [117] developed procedures for evaluating the geometric mean activity coefficient,  $\gamma_{\pm}$ , in strong electrolytes, from which the values of  $\gamma_+$  and  $\gamma_-$  (the individual ion activity coefficients) may be estimated. In the absence of information on  $\gamma$  for the ion pair  $\text{CuSO}_4$  a value of unity will be assigned. The basis of the strong electrolyte model is that experimentally determined values of the reduced activity coefficient,  $\Gamma^\circ$ , form a family of curves in pure solution at any temperature when plotted against stoichiometric or formal ionic strength,  $I$ . The relationship between  $\Gamma^\circ$  and  $I$  is expressed by a set of empirical equations involving the parameter  $q^\circ$  for each electrolyte and at some temperature.

$$\Gamma_{12}^\circ = \gamma_{\pm}^{\frac{1}{z_1+z_2}}, \quad \gamma_{\pm}^{z_1+z_2} = \gamma_+^{z_1} \gamma_-^{z_2} \quad (\text{B.13})$$

$$\Gamma_{12}^\circ = [1 + B(1 + 0.1I)^{q^\circ} - B] \Gamma^* \quad (\text{B.14})$$

where  $z_i$  are the ion charges, and the other terms are defined as follows

$$\Gamma^* = \exp \left[ -2.303 \left( \frac{0.5107\sqrt{I}}{1 + C\sqrt{I}} \right) \right] \quad (\text{B.15})$$

$$B = 0.75 - 0.065q^\circ \quad (\text{B.16})$$

$$C = 1 + 0.055q^\circ \exp(-0.023I^3) \quad (\text{B.17})$$

$$I = \frac{1}{2} \sum_i C_i Z_i^2 \quad (\text{B.18})$$

The value of the fitting parameter,  $q^\circ$ , at 25°C is given in tables in the references [116,117]. For  $\text{CuSO}_4$ , the value is 0.0. Unfortunately, no value of  $q^\circ$  for  $\text{H}_2\text{SO}_4$  is given because this electrolyte does not follow the general relationship. This is attributable to the fact that the partial dissociation of  $\text{HSO}_4^-$  is a function of the real ionic strength,  $I_R$ , as discussed above.

Tozawa and Sasaki [118] avoided this difficulty by defining an ionic strength dependant  $q^\circ$  value for  $H_2SO_4$  based on data from a reference cited in their paper. The correlation they proposed was

$$q_{H_2SO_4}^\circ = -\exp[2.303(0.8805 - 0.4316\sqrt{I})] \quad (B.19)$$

where  $I$  is the total stoichiometric ionic strength. Presumably, this relationship accounts for the variable  $HSO_4^-$  dissociation with real ionic strength by expressing the problem in terms of  $H^+$  and  $SO_4^{2-}$  and in terms of the stoichiometric ionic strength. Thus, the presence of  $HSO_4^-$  and its activity are disregarded.

The temperature correction for each ion pair proposed by Meissner is [117]

$$q_i = q^\circ [1 - 0.0027(t - 25)/z_1 z_2] \quad (B.20)$$

Meissner recognized the importance of electrolyte mixtures and recommended the following correlation

$$q_{mix} = \sum_i \frac{I_i}{I_T} q_{ij}^\circ + \sum_j \frac{I_j}{I_T} q_{ij}^\circ \quad (B.21)$$

where  $i$  and  $j$  are the subscripts for the cation and anion respectively, and  $q_{ij}^\circ$  is the value of  $q^\circ$  or  $q_i$  for each cation-anion pair.

Finally, Bates et al. [119] recognized that  $\gamma_{\pm}$  is not necessarily equal to either  $\gamma_+$  or  $\gamma_-$  because the cation is usually more strongly hydrated than the anion. The expectation is that the value of  $\gamma_+$  increases substantially, leading to a large difference between  $\gamma_+$  and  $\gamma_-$ , as the activity of water decreases (as in very strong electrolytes) due to the decreasing hydration of the cation. Unfortunately, these authors only proposed correlations for chloride electrolytes. However, the hydration number for chlorine is probably close to zero and that of sulphate is probably around one. Furthermore, in the electrolyte used in this thesis, the activity of water is probably around 0.9 (shown later in this Appendix). Thus, in the absence of information for sulphate electrolytes, the assumption that  $\gamma_+$  is equal to  $\gamma_-$  may be as accurate as applying the correlations applicable to chloride electrolytes.

Although the determination of activity coefficients requires concentrations to be expressed on a molal basis, it will be assumed that the errors introduced in using molar concentrations is very small. The real ionic strength for 1.68M  $H_2SO_4$  and 0.71M  $CuSO_4$  is 7.79, from which the value of  $q^\circ$  for  $H_2SO_4$  from Eq. (B.19) is -0.47. The value of  $q^\circ$  for  $H_2SO_4$  at 50°C is -0.45 by Eq. (B.20). Thus, using Eq. (B.21),  $q^{mix}$  for  $CuSO_4$  at 50°C is -0.10. Using Eqs. (B.13)-(B.17), the value for  $\gamma_{\pm}$  (assumed to be equal to  $\gamma_+$  and  $\gamma_-$ ) is calculated to be 0.026.

The ionization constant for  $CuSO_4$  at infinite dilution and at 25°C,  $K_M^\circ$ , is given in Sillen [120]. Helgeson [121] presented various methods to extrapolate values of  $K_M^\circ$  at 25°C to higher temperatures. Calculations for  $NiSO_4$  and  $ZnSO_4$  at 50°C using the method recommended for sulphate salts gave values of  $10^{-2.5}$  and  $10^{-2.6}$  respectively. A value of  $10^{-2.55}$  was assigned to the value of  $K_M^\circ$  for  $CuSO_4$ .

The calculation of the species concentrations may be summarized in the following steps

1. Calculate the activity coefficients for  $Cu^{2+}$  and  $SO_4^{2-}$ .
2. Adjust the value of the ionization constant for  $CuSO_4$ ,  $K_M^\circ$ , by these coefficients so that an ionization constant in terms of concentration units,  $K_M$ , may be calculated.

$$K_M^o \frac{\gamma_{CuSO_4}}{\gamma_{Cu^{2+}}\gamma_{SO_4^{2-}}} = K_M = \frac{[Cu^{2+}][SO_4^{2-}]}{[CuSO_4]}$$

3. Make an initial guess for the species concentrations.
4. Calculate the ionic strength and bisulphate equilibrium constant, K. ( $K^o$  and  $K_M^o$  are replaced by K and  $K_M$ , respectively, to permit the use of concentration units in the equilibrium calculations).
5. Calculate the concentrations of the species by solving Eqs. (B.7)-(B.11) using Newton's method with a Gaussian matrix routine.
6. Compare the "new" real ionic strength with the previous value and iterate to a solution of  $I_R$  using the bisection method.

The concentrations of the various species in mol/l at 50°C, with  $C_1=1.68\text{mol/l}$  and  $C_2=0.71\text{mol/l}$  are summarized below for calculations (a) accounting for the activity coefficients of  $Cu^{2+}$  and  $SO_4^{2-}$ , and (b) disregarding these coefficients.

species	concentration of species	
	$\gamma_+, \gamma_-$ included in the calculation of $C_i$	$\gamma_+, \gamma_-$ disregarded in the calculation of $C_i$
$H^+$	1.205	1.732
$HSO_4^-$	2.155	1.628
$SO_4^{2-}$	0.202	0.077
$Cu^{2+}$	0.676	0.025
$CuSO_4$	0.037	0.685

### Equivalent Ionic Conductance of $H^+$

Several correlations were reviewed in Chap. 3 Sec. 3.10 for estimating  $CuSO_4$ - $H_2SO_4$  electrolyte conductivity. Using Eq. (3.35), the value for  $\kappa^o$ , the electrolyte conductivity, is estimated to be  $0.63\Omega^{-1}\text{cm}^{-1}$  (45g/l  $CuSO_4$ , 165g/l  $H_2SO_4$ , 50°C). When Eq. (3.36) is used,  $\kappa^o$  is estimated to be  $0.54\Omega^{-1}\text{cm}^{-1}$ . The average of these values is  $0.59\Omega^{-1}\text{cm}^{-1}$  and is close to the range  $0.6$ - $0.7\Omega^{-1}\text{cm}^{-1}$  cited as generally being typical of copper refining electrolyte by Biswas and Davenport [1] and to a measured value of  $\approx 0.54\Omega^{-1}\text{cm}^{-1}$ .

Majima et al. [122,123] studied the conductivity of acidic electrolytes and showed that there is a relationship between the ratio  $\kappa^o/[H^+]$  and the activity of water. From a figure in the first paper [122] (Fig. 2) it may be inferred that the activity of water in the electrolyte used in the present study (i.e., when  $\kappa^o$  is  $0.59\Omega^{-1}\text{cm}^{-1}$ ) is roughly 0.9. Approximately this value may also be determined using methods proposed by Meissner [117], although Meissner cautioned that results in  $H_2SO_4$  electrolytes may not be reliable. At this activity for water, from a figure in the second Majima et al. paper [123] (Fig. 11) a value for the equivalent ionic conductance of  $H^+$  in acidic sulphate electrolytes of about  $220\Omega^{-1}\text{cm}^2\text{equiv}^{-1}$  at 25°C may be estimated, versus the value at infinite dilution of  $350\Omega^{-1}\text{cm}^2\text{equiv}^{-1}$  [40]. At 50°C the value of  $\lambda_i^o$  for  $H^+$  is  $465\Omega^{-1}\text{cm}^2\text{equiv}^{-1}$ , thus the value at a water activity of 0.9 may be about  $(220/350)465$  or  $292\Omega^{-1}\text{cm}^2\text{equiv}^{-1}$ .

### Transport Numbers

The transport numbers are equal to the fraction of the total current carried by an ion. Using the species concentrations (accounting for the activities of  $\text{CuSO}_4$  and  $\text{SO}_4^{2-}$ ) and equivalent ionic conductances calculated above, the transport numbers for the ionic species may be *estimated* as shown in Table B.2. The interesting point to note is that the total solution conductivity estimated in the Table B.2 is approximately equal to the value calculated using the empirical correlations, Eqs. (3.35) and (3.36). Table B.3 summarizes the transport numbers for the species calculated by disregarding activity coefficients.

**Table B.2** Summary of transport numbers for the various species at 50°C. The total concentrations of  $\text{CuSO}_4$  and  $\text{H}_2\text{SO}_4$  in the electrolyte are 45g/l (0.71M) and 165g/l (1.68M), respectively. The activity coefficients of  $\text{Cu}^{2+}$  and  $\text{SO}_4^{2-}$  have been included in the calculations of the species concentrations.

species	conc. (mol/l)	$\lambda_i$ ( $\Omega^{-1}\text{cm}^2\text{equiv}^{-1}$ )	$\kappa_i^\circ$ ( $\Omega^{-1}\text{cm}^{-1}$ )	transport number
$\text{H}^+$	1.205	292	0.352	0.60
$\text{HSO}_4^-$	2.155	67.2	0.145	0.25
$\text{SO}_4^{2-}$	0.202	67.2	0.027	0.05
$\text{Cu}^{2+}$	0.676	46.7	0.063	0.11
		total .....	0.587	

### Discussion

The transport numbers calculated in this appendix must be considered as *approximate* values. For example, the ratio of equivalent ionic conductance of  $\text{Cu}^{2+}$  to  $\text{SO}_4^{2-}$  is not necessarily constant with increasing ionic strength, the equivalent ionic conductances of  $\text{HSO}_4^-$  and  $\text{SO}_4^{2-}$  are not necessarily equal, and the equivalent ionic conductance of the hydrogen ion may be higher than  $292\Omega^{-1}\text{cm}^2\text{equiv}^{-1}$  at 50°C. In addition, while convenient to use Eq. (B.19) to estimate the value of  $q^\circ$  for  $\text{H}_2\text{SO}_4$ , this procedure may not be rigorously reliable. Thus, the true transport number for  $\text{Cu}^{2+}$  may lie between the values calculated in Tables B.2 and B.3. Nevertheless, these calculations show that  $\text{Cu}^{2+}$  probably carries not more than about 10% of the current, and so its mass transport in solution is essentially due to other processes.

**Table B.3** Summary of transport numbers for the various species at 50°C disregarding the activity coefficients for  $\text{Cu}^{2+}$  and  $\text{SO}_4^{2-}$  in the determination of the species concentrations. The total concentrations of  $\text{CuSO}_4$  and  $\text{H}_2\text{SO}_4$  in the electrolyte are 45g/l (0.71M) and 165g/l (1.68M), respectively.

species	conc. (mol/l)	$\lambda_i$ ( $\Omega^{-1}\text{cm}^2\text{equiv}^{-1}$ )	$\kappa_i^\circ$ ( $\Omega^{-1}\text{cm}^{-1}$ )	transport no.
$\text{H}^+$	1.732	292	0.506	0.81
$\text{HSO}_4^-$	1.628	67.2	0.109	0.17
$\text{SO}_4^{2-}$	0.077	67.2	0.010	0.02
$\text{Cu}^{2+}$	0.025	46.7	0.002	0.004
		total .....	0.627	

## APPENDIX C

### DERIVATION OF EQUATIONS (6.11) AND (6.12)

When the rate controlling step in a shrinking core reaction model is the diffusion of species through the pores of the product layer, Eq. (C.1) describes the reaction rate [124].

$$-\frac{dQ}{dt} = -4\pi r^2 \mathcal{D}_e M^{-1} \frac{dC}{dr} = \text{constant} \quad (\text{C.1})$$

where  $-dQ/dt$  ( $Q$  is in moles) may be equated, in this system, to the extraction rate for copper at a single particle and  $\mathcal{D}_e$  is the effective diffusivity of copper in the product layer,  $C_c$  is the copper ion concentration at the reaction interface and  $C$  is the copper concentration at the particle surface (in  $\text{g/cm}^3$ ), and  $M$  is the molecular weight of copper. The boundary conditions are

$$\begin{aligned} @ \quad r = r_c, \quad C &= C_c \\ @ \quad r = r_p, \quad C &= C \end{aligned} \quad (\text{C.2})$$

where  $r_p$  is the particle radius,  $r_c$  is the radius of the shrinking core, Integration of Eq. (C.1) subject to these boundary conditions gives

$$-\frac{dQ}{dt} = 4\pi \mathcal{D}_e M^{-1} (C_p - C) \left( \frac{r_p r_c}{r_p - r_c} \right) \quad (\text{C.3})$$

In order to convert the single particle reaction rate into the volumetric reaction rate,  $di_p/dx$ , this equation must be multiplied by the number of particles of radius  $r_p$  per unit volume of electrode

$$\begin{aligned} \left( \frac{\text{number of particles of radius } r_p}{\text{cm}^3 \text{ of electrode}} \right) &= \\ \left( \frac{\text{fraction of bed occupied by solids}}{\text{volume of single particle of radius } r_p} \right) &= \frac{1 - \epsilon}{(4/3)\pi r_p^3} \end{aligned} \quad (\text{C.4})$$

to give

$$-\frac{dQ}{dt} \left( \frac{1 - \epsilon}{(4/3)\pi r_p^3} \right) = 3(1 - \epsilon) \mathcal{D}_e M^{-1} (C_c - C) \frac{1}{r_p^2} \left( \frac{r_c}{r_p - r_c} \right) \quad (\text{C.5})$$

Both sides of this equation are proportional to the volumetric reaction rate. Finally, by selecting the right side

$$\frac{di_p}{dx} = 3nF(1 - \epsilon) \mathcal{D}_e M^{-1} (C_c - C) \frac{1}{r_p^2} \left( \frac{r_c}{r_p - r_c} \right) \quad (\text{6.11})$$

An expression must also be included to permit an estimate of the shrinking core radius to be used in this equation as a function of copper extraction. If the copper extraction is approximately proportional to the time a particle is subject to corrosion, Eq. (C.3) may be used. Substitution of  $4/3 \cdot \rho_M r_c^3$  for Q, integration of Eq. (C.3) from  $r_c=r_p$  at  $t=0$  and rearrangement of the variables gives

$$t = \frac{\rho_M r_p^2}{6D_e M^{-1}(C_c - C)} \left[ 1 - 3 \left( \frac{r_c}{r_p} \right)^2 + 2 \left( \frac{r_c}{r_p} \right)^3 \right] \quad (6.12)$$

where  $\rho_M$  is the molar density of chalcocite.

---

## APPENDIX D

---

### DISCUSSION OF THE LINEAR APPROXIMATION AND ESTIMATION OF THE EXCHANGE CURRENT DENSITY, $i_0$

One could debate that since the oxidation of chalcocite is not a particularly reversible reaction (the cathodic process generates metallic copper and hydrogen sulphide gas) the linear analysis is unsatisfactory because it depends on both reaction directions being described by the same half cell reaction, such as Eq. (3.1). To get around this difficulty for chalcocite electrolysis, Eq. (6.21) could be replaced by

$$\frac{di_p}{dx} = \frac{C_{[Cu]}}{C_{[Cu]}^0} K (\Phi_p - \Phi_e - E_r) \quad (D.1)$$

with the value of the constant,  $K$ , taken as the slope of the best straight line approximation to the overpotential versus time data over the expected range of  $i_0$ , and preferably defined such that  $di_p/dx=0$  at  $\Phi_p - \Phi_e - E_r=0$ . In other words,  $K$  simply replaces  $ai_0 n^+ F/RT$  and  $C_{ss}/C_{ss}^0$  replaces the concentration terms.

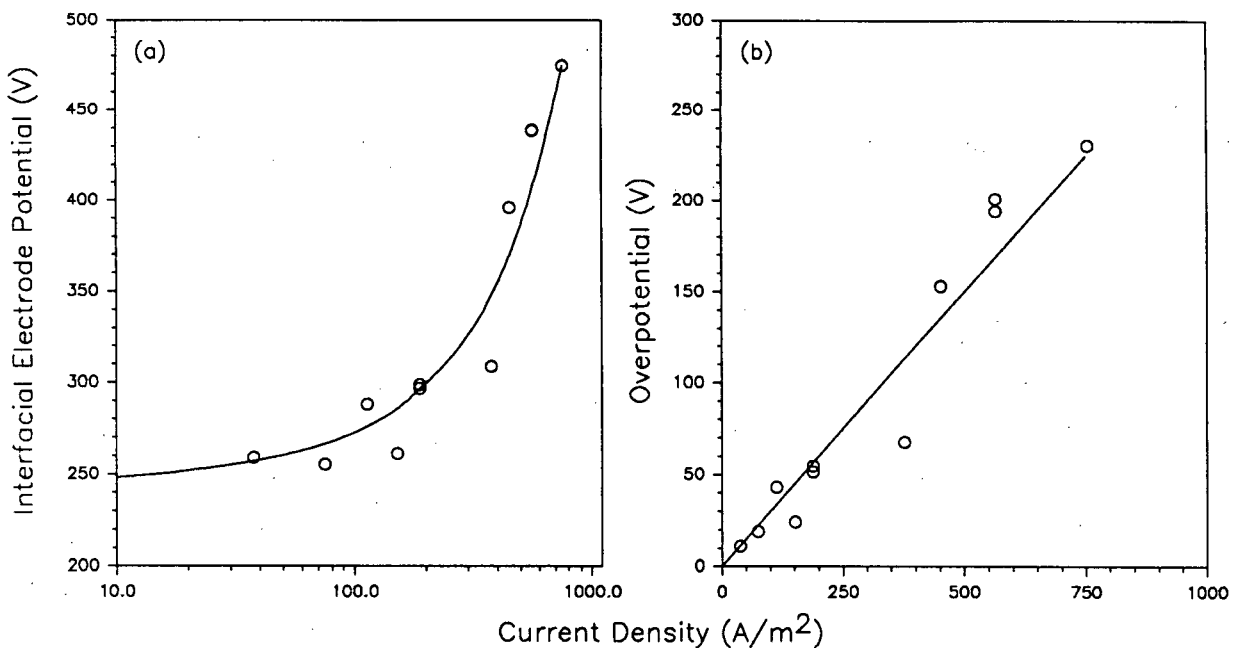


**Figure D.1** Interfacial potential and overpotential of digenite ( $\approx \text{Cu}_2\text{S}$ ) anodes with respect to current density. Electrolyte: 0.1M  $\text{CuSO}_4$ , 0.1M  $\text{H}_2\text{SO}_4$ , 25°C. [5].

---

Etienne [5] estimated an interfacial potential of rotating disc digenite anodes as a function of current density by extrapolating to zero time a tangent to the linear portion of the overpotential versus time curves. (This occurred before the transition time). These estimates included a correction for ohmic and diffusion overpotential effects which were inherent in the measurements, and are shown in Fig. D.1a. Faradaic overpotential versus current density may be calculated by taking the difference between the interfacial potential and the potential measured prior to the application of current as shown in Fig. D.1b.

Provided the current density is approximately uniformly distributed in the anode, the current density at the particles,  $i_p$ , may be approximated as follows

$$i_p = \frac{i_{total}}{La} = \frac{400A/m^2}{2cm \cdot 15cm^{-1}} = 13A/m^2$$

Figure D.1b suggests that the overpotential at this current density is much less than 30mV. In fact, at ten times this current density, the overpotential appears to be only about 35mV. In Fig. D.1a, the current density is plotted in the conventional way, that is using logarithmic scaling. However, Fig. D.1b demonstrates that the overpotential values calculated from Etienne's data appear to be well represented using a linear scale for current density. This provides support for the linear analysis and suggests that Eq. (6.21) could be essentially written as Eq. (D.1) and extended to overpotentials larger than 30mV.

Figure D.2 summarizes the effect of exchange current density on the reaction distribution through the particulate anode. As the value for  $i_0$  increases, the reaction becomes increasingly non-uniformly distributed through the electrode. This is because an increase in  $i_0$  is equivalent to a reduction in the Faradaic reaction impedance, or a decrease in the slope of the line in the Fig. D.1b, leading to an increase in reaction rate at constant overpotential.

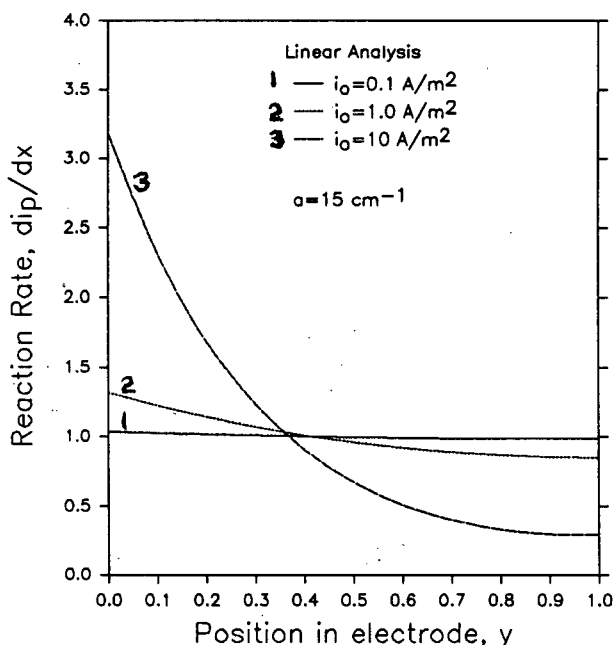


**Figure D.2** Effect of exchange current density on the reaction distribution in a particulate anode composed of copper sulphide particles.  $T=50^{\circ}C$ ,  $\kappa=0.21\Omega^{-1}cm^{-1}$ ,  $\sigma=21\Omega^{-1}cm^{-1}$ .

---

## APPENDIX E

---

### REVERSIBLE POTENTIAL FOR THE $\text{Cu}^{2+}|\text{Cu}^\circ$ ELECTRODE & DECOMPOSITION POTENTIALS FOR VARIOUS SULPHIDE SPECIES

Determination of the reversible potential for the  $\text{Cu}^{2+}|\text{Cu}^\circ$  reference electrode is necessary to relate the potential data presented in this thesis to the standard hydrogen electrode and must account for the activity of  $\text{Cu}^{2+}$  in the electrolyte as well as a temperature of 50°C.

#### Temperature Compensation

Determination of half-cell potentials at elevated temperatures is complicated by the fact that the entropy and enthalpy of ions do not vary with temperature in the same manner as that of compounds. This is because these thermodynamic properties of ions include the thermodynamic properties of the molecules in the solvation shell (or hydration shell), and the latter are closely related to the solvents dielectric constant, which is a function of temperature. Thus, the familiar equation

$$\Delta G = \Delta H - T\Delta S \quad (E.1)$$

cannot be applied to reactions involving ionic species. Fortunately, Criss and Cobble provided a way to deal with this problem by providing an entropy correspondence principle [126,127]. Basically, the principle of entropy correspondence is that ionic entropies at some temperature are linearly related to their values at 25°C, provided the standard state is chosen properly. This is achieved by specifying a value for the absolute entropy of the hydrogen ion at various temperatures of interest. (This absolute value generally is not equal to zero, which is the reference value normally implied in thermodynamic tabulations). Then, the absolute entropies for the other ions,  $S_i^{o,abs}$ , are obtained by adding  $S_{\text{H}^+}^{o,abs} \cdot z_i$  to the values for these ions tabulated in the literature (as  $S_i^o$ ).

The free energy change at some temperature  $T_2$  is given by the following equation, the derivation of which follows from the referenced papers [126,127]

$$\Delta G_{T_2}^o = \Delta G_{T_1}^o + \Delta \bar{C}_p \left[ T_2 - T_1 - T_2 \ln \left( \frac{T_2}{T_1} \right) \right] - \Delta S_{T_1}^{o,abs} (T_2 - T_1) \quad (E.2)$$

where  $\bar{C}_p$  is the mean molar heat capacity for each species in the half cell reaction over the temperature interval of interest, and  $S_{T_1}^{o,abs}$  is the entropy of the species, but with the entropy of the ions corrected for the absolute entropy of hydrogen. Additionally, for the ionic species and  $\text{H}^+$ , respectively

$$\bar{C}_p = \frac{a_{T_2} + S_{T_1}^{o,abs}(1 - b_{T_2})}{\ln\left(\frac{T_2}{T_1}\right)}, \quad \bar{C}_p = \frac{S_{T_2}^{o,abs} + S_{T_1}^{o,abs}}{\ln\left(\frac{T_2}{T_1}\right)} \quad (E.3)$$

where the parameters  $a(T)$  and  $b(T)$  are the "fitting" coefficients of the entropy correspondence model and are functions of the ion type (i.e., cation, oxy-anion ...). Values for the copper ion are given in the following table along with the reference entropy for  $H^+$ .

**Table E.1** Value of the fitting parameters  $a(T)$  and  $b(T)$  for cationic species, and the absolute entropy of the hydrogen ion at several temperatures [126,127].

T (°C)	a(T) (J/mol·K)	b(T)	$S_{H^+}^{o,abs}$ (J/mol·K)
25	0	1	-20.92
60	16.32	0.995	-10.46
100	43.10	0.876	8.37

As at 25°C, at elevated temperatures, the reversible potential generally is referred to the standard hydrogen electrode at that same temperature. Therefore, the potential of the  $H^+|H_2$  couple at 50°C is also required. The values required by Eq. (E.2) are tabulated below. The values of  $\bar{C}_p$  for the ions were obtained using Eq. (E.3). The values of the heat capacities for  $Cu^{2+}$  and  $H_2$  were obtained from reference 120. The mean value of the heat capacity of  $H_2$  was obtained by integrating the  $C_p(T)$  function over the temperature interval of interest and dividing by the temperature difference.

**Table E.2** Summary of the various parameters used in Eq. (E.2).  $\Delta$  refers to  $\Delta G^\circ_{298}$ ,  $\Delta S^\circ_{298}$  etc.

	$Cu^{2+}$	$Cu^\circ$	$\Delta$	$2H^+$	$H_2$	$\Delta$
$G_{298}$ (kJ/mol)	65.7	0.0	-65.7	0.0	0.0	0.0
$S^\circ_{298}$ (J/mol·K)	-97.2	33.2	0.0	0.0	130.7	0.0
$S_{298}^{o,abs}$ (J/mol·K)	-139.0	33.2	172.2	(-20.9)2	130.7	171.8
$\bar{C}_p \Big _{298}^{333}$ (J/mol·K)	90.64	20.8	-69.8	(94.2)2	28.8	-159.6
$\bar{C}_p \Big _{298}^{373}$ (J/mol·K)	232.9	20.8	-212.1	(130.5)2	28.9	-232.1

$$C_p |_{H_2} = 27.3 + 3.27(10^{-3})T + 0.5(10^5)/T \text{ J/mol}\cdot\text{K} \quad [128]$$

$$C_p |_{Cu} = 20.8 \text{ J/mol}\cdot\text{K} \quad [128]$$

Now, using Eq. (E.2), the values of  $\Delta G^\circ$  at 60°C and 100°C for the  $Cu^{2+}|Cu^\circ$  and  $H^+|H_2$  electrodes may be calculated. The results are tabulated below.

#### Activity Compensation

The activity coefficient,  $\gamma_+$ , for  $Cu^{2+}$  was estimated in Appendix B to be 0.026. Using this value, the potential of the  $Cu^{2+}|Cu^\circ$  electrode at 50°C may be calculated as follows

**Table E.3** Summary of the free energy and reversible potential for the hydrogen and copper electrodes at 60°C and 100°C.

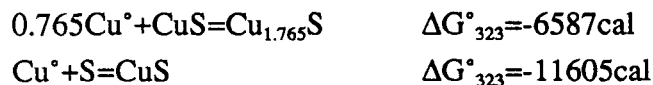
Electrode	$\Delta G^\circ_{60}$	$E_{r,60}$	$\Delta G^\circ_{100}$	$E_{r,100}$
$H^+ H_2$	-5.7	0.03	-10.9	0.06
$Cu^{2+} Cu^\circ$	-71.7	0.37	-76.8	0.40
$Cu^{2+} Cu^\circ$ vs $H^+ H_2$		0.34		0.34

$$\begin{aligned}
 E_{r,50^\circ C} &= E^\circ - \frac{RT}{nF} \ln \left( \frac{1}{a_{Cu^{2+}}} \right) \\
 &= 0.34 - \frac{1.987 \cdot 323}{2 \cdot 23,060} \ln \left( \frac{1}{0.0226 \cdot 0.71} \right) \\
 &= 0.28V
 \end{aligned}$$

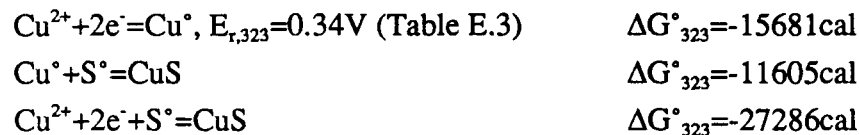
Thus, to obtain the electrode potential relative to the standard hydrogen electrode at 50°C, 0.28V must be added to all the potentials referred to the  $Cu^{2+}|Cu^\circ$  reference electrode.

#### Data on Other Sulphide Species

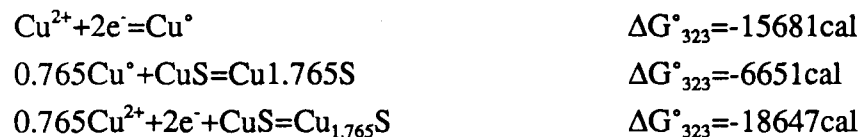
Free energy of formation and half cell potentials at 25°C for other sulphide species are summarized in the following tables. Using the values of  $\Delta G^\circ$  from reference 5 in Table E.4, the following values may be calculated



The potentials for the reactions which are assumed for the reactions appearing in Table 7.2 may be estimated as follows. For  $Cu^{2+} + 2e^- + S^\circ = CuS$



This gives a value of  $E_r = 0.59V$  versus the SHE at 50°C, or no change from the value at 25°C. For  $0.765 + 2e^- + CuS = Cu_{1.765}S$



This gives a value of  $E_r = 0.53V$  versus the SHE at 50°C. The activity of the cupric ion is unimportant in the determination of the reaction process overpotential for line (e) of Table 7.2.

**Table E.4** Thermodynamic data for various copper sulphide species.

Ref.	Species	$\Delta G^\circ$ (cal/mol)	Conditions
40	Cu <sub>2</sub> S	-19,000-0.45T	?
	CuS	-11,600-0.25T	?
	Cu <sup>2+</sup>	15.39(10 <sup>3</sup> )	298K
5	Cu <sub>2</sub> S	-18,790-5.3T	
	Cu <sub>1.96</sub> S	-19,700-5.5(T-328)	
	Cu <sub>x</sub> S	-18,140-4.9(T-328)+(1.83-x)[-7910-3.2(T-328)]	1.765<x<1.83
	Cu <sub>1.765</sub>	-18,140-4.9(T-328)	
	CuS	-11,610-0.3T	
42	Cu <sub>2</sub> S	0.0	$\Delta G_{Cu_2S}^\circ - \Delta G_{Cu_2S}^\circ$
	Cu <sub>1.91-1.95</sub> S	-0.45(10 <sup>3</sup> )	$\Delta G_{Cu_xS}^\circ - \Delta G_{Cu_2S}^\circ$
	Cu <sub>1.80-1.86</sub> S	-1.24(10 <sup>3</sup> )	$\Delta G_{Cu_xS}^\circ - \Delta G_{Cu_2S}^\circ$
	Cu <sub>1.65-1.68</sub> S	-2.64(10 <sup>3</sup> )	$\Delta G_{Cu_xS}^\circ - \Delta G_{Cu_2S}^\circ$
	Cu <sub>1.40-1.36</sub> S	-5.15(10 <sup>3</sup> )	$\Delta G_{Cu_xS}^\circ - \Delta G_{Cu_2S}^\circ$
	CuS	-10.1(10 <sup>3</sup> )	$\Delta G_{Cu_xS}^\circ - \Delta G_{Cu_2S}^\circ$
43	CuS	-12,726-0.54T ±50	273<T<388 K
	Cu <sub>1.1</sub> S	-13,463-0.45T ±100	273<T<423 K
	Cu <sub>1.4</sub> S	-14,675-2.36T ±100	273<T<423 K
	Cu <sub>1.75</sub> S	-18,169-2.02T ±70	273<T<348 K
	Cu <sub>1.765</sub> S	-18,366-1.17T ±100	273<T<348 K
	Cu <sub>1.934</sub>	-19,063-3.28T ±100	233<T<348 K
	Cu <sub>1.965</sub>	-19,178-3.53T ±100	273<T<363 K
	Cu <sub>2</sub> S	-19,226-4.11T ±120	273<T<376 K
125	CuFeS <sub>4</sub>	-45.55(10 <sup>3</sup> )	298K
	CuFeS <sub>4</sub>	-45.57(10 <sup>3</sup> )	300K
	Cu <sub>5</sub> FeS <sub>4</sub>	-93.86(10 <sup>3</sup> )	298K
	Cu <sub>5</sub> FeS <sub>4</sub>	-93.88(10 <sup>3</sup> )	300K

**Table E.5** Reversible potential for various half cell reactions. All values are versus the hydrogen electrode at 25°C and unit activities of species unless otherwise specified.

Ref.	Half Cell	Electrolyte Conditions	E° (V)
40	$\text{Cu}^{2+} + 2\text{e}^- = \text{Cu}^\circ$		0.336
	$\text{Cu}^{2+} + \text{CuS} + 2\text{e}^- = \text{Cu}_2\text{S}$		0.50
	$\text{Cu}^{2+} + \text{S}^\circ + 2\text{e}^- = \text{CuS}$		0.59
5 <sup>1</sup>	$\text{Cu}^{2+} + \text{CuS} + 2\text{e}^- = \text{Cu}_2\text{S}$		0.53
	$0.2\text{Cu}^{2+} + \text{Cu}_{1.765}\text{S} + 0.4\text{e}^- = \text{Cu}_{1.965}\text{S}$		0.50
	$0.765\text{Cu}^{2+} + \text{CuS} + 1.53\text{e}^- = \text{Cu}_{1.765}\text{S}$		0.52
	$\text{Cu}^{2+} + \text{S}^\circ + 2\text{e}^- = \text{CuS}$		0.59
42	$0.05\text{Cu}^{2+} + \text{Cu}_{1.95}\text{S} + 0.1\text{e}^- = \text{Cu}_2\text{S}$	0.01M $\text{Cu}^{2+}$ , 0.1M $\text{H}_2\text{SO}_4$ , 23-27°C	0.143 <sup>2</sup>
	$0.05\text{Cu}^{2+} + \text{Cu}_{1.86}\text{S} + 0.1\text{e}^- = \text{Cu}_{1.91}\text{S}$	0.01M $\text{Cu}^{2+}$ , 0.1M $\text{H}_2\text{SO}_4$ , 23-27°C	0.173 <sup>2</sup>
	$0.12\text{Cu}^{2+} + \text{Cu}_{1.68}\text{S} + 0.24\text{e}^- = \text{Cu}_{1.80}\text{S}$	0.01M $\text{Cu}^{2+}$ , 0.1M $\text{H}_2\text{SO}_4$ , 23-27°C	0.190 <sup>2</sup>
	$0.25\text{Cu}^{2+} + \text{Cu}_{1.40}\text{S} + 0.5\text{e}^- = \text{Cu}_{1.65}\text{S}$	0.01M $\text{Cu}^{2+}$ , 0.1M $\text{H}_2\text{SO}_4$ , 23-27°C	0.202 <sup>2</sup>
	$0.36\text{Cu}^{2+} + \text{CuS} + 0.72\text{e}^- = \text{Cu}_{1.36}\text{S}$	0.01M $\text{Cu}^{2+}$ , 0.1M $\text{H}_2\text{SO}_4$ , 23-27°C	0.268 <sup>2</sup>
43 <sup>1</sup>	$\text{Cu}^{2+} + \text{CuS} + 2\text{e}^- = \text{Cu}_2\text{S}$		0.50
	$\text{Cu}^{2+} + \text{S}^\circ + 2\text{e}^- = \text{CuS}$		0.62
125 <sup>1</sup>	$\text{CuFeS}_2 + 4\text{Cu}^{2+} + 2\text{S}^\circ + 8\text{e}^- = \text{Cu}_3\text{FeS}_4$		0.60
40	$\text{Pb}^{2+} + \text{S}^\circ + 2\text{e}^- = \text{PbS}$		0.35

Notes: 1. includes the value for the free energy of formation of the cupric ion taken from reference 40 as 15.5kcal/mol

2. versus a  $\text{Cu}^{2+}|\text{Cu}^\circ$  reference electrode at 0.01M  $\text{Cu}^{2+}$  for which  $E \approx 0.30\text{V}$  (assuming activity is equal to concentration at this low concentration)

# APPENDIX F

## POWDER X-RAY DIFFRACTION DATA

This appendix is a summary of the powder x-ray diffraction data for the various copper matte species tested in this thesis.

**Table F.1** Powder X-ray powder diffraction data for synthetic  $\text{Cu}_{2-x}\text{S}$  containing 4.7wt% Fe. Italics indicate  $\text{Cu}_2\text{S}$  card #23-961. Card numbers are shown in brackets. Troilite is FeS.

Experiment (32)		$\text{Cu}_{1.96}\text{S}$ (12-224)		$\text{Cu}_2\text{S}$ (12-227)		$\text{Cu}_{1.96}\text{S}$ (17-449)		$\text{Cu}_5\text{FeS}_6$ (13-0161)		Troilite (1-1247)	
d	I/Io	d	I/Io	d	I/Io	d	I/Io	d	I/Io	d	I/Io
3.78	11	3.76	30			3.77	10				
3.265	41	3.26	30			3.27	16	3.27	60		
3.145	27			<i>3.15</i>	<i>30</i>			3.14	100		
2.94	9			<i>2.942</i>	<i>45</i>					2.97	33
2.83	32	2.829	30			2.827	20	2.82	100		
2.745	100	2.743	100			2.74	100				
2.4	11		100	2.401	100						
				<i>2.396</i>	<i>85</i>						
2.305	69	2.304	100	2.39	50	2.302	80				
2.26	24	2.261	30			2.259	30				
2.00	55	1.999	60	<i>1.977</i>	<i>100</i>	1.998	30			2.06	100
1.97	36	1.97	60	1.975	50	1.967	30				
1.915	45			1.915	25						
				1.908	50			1.89	100		
1.88	28	1.888	30	1.879	100	1.883	30				
								1.85	100		
1.765	11	1.765	30			1.761	30				
1.707	22	1.707	40							1.71	33
								1.564	100		
1.405	11	1.403	60			1.401	30				
1.332	8	1.327	30			1.326	6				
								1.317	80		

**Table F.2** Powder X-ray diffraction data for synthetic  $\text{Cu}_{2-x}\text{S}$  containing 4.5wt% Fe. Card numbers are shown in brackets.

Experiment (20,24)		$\text{Cu}_{1.96}\text{S}$ (12-224)		$\text{Cu}_2\text{S}$ (12-227)		$\text{Cu}_5\text{FeS}_4$ (14-203)		$\text{Cu}_5\text{FeS}_6$ (13-161)	
d	I/Io	d	I/Io	d	I/Io	d	I/Io	d	I/Io
				3.77	50				
3.75	9			3.73	75				
3.27	32	3.76	30	3.27	75				
3.17	17	3.26	30	3.181	75	3.18	60		
3.12	15			3.118	25			3.14	100
2.945	7			2.95	75				
				2.93	75				
2.83	26	2.829	30					2.82	100
2.745	100	2.743	100	2.764	75	2.74	50		
2.54	8			2.56	75				
				2.53	50				
2.5	8			2.528	75				
2.406	10			2.401	100				
2.305	61	2.304	100						
2.265	21	2.261	30						
				2.008	50				
2.000	49	1.999	60	2.002	50				
				1.985	25				
1.975	35	1.97	60	1.978	75				
				1.972	100				
1.93	32					1.937	100		
1.92	29			1.915	25				
1.887	24	1.888	30	1.879	100			1.89	100
1.772	7	1.767	30						
1.71	26	1.707	40						
1.61	10	1.616	30					1.564	100
1.406	8	1.403	60						
1.322	7	1.327	30						

**Table F.3** Powder X-ray diffraction data for synthetic  $\text{Cu}_{2-x}\text{S}$  containing 4.5wt% Pb. Card numbers are shown in brackets.

Experiment (31)		$\text{Cu}_2\text{S}$ (12-227)		$\text{Cu}_{14}\text{Pb}_2\text{S}_{9-x}$ (20-360)		Pb (4-686)		PbS (5-592)	
d	I/I <sub>0</sub>	d	I/I <sub>0</sub>	d	I/I <sub>0</sub>	d	I/I <sub>0</sub>	d	I/I <sub>0</sub>
3.735	21	3.73	75	3.74	30				
3.6	13			3.63	30				
3.425	14			3.36	75			3.429	84
3.31	17	3.311	75	3.33	75				
3.27	19	3.27	75	3.27	50				
3.18	28	3.181	75						
3.16	23			3.16	10				
3.06	19	3.051	75	2.98	50				
2.96	45	2.96	50	2.92	100			2.969	10
2.86	31	2.864	50	2.85	100	2.855	100		
2.727	56	2.724	75						
2.67	21	2.665	75	2.65	50				
2.625	10								
2.53	26	2.53	75						
		2.528	75						
2.48	46	2.475	75	2.47	50	2.475	50		
2.4	68	2.401	100	2.41	50				
2.24	18	2.24	50	2.24	30				
2.33	31	2.328	50						
2.215	21	2.215	25	2.22	50				
2.125	13								
2.098	15			2.09	75			2.099	57
1.977	100	1.978	75	1.99	50				
		1.972	100	1.96	30				
1.88	72	1.879	100	1.88	50				
1.79	15	1.795	50	1.79	30			1.79	35
1.75	10					1.75	31		
1.709	27			1.71	30			1.714	16
1.53	8			1.55	30				
1.496	9					1.493	32		
1.288	8								

**Table F.4** Powder X-ray diffraction data for synthetic  $\text{Cu}_{2-x}\text{S}$  containing 4.1 wt% Pb. Card numbers are shown in brackets.

Experiment (25)		$\text{Cu}_2\text{S}$ (12-227)		$\text{Cu}_{14}\text{Pb}_2\text{S}_{9,x}$ (20-360)		Pb (4-686)		PbS (5-592)	
d	I/I <sub>0</sub>	d	I/I <sub>0</sub>	d	I/I <sub>0</sub>	d	I/I <sub>0</sub>	d	I/I <sub>0</sub>
3.72	13	3.73	75	3.74	30				
3.6	7	3.591	75	3.63	70				
3.43	9			3.36	75			3.429	84
3.315	10	3.311	75	3.33	75				
3.27	10	3.27	75	3.27	50				
3.18	24	3.181	75	3.16	10				
3.055	21	3.051	75	2.98	50				
		2.960	50						
2.955	35	2.950	75	2.92	100			2.969	10
2.86	40	2.864	50	2.85	100	2.855	100		
2.723	54	2.724	75	2.76	75				
2.665	22	2.665	75	2.65	50				
2.528	29	2.528	75						
2.476	49	2.475	75	2.47	50	2.475	50		
2.401	61	2.401	100	2.241	50				
2.24	15	2.24	50	2.24	30				
2.23	28	2.229	25						
2.215	17	2.215	25	2.22	50				
2.125	10			2.19	30				
2.095	10			2.09	75			2.099	58
2.002	17	2.002	50	1.99	50				
1.978	100	1.978	75						
		1.972	100						
1.953	24	1.959	25	1.96	30				
1.881	66	1.879	100	1.88	50				
1.805	10								
1.79	12	1.795	50	1.79	30	1.75	31	1.79	35
1.707	23			1.71	30				
1.492	7					1.493	32		
1.285	6								

**Table F.5** Powder X-ray diffraction data for synthetic  $\text{Cu}_{2-x}\text{S}$ . Card numbers are shown in brackets.

Experiment (23)		$\text{Cu}_2\text{S}$ (12-227)		$\text{Cu}_2\text{S}$ (23-959)	
d	I/I <sub>0</sub>	d	I/I <sub>0</sub>	d	I/I <sub>0</sub>
3.72	17	3.73	75	3.73	20
3.595	11	3.591	75		
3.305	13	3.311	75		
3.185	23	3.181	75		
2.955	30	2.96	50	2.942	45
		2.95	75		
2.789	11				
2.765	13	2.764	75		
2.728	55	2.724	75		
2.665	19	2.665	75		
2.53	31	2.53	75		
2.478	32	2.475	75		
		2.401	100		
2.40	61	2.398	100	2.389	85
2.325	28	2.328	50		
2.241	19	2.24	50	2.237	25
2.213	19	2.215	25	2.117	12
2.125	9	2.116	50		
1.975	100	1.978	100	1.977	100
		1.972	75		
1.95	21	1.949	75	1.949	30
1.88	47	1.879	100	1.876	90
1.79	6	1.795	50		
1.705	20			1.704	35
1.658	9			1.657	12
1.525	2			1.526	25
1.429	2				
1.355	2				

**Table F.6** Powder X-ray diffraction data for industrial matte. Card numbers are shown in brackets. Italics are for  $\text{Cu}_5\text{FeS}_4$ , card number 14-323. Underlined values are for  $\text{PbS}$ , card number 5-0592. Double underlined values are for  $\text{Cu}_{14}\text{Pb}_2\text{S}_{9-x}$ , card number 20-0360.

Experiment (41,42,50)		$\text{Cu}_{1.96}\text{S}$ (12-224)		$\text{Cu}_2\text{S}$ (12-227)		$\text{Cu}_{1.96}\text{S}$ (17-449)		$\text{Cu}_5\text{FeS}_4$ (3-1076)		$\text{Pb}$ (4-0686)	
d	I/I <sub>0</sub>	d	I/I <sub>0</sub>	d	I/I <sub>0</sub>	d	I/I <sub>0</sub>	d	I/I <sub>0</sub>	d	I/I <sub>0</sub>
3.78	15	3.76	30	3.77	50	3.77	10				
3.74	19			3.73	75					<u>3.74</u>	<u>30</u>
3.61	14			3.591	75					<u>3.63</u>	<u>30</u>
								3.32	30	<u>3.429</u>	<u>84</u>
3.31	26			3.31	75			3.31	40	<u>3.36</u>	<u>75</u>
3.265	50	3.26	30	3.30	50	3.27	16				
3.16	37							3.16	30		
3.12	50			3.118	25						
3.05	17			3.051	75						
2.95	31			2.95	75					<u>2.92</u>	<u>100</u>
2.855	63									<u>2.855</u>	<u>100</u>
										<u>2.85</u>	<u>100</u>
								2.75	30		
2.745	100	1.743	100			1.74	100	2.74	50		
2.67	26			2.665	75						
2.525	28			2.528	75			2.52	70		
2.475	50			2.457	75					<u>2.47</u>	<u>50</u>
				2.401	100					<u>2.475</u>	<u>50</u>
2.398	48			2.398	100						
2.365	15			2.369	50						
2.30	67	2.303	100			2.302	80			<u>2.969</u>	<u>100</u>
2.255	33					2.259	30				
2.240	26			2.24	50					<u>2.24</u>	<u>30</u>
2.21	22			2.206	75					<u>2.22</u>	<u>50</u>
2.12	15			2.116	50			2.13	20		
2.09	16									<u>2.099</u>	<u>58</u>
										<u>2.09</u>	<u>75</u>
1.995	63	1.999	60	2.002	50	1.998	30				
1.975	76	1.97	60	1.972	100	1.994	40				
1.935	37							1.937	100		
1.910	52			1.908	50						
1.88	65	1.888	30	1.879	100	1.883	35			<u>1.88</u>	<u>50</u>
1.75	20					1.753	18			<u>1.75</u>	<u>31</u>
1.705	37	1.707	40							<u>1.71</u>	<u>30</u>
1.634	19										
1.494	13	1.492	30			1.495	6			1.493	32
1.406	15	1.403	60								
1.40	15										
1.33	11										
1.326	11	1.327	30								

**Table F.7** Powder X-ray diffraction data for re-melted industrial matte. Card numbers are shown in brackets. Italics are for  $\text{Cu}_5\text{FeS}_4$ , card number 14-323. Underlined values are for PbS, card number 5-0592. Double underlined values are for  $\text{Cu}_{14}\text{Pb}_2\text{S}_{9-x}$ , card number 20-0360.

Experiment (51)		$\text{Cu}_{1.96}\text{S}$ (12-224)		$\text{Cu}_2\text{S}$ (12-227)		$\text{Cu}_{1.96}\text{S}$ (17-449)		$\text{Cu}_5\text{FeS}_4$ (3-1076)		Pb (4-0686)	
d	I/Io	d	I/Io	d	I/Io	d	I/Io	d	I/Io	d	I/Io
3.78	15	3.76	30	3.77	50	3.77	10				
3.35	5							3.32	30	<u>3.429</u>	<u>84</u>
3.265	38	3.26	30	3.30	50	3.27	16				
3.15	30							3.16	30		
3.12	30			3.118	25						
2.86	53									2.855	100
										<u>2.85</u>	<u>100</u>
								2.75	30		
2.75	100	1.743	100			1.74	100	2.74	50		
2.53	13			2.528	75			2.52	70		
										2.475	50
2.48	23			2.457	75					<u>2.47</u>	<u>50</u>
				2.401	100					<u>2.41</u>	<u>50</u>
2.40	13			2.398	100						
2.305	70	2.303	100			2.302	80			<u>2.969</u>	<u>100</u>
2.26	25					2.259	30				
2.09	18									<u>2.099</u>	<u>58</u>
										<u>2.09</u>	<u>75</u>
2.00	58	1.999	60	2.002	50	1.994	40				
1.975	38	1.97	60	1.972	100						
1.920	38			1.915	25						
				1.908	50						
1.885	28	1.888	30	1.879	100	1.883	35			<u>1.88</u>	<u>50</u>
1.765	15	1.767	30								
1.75	12					1.753	18			1.75	31
1.705	30	1.707	40							<u>1.71</u>	<u>30</u>
1.618	12	1.616	30								
1.495	12	1.492	30			1.495	6			1.493	32
1.406	12										
1.402	12	1.403	60								

---

## **APPENDIX G**

---

### **SOME PRACTICAL ASPECTS OF THE PROCESS**

During the course of this study, observations were made which suggested that some practical aspects of this process would have to be addressed if consideration is given to future work on the process. These are, for example, (a) the effect of electrode height versus mechanical strength of the particles, particularly of those near the bottom of the packed bed, with increasing copper extraction, (b) the modest deterioration of the performance of the Pt-Ir coating on the titanium current distributor observed during the course of this study, and (c) the potential for contamination of the cathode product by pieces of the corroding particles (which become fragile at high copper extractions) which may pass through a relatively open diaphragm. The tests conducted in this thesis showed that some solid material from the particles actually passes through the diaphragm at high copper extractions (>50-60%).

A particulate electrode is a natural application of bipolar electrolysis because a current distributor is necessary which may simultaneously serve as the cathode on its opposite side. Unfortunately, current has a tendency to "leak" around the bipolar electrodes. Some effort was given to the design of the electrode to minimize this difficulty during the course of this study. However, this is an area which would benefit from technological innovation.